

GASEOUS MERGER SIGNATURES IN EARLY-TYPE GALAXIES

Jodie Rachelle Morgan
Charlottesville, VA

B.S. Physics, University of Texas at Austin, 2000
B.A. Astronomy, University of Texas at Austin, 2000
M.A. Astronomy, University of Virginia, 2002

A Dissertation Presented to the Graduate
Faculty of the University of Virginia
in Candidacy for the Degree of
Doctor of Philosophy

Department of Astronomy

University of Virginia

May 2009



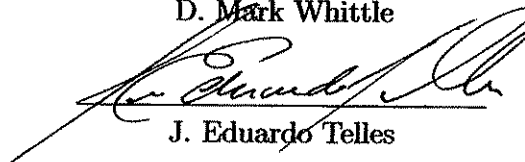
Robert W. O'Connell



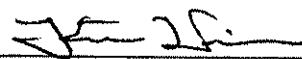
John E. Hibbard



D. Mark Whittle



J. Eduardo Telles



Keith A. Williams

© Copyright by
Jodie Rachelle Morgan
All rights reserved
May 2009

Abstract

Two samples of early type galaxies are examined through very high spatial resolution studies of the surface brightnesses, colors sensitive to small admixtures of youthful stellar populations to probe the recent and possible future star formation histories of these galaxies and the spatial distributions of stellar populations. The two samples of early type galaxies are a test sample which have stellar surface brightness profiles with a central spike in light above a smoothly increasing profile and a control sample of galaxies which do not have the central light spike. This study used the Hubble Space Telescope in the Near-Ultraviolet, the Ultraviolet, and the V bands. The high spatial resolution of $0''.027$ per pixel and the spectral sensitivity ($\langle S/N \rangle \gtrsim 10$) allow us to examine to high accuracy the spatial distribution of light in each band, the total integrated colors of the galaxies and the color changes with radius within each galaxy, and the structure and colors of the detected central components.

Bright (M_V of -10.5 to -13.5 mag) and compact (r_c of 1–16 pc) central components are detected through fits to the surface brightness profiles. Total galaxy colors, which are unaffected by the central components, as well as the radial distributions of color in the $NUV - VU - V$ plane are consistent with multiple generations and multiple structures of stellar populations in this sample of early type galaxies. Many of the compact central component colors are individually also consistent with multi-generational stellar populations.

The detections in this work of multiple spatial and temporal compositions of stellar populations in early-type galaxies, multiple generation compact stellar components coincident with the centers of some early-type galaxies lends support towards the formation of some early-type galaxies through recent (0.5 to 5 Gyr ago) gas-rich processes such as the hierarchical merging of gas-rich disk galaxies.

Table of contents

Abstract	ii
List of Figures	xi
List of Tables	xii
1 Introduction - Motivation and Review	1
2 Near-Ultraviolet Merger Signatures in Early-Type Galaxies I: Surface Brightness Profile Signatures	12
Abstract	13
2.1 Introduction	13
2.2 Sample Selection and Observations	18
2.3 Data Reduction and Analysis	23
2.3.1 Image Masks	24
2.3.2 Background Corrections	25
2.3.3 Isophotal Parameters	27
2.4 General Structure	45
2.4.1 Central Morphologies	45
2.4.2 Color Maps	46
2.4.3 Surface Brightness Profiles	48
2.5 Surface Brightness Profile Fits	51
2.5.1 Functional Forms of SBP Fits	51
2.5.2 Fitting Procedure	55
2.5.3 Comparison to Previous Nuker-Fit Studies	59
2.6 Results & Discussion	75
2.6.1 Central light properties	78
2.6.2 Central components and “Extra Light”	80
2.7 Conclusions	81
3 Near-Ultraviolet Merger Signatures in Early-Type Galaxies II: Color Signatures	88

Abstract	89
3.1 Introduction	89
3.2 Extracted Color Profiles	92
3.3 Stellar Population Models:	
SSPs and Composites	97
3.4 Results for Integrated Colors	105
3.4.1 $U - V$ Equivalent SSP Ages	108
3.4.2 Composite Populations	110
3.5 Multi-Aperture Color-Color Diagrams	124
3.5.1 Composite Synthetic Galaxies	128
3.6 Discussion	134
4 Near-Ultraviolet Merger Signatures in Early-Type Galaxies III: Central Source Identification	136
Abstract	137
4.1 Introduction	137
4.2 Central Object Sizes and Luminosities	140
4.3 Nuclear Stellar Populations	147
4.4 Nuclear Activity	151
4.5 Discussion	156
5 HI Emission in or near Early-Type Galaxies	159
Abstract	160
5.1 Introduction	160
5.2 Sample Selection	161
5.3 Observations and Data Analysis	163
5.4 Results	169
5.4.1 Individual Galaxies	170
5.4.2 Conclusions	172
6 Conclusions	191
7 The Bibliography	201

List of Figures

1.1	An example “core” Surface Brightness profile in xs and a “cusp” profile in open squares.	6
1.2	The Surface Brightness profile of an early-type galaxy with central “excess light”: NGC 7457 in the V-band.	7
1.3	The spectral energy distributions of solar metallicity 10 Myr and 12 Gyr stellar populations, upper and lower, respectively. Highlighted are the three bandpasses used here: NUV (2500 Å), U (3330 Å), and V (5550 Å)	11
2.1	(left) The surface brightness profiles of NGC 3377 in each band as produced by ELLIPSE of NGC 3377. (right) The resulting $NUV - V$ and $U - V$ color radial profiles. The open squares identify the locations where there is an erratic change in the color profiles indicating that the colors are dominated by the uncertainties in the background subtractions and, thus, indicate the edge of reliability in the U- or NUV-band. R_{Good} is the minimum of these radii, set by the $NUV - V$ color profile in this case. The measured background values and their errors for each band are indicated in the left plot.	31

2.2	Top Left: The extracted surface brightness profiles, in units of monochromatic STMAG magnitudes / \square'' , where the \times , plus, and diamond symbols represent the V, U, and NUV band profiles, respectively. The label at the $1''$ tick-mark gives the spatial scale of the profiles for each object. Middle Left: Ellipticity, ϵ , as a function of radius. Bottom Left: The fourth-order cosine moment, B_4 , of the isophotes as a percentage of the semi-major axis. ϵ and B_4 are determined from the V band images. Error bars (standard error) are present for all data points but the symbols are often much larger than the errors. Top Right: The contour plot of the central $10'' \times 10''$ of the observed V band image (north is up, east is left). There is a $1''$ bar in the lower right hand corner. The contour levels begin at $12.5 \text{ mag}/\square''$ and increase by 1 magnitude intervals. Middle Right: The $U - V$ color map. Bottom Right: The $NUV - V$ color map. Both color maps cover the same central $10'' \times 10''$ region of the galaxy as the contour plot above and bluer colors are represented by whiter shades while redder colors by blacker shades.	32
2.2.a	NGC 2778	33
2.2.b	NGC 3377	34
2.2.c	NGC 3384	35
2.2.d	NGC 3640	36
2.2.e	NGC 4239	37
2.2.f	NGC 4474	38
2.2.g	NGC 4478	39
2.2.h	NGC 4482	40
2.2.i	NGC 4570	41
2.2.j	NGC 4621	42
2.2.k	NGC 5576	43
2.2.l	NGC 7457	44
2.3	SBPs of all galaxies in $\log(I)$ - $\log(r)$ space, separated by whether they belong to the ALP (left six panels, those with central upward departures from smooth “nuker” profiles) or non-ALP (right six panels) samples. Symbols are the same as for Fig. 2.2.	49
2.4	SBPs of all galaxies in $\log(I)$ - $r^{1/4}$ space, separated by whether they belong to the ALP (left six panels) or non-ALP (right six panels) samples. Symbols are the same as for Fig. 2.2.	52
2.5	Plot of three examples of analytical surface brightness profiles: a nuker only profile, a nuker+eponential profile with a small exponential component ($r_c = 0''.03$; $r_c/r_b = 0.04$), and a nuker+eponential profile with a larger exponential component ($r_c = 0''.12$; $r_c/r_b = 0.16$). The latter “fills-in” the central region and smoothly joins with the outer region of the nuker profile.	58

2.6	Comparison of the two model fits to the V-band surface brightness profile of NGC 4239 (top) and their residuals in magnitudes (bottom). From left to right, the figure pairs show (1) the nuker only fit and (2) the nuker plus central exponential source. χ^2_ν values are listed in the residual panels.	60
2.7	Fitted surface brightness profiles for each galaxy. Left to Right: V, U, and NUV fits. Top Row: The observed surface brightness profile for each band and its best fitting model. The total best fitting composite model is represented by a heavy solid line, the “nuker” portion is a dashed line, and the central component is a thin solid line. Middle Row: Residuals (in magnitudes) between the observed profile and (\times symbols) the “nuker”-only function. Bottom Row: Residuals (in magnitudes) between the observed profile and the “nuker” plus central exponential source function (open circles). The parenthetical values in the legends are the ratios of each fits’ χ^2_ν value to that of the overall best fit. “NO” indicates the nuker-only fit and “NE” indicates the nuker plus exponential fit.	62
2.7.a	NGC 2778	63
2.7.b	NGC 3377	64
2.7.c	NGC 3384	65
2.7.d	NGC 3640	66
2.7.e	NGC 4239	67
2.7.f	NGC 4474	68
2.7.g	NGC 4478	69
2.7.h	NGC 4482	70
2.7.i	NGC 4570	71
2.7.j	NGC 4621	72
2.7.k	NGC 5576	73
2.7.l	NGC 7457	74
3.1	Isophotal mean $NUV - V$ and $U - V$ colors as a function of radius for our galaxies, with the ALP sample on the left and the “control” sample on the right. The $1''$ tickmark is labeled with the physical scale for each galaxy. Bluer colors are higher in the diagrams.	95

3.2	A comparison of five stellar population model libraries in $NUV - V$ and $U - V$ colors (given in monochromatic STMAG magnitudes). Colors are plotted as a function of burst age for three different metallicities (from left to right: sub-solar, solar, and super-solar). Bluer colors lie higher in the plots. The color range plotted for $NUV - V$ is 2 magnitudes larger than for $U - V$. References: Pégase (Fioc & Rocca-Volmerange 1997); BC03 (Bruzual & Charlot 2003); Y-Y (Yi et al. 2001); Maraston (Maraston 2005); and SB99 (Leitherer et al. 1999; Vázquez & Leitherer 2005).	99
3.3	Reference stellar population models in the $U - V/NUV - V$ color-color plane we use to analyze our galaxy photometry. Bluer colors lie to the upper right. Plotted are SSP models for three metallicities from the Pégase library and two kinds of dual-component composite populations derived from those. See text for explanation. The grey zone, representing the locus of the SSPs and the dual-metallicity composites, is reproduced in later plots.	103
3.4	The integrated galaxy colors (filled squares) plotted in the color-color diagram with the SSP and composite model loci from Fig. 3.3 superposed. Coding of model loci is as in Fig. 3.3. Error bars are plotted for all galaxy photometry, but but most are smaller than the plotting symbols. The open square at the upper right of the diagram is the SSP for 1 Gyr at solar abundance.	106
3.5	A comparison of $U - V$ colors predicted for the Pégase SSP model library as a function of age (left panel) to the total integrated colors for our galaxies (right panel). The models are separated by metallicity.	109
3.6	Results from dual-generation model fits for two galaxies. Upper panels show contour diagrams of color offsets, expressed as $\sigma = \sqrt{\chi^2}$, between models and integrated colors as a function of (τ_Y, τ_O) pairs. The models assume $2.5Z_\odot$. Lower panels give the fraction of mass in the younger component associated with each pair. Axes give the logarithm of ages in Gyr. The solid dots represent the location of the best fitting model among the limited set in our grid; however, the center of the “L” shaped region surrounded by the 1σ contours contains many other models with zero residuals.	116
3.7	Isophotal aperture photometry in the two-color diagram. The large, medium, and small diamond symbols represent the color-color data in the $r \leq 0''.1$, $0''.1 < r \leq 1''$, and $1'' < r$ regions of the color profiles, respectively. Filled circles: the colors of the central components; filled squares: integrated colors. The SSP and composite model loci from Fig. 3.3 are superposed. Coding of model loci is as in Fig. 3.3. The color center in individual plots is adjusted for the values for each galaxy, but the differential color range on each axis is the same for all panels.	118

3.7.a CCRDs of: NGCs 2778 and 3377	118
3.7.b CCRDs of: NGCs 3384 and 3640	119
3.7.c CCRDs of: NGCs 4239 and 4474	120
3.7.d CCRDs of: NGCs 4478 and 4482	121
3.7.e CCRDs of: NGCs 4570 and 4621	122
3.7.f CCRDs of: NGCs 5576 and 7457	123
3.10 The properties of a fiducial merger remnant (A) and a modified fiducial merger remnant (B). For each model, the upper left plot displays the surface mass distributions relative to the mass at $R=0$ for the total galaxy in the heavy solid line and the sub-components in lighter solid lines. Often, the dominant older population and total mass distribu- tions cannot be distinguished. The radial color profiles are presented in the bottom left plot with the $NUV - V$ colors represented by the diamonds and the $U - V$ colors by the plus signs. To the right is the CCRD with the Pégase models superposed as in Figure 3.3, with sev- eral SSP model labeled. As with the observed CCRDs, the colors are represented by open diamonds with the largest sizes at the smallest radii and smallest sizes at largest radii with changes at each decadal increase in arcseconds.	132
3.11 The radial surface mass distributions, color profiles, and 2-color dia- grams of the three synthetic, composite galaxies arranged as in Figure 3.10.	133
4.1 A comparison of the half-light radii of the central objects of galaxies in this sample, in other HST samples of various Hubble types, and of the mean values for Milky Way and Virgo Cluster globular clusters. Data are shown for different filters if more than one was used. Refs: Ferrarese et al. (2006); Côté et al. (2006) - Large Es and SOs and dwarf Es - AV VI, VIII E,SO and dE; Carollo et al. (2002) - Spirals - C02 S0a-Sd; Böker et al. (2004) - Late-type Spirals - B04 Sc-d; Côté et al. (2006); Jordán et al. (2005) - Virgo globular clusters - Virgo GCs AV VII, X; Harris (1996) - Milky Way globular clusters - MW GCs H96.	143

- 4.2 A comparison of the absolute magnitudes (in the STMAG system) of globular clusters and nuclear stellar systems cross the UV-optical band. Average values are given for the various subtypes in each sample from the literature. Metal rich ($2.5 Z_{\odot}$) SEDs from the Pégase library for ages of 100 Myr, 1 Gyr, and 10 Gyr and power-law spectra with indices of 1.8, 1.5, and 1.0 are overplotted. For clarity, the stellar population spectra are normalized at $\lambda = 5550\text{\AA}$ to -13 mags and the power-law spectra are normalized at $\lambda = 2500\text{\AA}$ to -10 mags. Sources: Ferrarese et al. (2006); Côté et al. (2006) - Large Es and SOs and dwarf Es - AV VI, VIII E,SO and dE; Ravindranath et al. (2001) - Large Es and SOs and Early-type Spirals - Ra01 E,S0,Sa; Lauer et al. (2005) - Large Es and SOs and Early-type Spirals - La05 E,S0,Sa; Lotz et al. (2004) - dwarf Es - Lo04 dE; Carollo et al. (2002) - Spirals - C02 S0a-Sd; Böker et al. (2004) - Late-type Spirals - B04 Sc-d; Côté et al. (2006); Jordán et al. (2005) - Virgo globular clusters - Virgo GCs AV VII, X; Harris (1996) - Milky Way globular clusters - MW GCs H96. 145
- 4.3 The SEDs of five individual central objects from our sample, incorporating data from this and earlier studies. The reference SEDs from Fig. 4.2 are overplotted. For clarity, the stellar population spectra are normalized at $\lambda = 5550\text{\AA}$ to -13 mags, the power-law spectra are normalized at $\lambda = 2500\text{\AA}$ to -11 mags, and the F555W value from Lauer et al. (2005) is offset in wavelength from the F555W measurements of the current work. Sources: Côté et al. (2006); Ravindranath et al. (2001); Lauer et al. (2005). 146
- 4.4 Integrated colors of the central sources plotted in the two color diagram. The grey region and lines mark the location of models from the Pégase library, as in Fig. 3.4. See text for more details. The locations of simple stellar populations of 12 Gyr age for three metallicities are labeled. 149
- 4.5 The color-color plot of Figure 4.4 expanded to include the colors of power-law spectral energy distributions (SEDs) and blackbodies. The locus of blackbodies is the solid line with filled black squares; the locus of power-law SEDs similar to those observed in AGNs is the solid line with filled triangles. 153
- 4.5 Contour plots of the Chandra X-ray images of 5 galaxies in the range of 0.5 to 8 keV covering the central $10'' \times 10''$ of each galaxy. The location of the galax nucleus is at (0,0) in all cases. All plots are aligned so that north is up and east is left. The plotted levels, in units of 1e-4 counts/sec/pixel, are for **NGC 3377**: [0.2,0.5,1,2,3,5]; **NGC 3384**: [0.8,1.5,2.5,4.5,6,7]; **NGC 3640**: [0.2,1,2,2.01,2.5,3]; **NGC 4621**: [0.2,0.5,1,2,3,5]; **NGC 7457**: [0.2,1,2,2.01,3,5]. 155

5.1.ai NGC 2634 Field of View	184
5.1.ai NGC 2634 Spectrum	184
5.1.bi NGC 2636 Field of View	185
5.1.bi NGC 2636 Spectrum	185
5.1.ci NGC 2778 Field of View	186
5.1.ci NGC 2778 Spectrum	186
5.1.di NGC 3193 Field of View	187
5.1.di NGC 3193 Spectrum	187
5.1.ei NGC 3377 Field of View	188
5.1.ei NGC 3377 Spectrum	188
5.1.fi NGC 3384 Field of View	189
5.1.fi NGC 3384 Spectrum	189
5.1.gi NGC 5576 Field of View	190
5.1.gi NGC 5576 Spectrum	190

List of Tables

2.1	Basic Data for Sample	21
2.2	Observational Details	22
2.3	Sky Brightnesses	28
2.4	Mean Geometric Parameters From ELLIPSE	28
2.5	Surface Brightness Fit Results	83
2.5	Surface Brightness Fit Results	84
2.6	Integrated Total Absolute Magnitudes	85
2.6	Integrated Total Absolute Magnitudes	86
2.7	Central Object Contributions	87
3.1	Integrated colors.	94
3.2	SSP-Equivalent Ages for Integrated Colors	111
3.3	Dual-Generation Fits to Integrated Colors	117
3.4	Fiducial Merger Remnant and Synthetic Galaxy Stellar Population Components	131
4.1	Central Object Properties	142
4.2	Xray Emission Properties	158
5.1	Basic Data of Sample	176
5.1	Basic Data of Sample	177
5.1	Basic Data of Sample	178
5.2	HI Measurements and IRAS Dust property estimates.	179
5.2	HI Measurements and IRAS Dust property estimates.	180
5.2	HI Measurements and IRAS Dust property estimates.	181
5.3	Detected HI Emission Features, Integrated Fluxes and Residuals . . .	182
5.4	Residual HI Masses and other properties	182
5.5	Typical Dust and gas quantities of galaxy samples.	183

Chapter 1

Introduction - Motivation and Review

Historical Overview

Many decades of photographic, ground-based observations led to the general picture of two species of galaxies - ellipticals and spirals - with little overlap in the form of S0 galaxies. Elliptical galaxies were thought to be structurally simple and to evolve passively as they appeared to contain no or nearly no gas thus being overwhelmingly dominated by their stellar component. The stars within an elliptical form a single, oblate spheroid distribution with varying ellipticity from galaxy to galaxy (de Vaucouleurs et al. 1991; de Vaucouleurs & Pence 1979). Elliptical galaxies are generally dynamically hot or don't rotate but some with higher ellipticities and dimmer absolute brightnesses have some rotation (Davies et al 1983). The stars were thought to be uniformly old, typically older than 10 Gyr, yet often had metallicity gradients such that the central regions of a galaxy were more metal-rich than its outer regions (i.e.- Davis et al 1985, Franx Illingworth and Heckman 1989, Peletier 1990).

In contrast, the spiral galaxies are structurally complex and actively evolve with a bulge (which are dynamically hot like mini-elliptical galaxies), a halo, and a dynamically cold rotating disk stellar sub-structures as well as gas fueling on-going star formation (de Vaucouleurs et al. 1991; de Vaucouleurs & Pence 1979). The intermediate-morphology galaxies, the S0s, have substantial bulges as well as disks of stars and gas.

The apparent morphological dichotomy in galaxies led to the view that ellipticals and S0s, or early-type galaxies (ETGs), formed in the early universe when the universe was very dense by the monolithic collapse of isolated protogalactic clouds (Eggen et al. 1962). A monolithic collapse causes a significant starburst event which forms all the stars in the ETG after which, the fuel is fully consumed and the stars passively evolve and fade.

Through a study of the tidal responses of galaxies during their interactions, Toomre & Toomre (1972) postulated that interactions between galaxies should be common. The remnants of galaxy interactions should be normal galaxies since peculiar morphologies are so uncommon, and that, in fact, strong interactions between gaseous disk galaxies may form gas-poor remnant galaxies with very different stellar dynamics or elliptical galaxies.

The idea that elliptical galaxies are not necessarily formed in isolation but could be the results of mergers between gaseous disk galaxies met with skepticism in part because the dissipationless merging of disks was not expected to produce the high central densities characteristic of early types (Ostriker 1980; Gunn, J. E., 1987). This objection was overcome by the realization that the gaseous component of disk galaxies can dissipate a large amount of energy and flow to the central region, inducing concentrated star formation in the merger remnant (Toomre & Toomre 1972; Negroponte & White 1983; Barnes & Hernquist 1991; Kormendy & Sanders 1992).

Deep observations of the prototypical merger remnant, NGC 7252 (Schweizer, F. 1978; Schweizer 1982), provided firm support for the dissipational merger scenario, as it was shown to be the result of the merger of gas rich disk galaxies (Hibbard et al. 1994; Hibbard & Mihos 1995) and yet to have both a light profile (Schweizer 1982) and a phase space density (Lake & Dressler 1986) characteristic of ETGs.

The spatial resolution provided by the Hubble Space Telescope (HST) and the numbers of uniformly studied galaxies through large all-sky surveys such as the Sloan Digital Sky Survey (SDSS) lead to an understanding of ETGs which grows increasingly complex and to a better understanding of how the morphologies of galaxies go through transitions and evolve.

Colors and Stellar Populations

In rest-frame U-V (which is a proxy for recent star formation) vs. M_V , early samples of ETGs formed what is known as the “red-sequence” where ETGs of dimmer M_V have bluer U-V colors though all the ETGs are redder (U-V > 1.0 mag) than the spiral galaxies which occupied a “blue-cloud” in the same frame indicating that ETGs are not actively forming stars and that spirals are (i.e.- Bower et al 1992a,b). The large surveys such as SDSS, Galaxy Evolution from Morphology and Spectral energy distributions (GEMS), and Classifying Objects by Medium-Band Observations - 17 (COMBO-17), have been used to fill in the rest-frame U-V vs. M_V space with the color-magnitude results of thousands of galaxies. While the general trend is still observed that ETGs occupy a “red-sequence” and spirals a “blue-cloud” there is significant cross-contamination. Many ETGs, identified by their hot stellar dynamics, have the blue colors of spirals and vice-versa suggesting that many ETGs have acquired fresh fuel supplies and began star-forming (e.g. Bell et al. 2004, De Lucia et al. 2004, Schiavon et al. 2006, Bell et al. 2007, Faber et al. 2007, Conselice et al. 2007, Kaviraj et al. 2008).

High precision spectrophotometry has demonstrated the presence of stellar populations in the centers of nearby ETGs with mean ages younger than classically expected at up to ~ 7 Gyr though older than 0.5 Gyr, and that they have therefore experienced significant star formation since $z \sim 1$ (e.g. Trager et al. 2000, Caldwell et al. 2003, Thomas et al. 2005, Proctor et al. 2005, Schiavon 2007, Sánchez-Blázquez et al. 2007, Trager et al. 2008, Sarzi et al. 2008).

Surface Brightness Anomalies

The surface brightness profiles of most ETGs are well-described by Sérsic functions which go as $\log I(r) \sim -k r^{1/n}$ (Sérsic 1968; Caon et al. 1993) over many decades of radii from $r \sim \text{a few}''$ to a few $\times 100''$ or $\times 1000''$, depending on how large the galaxy

is. ETG light profiles show significant variation at small radii ($0''.03 < r < 10''$), as observed with HST (Byun et al. 1996; Rest et al. 2001; Ravindranath et al. 2001). The simple variations are collected into two groups known as “cusp” and “core”, examples of which are presented in Figure 1.1. The “cusp” galaxies have continuously increasing brightnesses from large radii into the smallest observable radii while the “core” galaxies display a break in their brightness profiles such that their brightnesses appear depressed relative to the larger scale Sérsic profiles. The parameter, γ , is used to quantify the central slope and the two groups are split at about $\gamma = 0.3$ to 0.4 . The central properties appear to be related to larger-scale properties of the galaxies as the central brightness slopes correspond to mass and rotation. The “core” galaxies have higher masses and little to no rotation while the reverse of true for the “cusp” galaxies (Faber et al, 1997).

More complex brightness features were also discovered at the centers of ETGs with the high spatial resolution of HST. Of particular interest is the presence of “excess light” which in many cases may be stellar nuclei (Byun et al. 1996; Rest et al. 2001; Ravindranath et al. 2001; Ferrarese et al. 2006; Côté et al. 2006), see Figure 1.2 for an example. These serendipitously discovered “excess light” features appear strikingly similar to the predicted “excess light” at the centers of remnant galaxies in gaseous galaxy merger simulations (Mihos & Hernquist 1994a) though the observed features are far smaller than those predicted.

Gaseous Merger Models

In a typical gaseous merger model, two equal-mass disk galaxies, with $\sim 10\%$ of their disk mass in the form of gas, fall together and merge. The pre-existing stars undergo violent relaxation while much of the gas ($\gtrsim 50\%$) flows into the central few hundred parsecs, producing a central rise in the surface mass density profile of the

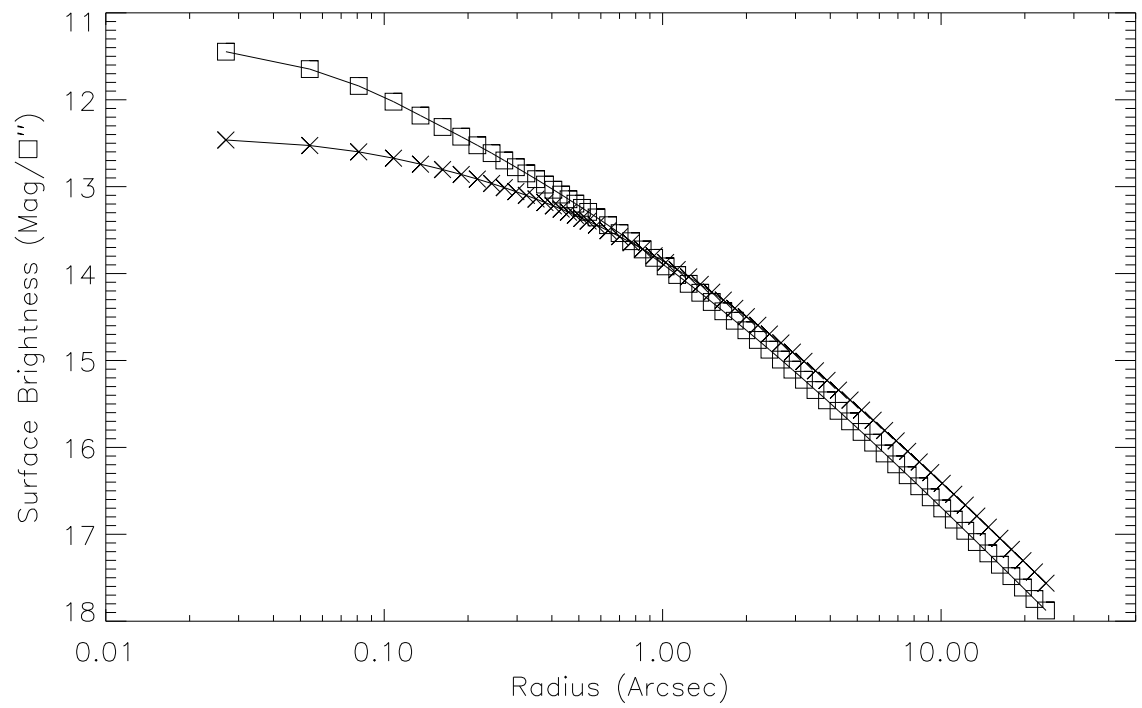


Fig. 1.1.— An example “core” Surface Brightness profile in **xs** and a “cusp” profile in open squares.

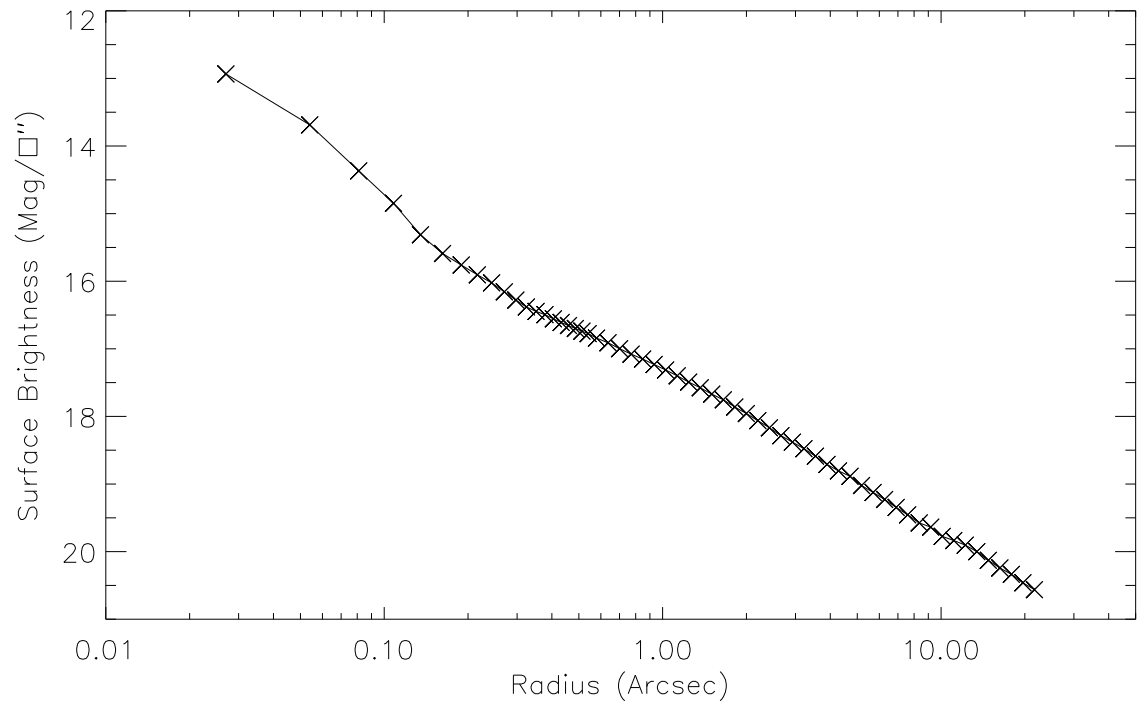


Fig. 1.2.— The Surface Brightness profile of an early-type galaxy with central “excess light”: NGC 7457 in the V-band.

remnant (e.g. Mihos & Hernquist 1994b; Springel 2000; Springel & Hernquist 2005, Ferreras et al. 2002; Cox et al. 2006, Hopkins et al. 2008a). This central knot of gas will undergo rapid star formation, leaving a dense burst population that lies within a projected radius of a few hundred parsecs (\sim a few arcseconds at a distance of 30 Mpc). At the far end of the tidally stretched streams of gas, there are gas particles which can have enough energy to reach escape velocity and leave the merger remnant (Barnes 2002).

The expected observational signatures of a merger-induced population include a discontinuity in the surface brightness profile and a younger spectral energy distribution (SED) than the main body of the galaxy, with a bluer continuum and absorption lines from warmer turnoff stars. With time, the stars will fade, reducing the profile discontinuity and population age differences. This general picture is supported by observations of the light profiles of recent merger remnants (Hibbard & Yun 1999, Rothberg & Joseph 2004, Hopkins et al. 2008a), E+A galaxies (Yang et al. 2004) and even otherwise normal ETGs (Kormendy 1999, Hopkins et al. 2008a, Kormendy et al. 2008).

The Need for Ultraviolet Stellar Population Studies

In hierarchical formation models, ETGs are assembled over a prolonged period from multiple mergers of smaller systems, many of them gaseous. This implies that the ETGs should contain multi-epoch stellar populations with the youngest and the most diverse populations at their centers. To date, the full advantage of the spatial resolution of HST has not been utilized to probe the central-most stellar populations of ETGs.

The “near-Ultraviolet” spectral region (1800 - 2800Å) is 3-10 times more sensitive to population ages and abundances than is the optical-band (Dorman et al. 2003)

when observed in a vacuum environment such as with the Galaxy Evolution Explorer (GALEX, Martin et al. 2005) or the Hubble Space Telescope (HST). That is because the spectral energy distributions (SED) of stellar populations in this region changes rapidly with the temperature (and hence age) of the main sequence turnoff, whereas the optical is dominated by the red giant branch, which has little age sensitivity. In the near-UV, even small admixtures of intermediate age components are detectable against an old background population. A number of nearby ETG samples exhibit considerably larger intrinsic scatter in colors including a near-UV filter than in optical-band colors (e.g. Ferreras & Silk 2000, Yi et al. 2005, Kaviraj et al. 2007, Schawinski et al. 2007, Kaviraj et al. 2008), and this implies that at least 20-30% of early types have experienced some star formation within the past 1 Gyr.

Neutral HI in ETGs

During a gaseous merger event, the gas that does not fall into the remnant center forms streamers and escaped gas particles which can be observed as rings, filaments, and clumps of gas in the environmental regions about merger remnants which should be detectable for a few Gigayears. Such environmental gaseous features have been observed about ETGs providing additional evidence that they may form from gaseous merger events (e.g. - Schiminovich et al, 2001; Hibbard & Sansom 2003; Horellou et al 2001).

Thesis Goals

Through the detailed study of the central-most stellar population compositions and the gas content of ETGs, the transitions of galaxies into ETGs can be more fully understood.

In this thesis, we examine two samples of ETGs through very high spatial resolution studies of the surface brightnesses, colors sensitive to small admixtures of

youthful stellar populations, and through a deep, neutral hydrogen gas survey to probe the recent and possible future star formation histories of these galaxies and the relative spatial distributions of older and younger populations. The two samples of ETGs are a test sample which have stellar surface brightness profiles with a central spike in light above a smoothly increasing profile and a control sample of galaxies which do not have the central light spike. The two samples were drawn from the monochrome surveys of ETGs with the Hubble Space Telescope which produced published high spatial resolution surface brightness profiles (Byun et al. 1996; Rest et al. 2001; Ravindranath et al. 2001) and from the set of ETGs with no evidence of either active galactic nuclei or dust as both features can alter the apparent distribution of stellar emission.

The first study involved photometry of twelve galaxies (six test, six control) using the High Resolution Camera of the Advanced Camera for Surveys on the Hubble Space Telescope in the Near-Ultraviolet, the Ultraviolet, and the V bands (Figure 1.3). The high spatial resolution of $0''.027$ per pixel and the spectral sensitivity ($< S/N > \gtrsim 10$) allow us to examine to high accuracy the spatial distribution of light in each band (Chapter 2), the total integrated colors of the galaxies and the color changes with radius within each galaxy (Chapter 3), and the structure and colors of the detected central components (Chapter 4). The second study surveyed 20 test and 35 control galaxies to previously unsurpassed sensitivity ($\lim(M_{HI}) \sim 1e7 M_{\odot}$) and examined the neutral hydrogen content in the environments of ETGs (Chapter 5). We summarize the detected signatures which may indicate that star formation within the sampled early-type galaxies continued up until recent (within a few Gigayears) times in Chapter 6.

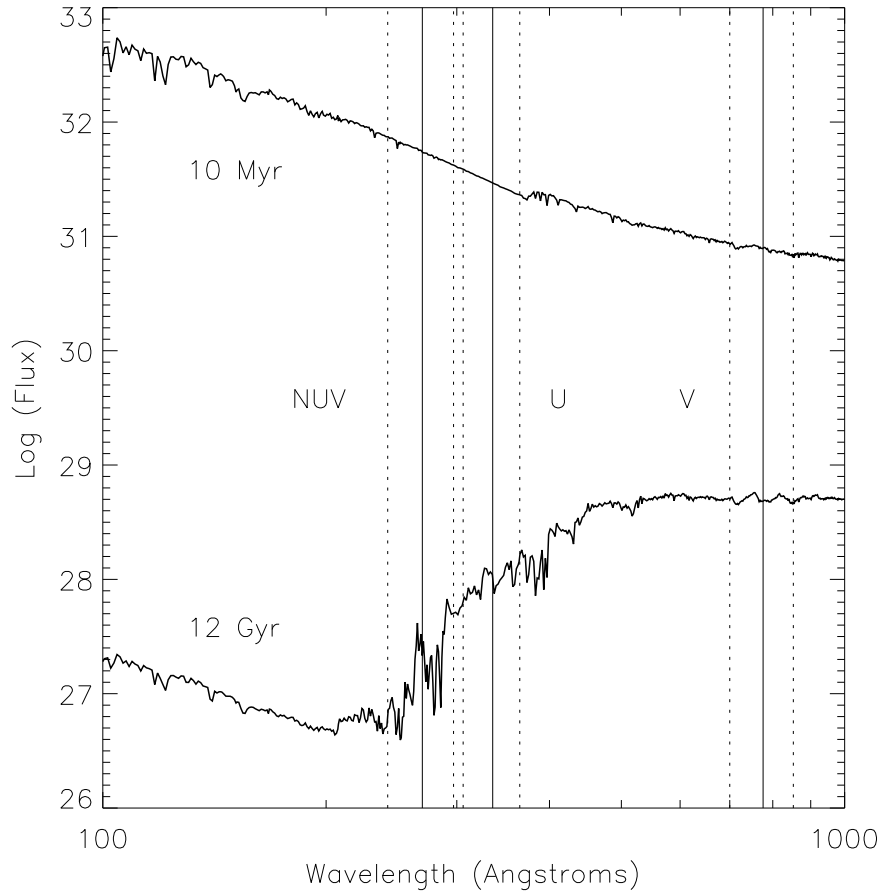


Fig. 1.3.— The spectral energy distributions of solar metallicity 10 Myr and 12 Gyr stellar populations, upper and lower, respectively. Highlighted are the three bandpasses used here: NUV (2500 Å), U (3330 Å), and V (5550 Å)

Chapter 2

Near-Ultraviolet Merger

Signatures in Early-Type Galaxies

I: Surface Brightness Profile

Signatures

Abstract

We present high quality, high resolution optical and NUV observations of 12 nearby early type galaxies taken with the High Resolution Camera of the Hubble Space Telescope. Half of the sample were selected because their light profiles (in V, R, or H) showed deviations from smooth power laws in previous studies which we refer to as Anomalous Light Profiles (ALPs), while the other half showed no such deviations. We present light profiles and isophotal parameters in the NUV, U, and V-bands, and $NUV - V$ and $U - V$ color images. We fit the surface brightness profiles with a double-power law function, both with and without an extra central component. We find that the profiles of nine out of the 12 systems (all six ALPs and three non-ALPs) are fit significantly better with composite functions. Seven of the nine central components are extended, but with quite small scale radii (1-15 pc). The central components can be quite bright with M_V ranging from -10.4 to -14.8 yet only contribute less than 1.5% of the observed galaxy light. These compact, bright, central components are not the canonical extra light regions produced during recent star formation episodes of gaseous merger events but constitute another type of object whose properties have yet to be fully explored, possibly related to the stellar clusters discovered in the central regions of many spiral and spheroidal galaxies.

2.1 Introduction

The idea that early-type galaxies could be formed through the merger of disk galaxies (Toomre & Toomre 1972) contradicted the prevailing view that they formed from the collapse of isolated protogalactic clouds in the early universe (Eggen et al. 1962). It was met with skepticism in part because the dissipationless merging of disks was not expected to produce the high central densities characteristic of early types (Ostriker

1980; Gunn, J. E., 1987). This objection was overcome by the realization that the gaseous component of disk galaxies can dissipate a large amount of energy and flow to the central region, inducing concentrated star formation in the merger remnant (Toomre & Toomre 1972; Negroponte & White 1983; Barnes & Hernquist 1991; Kormendy & Sanders 1992). Observations of the prototypical merger remnant NGC 7252 (Schweizer, F. 1978; Schweizer 1982) put the dissipational merger scenario on firm observational ground, as it was shown to be the result of the merger of gas rich disk galaxies (Hibbard et al. 1994; Hibbard & Mihos 1995) and yet to have both a light profile (Schweizer 1982) and a phase space density (Lake & Dressler 1986) characteristic of early-type galaxies (ETGs). With the advent of hierarchical cosmologies, the merger hypothesis has reached broader acceptance.

In hierarchical formation models, ETGs are assembled over a prolonged period from mergers of smaller systems, many of them gaseous, which implies that they should contain multi-epoch stellar populations. The nature of these will depend on the characteristics of each merger event, especially the mass ratio and gas fractions of the progenitors and the subsequent distribution of gas in the descendant system. Modern computational power enables sophisticated numerical simulations to follow the dissipational inflow of gas and the subsequent starburst during a gaseous merger. (e.g. Barnes 1992, Springel 2000). Early numerical models were resolved to scales of 100 to 500 pc for Milky Way size-scale galaxies, and current models can reach ~ 50 pc.

In a typical gaseous merger model, two equal-mass disk galaxies, with $\sim 10\%$ of their disk mass in the form of gas, fall together and merge. The pre-existing stars undergo violent relaxation while much of the gas ($\gtrsim 50\%$) flows into the central few hundred parsecs, producing a central rise in the surface mass density profile of the

remnant (e.g. Mihos & Hernquist 1994b; Springel 2000; Springel & Hernquist 2005, Ferreras et al. 2002; Cox et al. 2006, Hopkins et al. 2008a). This central knot of gas will undergo rapid star formation, leaving a dense burst population. Each burst generation will be dispersed to some extent by later mergers. Absent other dynamical effects (e.g. scouring by binary black holes - see Kormendy et al. 2008 and references therein), the most concentrated population of younger stars should lie within a projected radius of a few hundred parsecs (\sim a few arcseconds at a distance of 30 Mpc). The observational signatures of a merger-induced population should be a discontinuity in the surface brightness profile and a younger spectral energy distribution (SED) than the main body of the galaxy, with a bluer continuum and absorption lines from warmer turnoff stars. With time, the stars will fade, reducing the profile discontinuity and population age differences. This general picture is supported by observations of the light profiles of recent merger remnants (Hibbard & Yun 1999, Rothberg & Joseph 2004, Hopkins et al. 2008a), E+A galaxies (Yang et al. 2004) and even otherwise normal ETGs (Kormendy 1999, Hopkins et al. 2008a, Kormendy et al. 2008).

Recently, high precision, integrated light spectrophotometry has convincingly demonstrated that the centers of many nearby ETGs have light-weighted mean ages above 0.5 Gyr but less than ~ 7 Gyr (half a Hubble time), and that they have therefore experienced significant star formation since $z \sim 1$ (e.g. Trager et al. 2000, Caldwell et al. 2003, Thomas et al. 2005, Proctor et al. 2005, Schiavon 2007, Sánchez-Blázquez et al. 2007, Trager et al. 2008, Sarzi et al. 2008). These late episodes of star formation are more prevalent among lower luminosity galaxies and in lower density environments. These results comport with the general expectations of the hierarchical merger picture. They are also consistent with a number of studies of the evolution of luminosity functions and SEDs of intermediate redshift “red sequence” populations (e.g. Bell et

al. 2004, De Lucia et al. 2004, Schiavon et al. 2006, Bell et al. 2007, Faber et al. 2007, Conselice et al. 2007, Kaviraj et al. 2008).

The value of vacuum ultraviolet observations for detecting intermediate age (0.5 - 5 Gyr) populations in ETGs has been emphasized by a number of recent papers, most of them based on broad-band observations made with the Galaxy Evolution Explorer (GALEX, Martin et al. 2005). The spectral region covered by the GALEX “near-UV” filter (1800 - 2800 Å) is 3-10 times more sensitive to population ages and abundances than is the optical-band (Dorman et al. 2003). That is because the SED in this region changes rapidly with the temperature (and hence age) of the main sequence turnoff, whereas the optical is dominated by the red giant branch, which has little age sensitivity. In the near-UV, even small admixtures of intermediate age components are detectable against an old background population. A number of nearby ETG samples exhibit considerably larger intrinsic scatter in colors including a near-UV filter than in optical-band colors (e.g. Ferreras & Silk 2000, Yi et al. 2005, Kaviraj et al. 2007, Schawinski et al. 2007, Kaviraj et al. 2008), and this implies that at least 20-30% of early types have experienced some star formation within the past 1 Gyr.

Although the evidence is therefore good that ETGs contain multiple generations of stars, their temporal and spatial distributions remain to be established. They might be fueled not by strong interactions but by recycling of mass lost during advanced stellar evolution, accretion from the intergalactic medium, or capture of small gas-rich satellites, for instance. To explore the mechanisms driving late star formation in ETGs, it is important to try to map out the spatial structure of intermediate age populations in ETGs.

Many high resolution imaging studies of ETGs have been conducted with the

Hubble Space Telescope (HST) at pixel scales of $0''.04 - 0''.05$ per pixel (Ferrarese et al. 1994; Lauer et al. 1995; Faber et al. 1997; Rest et al. 2001; Ravindranath et al. 2001; Ferrarese et al. 2006). These have established the general structural features of ETGs and find increasingly good evidence for centrally concentrated merger-induced stellar populations (e.g. Kormendy 1999, Hopkins et al. 2008a, Hopkins et al. 2008b, Kormendy et al. 2008). However, these studies were not intended to study population age structure and most did not examine color gradients. They were also confined to wavelengths redward of 4500 \AA , which are not very sensitive to population age.

Our approach in this work is to extend the study of ETG structure at HST resolution to the near-UV band. We use the High Resolution Camera (HRC) of the Advanced Camera for Surveys (ACS) on HST (with $0''.027$ per pixel) and two filters centered below 4000 \AA to provide a sensitive wavelength lever for detection of multiple, centrally concentrated, intermediate age populations. HRC spatial resolution is higher than the cameras used in earlier work (mainly the Wide Field Camera 2 and the ACS/Wide Field Camera), though the field of view is smaller ($27''$).

We study two small samples of ETGs having earlier HST observations: a group that shows evidence of a discontinuity in their central light profiles possibly related to mergers, and a “control” sample of objects that lack such features. This is the first high resolution, high signal-to-noise study of the UV/optical spatial profiles and color structure and their implications for stellar population in ETGs. (The GALEX studies cited above were limited to a resolution of $\sim 6''$ by the optics and detector employed.)

This paper is organized as follows. Section 2 summarizes the sample selection and description of the observations. The methodology of our data reduction is described in Section 3. In Section 4, we summarize the observed features in the science-ready

color images, morphology distributions, and surface brightness profiles. The surface brightness profile fitting analysis is presented in Section 5. In Section 6, we discuss the implications of the surface brightness decompositions for the evolution of early-type galaxies. In Chapter 3 of this Thesis we present an analysis of our multi-color data.

2.2 Sample Selection and Observations

The outer regions of elliptical galaxies have smooth, featureless projected surface brightness profiles (SBPs) that are well described by “Sérsic functions” with $\log I(r) \sim -k r^{1/n}$ (Sérsic 1968; Caon et al. 1993). Good examples of Sérsic fits to modern HST and ground-based data are shown in Ferrarese et al. (2006), Hopkins et al. 2008a, 2008b, and 2008c, and Kormendy et al. (2008). Hopkins et al. (2008a) and Kormendy et al. (2008) argue that the physical origin of this characteristic light distribution is the violent, collisionless gravitational interactions of pre-existing stars in the disks of the progenitor systems that undergo a merger.

Most HST studies of SBPs are confined to the central regions of galaxies ($r \lesssim 20''$). Here, the best fits are found to be broken power laws, where each component is described by $I_i(r) \sim r^{-m_i}$, in which the outer component presumably joins smoothly with the large-radius Sérsic profile (Ferrarese et al. 1994; Lauer et al. 1995; Byun et al. 1996). The best-known version of a broken power law is the “nuker” profile of Lauer et al. (1995), which is described in more detail in §2.5.

We chose galaxies for this study based on their departures from the standard nuker fits in earlier monochromatic HST investigations. Since our goal is to explore the properties of spatially extended stellar populations and not activity related to supermassive black holes (SMBHs), we excluded galaxies with identified active galac-

tic nuclei (AGN), radio continuum emission, or non-thermal X-ray emission. We also excluded systems with obvious dust features. From the remaining objects, we selected six galaxies that showed significant excess light with respect to a nuker profile from Byun et al. (1996, in the F555W filter), Rest et al. (2001, in the F702W filter), and Ravindranath et al. (2001, in the F160W filter). The excess light in these galaxies typically dominates the profiles within $0''.5$, and the galaxies with these features are often described as “nucleated”. In this paper, we refer to profiles with these features as Anomalous Light Profiles (ALPs) to emphasize that they may not be associated with SMBHs. Because there were no earlier studies of galaxies at high resolution in the near-UV, we also included a sample of six non-ALP “control” galaxies. (These are “controls” only in the sense of having normal nuker light profiles in previously published work; they may exhibit unusual color structures here.) The sample includes seven Es, one dE and four S0s; three galaxies (NGC 4478, NGC 4621, NGC 7457) have kinematically decoupled components (Morelli et al. 2004, Emsellem et al. 2004).

We note that our definition of an ALP may be related to but is not equivalent to the “extra” or “excess” light components that have been identified in merger remnants (Rothberg & Joseph 2004; Hopkins et al. 2008a) and ETGs (Kormendy 1999; Hopkins et al. 2008b; Kormendy et al. 2008). The latter are defined with respect to the inward extrapolation of the outer Sérsic functions or double Sérsic function fits, and have typical scales of $\gtrsim 100$ pc, larger than most ALPs but comparable in size with the post-starburst components in numerical simulations of gas-rich mergers. Since our imaging field of view does not extend much beyond the “extra Sérsic light” components, we cannot use our images to determine the spatial structure of these regions with respect to the outer parts of the galaxies. However, our integrated colors will provide information on their star formation histories.

Our observing program (HST-GO-10435) consisted of imaging with the ACS-HRC instrument in the three bands F250W, F330W, and F555W, which for brevity we will refer to as the NUV, U, and V bands, respectively. The F330W filter is equivalent to the ground-based broad-band U filter. The F250W filter has a central wavelength of 2696 Å and a width of 549 Å; it lies about 300 Å redward of the GALEX NUV filter. The camera and bands were chosen for their high spatial resolution and sensitivity to intermediate-aged stellar populations. The pixel scale of the HRC is $0''.027 \text{ pix}^{-1}$ with a $27'' \times 27''$ field of view. The point spread function (PSF) full width half maxima, θ_λ , are very similar in each filter at $\theta_{NUV} = 0''.046$, $\theta_U = 0''.046$, and $\theta_V = 0''.056$, though they differ in structure (Anderson & King 2004). Average exposure times of 2550, 1900, and 430 seconds, respectively, were chosen to achieve similar sensitivity levels across the bands. The observations required two HST orbits per galaxy, and each exposure was dithered in four positions per filter for sub-pixel sampling and cosmic ray cleaning.

The sample galaxies are nearby, with distances¹ ranging 10.75 to 27 Mpc. The linear scale of θ_{NUV} then corresponds to 2.5 to 6.0 parsecs. Our field of view (FOV) corresponds to physical sizes in the range of 1.5-3.5 kpc on a side. The B-band absolute magnitudes range from -17.9 to -21.3. The effective radii (de Vaucouleurs et al. 1991) range from $13''$ to $40''$, which means that our FOV contains roughly 20-50% of the total B-band light of a given galaxy. Summaries of the basic data for our sample and observations are given in Tables 2.1 and 2.2.

¹We adopt $H_o = 72 \text{ km/s/Mpc}$ throughout this paper

Table 2.1. Basic Data for Sample

Galaxy NGC (1)	Type (2)	ALP (3)	B_T mag (4)	A_B mag (5)	m-M mag (6)	M_B mag (7)	Distance Mpc (8)	r_e kpc (") (9)
2778	E		13.39	0.09	31.80 ± 0.30^b	-18.50	22.9 ± 3.2	1.7(15.7)
3377	E5-6		10.97	0.15	30.25 ± 0.09^b	-19.43	11.22 ± 0.47	1.9(34.4)
3384	SB0-	x	10.68	0.12	30.16 ± 0.14^c	-19.60	10.76 ± 0.69	1.3(25.0)
3640	E3		11.10	0.19	32.16 ± 0.13^b	-21.25	27.0 ± 1.6	4.2(32.1)
4239	E	x	13.59	0.12	31.34 ± 0.17^d	-17.87	18.5 ± 1.5	1.4(15.4)
4474	S0pec	x	12.28	0.18	30.96 ± 0.07^a	-18.86	15.56 ± 0.50	1.6(20.8)
4478	E2	x	12.07	0.11	31.15 ± 0.06^a	-19.19	16.98 ± 0.47	1.1(13.4)
4482	dE,N	x	13.41	0.12	31.29 ± 0.06^a	-18.00	18.11 ± 0.50	1.8(20.3)
4570	S0(7)		11.67	0.10	31.16 ± 0.06^a	-19.59	17.06 ± 0.47	1.5(17.7)
4621	E5		10.62	0.14	30.87 ± 0.06^a	-20.39	14.93 ± 0.41	2.9(40.5)
5576	E3		11.80	0.14	32.03 ± 0.14^b	-20.37	25.5 ± 1.6	2.2(18.1)
7457	SA0-	x	11.82	0.22	30.45 ± 0.21^c	-18.85	12.3 ± 1.2	1.9(32.1)

Note. — (2) The morphological types are from NED. (3) The x s designate membership in the ALP sample. The remainder are controls (Section 2). (4) The total apparent B band magnitude from de Vaucouleurs et al. (1991) except for NGC 4482 which is from de Vaucouleurs & Pence (1979). (5) Foreground B band extinction (Schlegel et al. 1998). (6) The surface brightness fluctuation distance moduli from: (a) Mei et al. (2007), (b) Tonry et al. (2001), (c) Jensen et al. (2003), (d) Faber et al. (1989). (7) Absolute magnitudes from the B_T and distance moduli corrected for extinction. (8) Distances in Mpc from the distance moduli. (9) The effective radii (containing half the total light in the B band) in kiloparsecs and arcseconds from de Vaucouleurs et al. (1991) except for NGC 4482, which is from Ferrarese et al. (2006) in the g-band.

Table 2.2. Observational Details

Galaxy NGC (1)	Date (2)	τ_{NUV} sec (3)	τ_U sec (4)	τ_V sec (5)	θ_{NUV} pc (6)
2778	2005 Apr 20	2612	1940	460	5.1
3377	2005 Jul 08	2552	1912	432	2.5
3384	2005 Jun 04	2552	1912	432	2.4
3640	2005 Jul 19	2536	1904	424	6.0
4239	2005 Jul 27	2560	1912	432	4.1
4474	2005 Jul 14	2552	1912	432	3.5
4478	2005 Jul 28	2552	1912	432	3.8
4482	2005 Nov 26	2552	1840	360	4.0
4570	2005 Aug 02	2544	1904	424	3.8
4621	2005 Jun 03	2552	1912	432	3.3
5576	2005 Jul 30	2500	1880	424	5.7
7457	2005 Jan 01	2552	1912	432	2.7

Note. — (2) The date of the observations. (3-5) The exposure times for each filter. (6) The full width half maximum of the PSF in the NUV band converted to parsecs.

2.3 Data Reduction and Analysis

We used the ACS calibration pipeline software, `CALACS`, to perform bias and dark subtraction, flat fielding, and overscan removal. The sub-exposures were then combined using `MULTIDRIZZLE` (Koekemoer et al. 2002), a task in `PyRAF`, which we ran without sky subtraction. `MULTIDRIZZLE` performs the cosmic-ray rejection, registers the images according to their World Coordinate System positions, conducts the distortion correction for the ACS camera, and converts the images to count rates, $c_{x,y}$ ($e^- \text{ pix}^{-1} \text{ sec}^{-1}$). For the purpose of maintaining accurate statistics throughout the analysis, the exposure times were multiplied back in to produce total count images, $C_{x,y}$ ($e^- \text{ pix}^{-1}$). The final images are 1241×1146 pixels ($33''.5 \times 31''$), though thin wedges along the sides of the image area are not illuminated.

Although many earlier HST studies of brightness profiles have used image deconvolution to enhance spatial resolution further, we chose not to do that because of the concern that this might produce artifacts in the multi-color images. Instead, we used the images without deconvolution to study surface brightness profiles, and convolved our model fitting functions to match. For extraction of colors, we convolved the observed images to the same effective PSF. We used `TinyTim` (Krist & Hook 1997) to produce the PSF images for each galaxy in each band at the average position of the center of the galaxy in the four sub-exposures. The PSFs were used to make image masks for model convolution and image smoothing. A smoothed set of galaxy images was created by convolving images in a given band with the PSF images of the other two bands. The FWHM of the combined PSF (i.e. the result of the convolution of all three PSFs) is $0''.086$. All magnitudes in the NUV, U, and V bands discussed in this paper are given in the monochromatic STMAG system: $m_\lambda = -2.5 \log(f_\lambda) - 21.1$, where f_λ is the mean flux density within each filter in units of $\text{ergs sec}^{-1} \text{ cm}^{-2} \text{ \AA}^{-1}$.

2.3.1 Image Masks

We created bad pixel masks, which are images that identify structures on the scale of the PSF, such as dust, foreground stars, and star clusters, using “structure maps”, following the method of Pogge & Martini (2002). For this sample, structure maps, S , were made from the V-band images for each galaxy:

$$S = \left[\frac{C}{C \otimes P} \right] \otimes P^t \quad (2.1)$$

where C designates the science image, P the PSF image, and P^t is the transpose of the PSF image. A featureless science image with a PSF that is symmetric under transposition should produce a structure map that is flat with a mean value of 1.0. Our science images are mostly flat with broad peaks at the galaxy centers and PSF-sized peaks at the locations of the globular clusters, foreground stars, background AGN or galaxies, etc. The non-illuminated portions of the images left by the distortion correction and the side regions where only two sub-exposures were combined due to the dithering pattern are masked out and comprise 23% of the final image size. The standard deviation, σ , of the structure maps was calculated, and the pixels with values below -5σ and above 3σ were also masked. The pixels selected by the high and low deviation cuts are dominated by bad pixels, the occulting bar shadow, dust, foreground stars, and globular clusters; these account for only 0.01% – 0.2% of the science frames. The central regions of the galaxies can also exceed the $+3\sigma$ threshold, however, these regions were protected during the mask selection process.

While we do mask out features which include foreground stars, globular clusters, and dust, the galaxies are very smooth and do not exhibit characteristics such as super star clusters or spiral arm features which could indicate active star formation. NGC 3377 was known a priori to have filamentary dust. In the current imagery, the

dust can be seen in finer detail. It does extend all the way to the center yet is still filamentary in nature and is adequately masked.

2.3.2 Background Corrections

The FOV of the HRC is small, while the sample galaxies are large. In the V band, galaxy light is expected to dominate over the sky background throughout the FOV, so no uncontaminated pixels are available for a local sky determination. In the other bands, it is not obvious how far out in the frame the galaxy light extends.

To establish sky background values, we first measured the count rate, $c_{out,i,\lambda}$, of the outermost 5×10^4 pixels (typically $\sim 4\%$ of the FOV) of galaxy i in filter λ , using a median sigma-clip IDL² algorithm, FINDSKY, which iteratively measures the median of an array and rejects all elements outside a specified number of standard deviations of the mean. Three standard deviations and 15 iterations are used here. Several measurements of $c_{out,i,\lambda}$ are negative, particularly in the NUV. The negative backgrounds are caused by bias and dark count over-subtraction during the CALACS process. The bias and dark count subtraction is good to about $\delta C_{CALACS} = 0.5 \text{ e}^- \text{pix}^{-1}$ (M. Stiavelli, private communication).

To acquire an independent estimate of the sky brightness, we searched the HST Archive for a minimum of 30 blank field images in each of our filters taken with the ACS-HRC. First preference was given to the “ANY” fields taken during calibration or parallel observations. To reach the 30 image standard, we accepted some images that contained faint stars or small, faint galaxies. The background was measured via FINDSKY to get c_{blank} , in the same manner as the $c_{out,i,\lambda}$ measurements described above. FINDSKY was able to satisfactorily clip pixels affected by any faint objects.

²The Interactive Data Language is distributed by ITT Visual Information solutions

The galactic coordinates of the blank field images are randomly distributed across the sky, though for the most part are outside the galactic plane, $|b| > 20^\circ$. Most of the galaxy images are within 20° of the ecliptic but outside the galactic plane. There are no trends of sky brightness values with either galactic or ecliptic latitude or with angular distance to the earth, moon, or sun for either set of galaxy images or blank field images. Table 2.3 summarizes the background values from the blank field images and from the galaxy images' outer regions.

For each galaxy in each filter, we adopted the lower of the two rates ($\langle c_{blank} \rangle$ or $\langle c_{out,i,\lambda} \rangle$) as the best background estimate, with one exception. For NGC 4621, the NUV outer region brightness value is significantly higher than that for the rest of the galaxies and displays a surface brightness plateau at large radius unlike any other galaxy or in the other bands for NGC 4621. A subtraction of the lower background estimate value (in this case, from the blank fields) does not remove the plateau, whereas the subtraction of the higher estimate (from the galaxy image) does. We consider the higher background value the better estimate in this one case. The adopted V band background values are all taken from the blank images. The adopted NUV band background values are all taken from the galaxy images. The uncertainties given in Table 2.3 are the standard errors across the twelve galaxies for the $\langle c_{out,i,\lambda} \rangle$, $\langle c_{i,\lambda} \rangle$, $\langle \mu_{out,i,\lambda} \rangle$, and $\langle \mu_{i,\lambda} \rangle$ measurements and the standard errors across all the blank images for the $\langle c_{blank} \rangle$ and $\langle \mu_{blank} \rangle$ measurements. We note that uncertainties in the background level do not affect structures or colors determined for the central parts of the data frames, which are well above the background in all cases.

The limiting magnitudes of a point source that is five times brighter than the outer regions of the galaxy images are on average 23.8, 25.2, and 25.9 for the V, U,

and NUV bands, respectively, across all the sample galaxies.

2.3.3 Isophotal Parameters

We determined the 1-dimensional surface brightness profiles of the galaxies using the IRAF program ELLIPSE, in the STSDAS package. ELLIPSE finds the best-fitting elliptical isophote at a given semi-major axis distance, a . The values for the center, ellipticity ϵ , and position angle ϕ are fit for each ellipse (Jedrzejewski 1987). The radial deviation of an isophote from an ideal ellipse is then expanded in a Fourier series

$$\Delta a(\phi') = \sum_{k=3}^4 [A_k \sin(k\phi') + B_k \cos(k\phi')] \quad (2.2)$$

where ϕ' is the azimuth relative to the position of the major axis, and A_k and B_k are the harmonic coefficients that quantify deviations from the underlying ellipse. For $k=3$, the deviations are triangular or egg-shaped, while $k=4$ indicates boxy or disk-like deviations. A_k and B_k are normally expressed as percentages of the semi-major axis. (The labels for the sin and cos components are reversed in some of the literature, so that B_4 here corresponds to a_4 in Kormendy 2008, for instance.)

To apply ELLIPSE to our data set, we proceeded as follows. For each galaxy, ELLIPSE was first used to extract the set of best-fitting ellipses at each a from the V-band image. We fit isophotes at integer pixel radii, progressing linearly, between 1 and 20 pixels radius. Beyond this range, we allowed ELLIPSE to fit logarithmically outward, fitting ellipses at each 10% increase in a . The central position, ϕ , and ϵ were fit freely at each a as long as the consecutive isophotes do not overlap. The run was then iterated with the initial conditions set equal to the error-weighted mean central position, ϕ , and ϵ until the mean values stabilized. It is well known that

Table 2.3. Sky Brightnesses

Filter (1)	$\langle c_{blank} \rangle$ (2)	$\langle c_{out,i,\lambda} \rangle$ (3)	$\langle c_{i,\lambda} \rangle$ (4)	$\langle \mu_{blank} \rangle$ (5)	$\langle \mu_{out,i,\lambda} \rangle$ (6)	$\langle \mu_{i,\lambda} \rangle$ (7)
F250W	1.28(0.14)	0.53(0.22)	0.53(0.22)	21.59(0.12)	22.52(0.44)	22.52(0.44)
F330W	1.87(0.20)	1.98(0.44)	0.99(0.13)	22.01(0.11)	21.94(0.24)	22.41(0.14)
F555W	7.44(0.78)	48. (8.7)	7.44(0.78)	22.68(0.11)	20.65(0.20)	22.68(0.11)

Note. — The error-weighted average sky brightness measurements from the blank fields (subscripts “blank”), the outer 5×10^4 pixel regions of the galaxy images (subscripts “out, i,λ ”), and the final set adopted (subscripts “ i,λ ”). Columns (2-4) are in count rates, $10^{-3}\text{e}^{-}\text{pix}^{-1}\text{sec}^{-1}$. Columns (5-7) are in monochromatic surface brightnesses, mag arcsec $^{-2}$. Numbers in parentheses give the standard errors.

Table 2.4. Mean Geometric Parameters From ELLIPSE

Galaxy (1)	ϵ (2)	ϕ (3)	$A_3 * 100/a$ (4)	$A_4 * 100/a$ (5)	$B_3 * 100/a$ (6)	$B_4 * 100/a$ (7)
NGC2778	0.14(0.01)	46.7(0.4)	0.57(0.11)	-0.20(0.11)	-0.12(0.15)	0.03(0.11)
NGC3377	0.47(0.01)	41.4(0.2)	0.38(0.09)	-0.24(0.07)	-0.35(0.10)	1.36(0.10)
NGC3384	0.33(0.02)	47.0(0.5)	0.17(0.07)	-0.46(0.10)	-0.01(0.11)	1.38(0.08)
NGC3640	0.19(0.01)	92.1(0.6)	-0.01(0.21)	0.14(0.08)	0.11(0.24)	0.21(0.10)
NGC4239	0.42(0.02)	114.2(1.8)	-0.39(0.20)	-0.09(0.20)	-0.22(0.17)	0.67(0.15)
NGC4474	0.28(0.01)	79.5(0.2)	-0.18(0.12)	0.01(0.10)	0.28(0.12)	0.55(0.28)
NGC4478	0.30(0.01)	151.4(0.6)	0.19(0.10)	0.21(0.08)	0.03(0.10)	0.32(0.15)
NGC4482	0.19(0.02)	133.6(2.1)	0.51(0.28)	-0.40(0.45)	-1.48(0.43)	0.70(0.43)
NGC4570	0.39(0.01)	158.4(0.2)	0.11(0.10)	0.21(0.06)	-0.03(0.05)	0.41(0.29)
NGC4621	0.32(0.01)	163.1(0.3)	0.22(0.08)	0.17(0.08)	-0.22(0.04)	2.40(0.17)
NGC5576	0.25(0.01)	89.1(0.9)	-0.10(0.07)	0.16(0.08)	0.03(0.09)	-0.72(0.09)
NGC7457	0.27(0.02)	127.2(1.6)	0.71(0.13)	0.23(0.09)	0.07(0.14)	0.48(0.13)

Note. — The table gives error-weighted mean isophotal geometry parameters for each galaxy, with their standard errors given in parentheses. (2) Ellipticity. (3) Position angle in degrees east of north. (4-7) The coefficients of the third- and fourth- harmonics expressed as percentages of the semi-major axis.

for some ETGs these parameters can systematically vary with radius (Rest et al. 2001; Peng et al. 2002). The final set of ellipses from the V image was then used as the input template from which the mean intensity values were measured for the U and NUV images. Isophotal parameters were typically obtained to a radius of $15''$. The sky background values were subtracted from the light profiles, and the corrected electron counts converted to magnitudes in the STMAG system and the magnitudes were dereddened for foreground extinction. The maximum dereddening values are $A_{V,max} = 0.17$, $A_{U,max} = 0.27$, and $A_{NUV,max} = 0.34$ mag. The errors in intensity, $\delta I(a)$, produced by ELLIPSE are the standard errors of the mean brightness in a given isophote; these are added in quadrature to the estimated errors in the sky background values to yield the estimated errors for the net brightnesses. This procedure yields surface brightnesses and colors for an identical set of ellipsoidal annuli in all three bands.

Since colors are more sensitive to deviations from the correct background values than are the fluxes, we used the presence of erratic changes in the isophotal $U - V$ and $NUV - V$ colors to determine the maximum radius, R_{Good} , out to which we believe the colors are unaffected by uncertainties in the background subtraction. A single R_{Good} is determined for each galaxy, based on the minimum R_{Good} from each of the color combinations. Final R_{Good} values range from $7''$ to $18''$, or 400 to 1500pc; the typical ratio of the galaxy surface brightness at R_{Good} to the background for those cases that are background limited is 3.5. At R_{Good} , the surface brightness profile errors are on average 0.01, 0.03, and 0.10 mag for the V, U, and NUV bands, respectively.

Figure 2.1 demonstrates the method of using colors to define the radial limits of the U- and NUV-band SBPs with NGC 3377. All V-band isophotes are much brighter than the background measurements so R_{Good}^V is the maximum radial extent available

from the ELLIPSE output for each galaxy. The NUV - V and U - V color profiles are examined to find $R_{Good,NUV}$ and $R_{Good,U}$. The minimum of these radii is used to determine the maximum region over which integrated fluxes or isophotal color-color distributions are determined.

Table 2.4 summarizes the final mean geometric parameters ϵ , ϕ , A_3 , A_4 , B_3 , and B_4 over the entire fitted range for each galaxy in our sample.

Selected data from the ELLIPSE reduction are presented in Figures 2.2.a-1. For each galaxy we show (left, top to bottom) the surface brightness profiles in each band, the ellipticity and the B_4 profiles against semi-major axis radius, and (right, top to bottom) a contour map of the V image, and color images in $U - V$ and $NUV - V$.

As an external check of our SBPs, we compare our final V-band light profiles against those painstakingly derived and calibrated by Kormendy et al. (2008). Our sample contains four systems in common with Kormendy et al.'s sample of Virgo ETGs: NGC 4478, NGC 4482, NGC 4570 and NGC 4621. We find excellent agreement outside of the central regions (where deconvolution effects create differences): the rms difference between the two sets of profiles over the radial range $0.1''$ to R_{good} is $0.07 \text{ mag arcsec}^{-2}$. There is also very good agreement between the ϵ and B_4 (a_4 in Kormendy et al. 2008) profiles that we derive and those published in Kormendy et al. (2008). Within $0.1''$ the Kormendy et al. (2008) deconvolved light profiles of NGC 4478 and NGC 4621 rise more sharply than our un-deconvolved profiles, a well known result of deconvolution (Lauer et al. 1991, 1998). This will not affect our results, as we convolve our fitting function with the PSF as part of the fitting procedure rather than fitting deconvolved profiles.

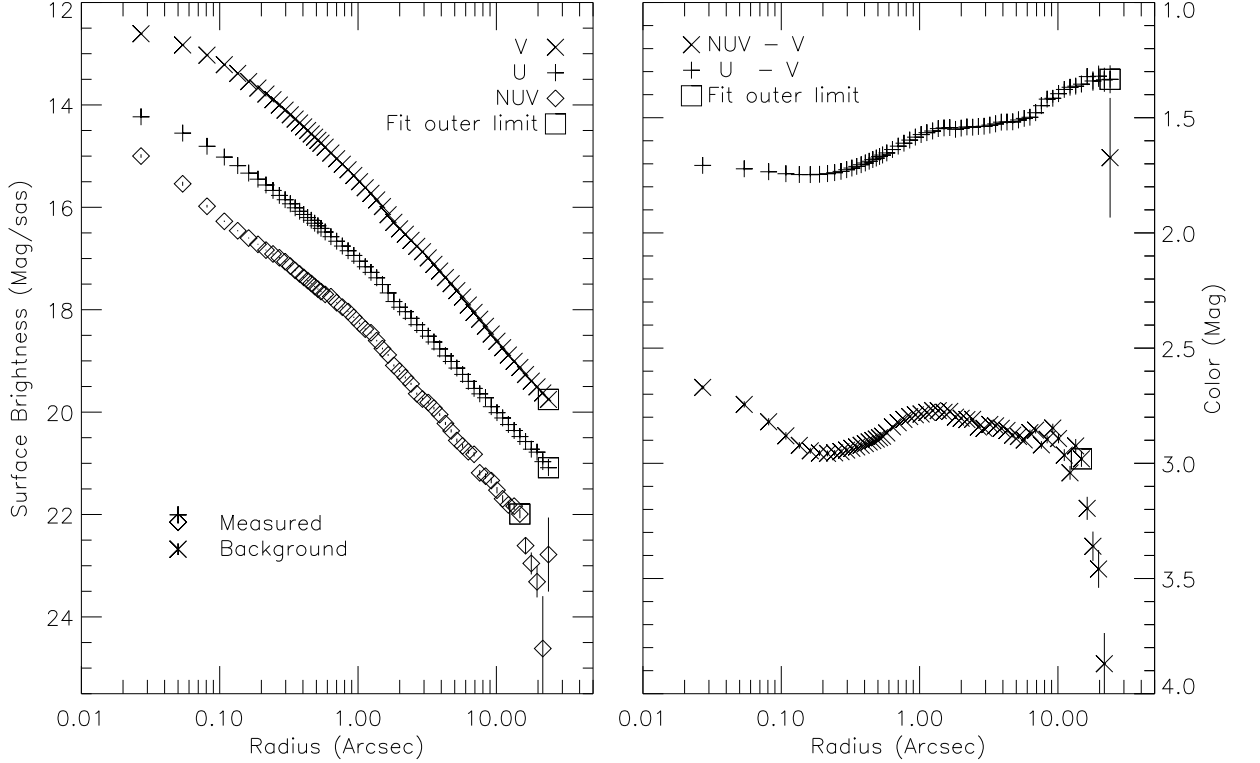


Fig. 2.1.— (left) The surface brightness profiles of NGC 3377 in each band as produced by ELLIPSE of NGC 3377. (right) The resulting $NUV - V$ and $U - V$ color radial profiles. The open squares identify the locations where there is an erratic change in the color profiles indicating that the colors are dominated by the uncertainties in the background subtractions and, thus, indicate the edge of reliability in the U- or NUV-band. R_{Good} is the minimum of these radii, set by the $NUV - V$ color profile in this case. The measured background values and their errors for each band are indicated in the left plot.

Fig. 2.2.— **Top Left:** The extracted surface brightness profiles, in units of monochromatic STMAG magnitudes $/\square''$, where the \times , plus, and diamond symbols represent the V, U, and NUV band profiles, respectively. The label at the $1''$ tick-mark gives the spatial scale of the profiles for each object. **Middle Left:** Ellipticity, ϵ , as a function of radius. **Bottom Left:** The fourth-order cosine moment, B_4 , of the isophotes as a percentage of the semi-major axis. ϵ and B_4 are determined from the V band images. Error bars (standard error) are present for all data points but the symbols are often much larger than the errors. **Top Right:** The contour plot of the central $10'' \times 10''$ of the observed V band image (north is up, east is left). There is a $1''$ bar in the lower right hand corner. The contour levels begin at $12.5 \text{ mag}/\square''$ and increase by 1 magnitude intervals. **Middle Right:** The $U - V$ color map. **Bottom Right:** The $NUV - V$ color map. Both color maps cover the same central $10'' \times 10''$ region of the galaxy as the contour plot above and bluer colors are represented by whiter shades while redder colors by blacker shades.

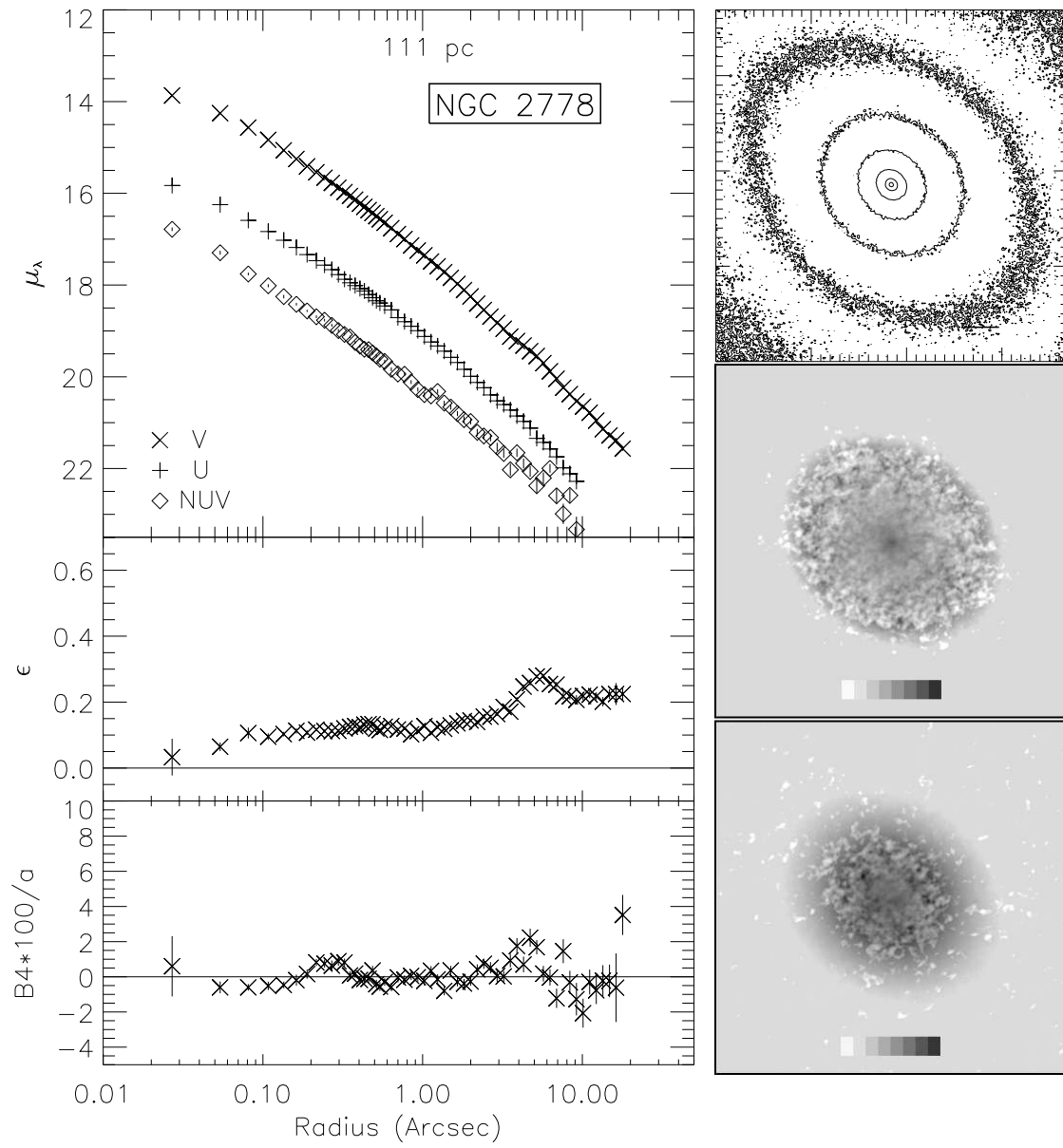


Fig. 2.2.a.— **NGC 2778**

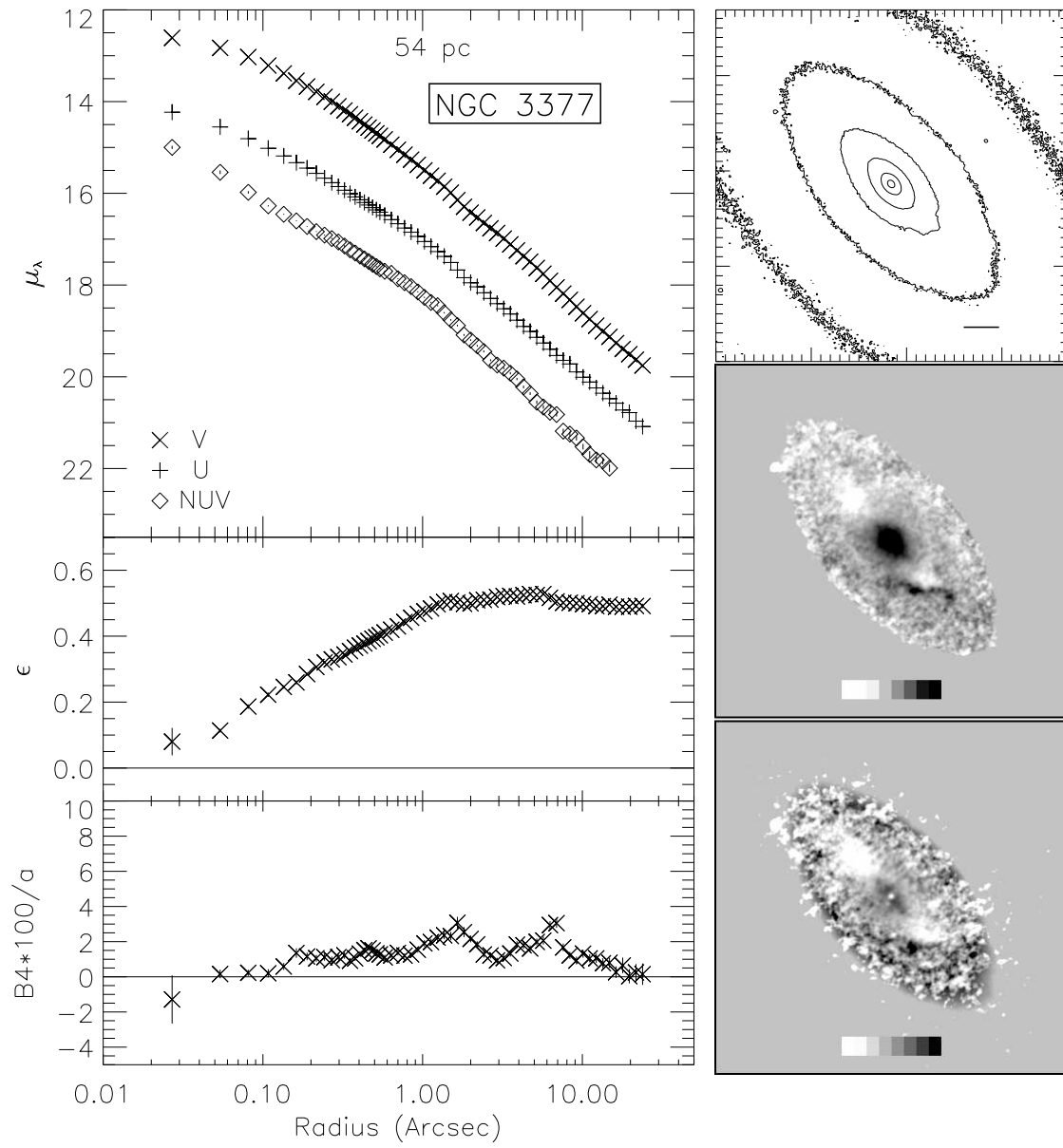


Fig. 2.2.b.— NGC 3377

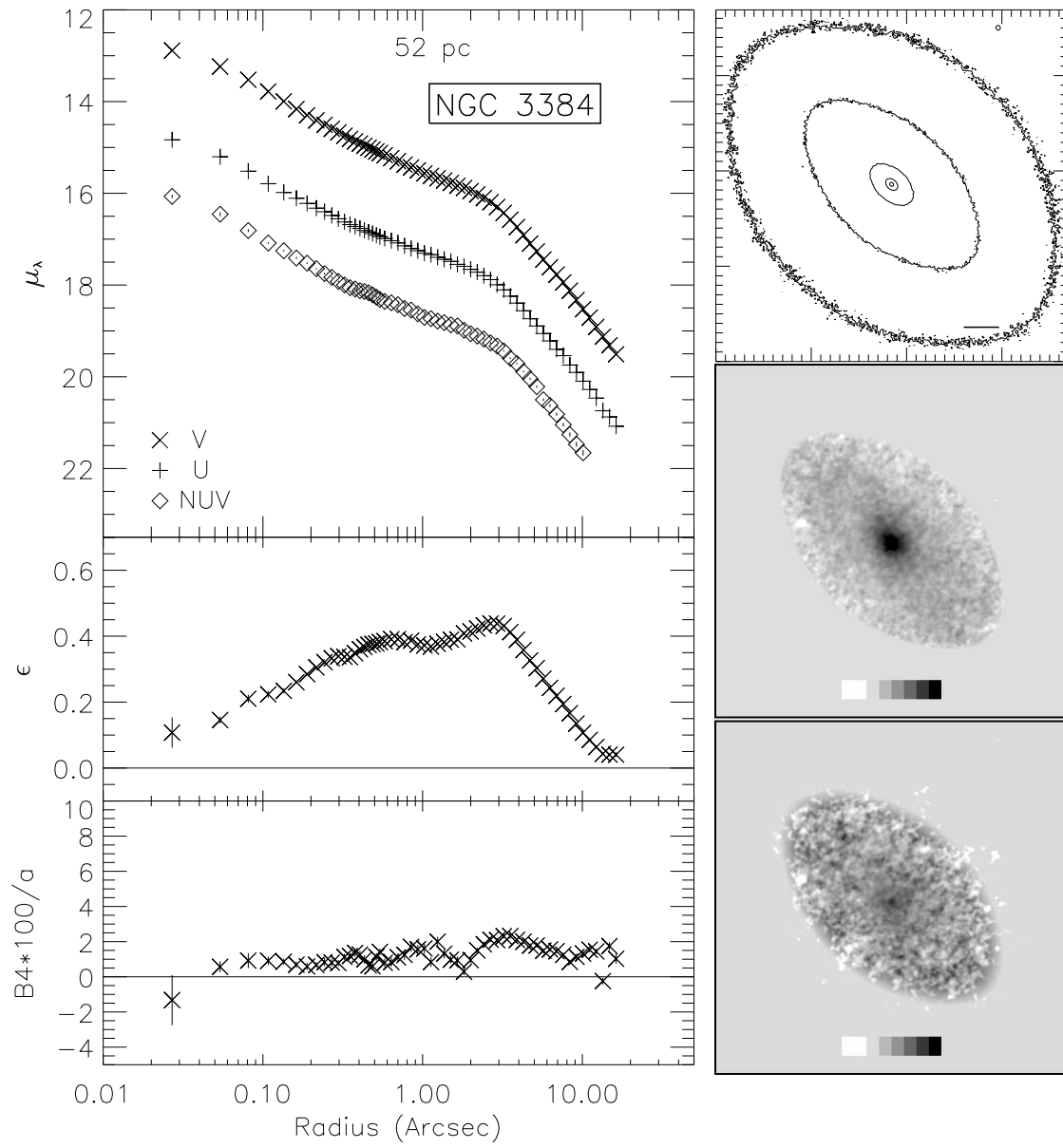


Fig. 2.2.c.— NGC 3384

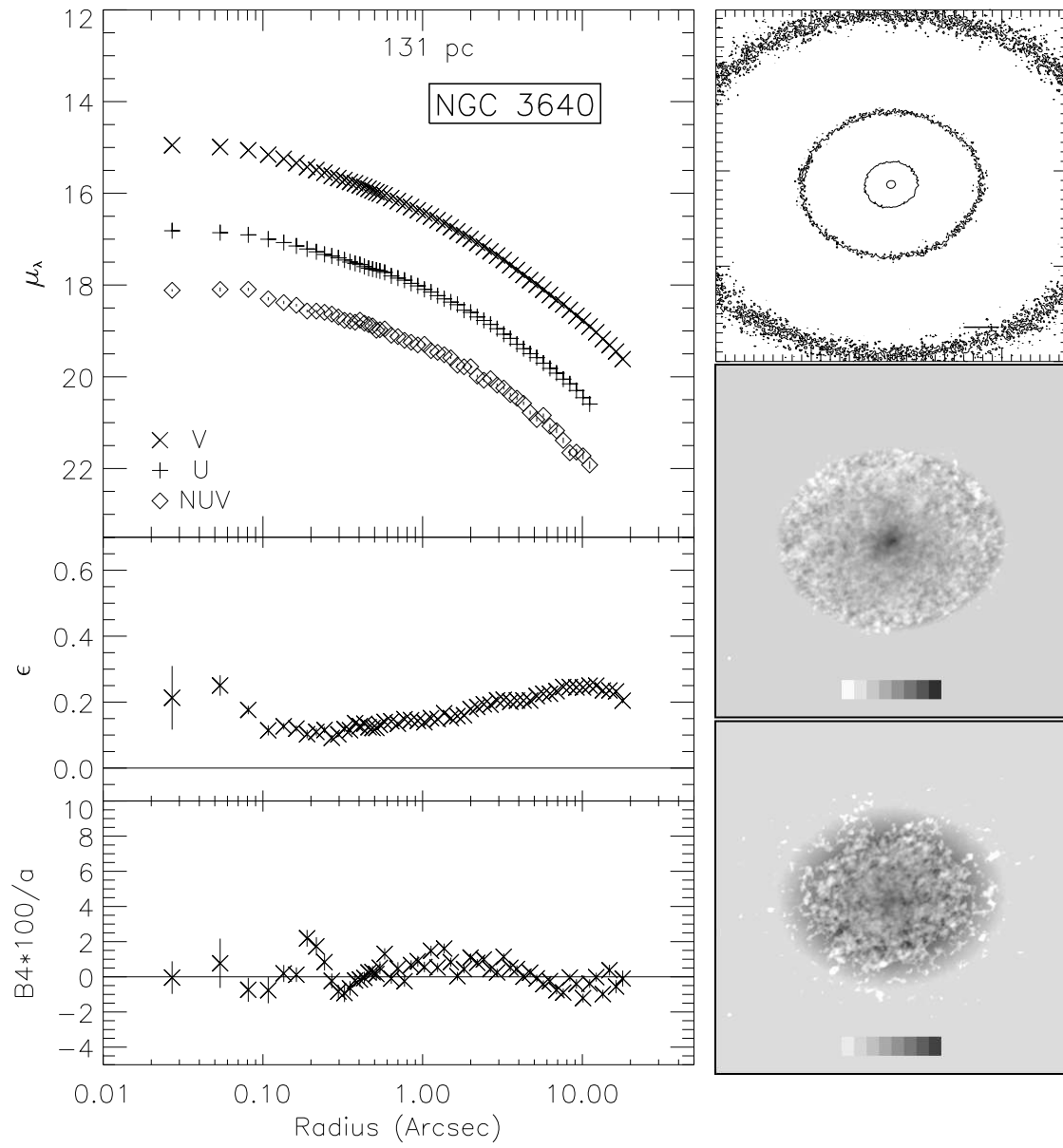


Fig. 2.2.d.— NGC 3640

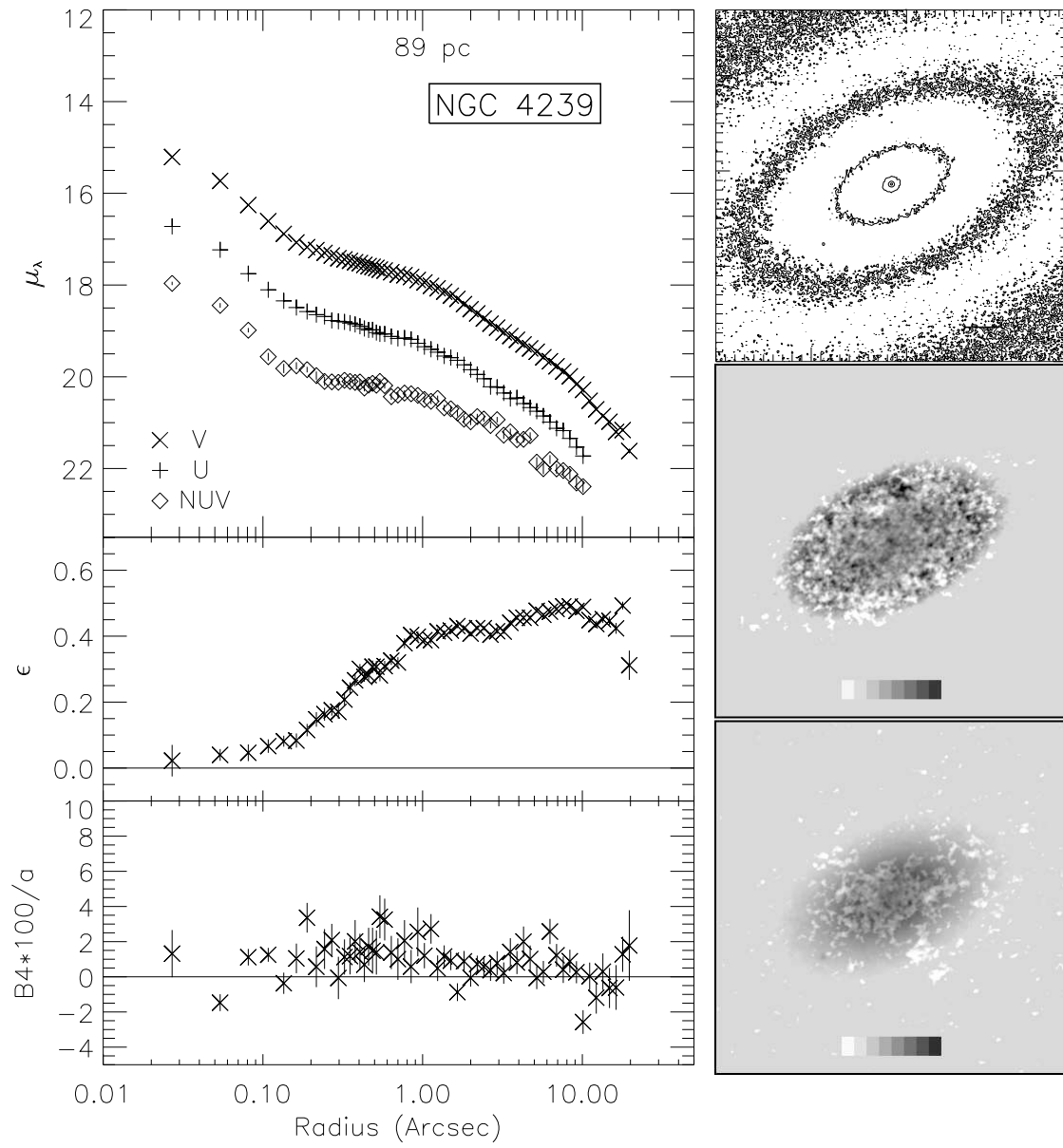


Fig. 2.2.e.— NGC 4239

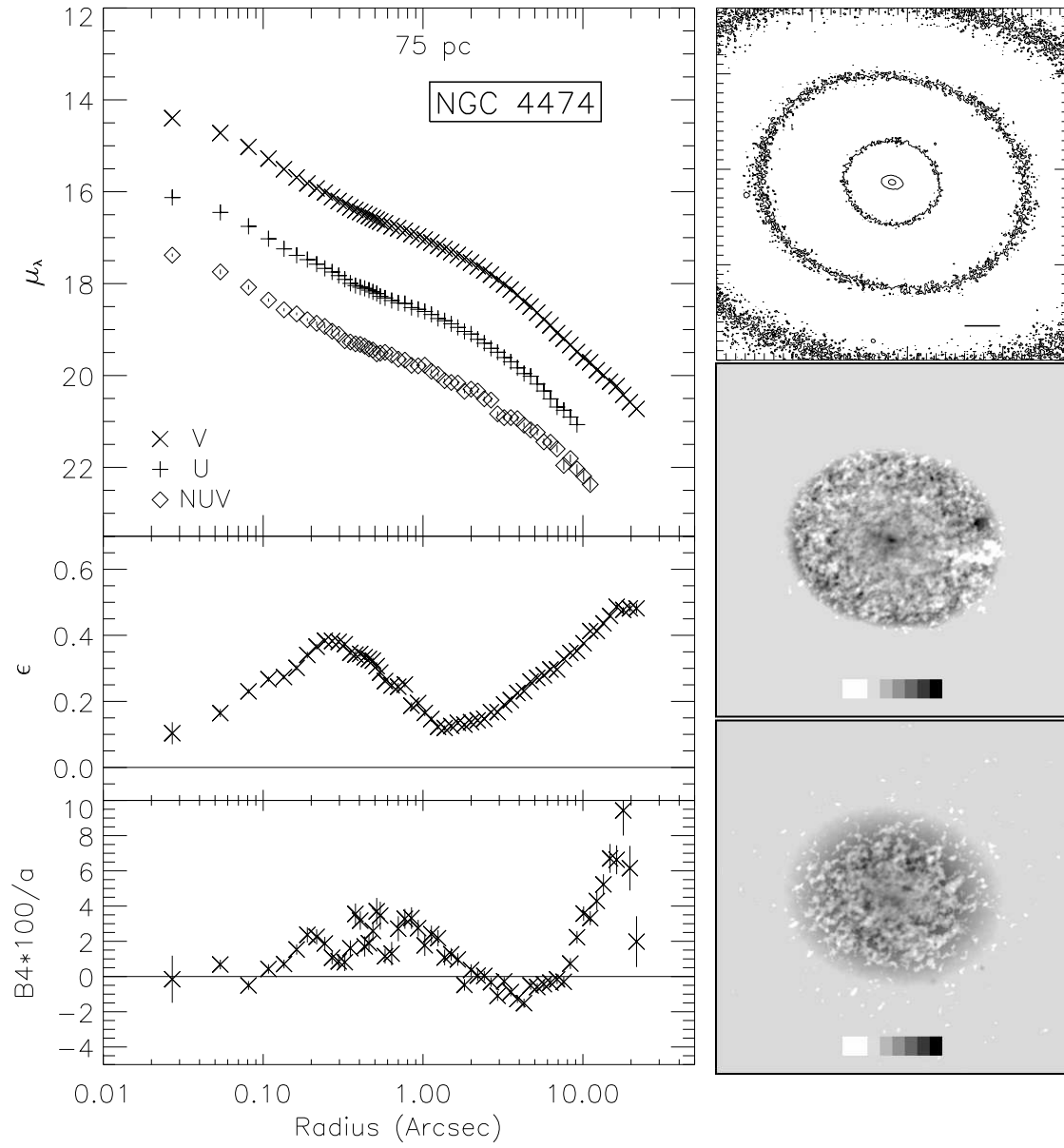


Fig. 2.2.f.— NGC 4474

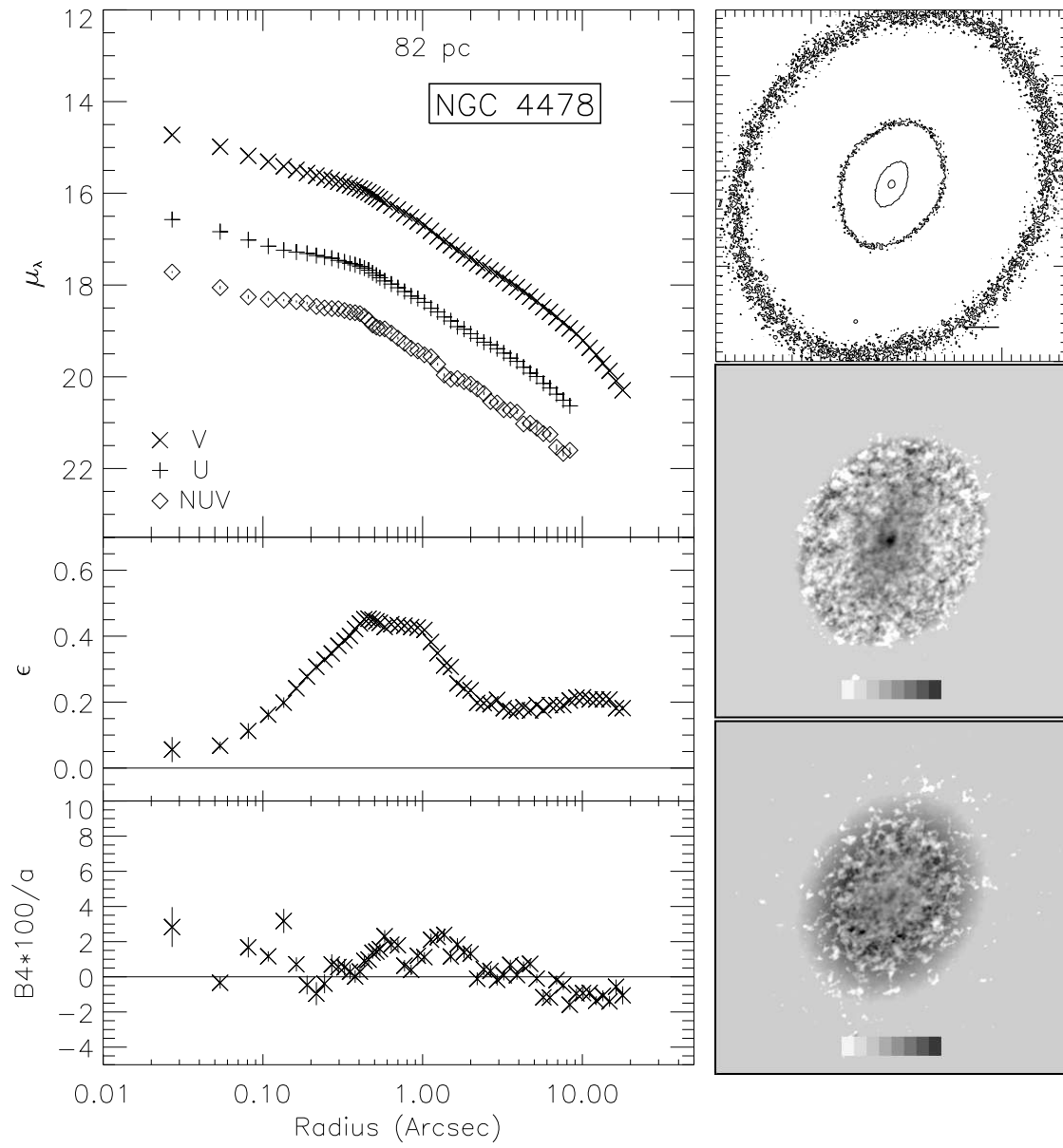


Fig. 2.2.g.— NGC 4478

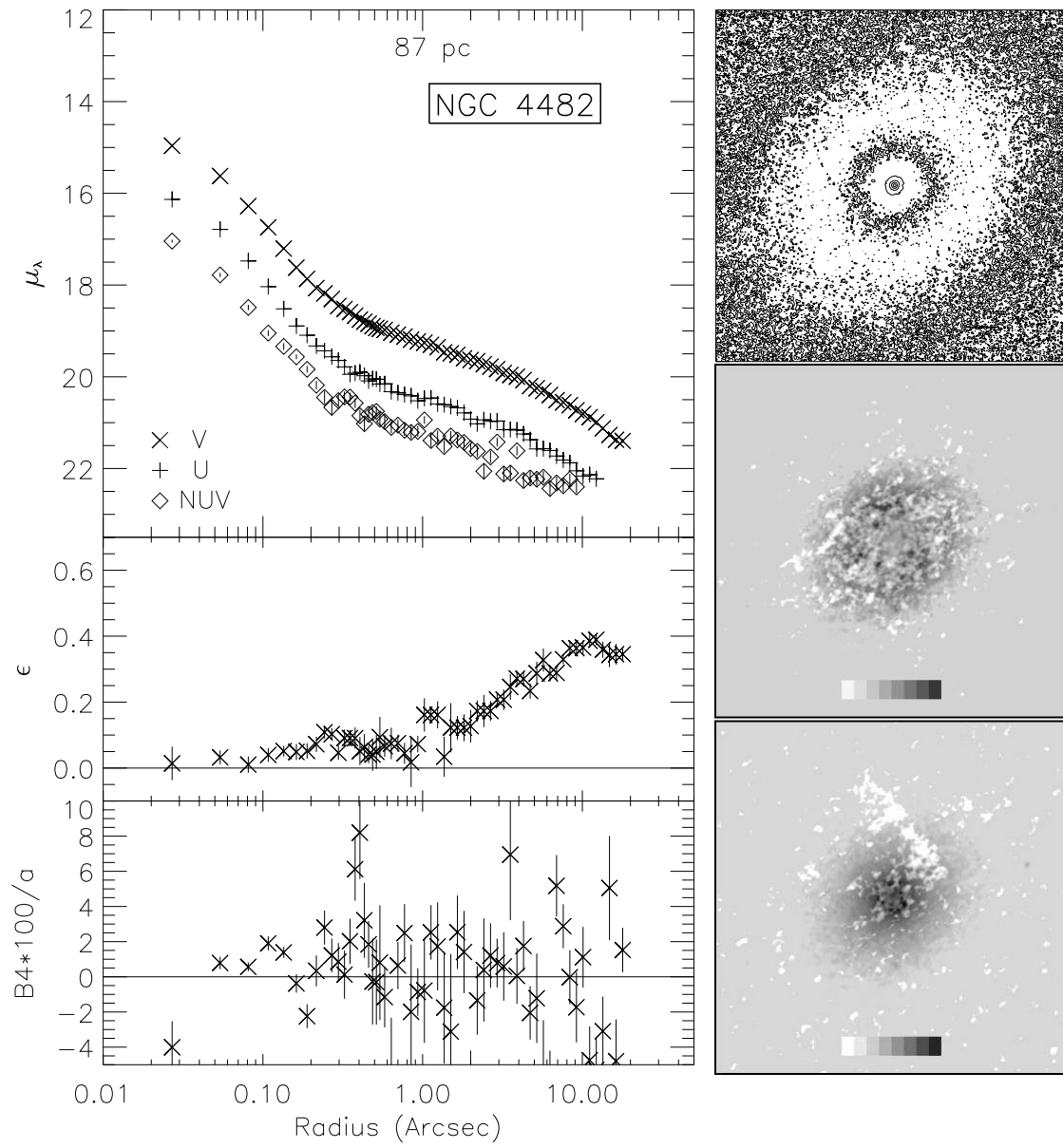


Fig. 2.2.h.— NGC 4482

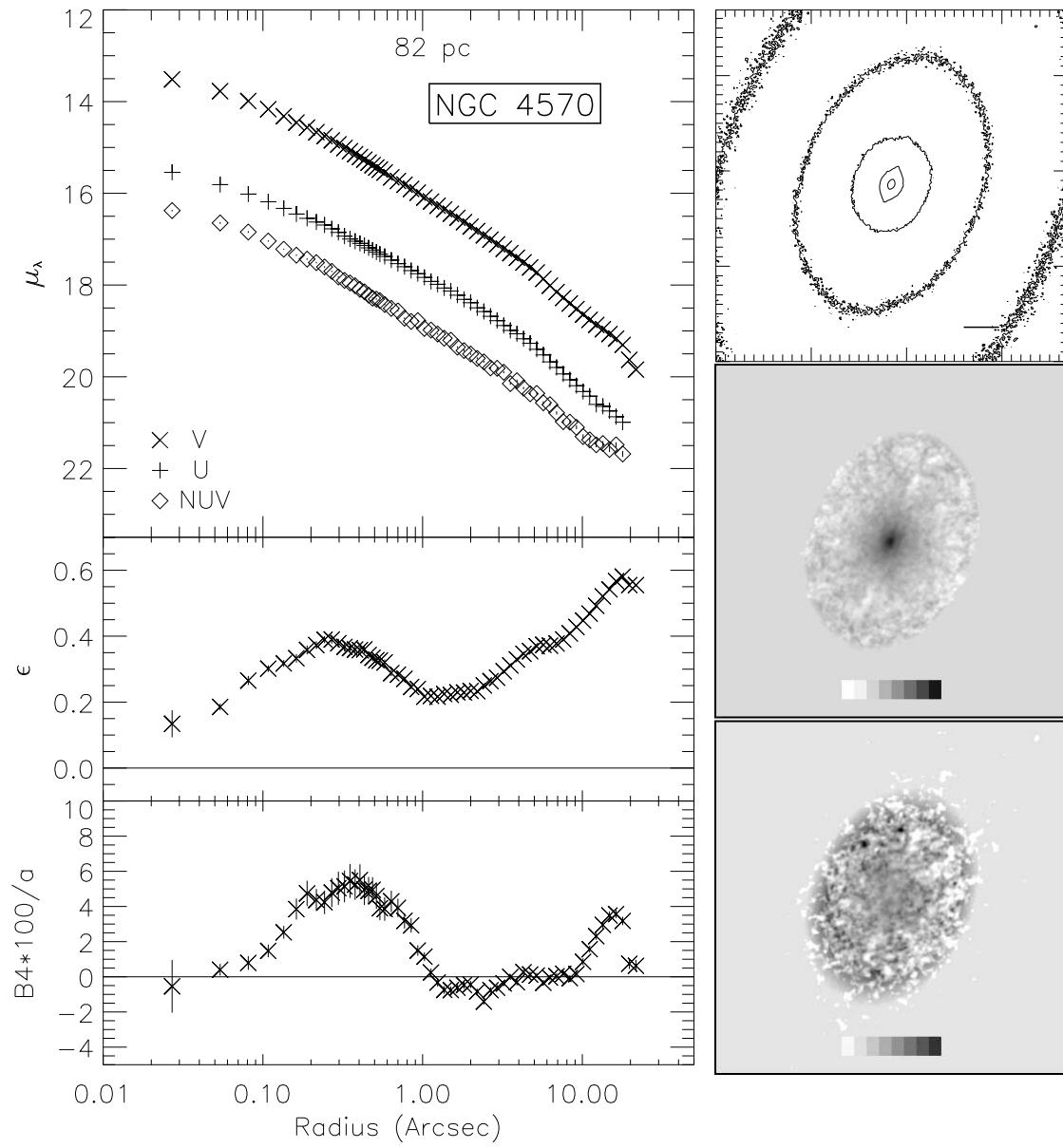


Fig. 2.2.i.— NGC 4570

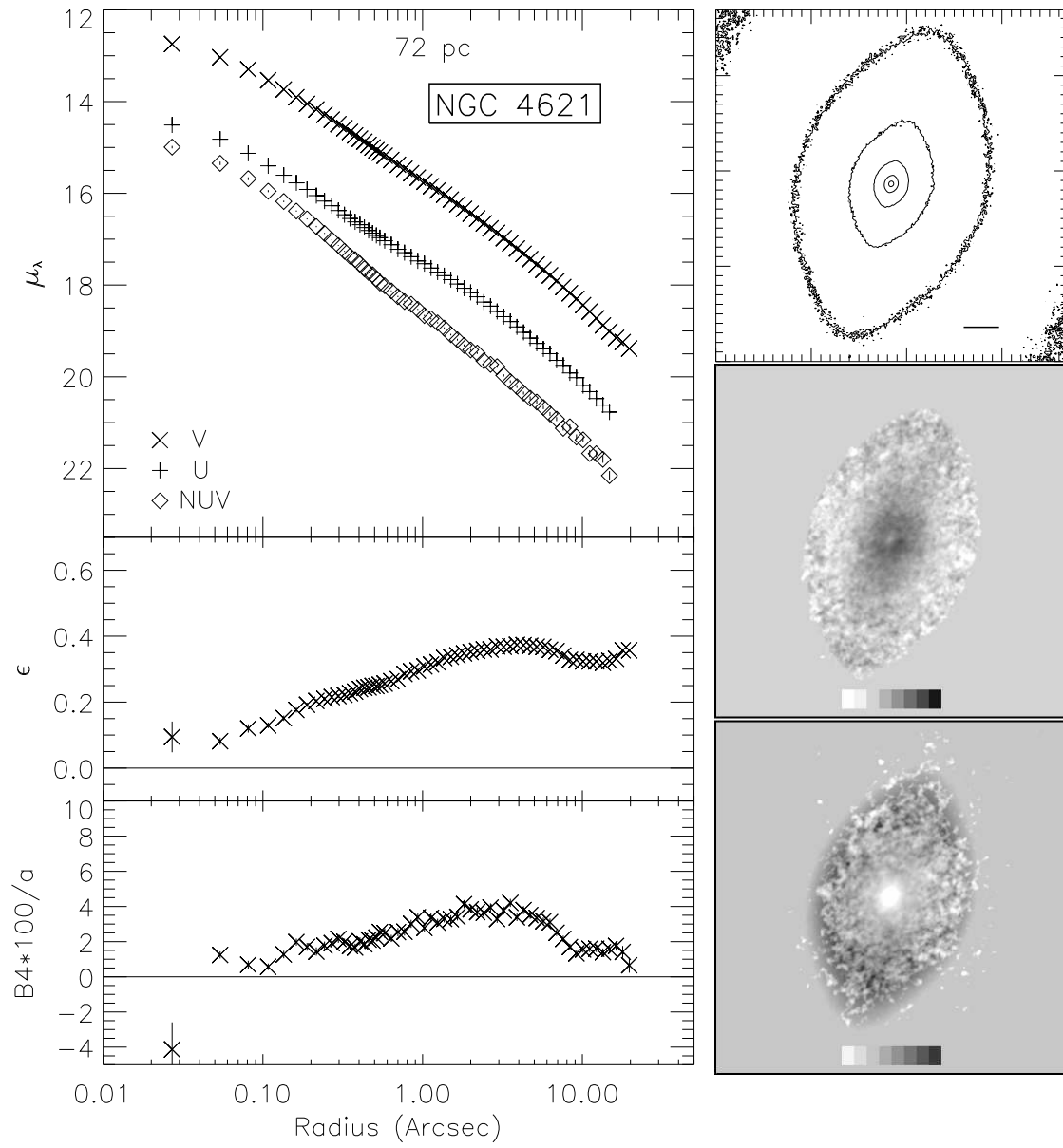


Fig. 2.2.j.— NGC 4621

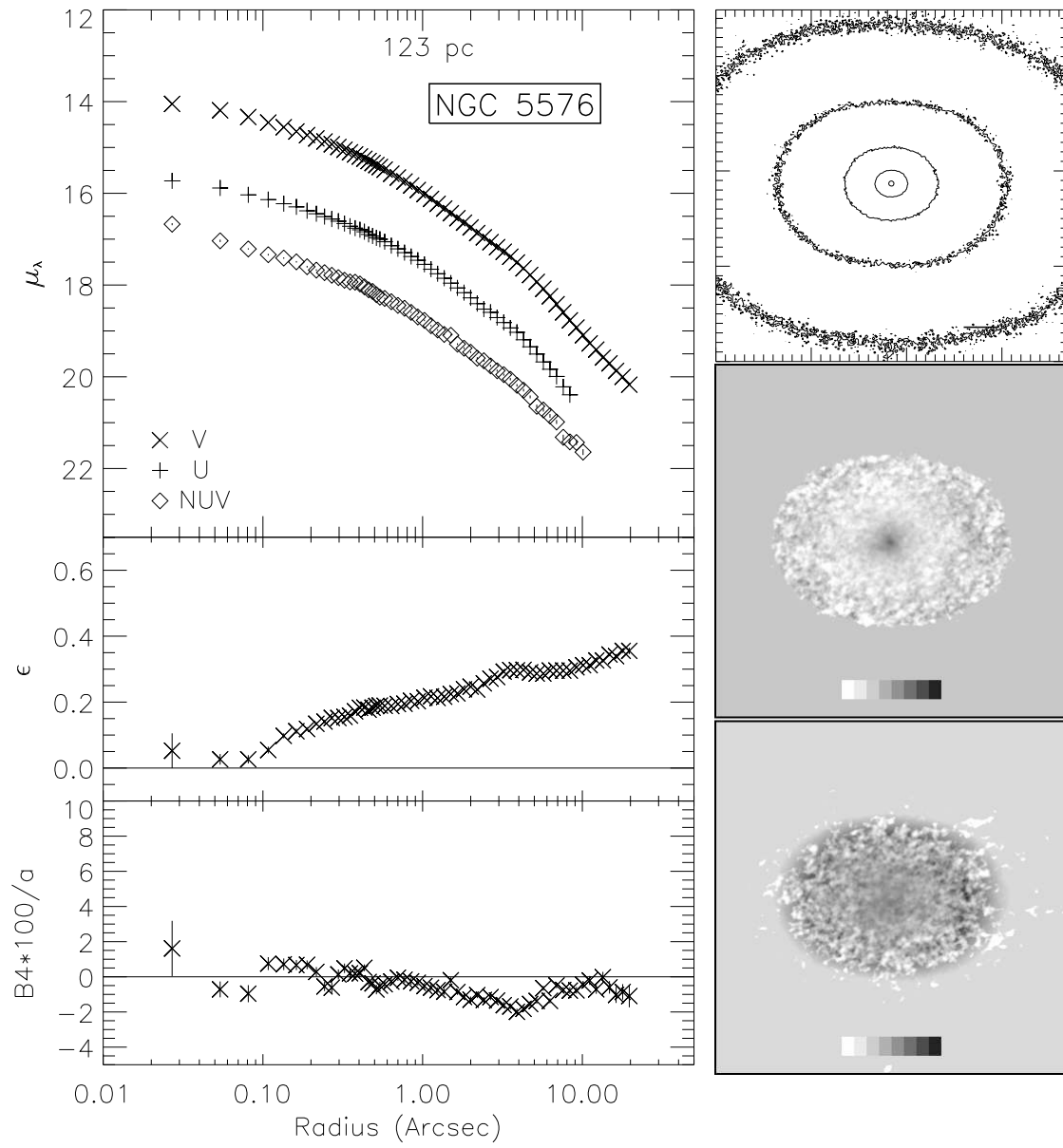


Fig. 2.2.k.— NGC 5576

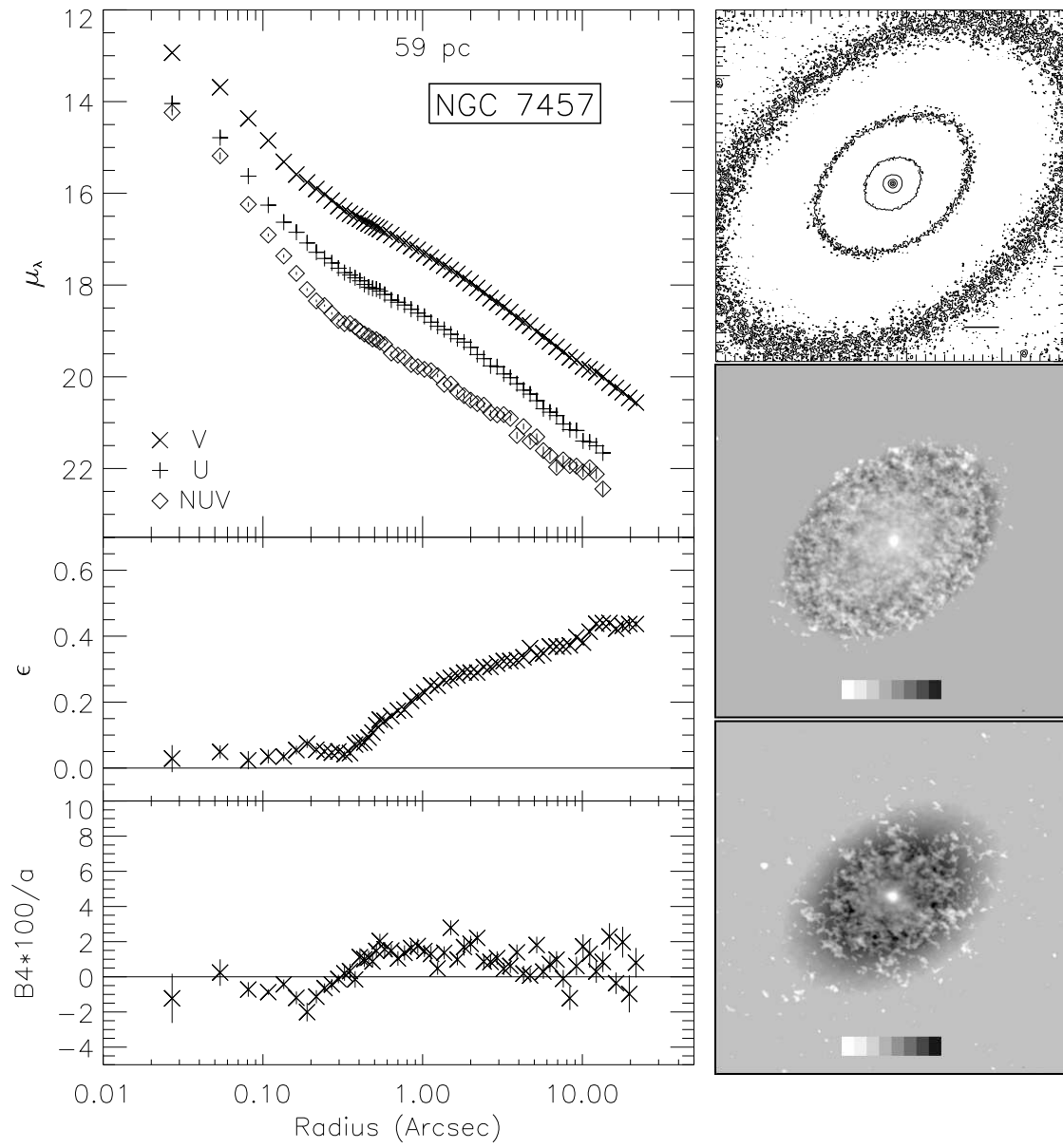


Fig. 2.2.1.— NGC 7457

2.4 General Structure

In this section we describe the overall appearance of the galaxies in our sample, mostly qualitatively. The next section describes detailed fits to the extracted light profiles.

2.4.1 Central Morphologies

The upper right hand panels in Fig. 2.2 show V-band contour plots, which illustrate isophotal shapes and central concentrations. By initial selection, our sample was intended to be free of conspicuous dust lanes, disks, or other substructure, and that is mostly confirmed by the contour plots (although NGC 3377 shows some features; see Section 2.4.2). The contours show subtle indications of changes in ellipticities and elliptical distortions that are quantified by the accompanying ϵ and the B_4 profiles.

The presence of a disk can be quantitatively detected through positive values of B_4 . Abrupt changes in either B_4 or ellipticity indicate the presence of multiple structural components. A galaxy classified as an S0 is intrinsically multi-component, as it has a centrally concentrated bulge and an extended disk. Historically, objects with detected disk components were not classified as E galaxies. In recent decades, however, the elliptical galaxies have been found to frequently include inner disk components (Rix & White 1990). Kormendy & Bender (1996) suggest a modification to the standard Hubble Sequence classification scheme in which the earliest type ellipticals are boxy and the diskier are adjacent to S0s in classification index. This schema reflects underlying physics, such as rotation, better than the previous classification by ellipticity, which is susceptible to projection effects. S0s should have large positive B_4 values over a range of radii, whereas diskier ellipticals will have weaker positive B_4 features and boxy ellipticals will have negative values of B_4 .

Four of the sample galaxies, NGC 3384, NGC 4474, NGC 4570, and NGC 7457,

are classified as S0s. NGC 4474 and NGC 4570 both distinctly show the presence of disks through abrupt and large changes in their B_4 and ϵ profiles, verifying that both these galaxies are S0s. The SB0- classification of NGC 3384 indicates the presence of a bar, which can increase ellipticities and should also produce boxy isophotes. There is no evidence for a bar in our data, which exhibit mildly disk behavior throughout, so any bar must be a larger scale feature (Meusinger et al. 2007). The B_4 profile of NGC 7457 also does not have the large positive deviations expected of an inner disk. It is mildly boxy to $0''.4$, with low ellipticity, then mildly disk to $10''$. Again, any S0 disk must be a larger scale feature (Michard & Marchal 1994).

Four additional galaxies would be classified as disk ellipticals by their B_4 profiles: NGC 3377, NGC 4239, NGC 4478, and NGC 4621. NGC 3640 and NGC 2778 have very weak disks. NGC 5576 is our sole boxy galaxy. The B_4 values for NGC 4482 are not well constrained. Half the galaxies have ϵ profiles that start out round and become more elongated with increasing radius. These trends are not caused by PSF smoothing, which should only be important to radii of $\sim 1.5 \theta$, or about $0''.8$.

2.4.2 Color Maps

To construct the color maps for each galaxy, we converted the $10'' \times 10''$ central regions from each co-registered, sky-subtracted image to monochromatic magnitude units and subtracted them from one another. The displays were clipped where fluxes were within 1 standard deviation of the background level. The resulting color maps are presented in Fig. 2.2. The scale and orientation of the color images match those of the contour plots. The middle right panel shows the $U - V$ image, and the lower right panel shows the $NUV - V$ image. Darker values represent redder (more positive) colors. The windowing was adjusted separately in each color map to best illustrate the

range of colors present. The zeropoints (mean colors) and amplitudes of the displayed images therefore differ from one another. The step size in the overlaid reference scale is usually about twice as large in the $NUV - V$ display as in $U - V$; step sizes for $U - V$ images are in the range 0.03-0.1 mags, and in the $NUV - V$ images, 0.07-0.25 mags.

As expected, most of the sample does not exhibit strong structural elements in the color images. Symmetrical color gradients are present in some, but there is not much evidence for extended structure in most cases. NGC 4570 exhibits a low-contrast blue linear feature along the major axis, possibly an edge-on disk, and other hints of blue radial structures on its western side. NGC 4239 shows low amplitude, blue spiral-like features.

The most dramatic features are found in the well-known E5-6 galaxy NGC 3377, which exhibits an elongated red core, about $0''.5$ in radius, adjacent to extended bluer (disklike?) zones along the major axis and a red dust filament. It contains a blue, point-like central source that we detect only on the NUV frame. Two other galaxies (NGC 4621 and 7457) exhibit bright, compact blue cores. In both cases, these are more conspicuous in $NUV - V$ than $U - V$, but both are detected in $U - V$.

The most unexpected result is that there are several cases of extended red cores that appear in the $U - V$ images but are either much weaker or absent in the $NUV - V$ images. The best examples are NGC 3384, NGC 4570 and NGC 5576. The normal expectation for single-generation ETG populations is that they become redder in their centers because metallicities are higher there. Since line blanketing is stronger at shorter wavelengths, gradients should be stronger in $NUV - V$ than $U - V$. These unusual color images indicate that other population effects are important. Quantitative analysis of the color gradients is presented in Chapter 3.

2.4.3 Surface Brightness Profiles

Here we consider the general features of our derived surface brightness profiles in the context of the earlier studies of ETG structure described in §2.2. Detailed fits to the profiles will be carried out in §2.5.

The preferred functional form used to describe the dominant stellar light distribution of ETGs is a matter of great debate (Lauer et al. 1995; Graham et al. 2003; Trujillo et al. 2004; Ferrarese et al. 2006) and primarily involves the two empirical profiles, “nuker” (Lauer et al. 1995) and “Sérsic” (Sérsic 1968).

The nuker profile, $I_{nuker}(r)$, is given by the following function:

$$I_{nuker}(r) = I_b 2^{(\beta-\gamma)/\alpha} \left(\frac{r}{r_b}\right)^{-\gamma} \left[1 + \left(\frac{r}{r_b}\right)^\alpha\right]^{(\gamma-\beta)/\alpha} \quad (2.3)$$

It is a broken power law characterized by five parameters: an inner slope, γ , and outer slope, β ; a break radius, r_b , marking the transition between the two slopes; a break intensity, I_b , which is the brightness at r_b ; and a sharpness factor between the two slopes, α .

In Fig. 2.2, we display our extracted SBPs in $\log(I)$ - $\log(r)$ space. These are collected in Fig. 2.3, where they are grouped according to their original designation, where an ALP designation indicates SBPs with departures from nuker fits at wavelengths longer than 5000 Å. In Fig. 2.3 ALPs are plotted in the six panels on the left, and non-ALPs plotted in the six panels on the right. As in Fig. 2.2, the profiles from all three bands are plotted. In these coordinates, a nuker profile consists of two straight lines, connected by a curved transition zone, and departures from a nuker law show up as additional inflection points.

The profiles shown in Fig. 2.3 support the original designation of the six ALP galaxies (NGC 3384, NGC 4239, NGC 4474, NGC 4478, NGC 4482, NGC 7457), which

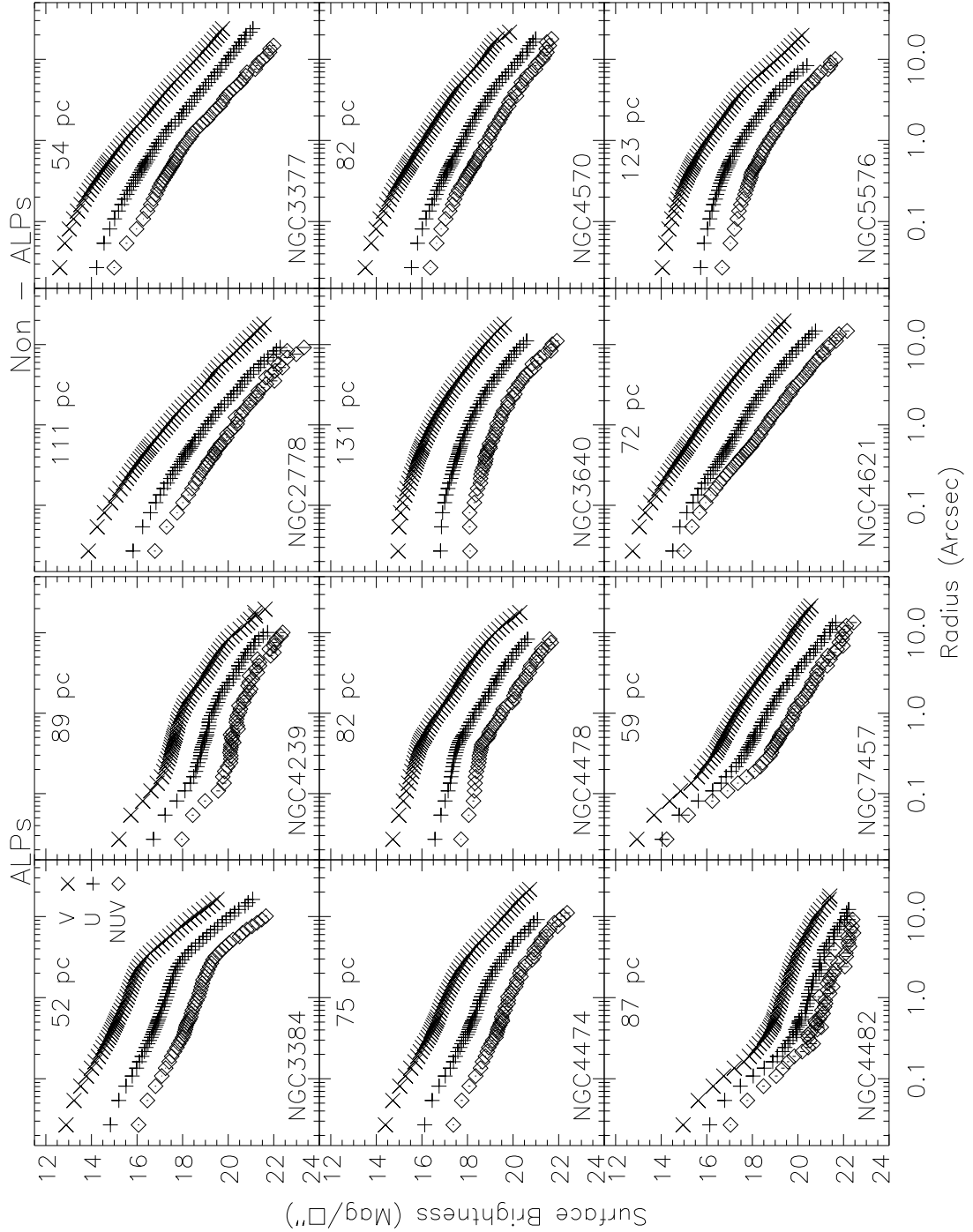


Fig. 2.3.— SBPs of all galaxies in $\log(I)$ - $\log(r)$ space, separated by whether they belong to the ALP (left six panels, those with central upward departures from smooth “nuker” profiles) or non-ALP (right six panels) samples. Symbols are the same as for Fig. 2.2.

mostly have second inflection points in their V-band profiles (we verify this explicitly below when we fit nuker functions to all profiles). The inflections are at least as prominent in the shorter wavelength U and NUV bands; in the case of NGC 7457, the central NUV departure is considerably stronger than in either V or U. The radii where the additional inflections occur are in the $0''.3$ to $0''.5$ range, except for NGC 4478, where it occurs at $\sim 0''.1$.

The control sample galaxies (NGC 2778, NGC 3377, NGC 3640, NGC 4570, NGC 4621, NGC 5576) are all nuker-like in the V band with no obvious second inflection points, but several show departures in the shorter bands, notably NGC 3377 and NGC 4621, both of which exhibited NUV-bright central sources in the color images discussed above.

The other popular fitting function for ETGs is the Sérsic profile, I_{Sersic} (Sérsic 1968):

$$I_{Sersic}(r) = I_e \exp(-b[(r/r_e)^{1/n} - 1]) \quad (2.4)$$

This function employs three parameters and improved upon earlier profile forms by having an adjustable slope index, n (Graham et al. 2003). The effective radius, r_e , is the radius within which half the total light is contained, the effective brightness, I_e , is the surface intensity at r_e , and the scaling factor in the exponent is $b = 1.99n - 0.327$.

As described in §2.2, simulations of gaseous mergers (Hopkins et al. 2008a) produce remnants with central concentrations of younger stars inside an extended envelope of relaxed pre-merger stars that is well described by a Sérsic profile (Sérsic 1968). In $\log(I)-r^{1/4}$ space, galaxies whose SBPs decay with Sérsic index $n=4$ (equivalent to the classic de Vaucouleurs 1948 profile) appear as straight lines, those with higher indices have concave-up distributions, and those with lower indices are concave-down.

In Fig. 2.4, we show our extracted SBPs this time plotted against $r^{1/4}$, again with the ALP systems collected on the left-hand side and the non-ALPs on the right.

The ALP galaxies in Fig. 2.4 mostly show Sérsic-like behavior in their outer regions but have significant central departures from the smooth Sérsic shape. These are of the same or larger amplitude in the NUV and U bands as in V. Four of the non-ALPs, NGC 2778, NGC 3377, NGC 4570, and NGC 4621, exhibit the concave-up profiles associated with excess central light components, and these are accentuated in the NUV band. NGC 3640 and NGC 5576 are the only two objects in the entire sample that do not possess indications of excess central light in Figs. 2.3 or 2.4. Overall, evidence for excess light components is marginally stronger in $\log(I)$ - $r^{1/4}$ space than in $\log(I)$ - $\log(r)$ space and stronger in the U and NUV bands than in V or longer-wavelength bands. The fact that two of our “controls” actually contain anomalies in the NUV and/or U band emphasizes the limitations of the longer wave bands for analyzing structure in ETGs.

2.5 Surface Brightness Profile Fits

2.5.1 Functional Forms of SBP Fits

We wish to quantify the departures from smooth functions seen in Figs. 2.2-2.4 to see if there is evidence for an additional central component, and if so how it contributes in the different observing bands. To do this we fit 1-dimensional composite functions, one component to represent the underlying light of the body of the ETG, and another component to represent any centrally concentrated component. In total, we investigated many functional forms: both nuker and Sérsic for the underlying component and point sources, exponential functions, Elson spheres and King models

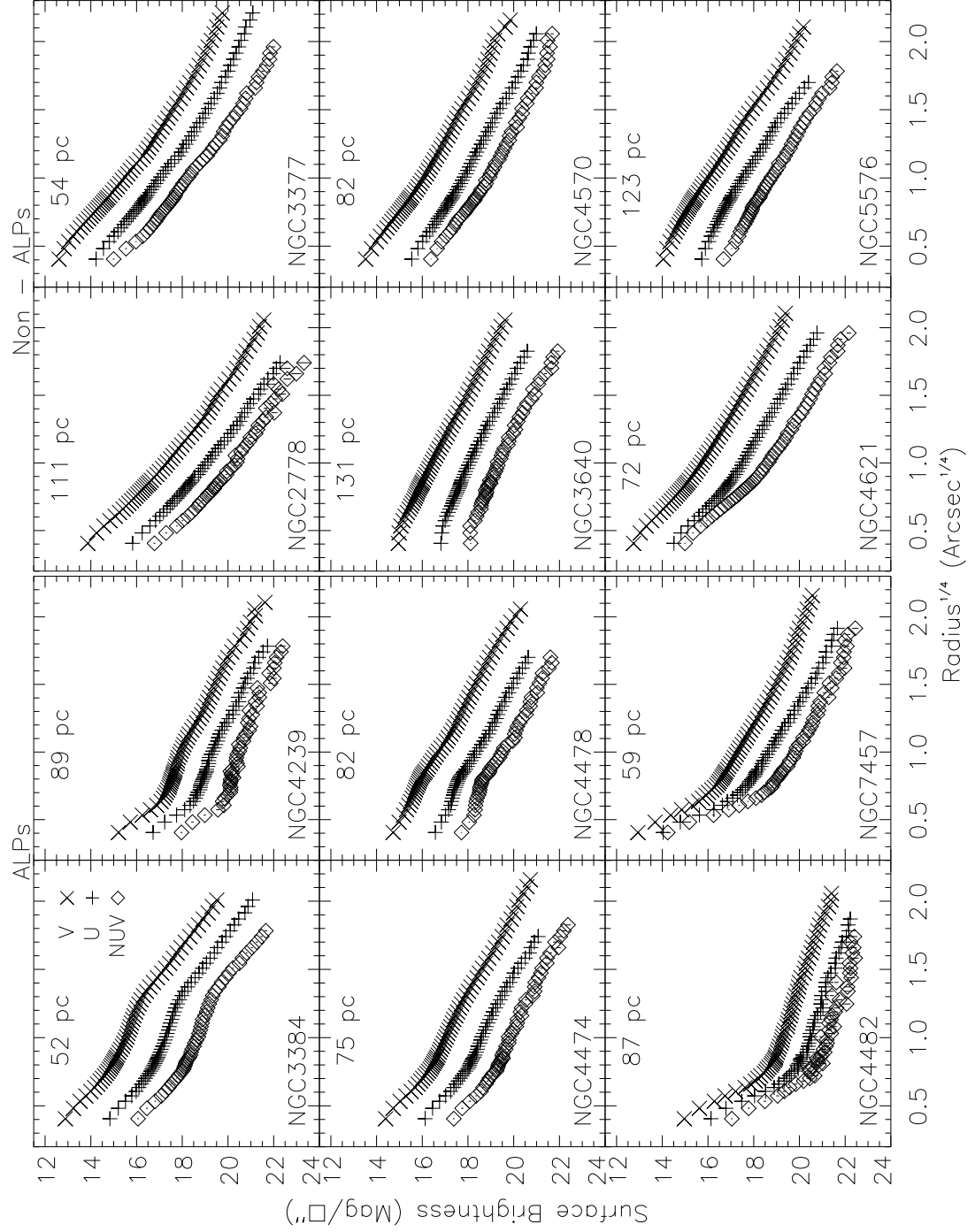


Fig. 2.4.— SBPs of all galaxies in $\log(I)-r^{1/4}$ space, separated by whether they belong to the ALP (left six panels) or non-ALP (right six panels) samples. Symbols are the same as for Fig. 2.2.

for the central component. Differences were evaluated on the basis of the resulting reduced χ^2 (χ_ν^2) of the fits (described later), and in this paper we present the best fit parameters of a reduced set of composite functions: a nuker-only profile and a nuker profile with a central exponential. Before presenting the details and results of these fits, we briefly comment on the resulting choice of functional forms.

For the outer light component, both nuker and Sérsic functions were evaluated. Both functions are robust, meaning that their parameters are well constrained by the data. However, in an initial series of fits to the observed surface brightness profiles with the central regions excluded, the nuker functions proved to provide far superior fits to the data, as judged by the reduced χ_ν^2 of the fits. Overall, the χ_ν^2 values of the nuker fits were on average a factor of 10 times smaller than those of the Sérsic fits. This comports with previous studies that the nuker function more accurately describes the distribution of light in the central few kiloparsec regions of ETGs, while Sérsic profiles are better on larger scales out to tens of kiloparsecs: ETG images from HST with the Planetary Camera ($FOV = 36'' \times 36''$) of the Wide Field and Planetary Camera 2 (WFPC2) (Lauer et al. 1995; Rest et al. 2001) and the NIC2 and NIC3 cameras ($FOV = 19'.2 \times 19'.2$ and $51'.2 \times 51'.2$, respectively) of the Near Infrared Camera and Multi-Object Spectrograph (NICMOS) (Ravindranath et al. 2001) are best fit with nuker profiles. Those acquired with larger FOVs such as with the HST ASC Wide Field Camera ($FOV = 202'' \times 202''$) (Ferrarese et al. 2006) and from ground-based observatories (Kormendy et al. 2008 and references therein) are better fit with Sérsic profiles.

We could have taken a different approach and fit the outer regions of our sample with a single functional form, and measured departures from inner extrapolations of these fits (Rothberg & Joseph 2004; Kormendy et al. 2008). However, such fits require

good measurements at large radii (Kormendy 1999; Kormendy et al. 2008), which are not available for our UV and NUV profiles. Given the limitations imposed by our limited FOV, we adopt the nuker function as the empirically preferred description of the \sim kpc scale light, and explicitly fit for any central excesses.

For the inner light component, we considered an unresolved source (represented by the PSF), and three extended functions: an Elson sphere (Elson et al. 1989), a King model (King 1966), and an exponential. Extensive testing of the surface brightness fitting method (more details below) indicated that fits using exponential functions produced significantly more robust results than those using either Elson spheres or King models. The exponential function has only two parameters while both the Elson and King functions have three. When combined with the small number of data points over which the central components are typically fit, the number of parameters within the function dictates the robustness of the fit. The exponential function is given by the equation:

$$I_{exp}(r) = I_o \exp(-r/r_c) \quad (2.5)$$

where r_c is the scale radius, I_o is the central intensity, and the total integrated light of the exponential profile for circular symmetry is given by $I_{T,exp} = I_o 2\pi r_c^2$. Note that the functional form here does not imply a disk-like structure, and there is no allowance for the inclination of a disk. An exponential is simply an empirically successful and convenient description.

The point source model is created by scaling the semi-major axis brightness profiles of the PSF images produced by `TinyTim` and scaling factors are produced by the fitting algorithm. The fits to the observed SBPs which include the scaled PSFs never provide better fits relative to those with no central component or to those fits which

include a central exponential component. The scaled PSFs are thus not considered further.

2.5.2 Fitting Procedure

Based on the foregoing, we present the results of fitting each SBP with the following two functions:

1. A single-component nuker-only profile (hereafter referred to as **NO**)
2. A two-component nuker plus exponential central source (hereafter **NE**)

Rather than fitting deconvolved light profiles, we choose instead to convolve each fitting function with the appropriate PSF and fit to the originally extracted profiles. The data are fit over the radial range from $0''.027$ to the R_{Good}^λ , where R_{Good}^λ are listed in Table 2.5.

The IDL routine, **MPFITFUN**, is used to fit the profiles. This program performs a Levenberg-Marquardt nonlinear least-squares minimization. The SBPs of all 12 galaxies are fit in the same manner with each of the above two functions. For a single galaxy, the SBP of each filter is fit independently because we do not expect the light distribution to be the same in all three bands: a stellar population gradient with radius will cause an intrinsic gradient of r_b with wavelength, and possibly, a gradient in β and γ with wavelength as well. In the fits, the parameters of the nuker function are constrained to $\gamma < \beta$ and $\alpha < 10$. The fits were conducted in $\log(C(a))$ - a space, where $C(a)$ are the background subtracted mean electron counts per pixel for the elliptical isophote with semi-major axis a in pixels. This maintains accurate statistics using measured errors and counters the effects of the large dynamic range in the brightness profiles.

The fitting routine requires a weight to describe each data point. These are given by the normalized ratio of intensity to errors in counts, where the errors are the combination of the standard errors about the mean intensity per isophote as produced by ELLIPSE and the measured background errors. The resulting weights are highest for the data in the middle of the radial range at about $1''$. Data at large and small radii typically have lower weights because the central regions have more counts per pixel but fewer pixels and, at large radius, many pixels but few counts per pixel, although galaxies with very bright centers (i.e. those with strong ALP features or very steep central profiles) can have high central weights. The fitting routine returns the best fit parameters and their errors and the resulting χ^2_ν . The best fit of the two test functions is defined as the fit with the minimum χ^2_ν .

To test the ability of our fitting technique to recover the true functional parameters, we constructed one-dimensional synthetic surface brightness profiles with known functional parameters, added Poisson noise and fitted them using exactly the same technique. A total of 11 random realizations of 189 sets of **NE** functions were generated, using 21 values of I_o and values of 9 r_c spanning the range of I_o, r_c values derived for the program galaxies. The analytic profiles were convolved with a PSF, and randomly generated Poisson noise was added to each intensity data point to create the synthetic SBPs. All 11x189 SBP realizations were fit with the two test functions: **NO** and **NE**. The **NE** function almost always produced the minimum χ^2_ν values, with a mean and spread of 1.01 ± 0.01 , and the resulting functions fit the synthetic profiles to within 0.2%. The total light of the fitted exponential component is within 0.6% of the input, and the resulting best-fit parameter values are within 10% of the input values.

The tests fail when the exponential component begins to fill in the central region of the SBPs by having a high central brightness as well as a large scale radius. In these cases, the nuker-only fit gives the smallest χ_ν^2 values. This is illustrated in Figure 2.5, which displays three examples of analytical surface brightness profiles: a nuker only profile, a nuker+exponential profile with a small exponential component ($r_c = 0''.03; r_e/r_b = 0.04$), and a nuker+exponential profile with a larger exponential component ($r_e = 0''.12; r_e/r_b = 0.16$). The smaller exponential creates obvious features in the SBP, while the larger exponential joins smoothly onto the outer nuker profile. The smooth joining of the large disk and the underlying galaxy demonstrates the limitations imposed on SBP-fitting: inner light components need not give rise to surface brightness discontinuities. However, one would hope that a color analysis would help break this structural degeneracy.

We return now to the results of fitting the profiles of the program galaxies. As mentioned above, the best fit of the three test functions is defined as the fit with the minimum χ_ν^2 . A problem encountered here is that the absolute values of the minimum χ_ν^2 are usually much larger than 1.0. Although a variety of systematic errors (e.g. geometric distortion, scattered light, etc.) may contribute to the large χ_ν^2 values, it seems clear that the fitting functions adopted are actually not good representations of the light profiles—that real galaxy profiles exhibit subtle structure that is not captured by the relatively simple mathematical formulations used. This difficulty is apparently common to all recent studies of ETG profiles in the literature, but it is not often discussed. The quality of digital photometry is very high, and the χ_ν^2 values reflect departures from the simple fitting functions that would not have been detectable in earlier photographic data sets.

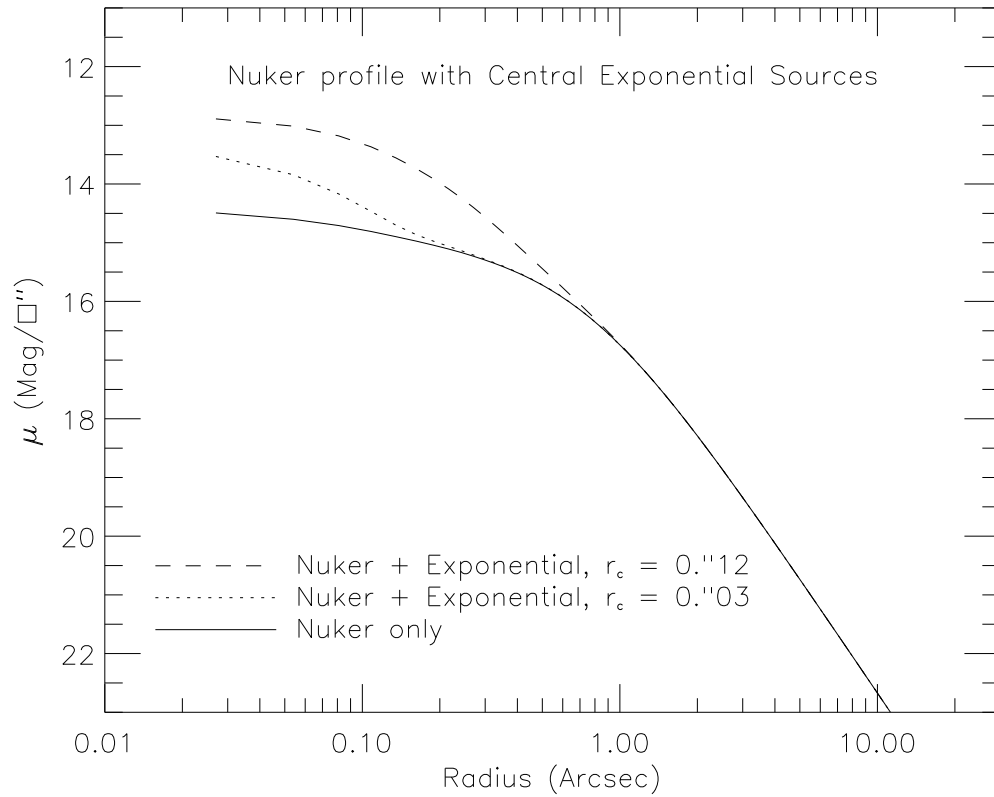


Fig. 2.5.— Plot of three examples of analytical surface brightness profiles: a nuker only profile, a nuker+exponential profile with a small exponential component ($r_c = 0.''03$; $r_c/r_b = 0.04$), and a nuker+exponential profile with a larger exponential component ($r_c = 0.''12$; $r_c/r_b = 0.16$). The latter “fills-in” the central region and smoothly joins with the outer region of the nuker profile.

However, we can judge the performance of different model fits by their *relative* χ^2_ν values. The parameters of the best-fitting profiles for each galaxy are summarized in Table 2.5. In Figure 2.6, we illustrate the performance of our two adopted fitting functions in reproducing the V-band SBP of NGC 4239. The upper panels show the profiles and fitted functions, while the lower panels show the residuals (in magnitudes). From left to right the fitting functions are nuker only and nuker plus an exponential central source. Of the two test function fits, the nuker plus exponential profile clearly has the smallest χ^2_ν and the smallest magnitude residuals in the central regions. Note that neither of the models is able to eliminate the 0.1 mag ripple in the residuals at radii of 5-10''; this failure results in a large χ^2_ν for both models.

In Fig. 2.7, we plot the results of the two model fits for each galaxy in each band, together with their residuals. Residuals of the nuker only (NO) are plotted in the middle panels, while residuals of the nuker+exponential (NE) fits are plotted in the lower panel. The fit with the lowest resulting χ^2_ν is identified by the label of “(1.00)” next to the fit designation NO, or NE. The parenthetical numbers next to the other fit designations report the ratio of the χ^2_ν for that fit to that of the best fit. They therefore represent how much better the best fit is compared to the other fits: values close to 1.00 are quite similar, while values $\gtrsim 2$ are quite noticeably worse.

2.5.3 Comparison to Previous Nuker-Fit Studies

We compare the nuker-only (NO) fits to our V-band surface brightness profiles to previously published SBP fits that were also conducted in the V-band for consistency checks. We find good agreement, within the quoted errors, for six galaxies in our sample, NGC 2778, NGC 3377, NGC 4239, NGC 4478, NGC 4570, and NGC 5576, to results published by Byun et al. (1996); Lauer et al. (2005).

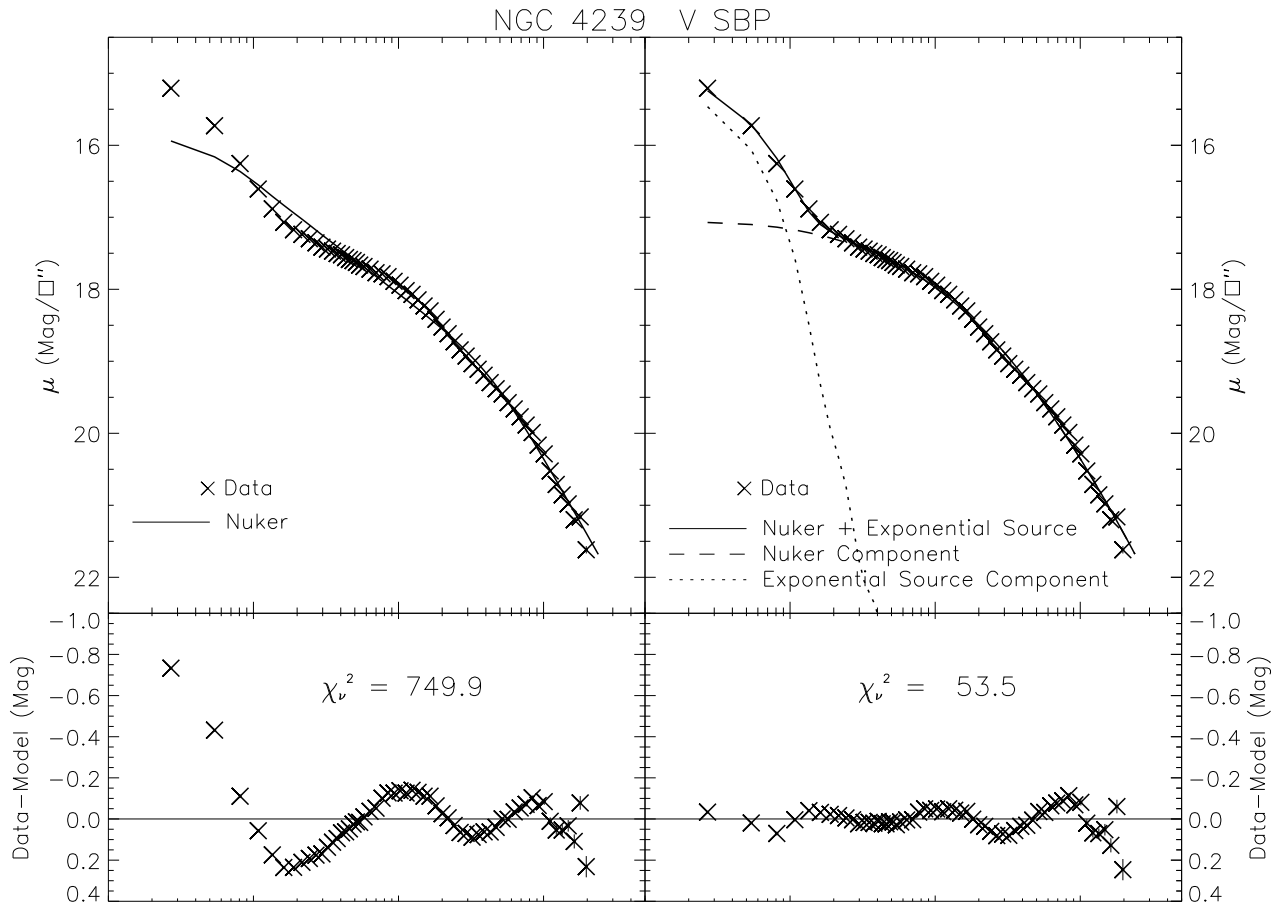


Fig. 2.6.— Comparison of the two model fits to the V-band surface brightness profile of NGC 4239 (top) and their residuals in magnitudes (bottom). From left to right, the figure pairs show (1) the nuker only fit and (2) the nuker plus central exponential source. χ^2_ν values are listed in the residual panels.

Comparisons to previous results for the other six galaxies, NGC 3384, NGC 3640, NGC 4474, NGC 4482, NGC 4621, and NGC 7457 are not possible due to different band selections, different analysis methods, and the use of compromised (image saturation at the galaxy centers) data in other studies. The V-band used here detects a higher portion of main sequence turn-off stellar emission relative to red giant branch stellar emission than in redder bands, which will result in different shaped profiles than in redder (R and H) bands used in Rest et al. (2001); Ravindranath et al. (2001).

Fig. 2.7.— Fitted surface brightness profiles for each galaxy. **Left to Right:** V, U, and NUV fits. **Top Row:** The observed surface brightness profile for each band and its best fitting model. The total best fitting composite model is represented by a heavy solid line, the “nuker” portion is a dashed line, and the central component is a thin solid line. **Middle Row:** Residuals (in magnitudes) between the observed profile and (\times symbols) the “nuker”-only function. **Bottom Row:** Residuals (in magnitudes) between the observed profile and the “nuker” plus central exponential source function (open circles). The parenthetical values in the legends are the ratios of each fits’ χ^2_ν value to that of the overall best fit. “NO” indicates the nuker-only fit and “NE” indicates the nuker plus exponential fit.

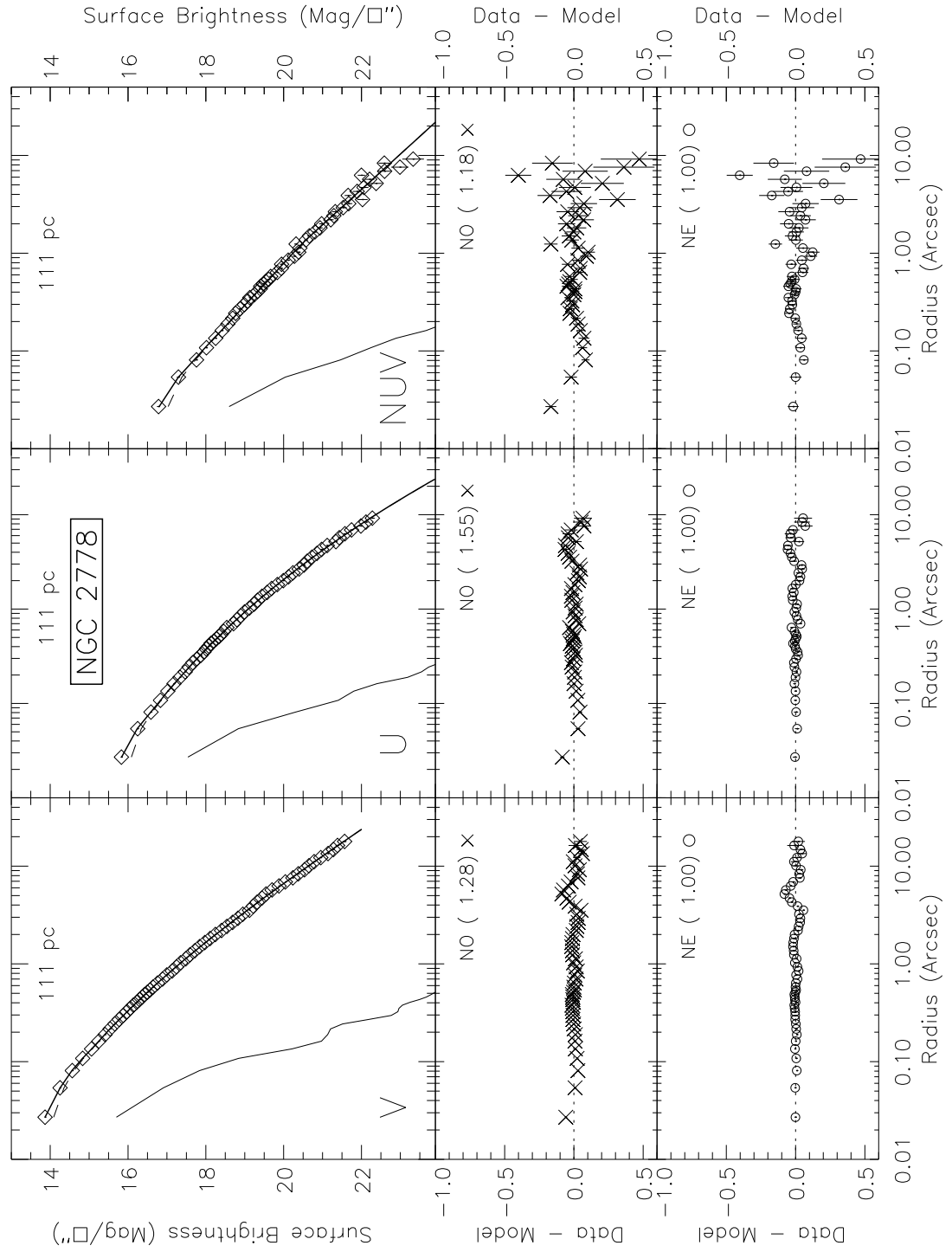


Fig. 2.7.a.— NGC 2778

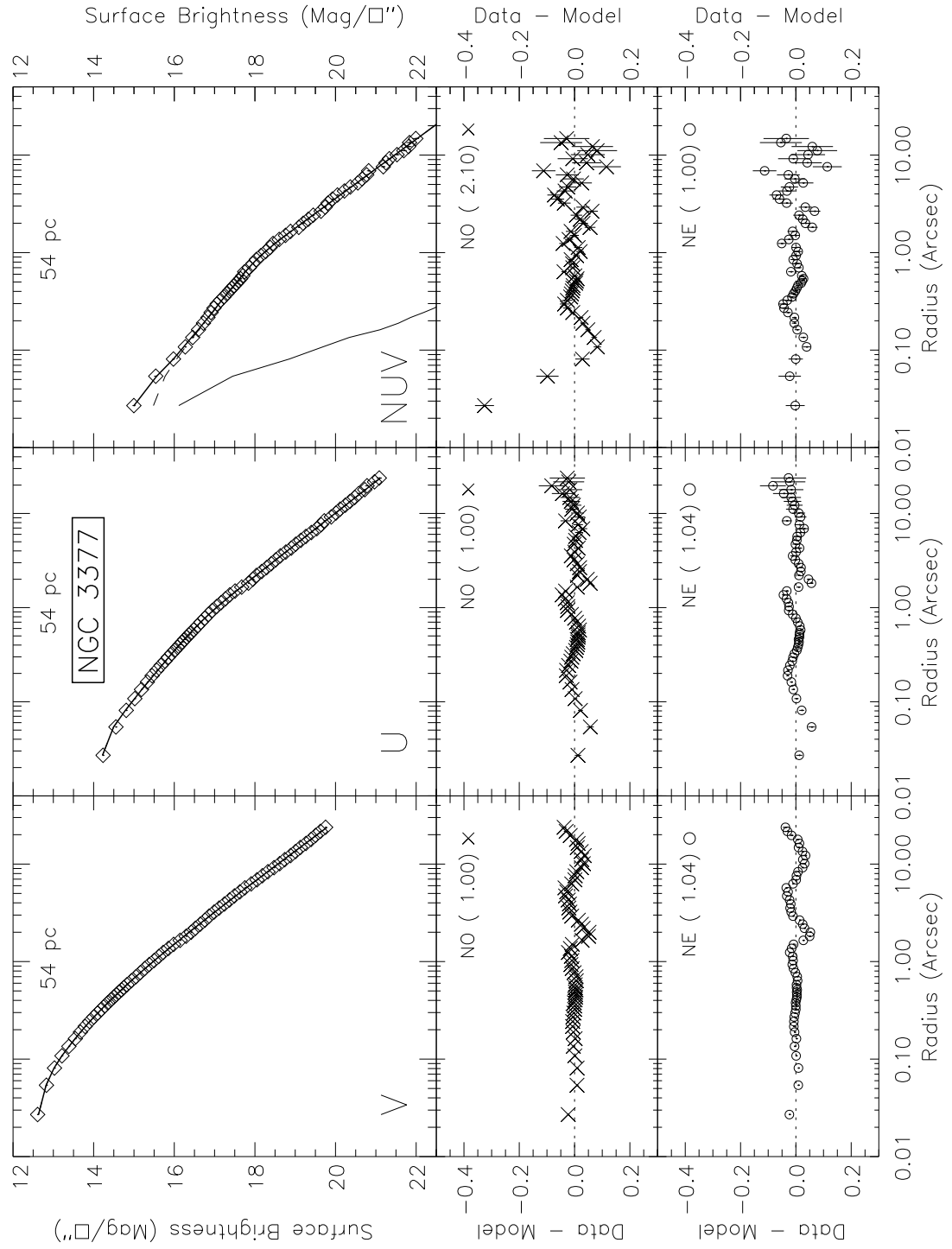


Fig. 2.7.b.— NGC 3377

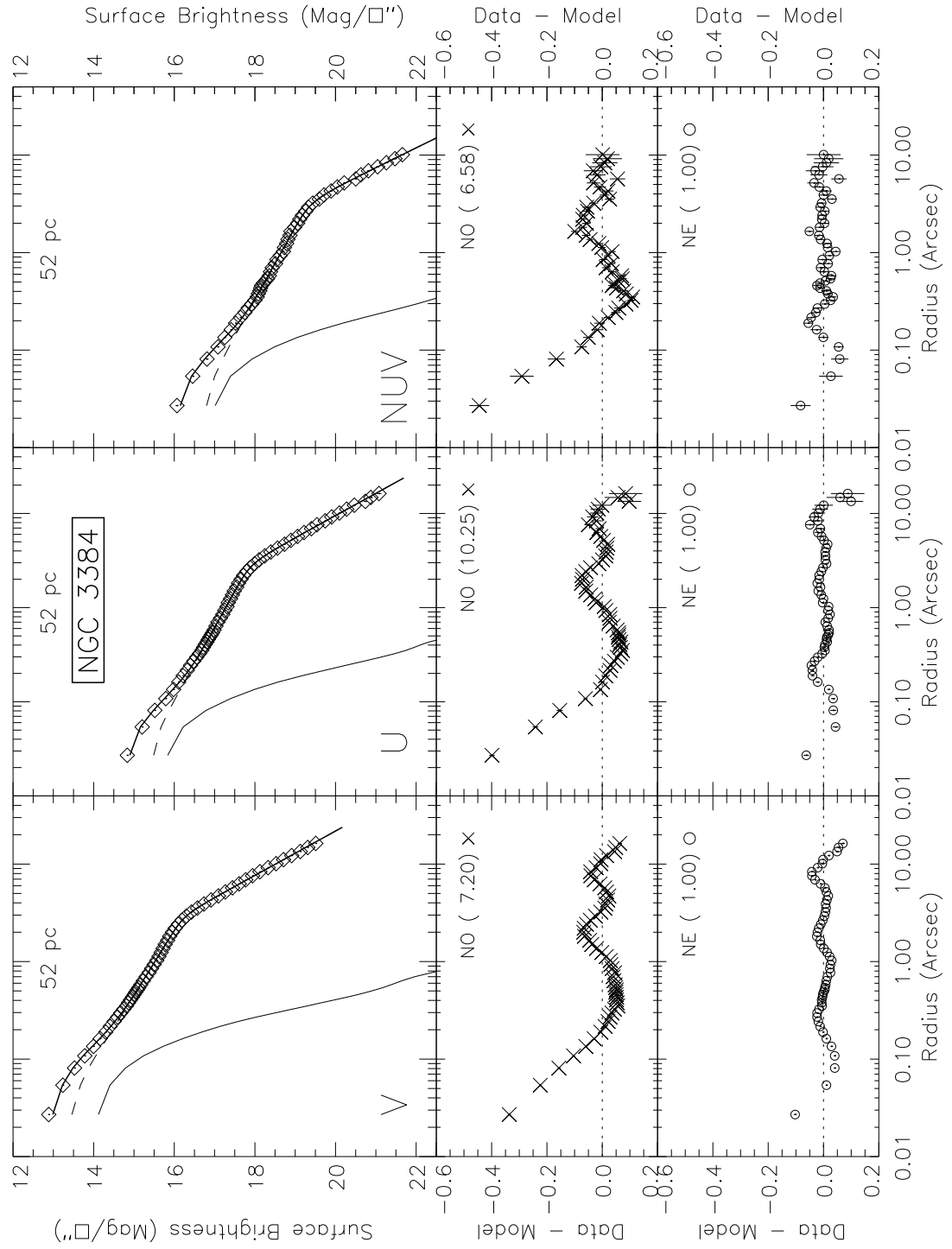


Fig. 2.7.c.— NGC 3384

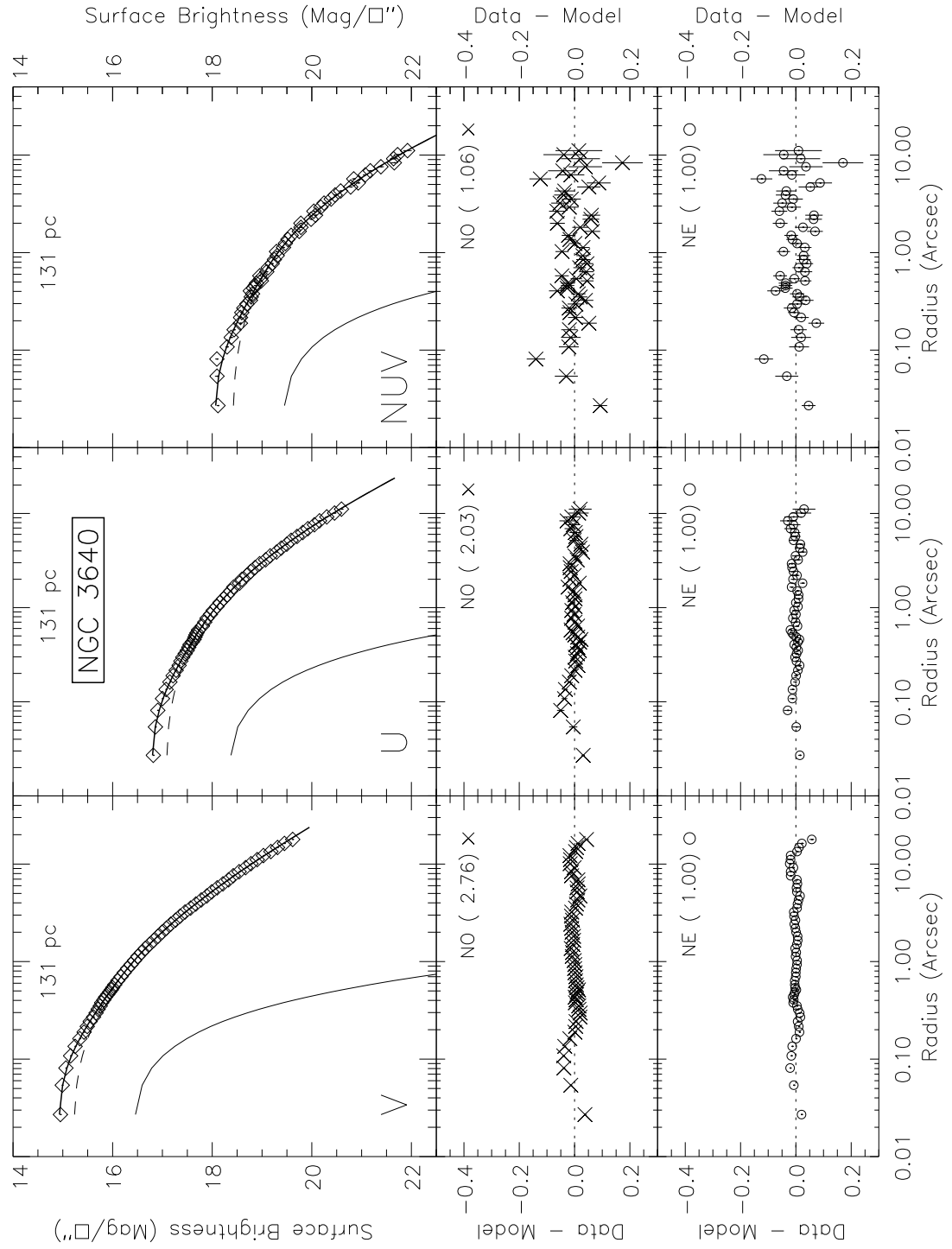


Fig. 2.7.d.— NGC 3640

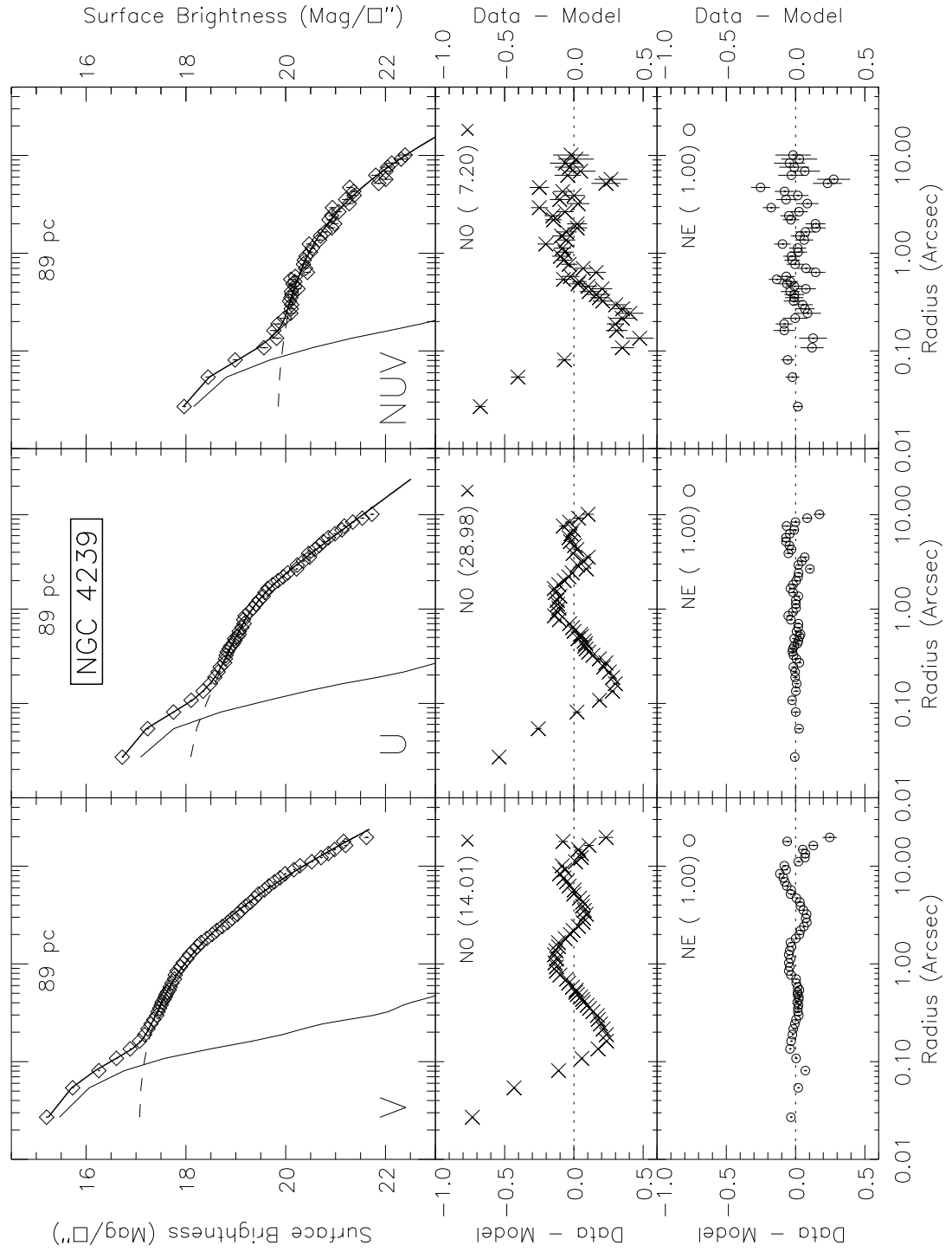


Fig. 2.7.e.— NGC 4239

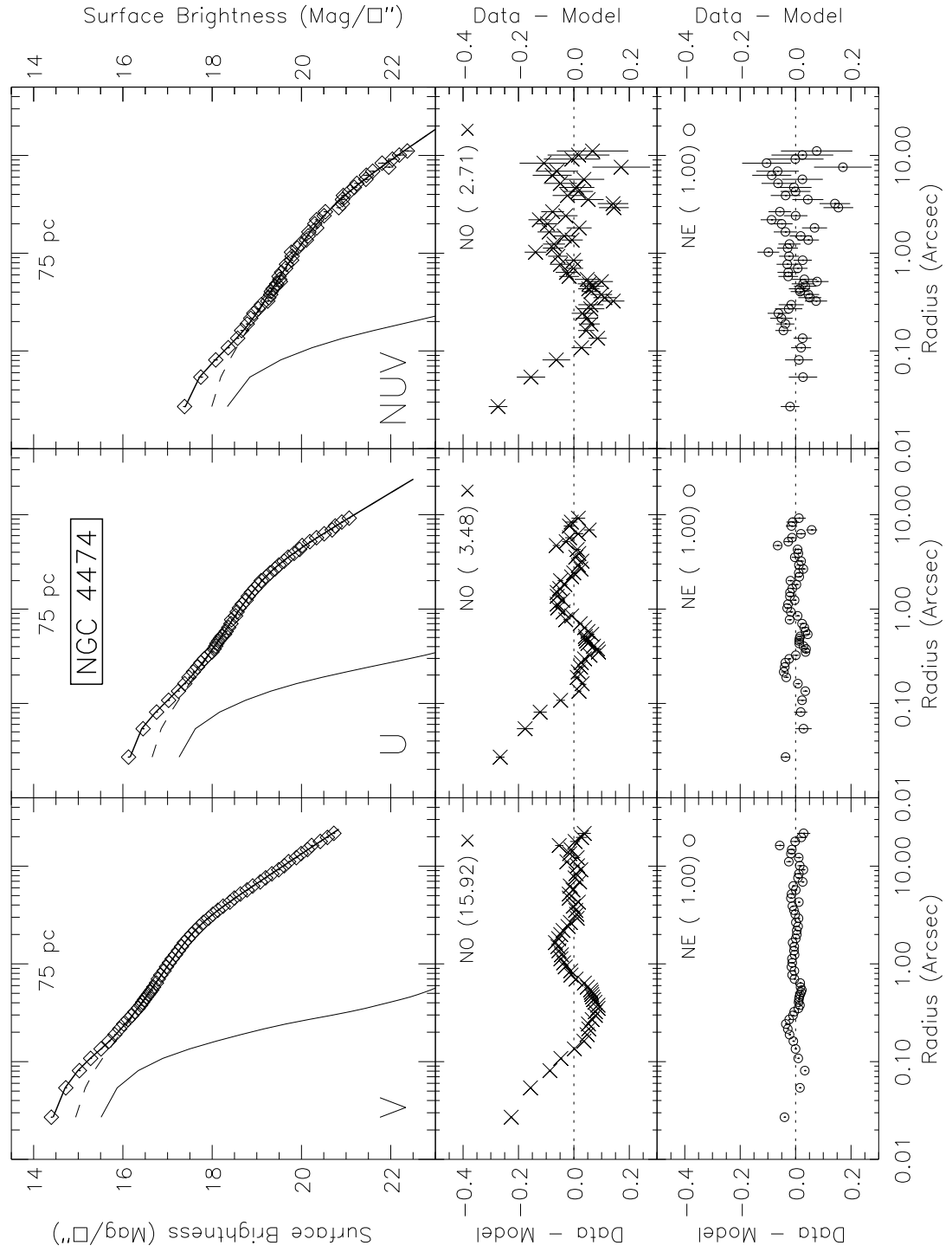


Fig. 2.7.f.— NGC 4474

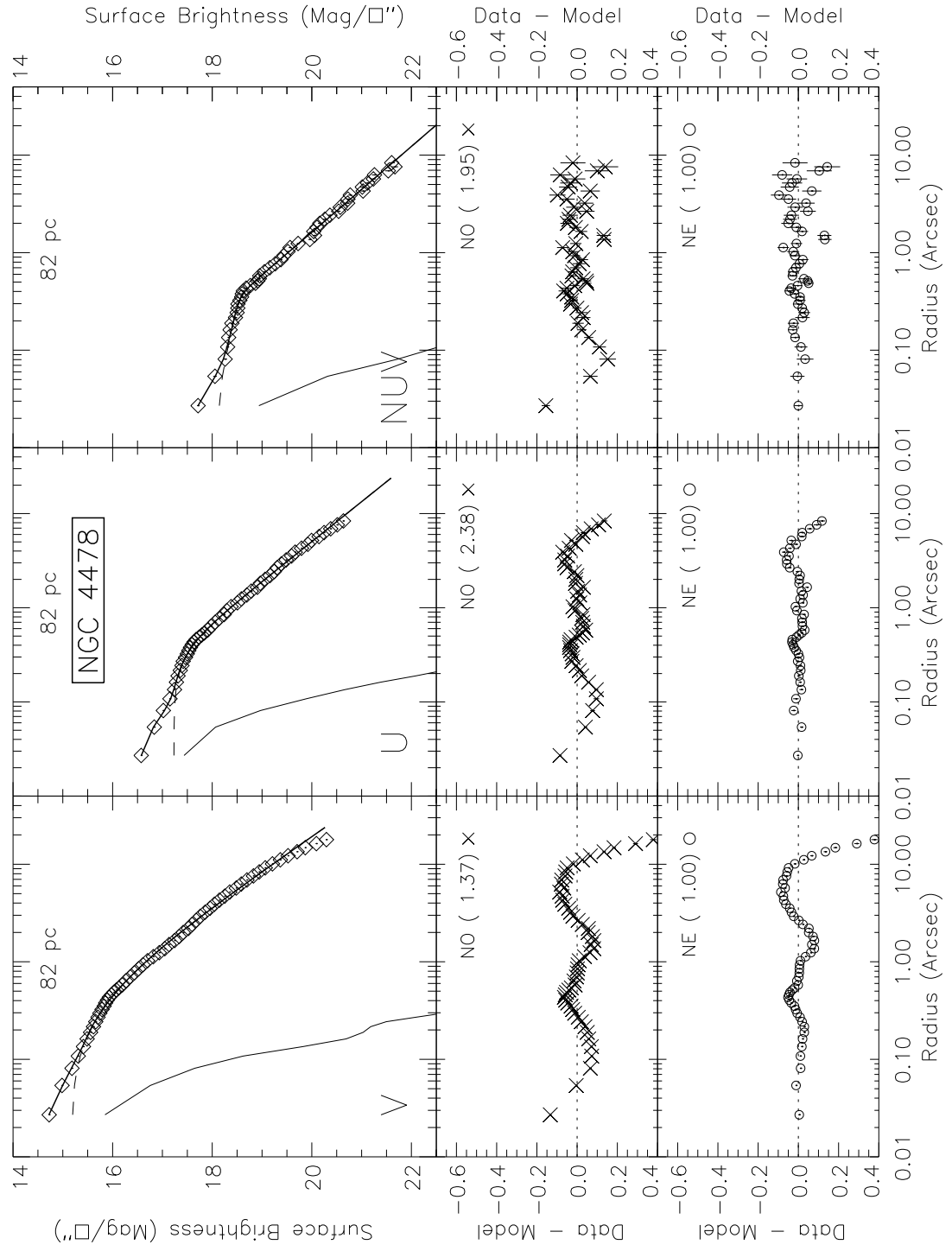


Fig. 2.7.g.— NGC 4478

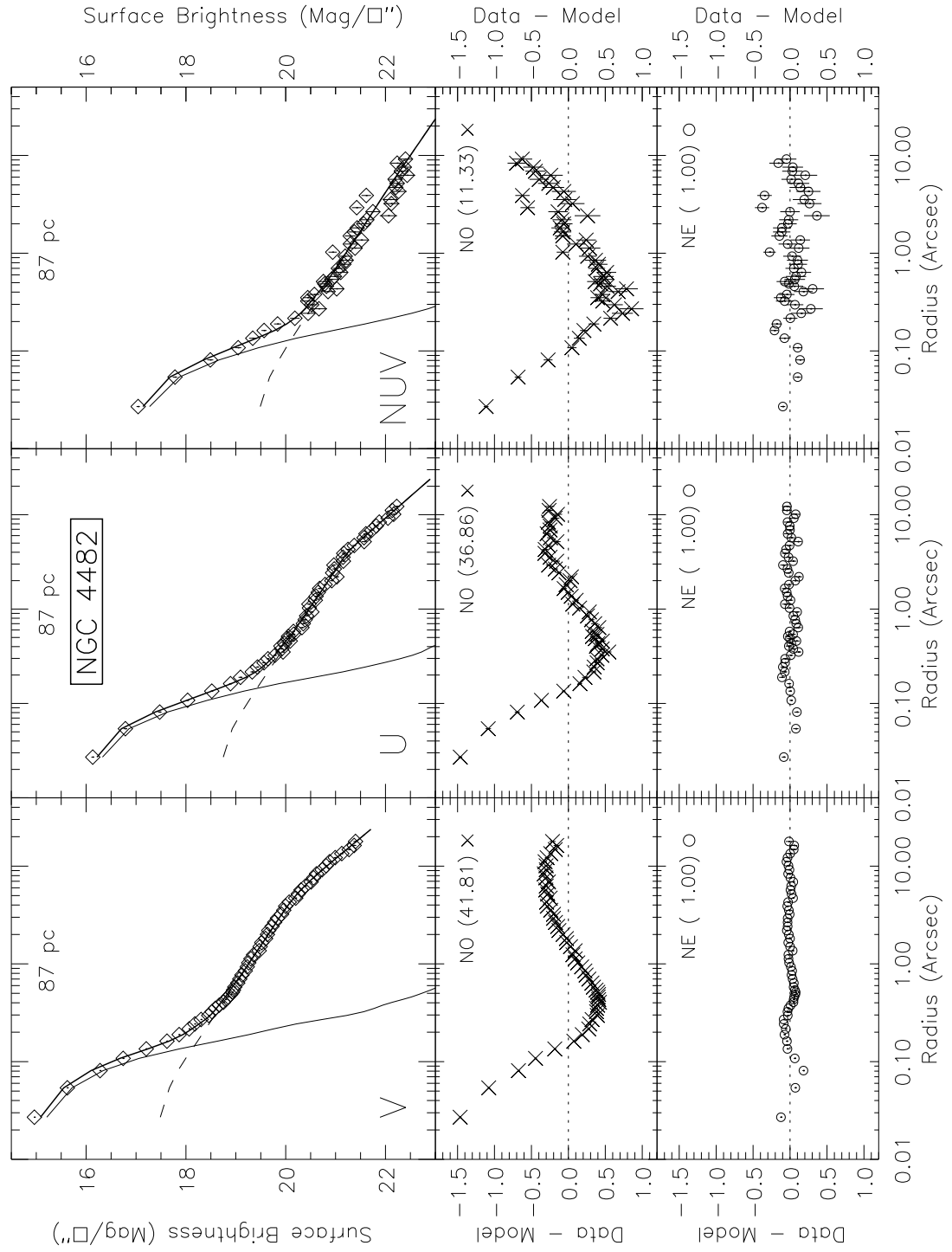


Fig. 2.7.h.— NGC 4482

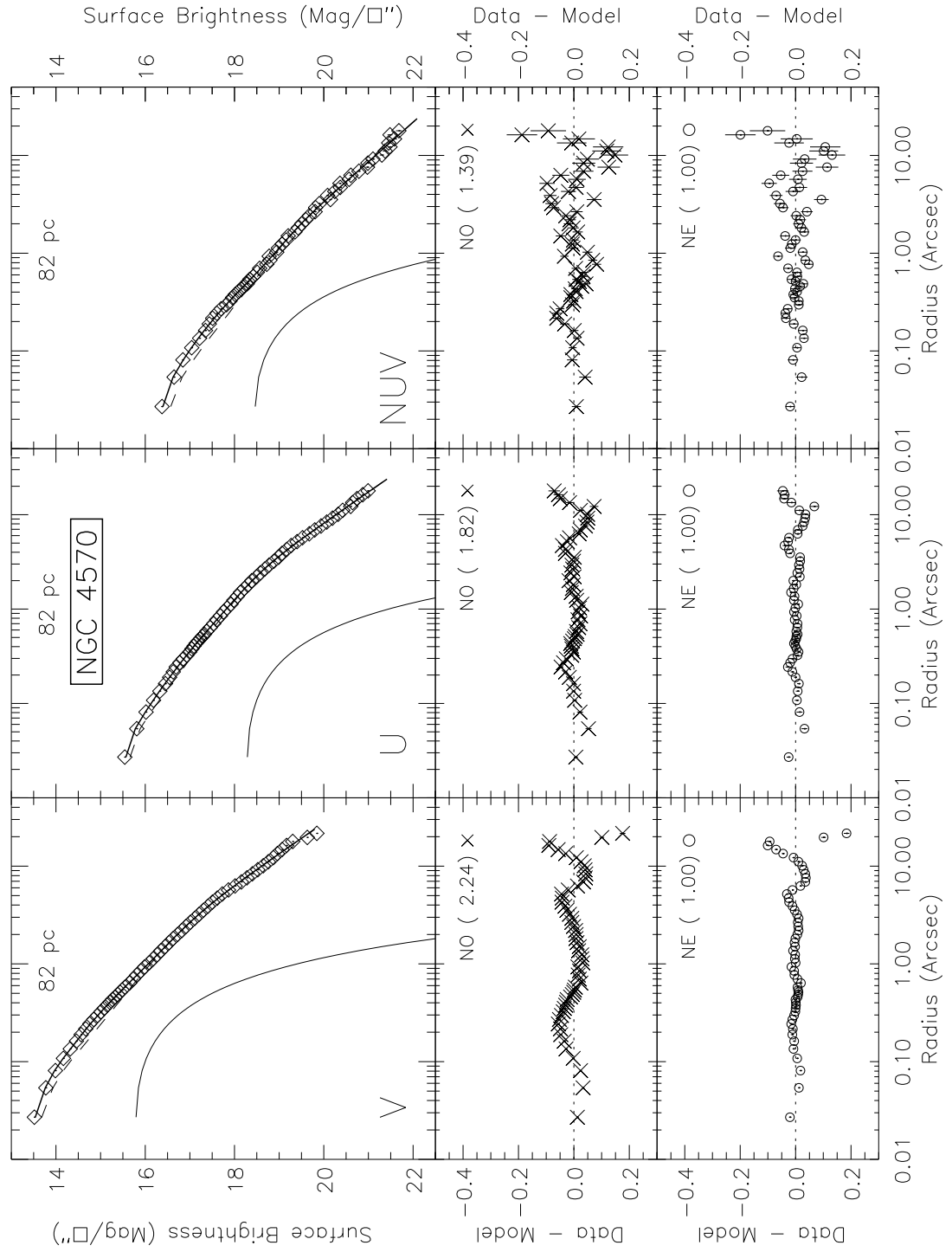


Fig. 2.7.i.— NGC 4570

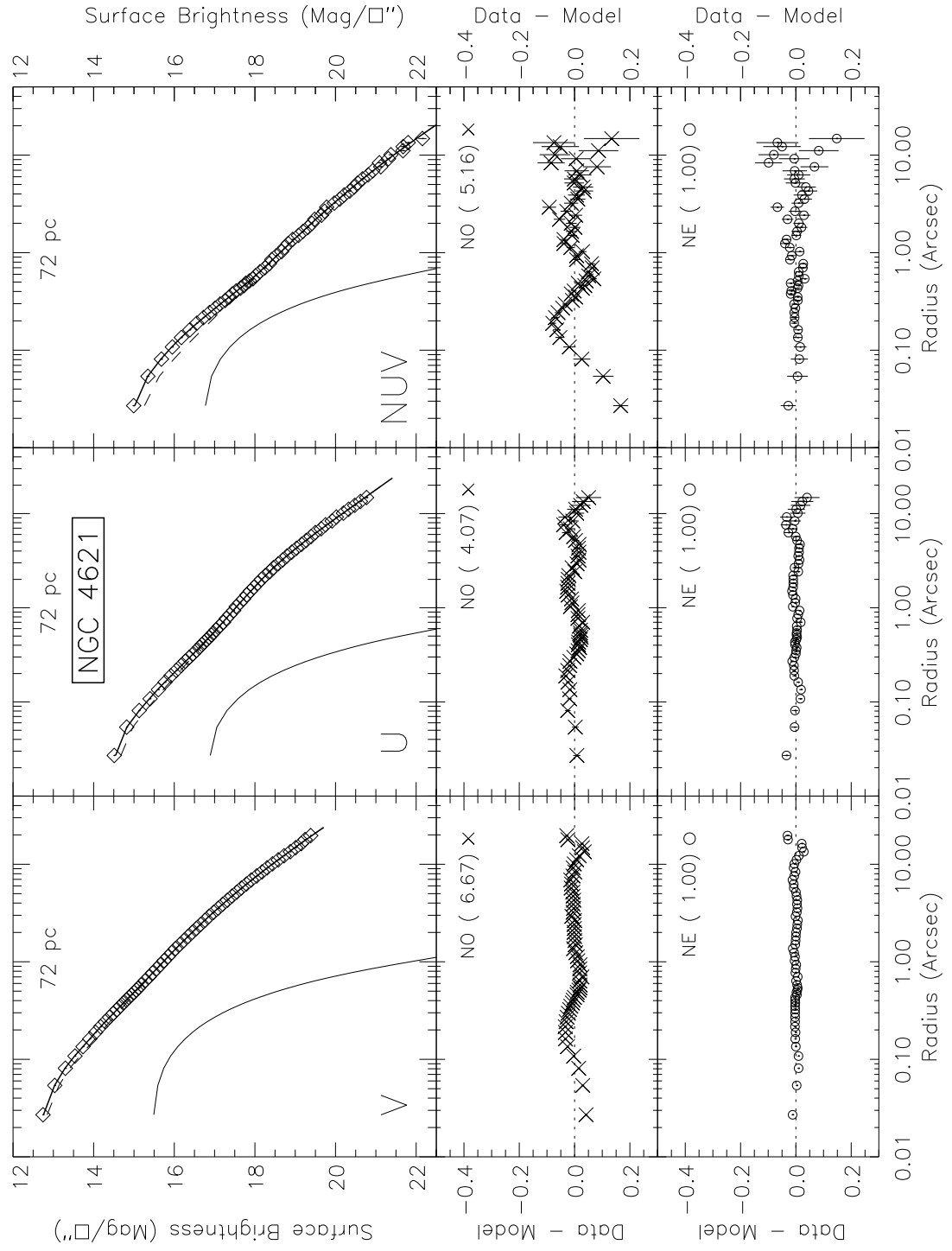


Fig. 2.7.j.— NGC 4621

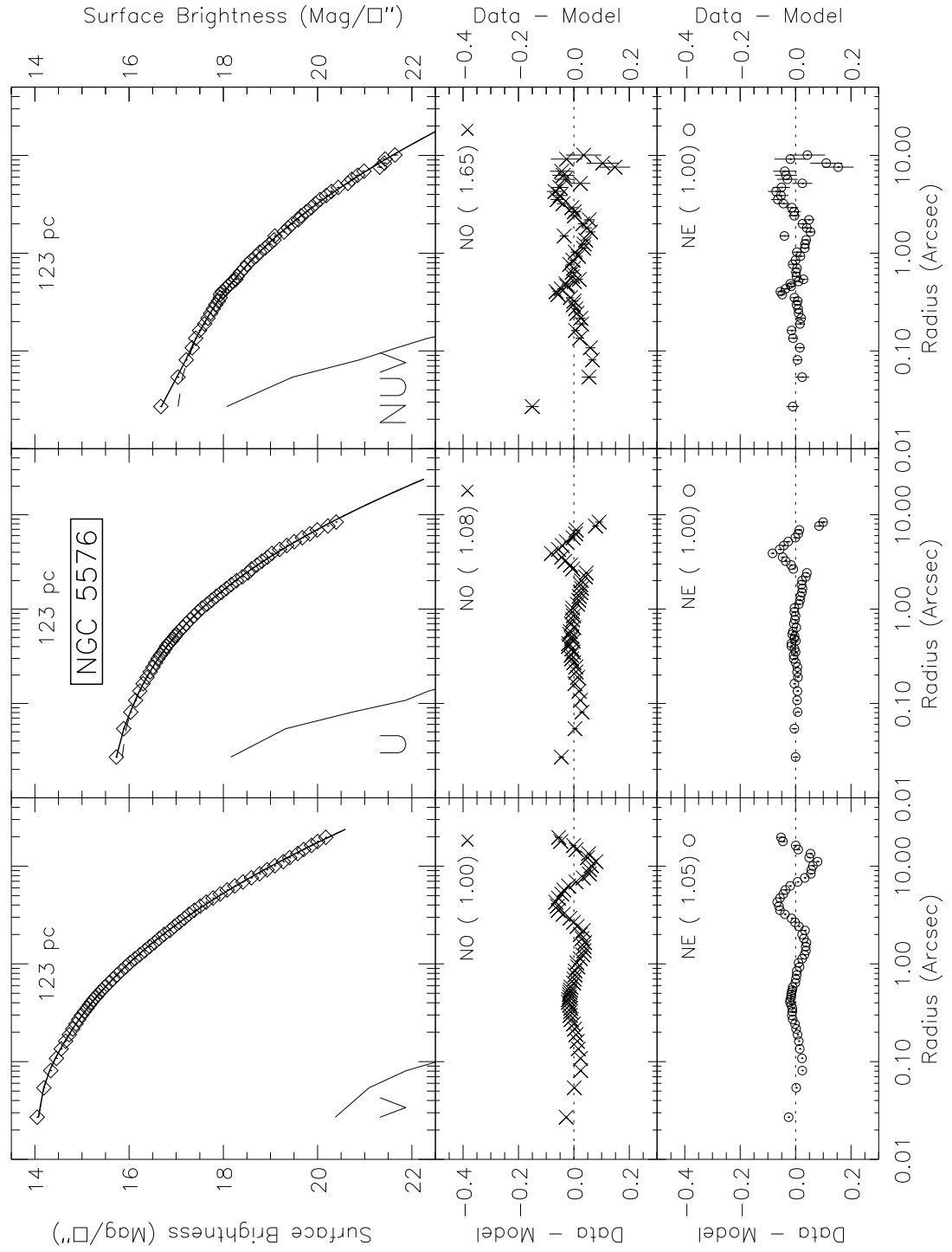


Fig. 2.7.k.— NGC 5576

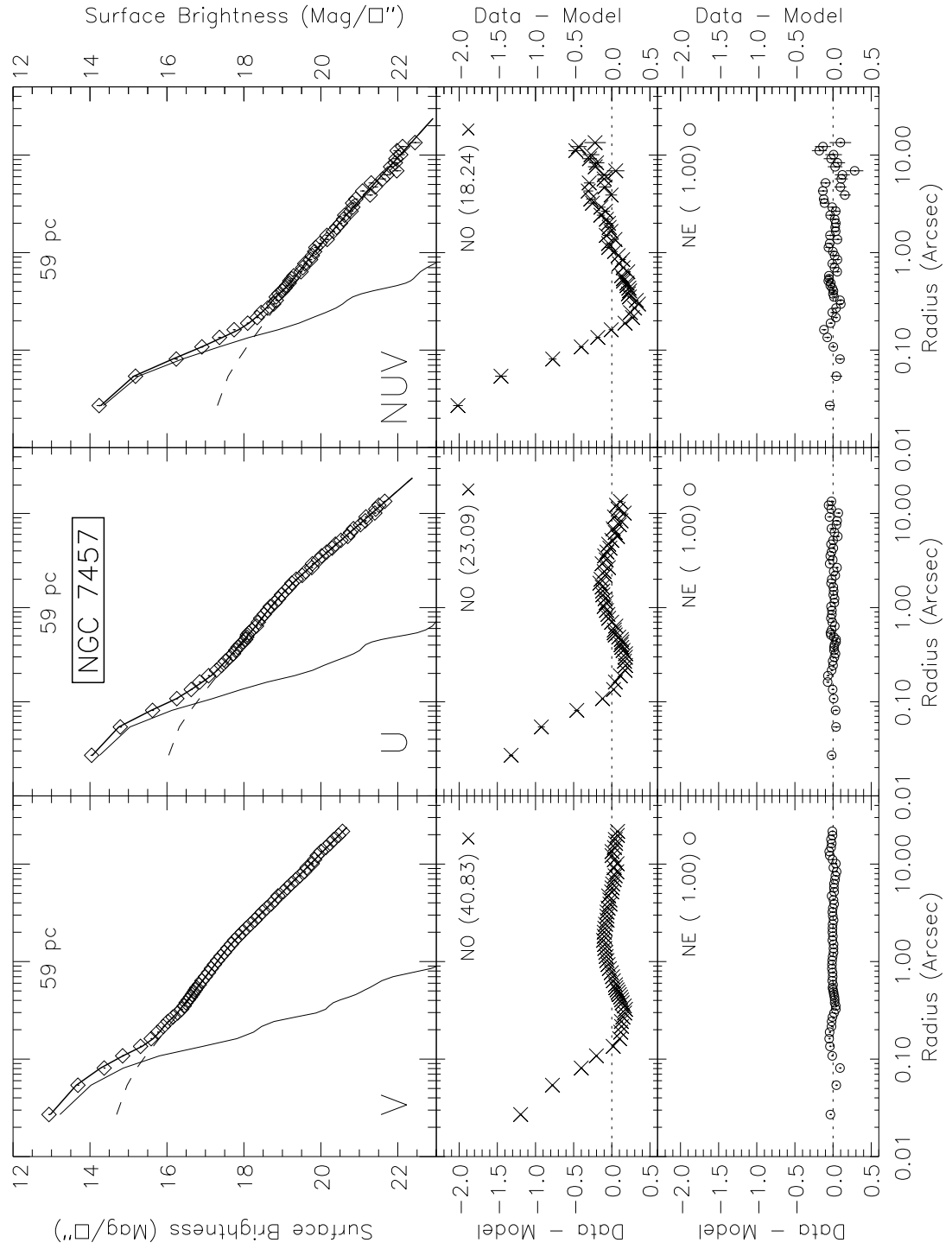


Fig. 2.7.1.— NGC 7457

2.6 Results & Discussion

Table 2.5 summarizes the parameters of the best-fitting composite models for each galaxy and each filter, along with their errors. Figures 2.7a-l display the SBPs and their best-fitting model profiles along with the residuals to the three adopted fitting functions. Residuals between the best-fitting profiles and the observed SBPs are less than 0.07 mag for over 90% of the galaxy data points. The last column of Table 2.5 lists the χ^2_ν of the best fit, while the panels plotting the residuals in Fig. 2.7 list the ratio of the χ^2_ν of each fit to the best-fit χ^2_ν .

The fits in the various bands often, but not always, favor the same fitting function. This is indicated in column (2) of Table 2.5. To decide whether a central component is strongly supported by the fits, we adopt the following criteria: first we evaluated whether a central component (**NE**) is favored over no central component (**NO**) by evaluating the ratio of the corresponding χ^2_ν 's. If the χ^2_ν of the **NE** fits are a factor of two or more lower than those of the **NO** in two or more bands, we conclude that a central component is statistically favored. The exception is for NGC 3377, where the color maps lead us to conclude that there is an unresolved NUV central component, even though the V and U band profiles do not strongly indicate the presence of a central component.

Upper brightness limits for undetected central components were calculated by assuming a radial extent of half a resolution element (or $\sim 0''.0135$) and an object central brightness, I_o , that would increase the galaxy central brightness by 5 times the errors in the observed galaxy central brightness. The V band upper limits range from >-11.7 up to >-1.2 where the surface brightness errors were very small.

The results of this test are given in Table 2.7. Column (1) lists the galaxy, and column (2) indicates which systems belong to the ALP subsample. Column (3) gives

a three-character code for whether the central component models have a χ_ν^2 a factor of two more more lower than the nuker-only model, where “Y” means yes, “N” means no, and the three characters are the results for the V, U, and NUV bands respectively. Column (4) gives the same code, this time for testing the **NE** model against the **NP** model (a “-” is given if a central component is not favored over the nuker-only profile in the previous comparison). Our final evaluation of the central component type based on this analysis is given in column (5). A “?” is given if there is only one “Y” in the model comparison. When an extended central component is favored, we list the scale height (in parsecs) of the best fitting exponential, averaged over all relevant bands, in parenthesis. The galaxies are listed in order of the decreasing fraction of the total light contained in the central component, which will be described below (§ 2.6.1) and which is listed in column (7).

The SBP modeling indicates that composite profiles (**NE**) best describe all six of the original ALP galaxies. Composite profiles also provide better fits to three of the six non-ALP galaxies. We now discuss the individual galaxies in each sub-sample.

ALPs

For the ALP sample, an extra central exponential component (**NE**) is clearly favored over no central component (**NO**) or an unresolved central component (**NP**) for four of the six galaxies: NGC 3384, NGC 4239, NGC 4482, and NGC 7457. The **NE** functional form is preferred with a high confidence: the χ_ν^2 values of the **NP** fits are 1.3—13 times larger than the **NE** values, and the χ_ν^2 values of the **NO** fits are 3—43 times larger. The largest central exponential scale radii (column 9 of Table 2.5) are found in NGC 3384 and NGC 4474, and are 1.4-2 times larger than the half width of the corresponding PSF ($\frac{1}{2}\theta_\lambda$). The extended nature of the exponential function al-

lows us to find components in NGC 4239 and NGC 7457 that have scale radii smaller than or of order $\frac{1}{2}\theta_\lambda$. The color images of NGC 7457 (Fig. 2.2l) clearly show a compact central feature. The central surface brightness of the exponential components of these four galaxies range from 0.5-16 times the center-most surface brightness of their underlying nuker profiles.

In NGC 4474, a central component is strongly favored (Fig. 2.7f). The V-band profile is much better fit by an exponential than by an unresolved source, although the preference is less obvious in the U and NUV bands. It therefore receives an “Extended?” classification in Table 2.7.

A central component is also apparent in the fits for NGC 4478 (Fig. 2.7g), however the statistical significance is weaker than for the other five ALPs. For this system an unresolved central component fits almost as well as a small exponential in all three bands, so we cannot claim with confidence that it contains an extended component, and therefore classify it as “Unresolved”.

Non-ALPs

Of the original non-ALP sample, central components are clearly favored for NGC 3640 and NGC 4621, although the evidence in the NUV band of NGC 3640 is not strong. In both systems an extended component is preferred, with relatively large scale lengths (4.0 to 5.3 times larger than $\frac{1}{2}\theta_\lambda$) and fainter central surface brightness relative to the underlying nuker component (32–34% and 9–26% of the brightness at the center-most measurements for NGC 3640 and NGC 4621, respectively), making these central objects more difficult to recognize than their counterparts in the ALP sample. However, the $NUV - V$ color image of NGC 4621 (Fig. 2.2j) clearly supports the presence of an extended central component. This is a case where optical imaging alone would be

blind to important aspects of this galaxy. An analysis of these colors will be given in Chapter 3 of this Thesis.

NGC 3377 (Fig. 2.7b) is an unusual case. It is best fit by a nuker-only profile in the V and U-bands, but has an obvious unresolved central component in the NUV band. This is clearly seen in the $NUV - V$ color image (Fig. 2.2b). We re-emphasize that the color images were made by convolving the different images to a common resolution, so this is not an artifact of different PSFs.

The central component fits for the remaining three non-ALP systems, NGC 2778, NGC 4570, and NGC 5576, are not significantly favored over the nuker-only fits, so we do not claim we have detected central components in these systems. The color images do not suggest that we reconsider this decision.

2.6.1 Central light properties

Table 2.6 summarizes the total absolute magnitudes of the different galaxy components, based on our fits. Column (3) lists $M_{R_{good}}$, the integrated galaxy light contained within the ACS-HRC images out to R_{Good} (which range from 20 - 100% of R_e). Column (4) lists the luminosity of the “Body” of the galaxy, which is the $M_{R_{good}}$ minus the contribution from any central component. Column (5) lists the integrated light of any central component, using the parameters derived from the fitting procedure (total light for unresolved components; central surface brightness and scale radii for exponentials). Finally, column (6) lists the fractional contribution of any central component to the total luminosity averaged over all relevant bands ($< P_{CC} >$).

The central components contribute negligible light to their host galaxies outside of R_{Good} . In fact, all central components contribute less than 10% of the surface intensity at a radius of $1''$. The central components that are best described by exponentials

are generally much brighter than the unresolved central components, cover a larger range of absolute magnitudes, and comprise a larger fraction of their host galaxies' total light.

As noted above, not all surface brightness profiles were best-fit with a central component. An upper limit on the total brightness of a central component is not possible to calculate for an extended source since the total brightness relies on the scale radius, which is not possible to estimate for an undetected object. The marginal point source detections are allowed to stand as lower limits to the absolute magnitudes of the possible central point sources in NGC 2778 and NGC 5576. A comparison of the residual magnitude profiles for the **NO** fits to those SBPs with marginal and with certain detections of a central point source in Figures 2.7.a-l indicate that there is a cut-off at about -0.25 mag central residual below which the presence of a point source is not certain and above which a detection is certain. By using the -0.25 mag central residual cut-off, lower absolute magnitude limits can be placed on possible central point sources in NGC 3377 in the V and U bands and in NGC 4570 in the U and NUV bands. The lower absolute magnitude limits are included in Table 2.6 as well as the associated total light contribution limits.

In Table 2.7, we summarize the contributions of central objects in the sample galaxies. In Column (6), we list the percentage contributions of the central components to the total light, averaged over all three bands for each galaxy and arrange them from highest to lowest contributions. The mean central light percentages are very small ($<1.5\%$) and no single property (scale radius, central component luminosity, or galaxy luminosity) appears to correlate with it.

2.6.2 Central components and “Extra Light”

It is important to note that the central components that we detect are all very much smaller than the “extra light” components found in merger remnants (Hibbard & Yun 1999; Rothberg & Joseph 2004; Hopkins et al. 2008a) or otherwise normal early types (Kormendy 1999; Hopkins et al. 2008b; Kormendy et al. 2008). The latter “extra light” components are believed to be the result of merger-induced dissipation (Barnes & Hernquist 1991, 1996) and subsequent star formation (Mihos & Hernquist 1994b; Cox et al. 2006; Hopkins et al. 2008a). They have scales an order of magnitude or more larger than the spatial scales discussed here. As noted in §2.2, the limited FOV of our observations does not allow us to fit for these much more extended components. To illustrate this point, we refer the reader to Fig. 5 of Kormendy (1999), where the light profile of NGC 3377 is plotted over a radial range of $0''.03 - 200''$. The outer regions of the light profile are fit with a Sérsic function, and excess light is identified as an upward departure from an inward extrapolation of this function. Analyzed in this manner, the “extra light” extends from $0-4''$. Examining Fig. 2.7b, one sees that almost the entire profile used in the current work is part of the “extra light” defined by Kormendy (1999).

Similar results follow when comparing our results for other galaxies. Larger-scale merger-induced “extra light” components are claimed for NGC 2778, NGC 3377, NGC 3640, NGC 4478, NGC 4621, and NGC 5576 by Kormendy et al. (2008); Hopkins et al. (2008b,c) (see column 7 of Table 2.7 for the appropriate references for each galaxy). Kormendy et al. (2008) fits the profile of the S0 galaxy NGC 4570 with a Sérsic+outer exponential function (at a much larger scale than our inner exponential), finding no excess. They also plot the profile of the Spheroidal (also sometimes referred to as a dE) NGC 4482, finding the same compact central component that we find,

which they refer to as a Nucleus. Both Kormendy et al. (2008) (see their §9.7) and Hopkins et al. (2008b) (see their Appendix C) discuss at some length the distinction between merger induced “extra light” and the nuclei found in many dwarf spheroidal and disk galaxies.

The components we examine are thus distinct from the merger-induced light excesses. Additionally, Table 2.7 shows that they are not obviously related to the presence or absence of merger-induced extra light: there is no correspondence to central component type, size, or luminosity with the presence of extra light.

It is quite possible that the central components we find in the non-spheroidal are similar to the stellar nuclei found in dwarf spheriodals and spirals. The presence of stellar nuclei in normal-size early-type galaxies are more difficult to detect than those in dwarf spheriodals and spirals due to the high surface brightnesses of ETGs. A full assessment of the structure and colors of the detected central components will be performed in Chapter 4 of this Thesis.

2.7 Conclusions

High quality, high spatial resolution surface brightness profiles of twelve early type galaxies (six with ALP features, six without) in the V, U, and NUV bands are fit with functions that describe either an outer galaxy body plus a central component or just a galaxy body. We detect statistically robust (relative $\chi^2_\nu \gtrsim 5$) unique structural components in the form of central components in six galaxies and detect (relative $\chi^2_\nu \gtrsim 2$) an additional two central components. The detections of central components in five of the ALP galaxies are robust while that of the sixth galaxy is merely a detection with an unresolved central component. One detection and one robust detection are of central components of non-ALP galaxies. An unresolved central component is

detected in NGC 3377 in the NUV only.

The central components are generally small with scale radii $r_c < 15$ pc and bright with absolute V-band magnitudes, M_V , ranging from -10.5 to -13.5 mag. The central components of the non-ALP galaxies, NGC 3640 and NGC 4621, have properties which set them apart from those of the ALP galaxies. They are the two largest central components with scale radii of 15 and 8 pc, respectively. By comparison, the ALP-galaxy extended central components have scale radii which range from 1 to 3 pc. They are the two brightest central components in terms of absolute magnitudes and yet, they are fainter than those of the ALP sample galaxies compared to the surface brightness of the underlying galaxy bodies. No additional trend of central component size with brightness is observed.

All the central components detected here are much smaller than the extra light regions predicted by gaseous merger models and are possibly related to the stellar nuclei found in many galaxies across the Hubble Type spectrum. Similar central objects have been detected in normal-sized early type galaxies (Byun et al. 1996; Rest et al. 2001; Ravindranath et al. 2001; Ferrarese et al. 2006; Côté et al. 2006), however, the photometry used to detect and isolate the current set of central components has unprecedented spatial resolution and the bands were chosen for their sensitivity to the presence of multi-generational stellar populations.

The colors of the twelve early-type galaxies will be examined for their stellar population compositions and will be presented in Chapter 3. Further identifying traits of the central components will be determined through its own color analysis in Chapter 4.

Table 2.5. Surface Brightness Fit Results

Galaxy NGC (1)	Filter.Fit (2)	$R_{G^{good}}^{\lambda}$ (3)	μ_b mag/□'' (4)	r_b '' (5)	α (6)	β (7)	γ (8)	m_C mag (9)	r_c '' (10)	χ^2_b (11)
NGC2778	V.N	17.9	17.11(0.12)	0.84(0.08)	1.17(0.20)	1.44(0.04)	0.85(0.03)	> 24.0	(0.014)	25.10
...	U.N	9.2	19.69(0.39)	1.62(0.50)	1.22(0.30)	1.54(0.13)	0.82(0.03)	> 24.1	(0.014)	3.36
...	NUV.N	9.2	20.71(0.42)	1.51(0.60)	10.00(0.00)	1.10(0.06)	0.93(0.02)	> 23.2	(0.014)	2.42
NGC3377	V.N	23.8	13.69(0.24)	0.19(0.05)	0.89(0.11)	1.32(0.02)	0.31(0.12)	> 23.5	(0.014)	73.19
...	U.N	23.8	16.74(0.04)	0.75(0.03)	3.07(0.45)	1.19(0.01)	0.75(0.01)	> 22.8	(0.014)	11.50
...	NUV.E	14.8	18.15(0.05)	0.92(0.04)	4.80(1.26)	1.32(0.01)	0.75(0.02)	20.28(3.31)	0.008(0.006)	3.02
NGC3384	V.E	16.3	16.34(0.02)	3.04(0.04)	8.38(1.29)	1.76(0.02)	0.59(0.01)	17.55(0.17)	0.055(0.004)	155.96
...	U.E	16.3	18.02(0.03)	3.02(0.06)	7.14(1.05)	1.69(0.03)	0.51(0.01)	19.69(0.17)	0.041(0.003)	12.18
...	NUV.E	10.1	19.53(0.05)	3.45(0.11)	6.48(1.13)	1.97(0.06)	0.53(0.01)	20.79(0.20)	0.044(0.003)	2.52
NGC3640	V.E	17.9	16.57(0.11)	1.21(0.16)	0.70(0.06)	1.45(0.07)	0.00(0.00)	18.69(0.19)	0.116(0.006)	34.22
...	U.E	11.1	18.59(0.26)	1.96(0.59)	0.73(0.09)	1.62(0.17)	0.00(0.00)	20.61(0.25)	0.117(0.008)	1.69
...	NUV.N	11.1	20.62(0.01)	4.28(0.00)	0.92(0.09)	1.89(0.04)	0.25(0.03)	> 25.0	(0.014)	2.60
NGC4239	V.E	19.7	18.77(0.41)	2.69(1.13)	0.74(0.09)	1.80(0.26)	0.00(0.00)	19.76(0.21)	0.026(0.002)	53.53
...	U.E	10.1	19.55(0.06)	1.40(0.11)	2.70(0.73)	1.02(0.05)	0.33(0.04)	21.52(0.22)	0.022(0.002)	3.56
...	NUV.E	10.1	21.73(0.03)	5.70(0.00)	0.83(0.34)	1.92(0.18)	0.04(0.22)	22.54(0.38)	0.024(0.003)	1.73
NGC4474	V.E	21.6	17.80(0.03)	2.66(0.06)	4.31(0.49)	1.33(0.01)	0.60(0.01)	19.26(0.12)	0.044(0.002)	26.98
...	U.E	9.2	19.44(0.10)	2.81(0.26)	3.29(0.76)	1.41(0.09)	0.56(0.02)	21.04(0.25)	0.043(0.004)	7.26
...	NUV.E	11.1	20.75(0.35)	3.14(1.11)	2.26(1.19)	1.30(0.25)	0.53(0.04)	22.46(0.46)	0.033(0.006)	1.55
NGC4478	V.N	17.9	16.31(0.13)	0.65(0.11)	1.38(0.42)	1.12(0.06)	0.35(0.07)	> 25.6	(0.014)	523.77
...	U.E	8.3	17.51(0.02)	0.33(0.01)	2.39(0.30)	0.94(0.01)	0.00(0.00)	21.83(0.47)	0.024(0.004)	12.36
...	NUV.N	8.3	18.71(0.05)	0.42(0.03)	10.00(0.00)	0.91(0.01)	0.32(0.02)	> 25.1	(0.014)	4.39
NGC4482	V.E	17.9	20.29(0.22)	5.60(1.52)	5.01(5.19)	0.94(0.15)	0.51(0.01)	19.35(0.12)	0.031(0.001)	26.73
...	U.E	12.2	21.27(0.11)	4.12(0.65)	10.00(0.00)	0.87(0.07)	0.50(0.01)	20.56(0.13)	0.029(0.001)	2.91

Table 2.5—Continued

Galaxy NGC	Filter.Fit	$R_{G^{ood}}^{\lambda}$	μ_b mag/ \square''	r_b ''	α	β	γ	m_C mag	r_c ''	χ^2_{ν}
(1)	(2)	(3)	(4)	(5)	(6)	(7)	(8)	(9)	(10)	(11)
...	NUV.E	9.2	22.02(/nodata)	4.33(/nodata)	2.82(/nodata)	0.54(1.32)	0.49(0.08)	21.56(0.30)	0.027(0.003)	2.70
NGC4570	V.E	21.6	17.15(0.11)	3.05(0.30)	2.06(0.61)	1.28(0.05)	0.69(0.02)	16.35(0.34)	0.282(0.039)	64.99
...	U.N	17.9	18.99(0.25)	3.54(0.82)	1.22(0.19)	1.41(0.10)	0.61(0.01)	> 24.7	(0.014)	9.92
...	NUV.N	17.9	19.19(5.38)	1.40(8.18)	0.23(0.82)	1.45(2.35)	0.25(1.88)	> 24.0	(0.014)	4.76
NGC4621	V.E	19.7	17.45(0.20)	4.80(0.78)	1.14(0.13)	1.50(0.06)	0.79(0.01)	17.21(0.16)	0.154(0.009)	7.78
...	U.E	14.8	18.69(0.07)	3.25(0.19)	3.04(0.44)	1.32(0.03)	0.81(0.01)	19.45(0.17)	0.097(0.005)	2.16
...	NUV.E	14.8	20.94(2.01)	6.94(10.46)	1.26(0.82)	1.54(0.58)	0.94(0.03)	19.11(0.22)	0.110(0.007)	1.67
NGC5576	V.N	19.7	18.13(1.54)	5.75(5.89)	0.46(0.12)	2.70(0.75)	0.07(0.14)	> 25.3	(0.014)	250.79
...	U.N	8.3	19.39(0.01)	4.71(0.00)	0.59(0.04)	2.59(0.04)	0.15(0.05)	> 24.4	(0.014)	20.64
...	NUV.N	10.1	19.60(0.79)	2.31(1.61)	0.88(0.31)	1.72(0.44)	0.38(0.08)	> 23.8	(0.014)	5.23
NGC7457	V.E	21.6	17.64(0.05)	1.45(0.07)	9.97(7.26)	1.01(0.01)	0.75(0.01)	17.71(0.15)	0.018(0.001)	25.08
...	U.E	13.4	19.13(0.07)	1.58(0.11)	5.48(2.56)	1.12(0.02)	0.75(0.01)	18.79(0.17)	0.018(0.001)	5.18
...	NUV.E	13.4	20.17(0.33)	1.44(0.53)	4.53(9.24)	0.91(0.05)	0.72(0.05)	18.93(0.29)	0.016(0.001)	2.36

Note. — (1) Galaxy (2) Filter: V, U, and NUV; and best fitting test function: NO="Nuker"-only - No central component and NE="Nuker" plus exponential central component. (3) The radial limit of good data per filter. The parameters of the best-fitting model SBP: (4)-(8) Nuker parameters of Eqn 4: the surface brightness of the profile at the break radius, $\mu_b = -2.5 \log(I_b)$; the break radius r_b ; the slope transition strength, α ; the outer slope, β ; and the inner slope, γ . (9) The total apparent magnitude of the central component, m_C . (10) The scale radius of the central exponential component, r_c , where appropriate. (11) χ^2_{ν} of the best fit.

Table 2.6. Integrated Total Absolute Magnitudes

Galaxy NGC (1)	Filter (2)	$M_{R_{good}}$ mag (3)	M_{Body} mag (4)	Central Component mag (5)	P_{CC} % (6)
NGC2778	V	-18.25 ± 0.30	-18.25 ± 0.30	> -11.7	< 0.2
...	U	-16.51 ± 0.30	-16.51 ± 0.30	> -10.6	< 0.4
...	NUV	-15.58 ± 0.30	-15.58 ± 0.30	> -10.1	< 0.7
NGC3377	V	-17.89 ± 0.09	-17.89 ± 0.09	> -6.7	< 0.0
...	U	-16.34 ± 0.09	-16.34 ± 0.09	> -7.4	< 0.0
...	NUV	-15.04 ± 0.09	-15.03 ± 0.10	-9.97 ± 3.31	0.93 ± 2.84
NGC3384	V	-18.55 ± 0.14	-18.54 ± 0.14	-12.61 ± 0.22	0.42 ± 0.07
...	U	-16.88 ± 0.14	-16.88 ± 0.14	-10.47 ± 0.22	0.27 ± 0.04
...	NUV	-15.50 ± 0.14	-15.50 ± 0.14	-9.37 ± 0.24	0.35 ± 0.06
NGC3640	V	-20.23 ± 0.13	-20.23 ± 0.13	-13.47 ± 0.23	0.20 ± 0.03
...	U	-18.60 ± 0.13	-18.60 ± 0.13	-11.55 ± 0.28	0.15 ± 0.03
...	NUV	-17.33 ± 0.13	-17.33 ± 0.13	> -10.5	< 0.2
NGC4239	V	-17.52 ± 0.17	-17.52 ± 0.17	-11.58 ± 0.27	0.42 ± 0.08
...	U	-16.18 ± 0.17	-16.18 ± 0.17	-9.82 ± 0.28	0.29 ± 0.06
...	NUV	-15.38 ± 0.17	-15.37 ± 0.17	-8.80 ± 0.42	0.23 ± 0.08
NGC4474	V	-17.95 ± 0.07	-17.94 ± 0.07	-11.70 ± 0.14	0.32 ± 0.04
...	U	-16.37 ± 0.07	-16.37 ± 0.07	-9.92 ± 0.26	0.26 ± 0.06
...	NUV	-15.21 ± 0.07	-15.21 ± 0.07	-8.50 ± 0.47	0.21 ± 0.09
NGC4478	V	-18.56 ± 0.06	-18.56 ± 0.06	> -10.8	< 0.1
...	U	-16.90 ± 0.06	-16.90 ± 0.06	-9.32 ± 0.47	0.09 ± 0.04
...	NUV	-15.79 ± 0.06	-15.79 ± 0.06	> -8.3	< 0.1
NGC4482	V	-16.68 ± 0.06	-16.66 ± 0.06	-11.94 ± 0.13	1.28 ± 0.14
...	U	-15.44 ± 0.06	-15.42 ± 0.06	-10.73 ± 0.14	1.31 ± 0.16
...	NUV	-14.76 ± 0.06	-14.75 ± 0.06	-9.73 ± 0.31	0.97 ± 0.27
NGC4570	V	-19.48 ± 0.06	-19.47 ± 0.06	-14.81 ± 0.35	1.35 ± 0.43
...	U	-17.78 ± 0.06	-17.78 ± 0.06	> -12.6	< 0.8

Table 2.6—Continued

Galaxy NGC (1)	Filter (2)	$M_{R_{good}}$ mag (3)	M_{Body} mag (4)	Central Component mag (5)	P_{CC} % (6)
...	NUV	-16.84 ± 0.06	-16.84 ± 0.06	> -11.6	< 0.8
NGC4621	V	-19.48 ± 0.06	-19.47 ± 0.06	-13.66 ± 0.17	0.47 ± 0.07
...	U	-17.74 ± 0.06	-17.74 ± 0.06	-11.42 ± 0.18	0.30 ± 0.05
...	NUV	-16.53 ± 0.06	-16.51 ± 0.06	-11.76 ± 0.22	1.24 ± 0.25
NGC5576	V	-19.78 ± 0.14	-19.78 ± 0.14	> -6.7	< 0.0
...	U	-18.22 ± 0.14	-18.22 ± 0.14	> -9.5	< 0.0
...	NUV	-17.09 ± 0.14	-17.09 ± 0.14	> -10.2	< 0.2
NGC7457	V	-17.48 ± 0.21	-17.47 ± 0.21	-12.74 ± 0.26	1.26 ± 0.18
...	U	-15.98 ± 0.21	-15.96 ± 0.21	-11.66 ± 0.27	1.88 ± 0.30
...	NUV	-15.12 ± 0.21	-15.08 ± 0.21	-11.52 ± 0.36	3.64 ± 0.99

Note. — (1) Galaxy; (2) Filters; (3) absolute magnitude of the galaxy contained within R_{Good} ; (4) absolute magnitude of nuker-dominated Body of the galaxy; (5) absolute magnitude of any central component; (6) the percent of light from the central component (CC) relative to the total observed within R_{Good} .

Table 2.7. Central Object Contributions

Galaxy NGC	ALP	(NE) vs. NO V/U/NUV	Central Component Type (r_c)	$< P_{CC} >$ %	Extra Light? [ref]
(1)	(2)	(3)	(4)	(5)	(6)
NGC7457	x	YY Y	Extended (1.1 pc)	1.47	
NGC4482	x	YY Y	Extended (2.5 pc)	1.25	No (Sph,N) [1]
NGC4621		YY Y	Extended (8.4 pc)	0.37	Yes [1,2]
NGC3384	x	YY Y	Extended (2.4 pc)	0.33	
NGC4239	x	YY Y	Extended (2.2 pc)	0.31	
NGC4474	x	YY Y	Extended? (3.0 pc)	0.29	
NGC3640		YY N	Extended (15 pc)	0.17	Yes [3]
NGC3377		NN Y	Unresolved NUV source?	0.93	Yes [2,4]
NGC4570		YY N	None	<0.9	No (S0) [1]
NGC2778		NN N	None	<0.3	Yes [2]
NGC4478	x	YY N	None	<0.09	Yes [1,2]
NGC5576		NN N	None	<0.00	Yes [2]

Note. — (1) Galaxy name. (2) The original sample membership. The result of the χ^2_r criteria (see text) for discriminating (3) central source vs. no source. (4) the overall best-fitting central source type over the three bands. If the source is extended, then the scale height of the exponential fit is given in parenthesis. (5) the error-weighted mean percent of light from the central component relative to the total observed within R_{Good} over all three bands, from Table 2.6. (6) Notes whether the galaxy has been identified as having a merger-induced “extra light” component from one of the following references: [1]=Kormendy et al. (2008), [2]=Hopkins et al. (2008b), [3]=Hopkins et al. (2008c), [4]=Kormendy (1999). The galaxies are listed in order of decreasing $< P_{CC} >$

Chapter 3

Near-Ultraviolet Merger

Signatures in Early-Type Galaxies

II: Color Signatures

Abstract

We present the total galaxy colors and the radial colors of a sample of 12 nearby early type galaxies within their central 1.5 kpc that are derived from high quality, high resolution optical and NUV observations taken with the High Resolution Camera of the Hubble Space Telescope. The $NUV - V$ and $U - V$ colors provide the most sensitive probe to detect multi-generational stellar populations and, with the high resolution of our photometry, changes in population compositions can be followed from $15''$ inward to $0''.03$. All twelve galaxies exhibit either total galaxy colors or colors within individual radial bins which are consistent with multi-generational stellar populations. When restricted to a dual-generation scenario with an older population age of 12 Gyr, the total galaxy colors are consistent with younger generations which have a typical age of 1 Gyr and contribute as much as 20% of the total mass within the field of view.

3.1 Introduction

In this chapter, we examine the high-resolution ultraviolet photometry of early type galaxies we obtained in Ch 2 for evidence of the multiple epochs of star formation than are expected to be a product of hierarchical assembly involving gas-rich major mergers. The motivation for this program, sample selection, observations, basic data reductions, and fits to extracted radial profiles have been described in Paper I.

Briefly, our sample consists of six early-type (E, dE, and S0) galaxies with “Anomalous Light Profiles” (ALPs), defined to be excess central light with respect to a standard “nuker” broken power-law profile (Lauer et al. 1995), and six “control” galaxies without such features. The character of the light profiles was judged on the basis of

high-resolution *Hubble* Space Telescope (HST) imaging at wavelengths longer than 5000 Å. We obtained imaging of the 12 objects with the High Resolution Camera (HRC) of the Advanced Camera for Surveys on the HST in the three bands F250W, F330W, and F555W, which we will refer to as the NUV, U, and V bands, respectively. The F330W filter is the HST equivalent of the standard ground-based broad-band U filter. The angular scale in the HRC is $0''.027 \text{ pix}^{-1}$, and it has a $27'' \times 27''$ field of view.

This is the first high resolution, high signal-to-noise study of the UV/optical spatial profiles and color structure of early-type galaxies (ETGs) and their implications for stellar populations. We chose two bands below 4000 Å for this work because the region 2000-4000 Å is the most sensitive to the age and metallicity of the main sequence turnoff in older populations. The spectral energy distributions (SEDs) of such populations in the optical bands redward of 4500 Å are dominated by light from the red giant branch, which is relatively insensitive to age.

Few studies of ETG structure have been made at wavelengths below 4000Å. Most of these employ the standard ground-based “U” broad-band filter (e.g. de Vaucouleurs 1961, Peletier et al. 1990). There are significant gradients in $U - V$ or $U - R$ colors, in which the galaxies become redder at smaller radii, but there is little reported structure or unusual behavior to the limiting ground-based resolution of a few seconds of arc. The trends seen are consistent with gradients in optical-band absorption line strengths (e.g. Davies et al. 1993, Kuntschner et al. 2006, Sánchez-Blázquez et al. 2007) and appear to be driven mainly by a metallicity increase at smaller radii, which would induce both cooler main sequence turnoff temperatures and larger metallic line blanketing at short wavelengths.

Near-UV observations with the Galaxy Evolution Explorer (GALEX, Martin et

al. 2005) or with ground-based telescopes for higher redshift systems have shown that ETGs have diverse star formation histories, often experiencing star formation within the past Gyr (Yi et al. 2005, Kaviraj et al. 2007, Schawinski et al. 2007, (Kaviraj et al. 2008)), but the $\sim 6''$ resolution of GALEX prevents examination of spatial structure in galaxy centers on the scales of interest here. In the far-UV band (1200-1800 Å), cool main sequence stars are unimportant, and a different stellar component, the “UV-upturn” or “UVX” population, produces the light. This is believed to be extreme horizontal branch (small-envelope, helium-burning) stars in the dominant old, metal-rich population (e.g. Burstein et al. 1988, Greggio & Renzini 1990, O’Connell 1998, Yi et al. 1999, Brown et al. 2000, Rich et al. 2006, Donas et al. 2007). Strong gradients have been found in the optical/far-UV colors of ETGs (e.g. Ohl et al. 1998, Gil de Paz et al. 2007) at 3-6'' resolution. The colors generally become bluer at smaller radii, indicating a larger fractional population of hot stars. A variety of factors apart from a simple metallicity increase may be responsible for these gradients, including differences in age, giant branch mass-loss, or helium abundance. It is not yet possible to distinguish these.

The general trend toward higher metallicities in ETG galaxy centers was initially interpreted as evidence for “monolithic collapse” formation of ETG galaxies. In this scenario, massive galaxies form their stars at high redshift ($z \gtrsim 5-10$) in roughly synchronized, intense, short-lived bursts and evolve passively at later times, without the continuing star formation events expected from gas-rich mergers in the hierarchical assembly picture. Monolithic collapse models (e.g. Larson 1976, Carlberg 1984) predict that populations in galaxy centers will have formed from more highly enriched gas than will stars in their exteriors but that their ages should be nearly uniformly old (at the current epoch in nearby systems). However, high precision optical-band

spectrophotometry of ETG centers (discussed in Paper I), as well as the UV photometry cited above, demonstrates that many ETGs have experienced extended periods of star formation, lasting perhaps until ~ 0.5 Gyr ago. Our multiband photometry of galaxy cores was designed to search for spatial structures that might be associated with late episodes of ETG star formation.

This paper is organized as follows. We describe the extracted color profiles for our sample in Sec 3.2; adopted stellar population models in Sec 3.3; integrated colors and their interpretation in Sec. 3.4; isophotal color trends in the two-color diagram in Sec. 3.5; and summarize our findings in Sec. 3.6.

3.2 Extracted Color Profiles

Beginning with the pipeline-processed data frames, we masked out artifacts including dust lanes, converted to monochromatic flux densities f_λ (in units of $\text{ergs sec}^{-1} \text{cm}^{-2} \text{\AA}^{-1}$) in each pixel, and corrected for sky background. Details are given in Paper I.

Before further processing, we smoothed all data frames to the same effective point spread function (PSF) by convolving images in a given band with the PSF images of the other two bands, as derived from `Tiny Tim` software (Krist & Hook 1997). The FWHM of the compound PSF is $0''.086$. Note that this smoothing was not applied to the data frames used to derive the surface brightness profiles analyzed in Paper I. We then extracted color profiles for each galaxy with the IRAF `ELLIPSE` software. Elliptical isophote parameters were derived from the V-band image for each galaxy, and these were then used to define elliptical annuli from which mean “isophotal” surface brightnesses could be extracted for all three bands. The resulting mean fluxes as a function of radius were converted to monochromatic STMAG magnitudes, $m_\lambda = -2.5 \log(f_\lambda) - 21.1$, and subtracted from one another to form the $NUV - V$ and

$U - V$ isophotal color profiles.

We obtained “total” colors for our galaxies by integrating the isophotal photometry from the center to an outer radius given by the minimum of the three R_{Good} radii for the three bands. Fluxes inside R_{Good} in each band are believed to be unaffected by uncertainties in the background subtraction (see Paper I). In most cases, the integrated colors refer to regions smaller than the effective radius of each galaxy.

Finally, we determined colors for the central objects found to be necessary to fit the surface brightness profiles in Paper I. Two-thirds of these were found to be extended and were fit with an exponential profile. To obtain the central object colors, we simply integrated the fitted fluxes to R_{Good} in each band and combined them to produce colors. Background light from the surrounding galaxy is automatically removed by this procedure. The uncertainties in these colors are considerably larger than those for the isophotal colors because relatively few pixels normally contribute to the fit; these colors may also be affected by mismatches in the PSF between bands. The images and profiles from which the total integrated galaxy colors and the isophotal galaxy colors are computed have been corrected for foreground galactic extinction. Foreground galactic absorption values range up to $A_{V,max} = 0.17$, $A_{U,max} = 0.27$, and $A_{NUV,max} = 0.34$ mag.

The integrated colors for our sample are summarized in Table 3.1. The column labeled “Body” lists the total colors for the object after correction for light from the central source. The central sources contribute only a small fraction of the total light, so the corrections are very small. Only in the case of NGC 7457 is the change in either color as large as 0.03 mag.

In Figure 3.1, we present the derived isophotal mean color profiles (not corrected for light from the central component), with the ALPs grouped on the left hand side

Table 3.1. Integrated colors.

Galaxy NGC (1)	R_{max} ($''$) (2)	Color (3)	Total (mag) (4)	Body (mag) (5)	Central Source (mag) (6)
NGC2778	9.2	NUV-V	2.67 ± 0.02	2.67 ± 0.02	...
...	9.2	U-V	1.74 ± 0.01	1.74 ± 0.01	...
NGC3377	6.9	NUV-V	2.85 ± 0.00	2.86 ± 0.03	< -3.3
...	6.9	U-V	1.55 ± 0.01	1.55 ± 0.01	...
NGC3384	6.9	NUV-V	3.05 ± 0.00	3.05 ± 0.00	3.25 ± 0.26
...	6.9	U-V	1.67 ± 0.01	1.67 ± 0.01	2.14 ± 0.24
NGC3640	11.1	NUV-V	2.90 ± 0.01	2.90 ± 0.01	> 2.9
...	11.1	U-V	1.63 ± 0.01	1.63 ± 0.01	1.92 ± 0.31
NGC4239	10.1	NUV-V	2.14 ± 0.02	2.14 ± 0.02	2.78 ± 0.43
...	10.1	U-V	1.34 ± 0.01	1.34 ± 0.01	1.76 ± 0.31
NGC4474	9.2	NUV-V	2.74 ± 0.01	2.73 ± 0.01	3.20 ± 0.48
...	9.2	U-V	1.58 ± 0.00	1.58 ± 0.00	1.79 ± 0.28
NGC4478	8.3	NUV-V	2.77 ± 0.01	2.77 ± 0.01	...
...	8.3	U-V	1.66 ± 0.00	1.66 ± 0.00	< 1.4
NGC4482	9.2	NUV-V	1.92 ± 0.02	1.91 ± 0.02	2.21 ± 0.33
...	9.2	U-V	1.24 ± 0.01	1.24 ± 0.01	1.21 ± 0.17
NGC4570	17.9	NUV-V	2.64 ± 0.01	2.62 ± 0.01	> 3.2
...	17.9	U-V	1.70 ± 0.00	1.68 ± 0.01	> 2.2
NGC4621	14.8	NUV-V	2.95 ± 0.01	2.96 ± 0.01	1.90 ± 0.27
...	14.8	U-V	1.74 ± 0.01	1.74 ± 0.01	2.24 ± 0.24
NGC5576	8.3	NUV-V	2.69 ± 0.00	2.69 ± 0.00	...
...	8.3	U-V	1.56 ± 0.00	1.56 ± 0.00	...
NGC7457	13.4	NUV-V	2.36 ± 0.01	2.39 ± 0.02	1.21 ± 0.33
...	13.4	U-V	1.50 ± 0.01	1.51 ± 0.01	1.07 ± 0.23

Note. — (1) Galaxy name; further information on each galaxy is presented in Paper I. (2) Outer radius for integration. (3) Color identifier. (4) Integrated colors (corrected for extinction). (5) Integrated colors corrected for light from the central source. (6) Estimated integrated colors of central source.

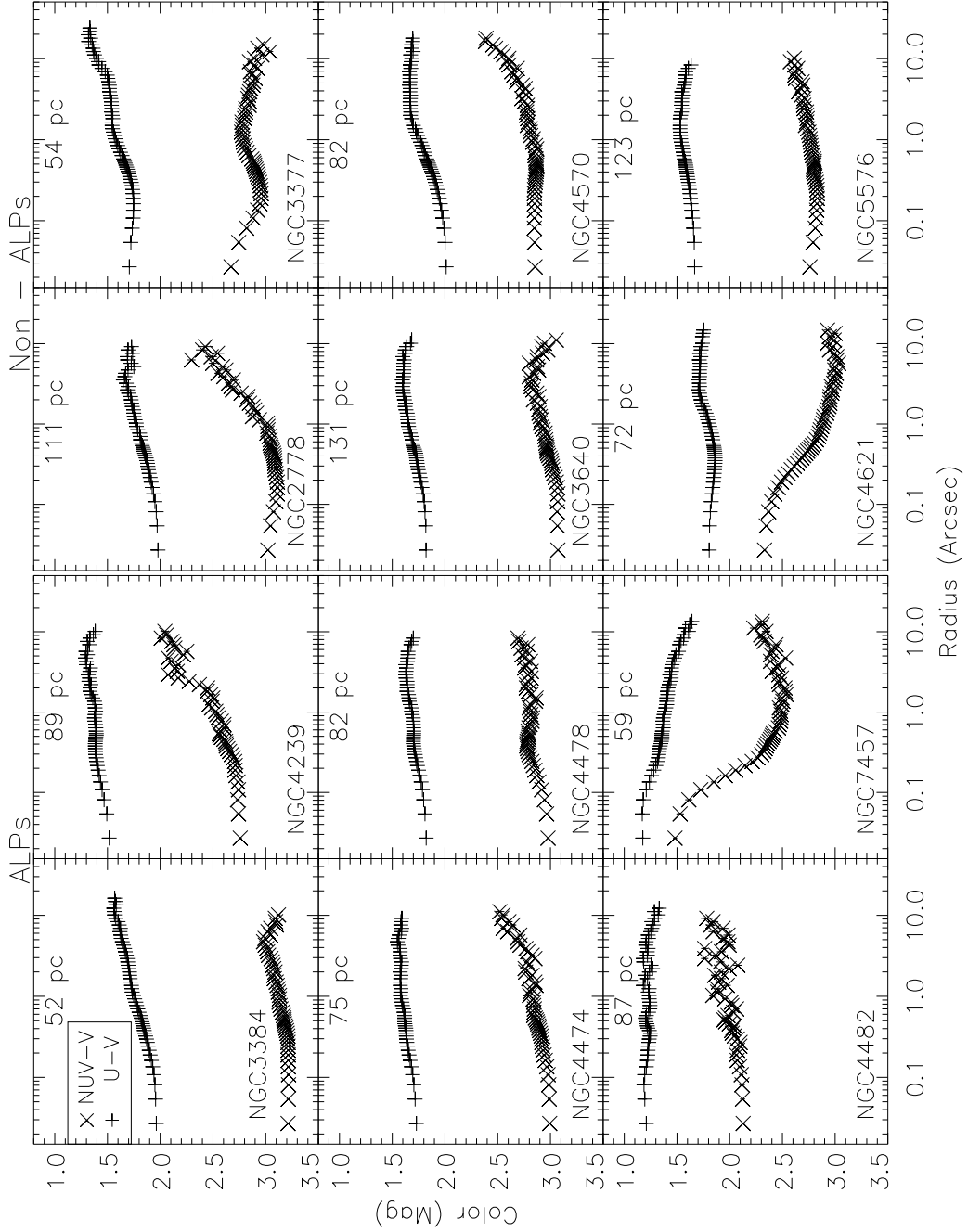


Fig. 3.1.— Isophotal mean $NUV - V$ and $U - V$ colors as a function of radius for our galaxies, with the ALP sample on the left and the “control” sample on the right. The $1''$ tickmark is labeled with the physical scale for each galaxy. Bluer colors are higher in the diagrams.

and the non-ALPS, on the right. There is no characteristic of the profiles in either group that distinguishes it from the other. The ALPs, defined to have central structures in excess of a standard “nuker” V-band profile, do not, for instance, all have blue central regions that are absent in non-ALPS. Light profile anomalies evidently do not imply color anomalies.

The $U - V$ profiles are roughly similar to one another, with a general trend to redder colors at smaller radii, consistent with the results obtained for ground-based $U - V$ photometry at larger radii cited in the Introduction. The main exceptions in $U - V$ are NGC 4482 and 7457, both of which have a reversed gradient at $r \gtrsim 5''$. In some cases (e.g. NGC 3377 and NGC 4570) there are inflections in the outer profiles suggesting discrete structures, but these have only modest amplitudes.

The $NUV - V$ profiles mostly have much larger amplitudes (in magnitude units and therefore as fractional changes in flux ratio) and more structure than the $U - V$ profiles. Interestingly, even outside the central regions there are few cases where the $NUV - V$ profile parallels that in $U - V$, and in several instances the outer gradients have opposite slopes. The $NUV - V$ gradients of NGC 2778, 4239, 4474, 4570, and perhaps 7457 are steeper at large radii than is true of any of the $U - V$ profiles. This means that the NUV band is, as expected, providing information on populations that is independent of the U or longer-wave bands.

The most conspicuous features in the profiles are found in the $NUV - V$ colors of NGC 3377 and 4621 (both non-ALPs) and NGC 7457 (an ALP). These exhibit strong blue excursions in their cores, amounting to -1 mag in the case of NGC 7457. Only small matching disturbances are present in $U - V$. The sensitivity of the NUV region to sources with color temperatures above that of the main sequence turnoff stars arises because of the rapid decline of the integrated SED below 3200 \AA . The

fall-off is enhanced in higher metallicity populations by heavy metallic line blanketing in the NUV region.

Many of the features evident in the isophotal color profiles are visible in the 2-dimensional color maps shown in Fig. 2.2 of Paper I. In comparing the two displays, keep in mind the difference in spatial scales (linear in the maps but logarithmic in the profiles) and that the zeropoint for the maps changes from frame to frame. The profiles, which are based on averages of many pixels, continue to radii beyond $10''$, but the maps are truncated at smaller radii where the signal to noise per pixel becomes small.

3.3 Stellar Population Models:

SSPs and Composites

To help interpret our photometry, we compare our galaxy colors to synthetic colors for the Pégase library of model stellar populations (Fioc & Rocca-Volmerange 1997). Before adopting this model set, we intercompared predictions of UV colors for five well-known population libraries: Pégase (Fioc & Rocca-Volmerange 1997); Bruzual & Charlot (2003), hereafter BC03; Starburst 99 (SB99; Leitherer et al. 1999 and Vázquez & Leitherer 2005), Maraston (2005), and Yonsei-Yale (Y-Y; Yi et al. 2001). Each of these includes a set of instantaneous burst “simple stellar populations” (SSPs) characterized by a single age, τ , and uniform helium and metal abundances. Metal abundances are specified by the metal mass fraction, Z . Predicted SEDs are given in the form of monochromatic luminosities per unit mass, $[S_\lambda] = (\text{erg/s}/\text{\AA}/M_\odot)$. Where possible, we compared SEDs computed for a Salpeter initial mass function (Salpeter 1955) over the mass range of $0.1 - 120 M_\odot$. We consider three different metallicities:

solar, sub-solar ($Z = 0.4 Z_{\odot}$ for Pégase, BC03, and SB99; $Z = 0.5 Z_{\odot}$ for Y-Y and Maraston), and super-solar ($Z = 2.5 Z_{\odot}$ for Pégase, BC03, and SB99; $Z = 2.0 Z_{\odot}$ for Y-Y and Maraston).

To derive $NUV - V$ and $U - V$ colors on our system, we integrated the model SEDs over the three HST/HRC filter bands. We took filter throughput functions from Pavlovsky et al. (2006). The resulting colors for the five SSP libraries in the three metallicity ranges are shown in Figure 3.2. All of our color plots use the STMAG system. For reference, the STMAG colors of Vega (α Lyrae, the standard reference for the broad-band magnitude system) are $U - V = -0.17$ and $NUV - V = -0.31$.

The libraries are mostly in good agreement. They demonstrate the expected improved sensitivity of the NUV to the properties of old stellar populations. For a given age ratio, they predict a significantly larger color range for $NUV - V$ than $U - V$ at solar abundance; the total range from 1 Myr to 20 Gyr is 6 mags in $NUV - V$ compared to 3.5 mags in $U - V$. At an age of 8 Gyr, the models predict a 1.5 mag color difference between a population with a metallicity of $0.4Z_{\odot}$ and one with $2.5Z_{\odot}$, a factor of two larger than in $U - V$.

Some differences between model sets are visible in the plots. Difficulties in modeling the evolution of short-lived, hot Wolf-Rayet phase in massive stars are responsible for the scatter in the colors near 5 Myr age; the effect of Wolf-Rayet evolution is largest in the sub-solar models. Similar difficulties related to modeling red supergiants affect colors between 5 and 30 Myr (cf. Vazquez & Leitherer 2005). The Maraston (2005) models are significantly bluer than the others at 10-500 Myr. These differences are apparently related to different adopted stellar evolution model sets and treatment of asymptotic giant branch stars (see Maraston 2005 and Vazquez & Leitherer 2005).

In all models sets, the slope of the color-age relation changes at about 1 Gyr, such

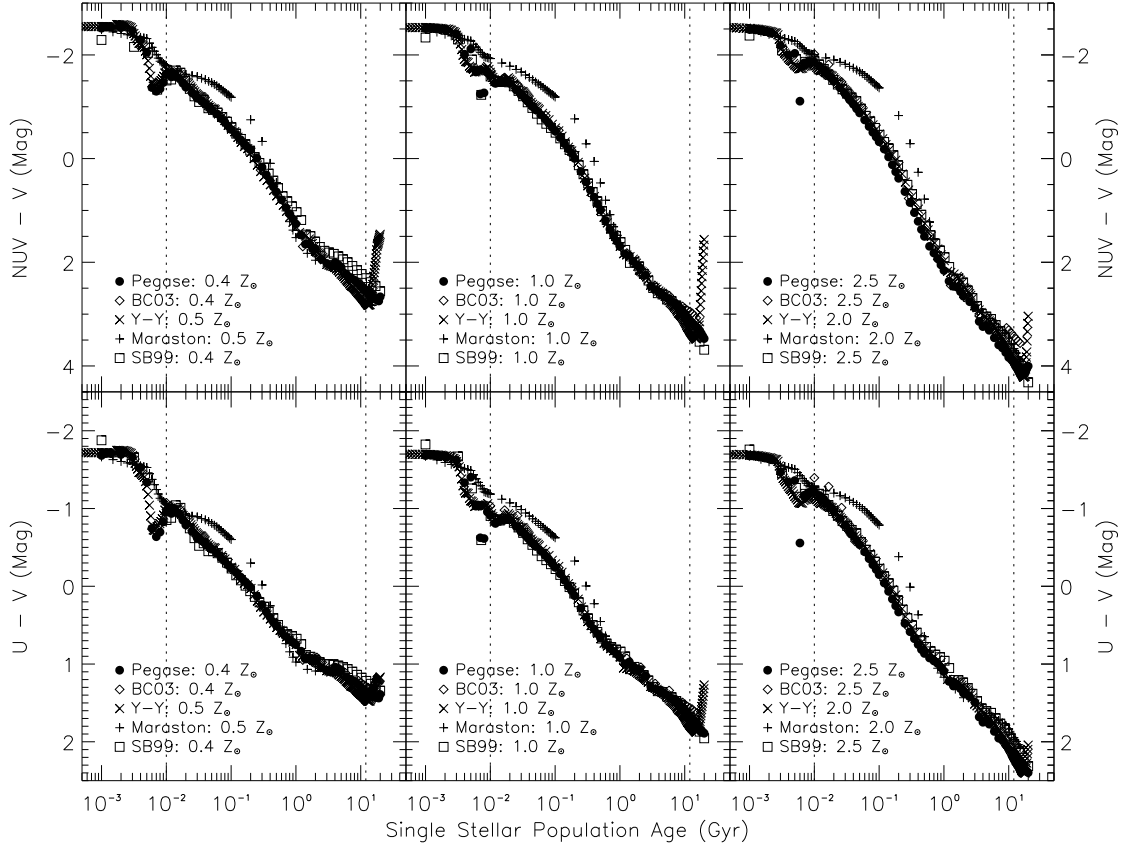


Fig. 3.2.— A comparison of five stellar population model libraries in $NUV - V$ and $U - V$ colors (given in monochromatic STMAG magnitudes). Colors are plotted as a function of burst age for three different metallicities (from left to right: sub-solar, solar, and super-solar). Bluer colors lie higher in the plots. The color range plotted for $NUV - V$ is 2 magnitudes larger than for $U - V$. References: Pégase (Fioc & Rocca-Volmerange 1997); BC03 (Bruzual & Charlot 2003); Y-Y (Yi et al. 2001); Maraston (Maraston 2005); and SB99 (Leitherer et al. 1999; Vázquez & Leitherer 2005).

that older models are bluer than the extrapolation from younger models. At least part of this effect is caused by the appearance of hot, low-mass, post-asymptotic giant branch (PAGB) stars in the populations. Apart from the Y-Y library, none of the model sets attempts to include the hot extreme horizontal branch (EHB) population expected to be present whenever giant branch mass-loss is large enough to produce HB stars with small envelopes. These can be much more important to the UV spectrum of an old population than are PAGB stars (e.g. Greggio & Renzini 1990, Brown et al. 2000). In sufficient numbers they will affect not just the far-UV region but the near-UV spectrum as well (e.g. Burstein et al. 1988, Ponder et al. 1998, Dorman et al. 2003, Yi 2003), and they are responsible for the “blue spike” in the $U - V$ and $NUV - V$ colors of the oldest models in the Y-Y library.

For our purposes, we will consider models only between the ages of 10 Myr and 12 Gyr. The minimum age of 10 Myr is chosen because there is no evidence in our sample for the gaseous line emission or substantial quantities of dust associated with younger populations. In fact, it is doubtful that there are any components younger than about 100 Myr in our galaxies because we do not see the conspicuous clumps of blue sources in our images that would be expected.

The upper age bound is set by the maximum likely age of a massive population in the consensus Λ -CDM cosmology (about 1.7 Gyr after recombination). Throughout this range, the Pégase models are good representatives of the mean of all five model sets, and we will adopt them in the subsequent analysis. None of our conclusions are strongly affected by the choice of either the model library or the age limits.

Despite the relatively good agreement between the model sets, there may be significant systematic errors in the predicted UV colors because it is well known that existing theoretical spectral synthesis codes, employed for most of the libraries, do

not accurately reproduce the strengths of ultraviolet absorption features in cooler stellar atmospheres (e.g. Heap et al. 1998, Peterson et al. 2001, Dorman et al. 2003, Maraston et al. 2008). The magnitude of these uncertainties cannot be estimated well at present, but their presence must be taken into account in comparing the models to photometry. We adopt a nominal uncertainty of 0.05 mag in each color to reflect these shortcomings of the models.

In the rest of the paper, we will compare extracted colors for our galaxies to the Pégase SSP colors and also to the composite colors of dual-component models derived from those. For simplicity, we consider only two kinds of dual-component populations: first, dual metallicity populations in which both components have the same age but different metallicities; and, second, dual generation populations in which both components have the same metallicity but different ages. Models with extended star formation histories (e.g. exponentially-declining) are less appropriate for nearby ETGs than are discrete component models. Dual metallicity models represent the kind of mixed abundance but uniformly old populations expected to be present in monolithic collapse models for ETG formation, while dual generation models reflect the multi-age structure expected for hierarchical assembly.

In each case, the SEDs of the dual-component populations are given by

$$G_{\lambda}(\lambda) = F_1 \times S_{\lambda}(Z_1, \tau_1, \lambda) + (1 - F_1) \times S_{\lambda}(Z_2, \tau_2, \lambda) \quad (3.1)$$

where G is the monochromatic luminosity per unit mass of the composite at wavelength λ , S is the monochromatic luminosity per unit mass of each component at λ , τ is the age of each component, Z is the metallicity of each component, and F_1 is the mass fraction of the first component. For the dual metallicity models, $\tau_1 = \tau_2$ while the Z s differ. For the dual generation models, $Z_1 = Z_2$ while the τ s differ. In the

latter models, we let F_1 be the mass fraction of the younger component and refer to this as F_Y in the subsequent discussion; we refer to the ages of the younger and older components as τ_Y and τ_O , respectively.

For application to our broad-band colors, in the above expression we substitute the mean monochromatic luminosity per unit mass in a given filter band for the S s. The color of the composite is then given by

$$C(i, j) = -2.5 \log[G_\lambda(\lambda_i)/G_\lambda(\lambda_j)]. \quad (3.2)$$

Figure 3.3 is a two-color diagram illustrating the Pégase SSPs and also the dual-metallicity and dual-generation models derived from them. Bluer colors lie to the upper right of the diagram; older populations for a given Z and higher metallicity populations for a given age lie to the lower left in the diagram. The locations of four of the Z_\odot SSPs are displayed with open squares and labeled with their ages. The 12 Gyr-old SSPs for sub-solar ($0.4Z_\odot$) and super-solar ($2.5Z_\odot$) metallicities are shown by small open circles and labeled MP and MR , respectively. The full set of Pégase SSPs falls along the locus connecting the labeled points.

There is considerable overlap between the loci for different Z s. This means that the age-metallicity degeneracy that is such a serious problem for interpretation of optical-band photometry (e.g. O’Connell 1986, Worthey 1994) is also a difficulty for the UV bands we use here. The region containing dual-metallicity composite models, each of which consists of two SSPs of the same age but different metallicities, is indicated by light grey shading in the figure. This nearly superposes with the SSP locus, and its width is generally $\lesssim 0.05$ mag despite covering a range of over 5 mags in $NUV - V$.

We reproduce the grey shaded region in later plots as a fiducial to indicate where

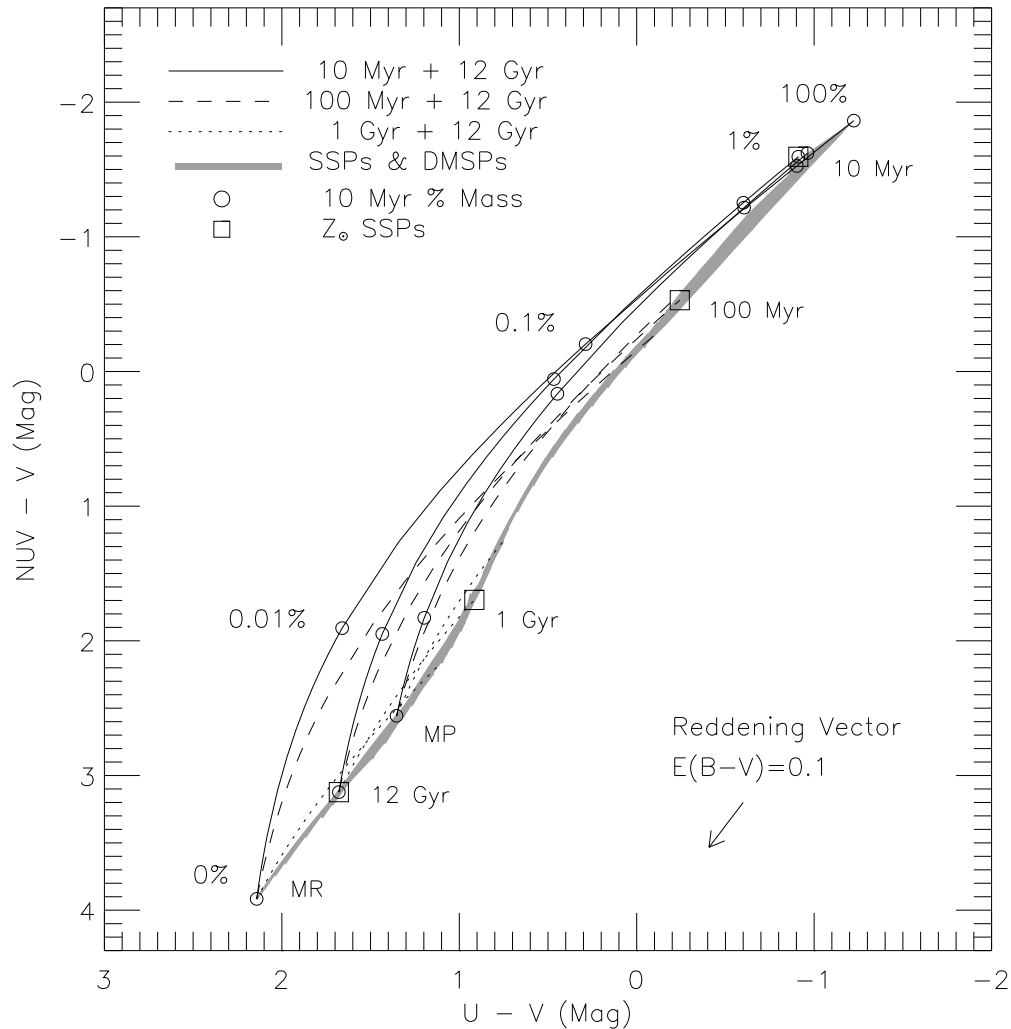


Fig. 3.3.— Reference stellar population models in the $U - V/NUV - V$ color-color plane we use to analyze our galaxy photometry. Bluer colors lie to the upper right. Plotted are SSP models for three metallicities from the Pégase library and two kinds of dual-component composite populations derived from those. See text for explanation. The grey zone, representing the locus of the SSPs and the dual-metallicity composites, is reproduced in later plots.

single-age populations fall in the two-color diagram. It marks an important boundary because the region below or to the right of this locus is a “forbidden” zone: no combination of SSP populations can fall in this area.

Figure 3.3 also shows the loci of 9 dual-generation models. Each of these consists of a $\tau_O = 12$ Gyr older generation (with super-solar, solar, and sub-solar Z , respectively). There are three possible younger generations ($\tau_Y = 10$ Myr, 100 Myr, and 1 Gyr, respectively). For each locus, we computed the composite color for 56 values of F_Y . Solid lines in Fig. 3.3 show the loci of models with different mixtures of 12 Gyr and 10 Myr components, dashed lines the 12 Gyr/100 Myr loci, and dotted lines the 12 Gyr/1 Gyr loci. Labeled open circles along the loci for the 10 Myr combinations mark places where the younger component contributes 0.01%, 0.1%, 1%, and 100% of the mass.

All the dual-age models fall to the upper left of the single-age region in the diagram and envelope a much larger volume of color space than do the single-age populations. Color separation of mixed populations containing 10 or 100 Myr younger components from the single-age locus is excellent, up to 1.4 mags in $NUV - V$ and 0.6 mags in $U - V$. Separation of mixed 1 and 12 Gyr populations is good (up to ~ 0.2 mags in $NUV - V$) even though this is not clear given the compressed scale of Fig. 3.3. (This region is magnified in later plots.)

The boundaries formed by the locus of the 12 Gyr/10 Myr mixture at each metallicity are also important fiducials. Given the assumption that populations cannot be older than 12 Gyr, any observed point lying to the left of such a boundary implies a metallicity Z higher than that of the boundary. The color-color space covered by sub-solar composites is a subset of that of the solar composites, which, in turn, is a subset of the super-solar composites.

The 10 Myr loci are important for two other reasons. First, just as the 12 Gyr/10 Myr mixture line yields a minimum value for the metallicity associated with a given observed color point, the $\tau_O/10$ Myr locus that passes through that point for a given Z yields the youngest age for the older generation. Second, because the 10 Myr models are good proxies for any hot source (say with $T_e > 15000$ K), the $\tau_O/10$ Myr loci represent the color trajectories of older populations containing a hot EHB “UVX” component (see the Introduction). The Pégase models do not include UVX components, but many real galaxies will have some level of UVX contamination in their NUV (and possibly U) bands.

3.4 Results for Integrated Colors

The integrated colors of each galaxy from Table 3.1, after correction for the central source contributions, are plotted in a color-color diagram in Figure 3.4, which enlarges the red end of the model envelope shown in Fig. 3.3. We have reproduced in Fig. 3.4 the single-age model region (in grey) and the loci for the same set of dual-generation models plotted in Fig. 3.3.

The total integrated colors span a magnitude range of 1.1 mag in $NUV - V$ and 0.5 mag in $U - V$. By comparison, typical samples of ETGs have a range of only 0.4 mag in $B - R$ and 0.2 mag in $B - V$ (Peletier et al. 1990a,b). The larger color-space coverage, particularly when combined with the improved photometric errors (our ultraviolet color errors range up to 0.02 mag whereas the optical colors are typically 0.05–0.1 mag) demonstrates the significant improvement in sensitivity to robustly detecting multi-generational stellar populations.

The first important point is that none of the data points lie in the “forbidden” zone to the right of the grey locus, meaning that the photometry and the theoretical

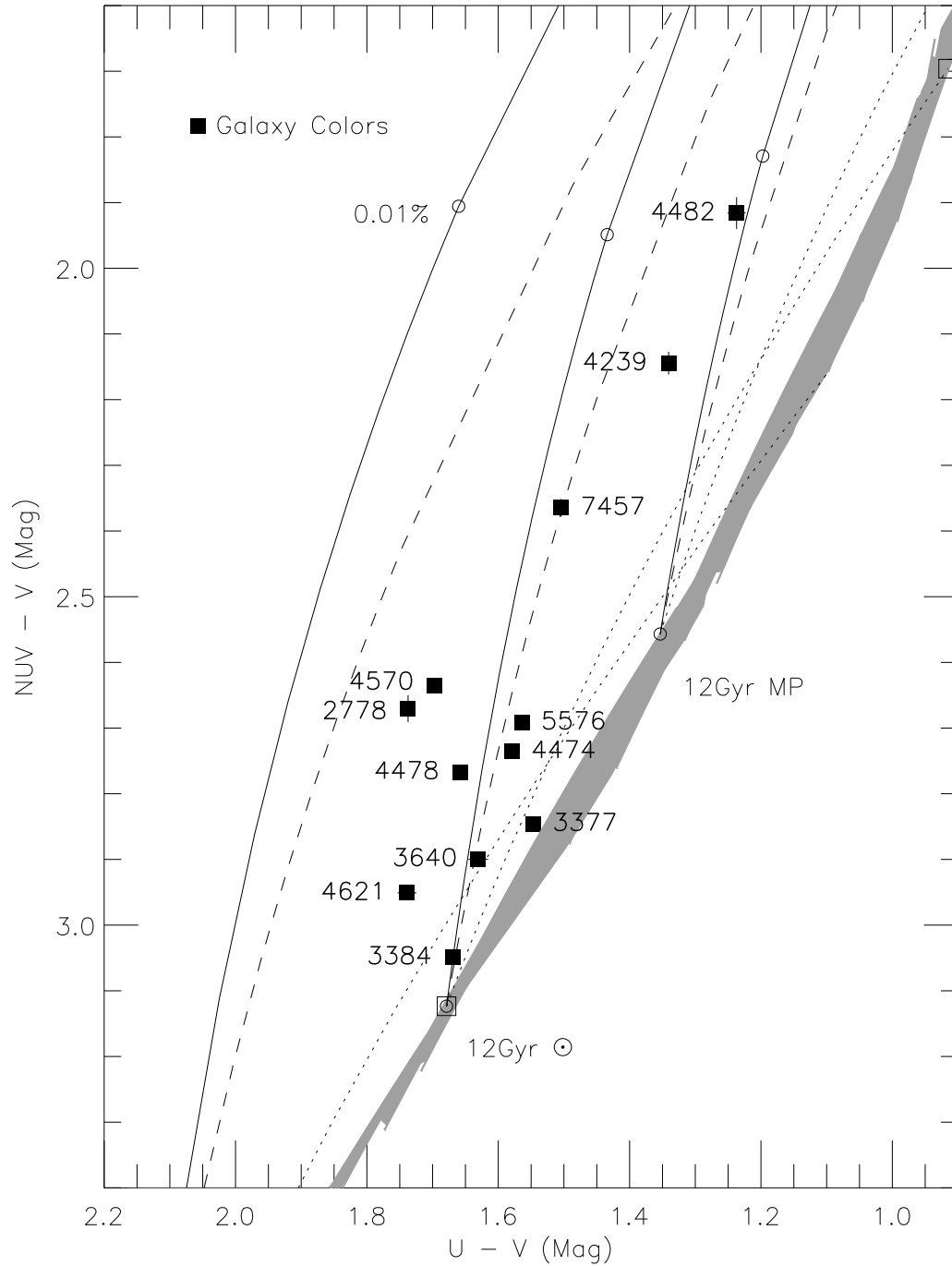


Fig. 3.4.— The integrated galaxy colors (filled squares) plotted in the color-color diagram with the SSP and composite model loci from Fig. 3.3 superposed. Coding of model loci is as in Fig. 3.3. Error bars are plotted for all galaxy photometry, but but most are smaller than the plotting symbols. The open square at the upper right of the diagram is the SSP for 1 Gyr at solar abundance.

models meet at least this minimum standard for consistency.

The second important point is that 10 of the 12 data points lie well off the grey locus. Departures are considerably larger than the observational errors or uncertainties in the models. This means that they are inconsistent with either SSP or dual-metallicity models and that they cannot contain homogeneous stellar populations—i.e. where all the stars formed within $\sim 1 - 2$ Gyr of one another.

The three bluest objects (NGC 4239, 4482, and 7457) are ALPs, but there is otherwise no distinction between ALPs and non-ALPs in the diagram (and there should not be any central ALP contamination in the colors plotted).

The plotted photometry represents most of the area of the HST/HRC field of view. In the terminology of Hopkins et al. (2008a) or Kormendy et al. (2008), the volumes observed correspond to much of the “extra light” components that are thought to be associated with gas-rich merger events. The UV photometry here shows that over 80% of the extra-light components in this sample exhibit evidence for multi-generation star formation, consistent with the hierarchical assembly picture including gas-rich mergers at late times. The signature of these effects would be more difficult to detect at longer wavelengths.

NGC 3377 and 3384 lie off the single-age locus but are close enough that when we assign a systematic uncertainty of about 0.05 mags to the Pégase model colors, they would be almost consistent with single-age models. Referring to the Pégase SSP models, NGC 3377 and 3384 are nearest single-age populations of 8 and 11 Gyr for Z_{\odot} , respectively, or 3.0 and 3.5 Gyr for $2.5Z_{\odot}$.

Based on their positions with respect to the 12 Gyr/10 Myr envelopes, all of the galaxies are more metal rich than $0.4Z_{\odot}$, and at least four are above solar metallicity.

3.4.1 $U - V$ Equivalent SSP Ages

Spectrophotometric analysis of absorption line spectra based on the Lick system (e.g. Worthey 1994) has been applied to many ETGs to deduce population age and abundance. This method determines the properties of the SSP that best fits high-precision line strengths, with emphasis on spectral indices in the 5000 Å region but more recently extending to 4000 Å (e.g. Schiavon 2007, Sánchez-Blázquez 2007). Because our $U - V$ color spans the wavelength region used in the line index studies, it is of interest to derive the equivalent SSP age, $\tau(U - V)$, from our photometry and compare it to literature values. From a single color, we cannot independently determine τ and Z , so we quote ages estimated for each viable Z .

In Figure 3.5 we compare the predicted $U - V$ colors of the Pégase library to the integrated $U - V$ colors for our galaxy sample. Because the grid is coarse, we interpolated the values at each metallicity and then determined the SSP-equivalent ages for each galaxy for that metallicity. Considering the observational errors and modeling limitations, we estimate that the derived ages have uncertainties of about 20%. The resulting ages are given in Table 3.2 and compared to literature values for the centers of the same galaxies. The fact that derived ages increase rapidly as assumed metallicities decrease for a given $U - V$ is clear in the table (and also the left hand panel of Fig. 3.5).

The $\tau(U - V)$ values generally agree with the spectroscopic results where the spectroscopically-determined metallicities are well matched with the Pégase library. Based on the spectroscopic studies, we should expect the typical metallicity in the regions we have studied to be $\sim 2 Z_{\odot}$. Only in the case of NGC 4621 is there a major discrepancy; the values deduced from the $H\beta$ and $H\gamma$ features by Yamada et al. (2006) would yield a $U - V$ in the Pégase calibration of 2.0, over 0.25 mag redder

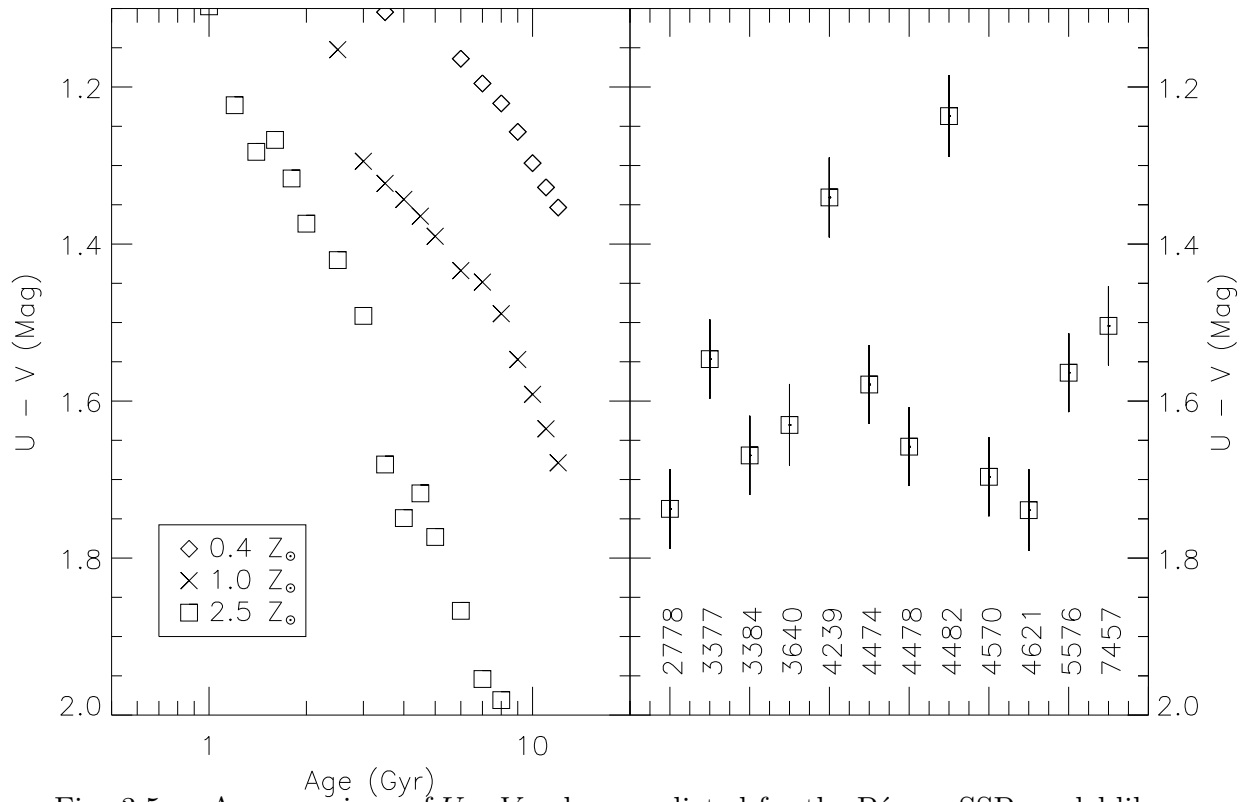


Fig. 3.5.— A comparison of $U - V$ colors predicted for the Pégase SSP model library as a function of age (left panel) to the total integrated colors for our galaxies (right panel). The models are separated by metallicity.

than we observe.

3.4.2 Composite Populations

Most optical-band absorption line studies of the kind cited in the last section arrive at SSP-equivalent characterizations. They do not consider multi-generation fits or attempt to analyze the distribution of ages or metallicities within populations; nor are the spectral indices used (especially if limited to small ranges of wavelengths longward of 4500 Å) particularly sensitive to multiple generations. Ultraviolet photometry, however, provides an additional lever that, as we saw in Fig. 3.4, offers a *prima facie* case for multiple generations.

In this section, we interpret the two-color integrated photometry of our galaxy sample in the context of the Pégase model set. We explore the mixtures of dual-generation populations that could explain the UV colors of each galaxy. Because we have only two observables and there are 4 unknowns (τ_O , τ_Y , Z , and F_Y), we cannot expect to obtain unique answers. A number of different dual-generation mixtures will be able to fit a typical point within the envelope shown in Fig. 3.4. (This is illustrated by the cross-overs between different model loci in the figure.) However, the range of possible mixtures is narrowed by the fact that a minimum metallicity can be set for each data point in Fig. 3.4.

To proceed, we generated a fine grid of models based on all possible (τ_O , τ_Y) pairs in each of the three selected metallicity ranges from the Pégase set. We then determined a χ^2 distance between each galaxy data point and the surrounding models. In principle, there are many models that will yield zero color residuals in each case; we could have interpolated in the coarsely-gridded Pégase model set to identify all of these. Instead, we explored the suboptimal models from the grid in the vicinity

Table 3.2. SSP-Equivalent Ages for Integrated Colors

Galaxy NGC (1)	This Work		Literature		Refs (6)
	[Z/H] (2)	$\tau(U-V)$ Gyr (3)	[Z/H] (4)	Age Gyr (5)	
2778	0.4	3.9	0.30 ± 0.09	5.4 ± 1.8	a
3377	0.0	9.0	
...	0.4	3.1	0.20 ± 0.06	3.7 ± 0.8	a
3384	0.0	11.8	
...	0.4	3.5	0.59 ± 0.01	3.1 ± 0.03	c
3640	0.0	10.9	
...	0.4	3.4	
4239	-0.4	11.5	
...	0.0	3.9	-0.16 ± 0.12	5.1 ± 2.3	b
...	0.4	1.9	
4474	0.0	9.7	
...	0.4	3.2	
4478	0.0	11.5	0.13 ± 0.12	8.1 ± 2.6	b
...	0.4	3.4	0.30 ± 0.10	4.6 ± 2.3	a
4482	-0.4	8.4	
...	0.0	2.8	
...	0.4	1.2	
4570	0.0	12.0	
...	0.4	3.6	
4621	0.4	3.9	0.29 ± 0.11	12.0 ± 2.6	b
5576	0.0	9.4	
...	0.4	3.2	
7457	0.0	8.3	
...	0.4	3.0	

Note. — Equivalent SSP ages derived from integrated $U - V$ colors and the Pégase models. (1) Galaxy name. (2) Log of the assumed metal abundance with respect to solar. (3) The $U - V$ equivalent SSP ages. (4) Log of the spectroscopically derived metal abundance with respect to solar. (5) Spectroscopically derived age. (6) Source of spectroscopic quantities: *a*: Trager et al. (2000); *b*: Yamada et al. (2006) using the mean of their $H\gamma$ - and $H\beta$ determinations; *c*: Sánchez-Blázquez et al. 2007

of each data point. We assigned a systematic uncertainty of 0.05 mag to the model colors in order to compute χ^2 values. We then explored the χ^2 contours in the (τ_O, τ_Y, F_Y) parameter space for each metallicity. Examples of the $\sigma = \sqrt{\chi^2}$ contours are shown for two galaxies in Fig. 3.6.

It is easier to picture the character of the dual-generation fits in a diagram like Fig. 3.4 but which plots the data and models in flux ratio coordinates, e.g. $G_\lambda(NUV)/G_\lambda(V)$, instead of colors. In those units, all dual-generation models based on a given pair of young and old components lie on a straight line. The pairs of components capable of exactly fitting a given data point lie wherever straight lines through that point cross the SSP locus. If we allow our choice of one member of the pair to move along the SSP locus, the fitting line will rotate about the data point. The range of perfect fits is limited by the positions of minimum and maximum ages on the locus for a given metallicity. For the distribution of data points in Fig. 3.4, one can always find a perfect fit for some model with $\tau_Y = 10$ Myr and for another model with $\tau_O = 12$ Gyr. The more interesting limits, then, are the oldest τ_Y and the youngest τ_O capable of fitting each data point and the mass fraction of the younger component (F_Y) in each case.

We locate those age limits along the 1σ contours. Referring to the contour plots shown in τ_O - τ_Y space in the upper left panel of Fig. 3.6, we see that there is an “L” shaped region within 1σ of the perfectly fitting models. At the left hand side of the plot for NGC 2778, we see that a 5 Gyr/10 Myr combination yields a 1σ color fit; at the top of that plot, we see that a 12 Gyr/450 Myr combination provides a comparable fit. The fractional mass contributions of the younger component associated with these solutions can be read from the contour plot of $\log F_Y$ in the lower left panel and are 4×10^{-5} and 0.02, respectively. The plots for NGC 4482 on the right hand side of

Fig. 3.6 exhibit a similar behavior, although the contours are more spread out.

Table 3.3 lists the range of component ages and young component mass fractions that provide 1σ fits to the integrated colors of each galaxy. These are given separately for each assumed metallicity that permits a fit. On a given row, the first entry in the τ_0 range column corresponds to the first entries in the other two range columns, and likewise for the second entry. Younger τ_O s are associated with younger τ_Y s because the fraction of light contributed by the young population decreases - the younger τ_O is contributing more of the blue light. As explained above, there is always a good fitting model with $\tau_0 = 12$ Gyr, which is always paired with the highest value for τ_Y , and there is always another good fitting model with $\tau_Y = 10$ Myr, paired with the lowest value for τ_O . Note that we have entered the negative of $\log(F_Y)$ in the fifth column, so that larger entries imply smaller mass fractions. Because very young populations have small mass-to-light ratios and are much bluer than the old components with which they are paired, the F_Y s for models including the 10 Myr-old components are always very small, $< 0.01\%$, even if they produce a significant fraction of the NUV light. However, the F_Y s for models in which the younger component is over 0.5 Gyr old can be much larger, 10-50% in some cases. The $\log(F_Y) = 0$ entries for NGC 3377 indicate that its colors are compatible with 100% of its mass in SSP models with ages of 8 or 3 Gyr, depending on metallicity (see discussion above).

The first conclusion from the dual-generation fitting is that the mean metallicities of most objects cannot be as low as $0.4 Z_\odot$, something that was apparent from Fig. 3.4 itself. Two objects (NGC 4239 and 4482) are compatible with subsolar models but also models at higher metallicity. Three objects (NGC 2778, 4570, and 4621) are compatible only with super-solar metallicity. The rest are compatible with solar or super-solar models. Although our photometry does not otherwise constrain metallic-

ity, we can assume from the results of the optical-band line analyses cited above that the metallicities of most of our objects are $\sim 2 Z_{\odot}$. This means that we should focus our attention on the Table 3.3 entries for super-solar ($2.5 Z_{\odot}$) metallicity.

Consider next the first entries in columns 3-5 of Table 3.3. These are the models containing $\tau_Y = 10$ Myr components. For super-solar metallicities, the ages of the older components all lie in the 1-5 Gyr range with an average of 3.5 Gyr. Mass fractions in the 10 Myr components are always tiny, averaging 4×10^{-5} , meaning that these “intermediate age” (0.5-5 Gyr) populations constitute over 99.9% of the mass.

Given our sample selection criteria and the appearance of our images, the presence of 10 Myr components is unlikely. Instead, these models are realistic only if we assume the hot light represents the UVX component. In that context, all of the photometry is consistent with dominant intermediate-age populations containing a significant UVX contribution at short wavelengths (although these constitute only $\lesssim 1\%$ of the V-band light). Whether such components are actually present can be checked with far-UV observations of these galaxies. The alternative of estimating the UVX contribution from Mg_2 or other long-wave indicators is not likely to be definitive because of the scatter in the relevant correlations (e.g. Burstein et al. 1988, O’Connell 1999, Rich et al. 2005, Donas et al. 2007).

Whether it is astrophysically plausible that UVX stars are important in populations as young as 3.5 Gyr is debatable. The models by Yi et al. (1999) predict that the EHB only becomes strongly populated at ages over 5 Gyr. However, this result is very sensitive to the adopted formulation for red giant branch mass loss (e.g. O’Connell 1999), which remains to be well established.

The second entries in columns 3-5 of Table 3.3 are models in which there is an intermediate age component superposed on an underlying old (12 Gyr) population.

(The results here are not strongly dependent on the age assumed for the older component in the range $\gtrsim 10$ Gyr.) Here, the younger components for $2.5Z_{\odot}$ range from 0.5 to 3 Gyr old and contribute on average 20% of the mass (13% if we exclude the case of NGC 3377) in the volume observed. In most cases, ages are only slightly higher at solar abundance, but fractional masses are smaller.

There are many intermediate dual-generation models and a host of multi-generation possibilities that could be examined, but it is clear that the UV colors of our sample cannot be explained without invoking significant contributions from intermediate age (0.5-5 Gyr) components. The components are only slightly older if we adopt the solar-abundance models rather than super-solar. Our results are consistent with the growing body of evidence described in the Introduction that many moderate-mass early type galaxies experience very extended periods of star formation lasting up to perhaps 90% of a Hubble time. Presumably, most of this activity is related to interactions with gas-rich companions.

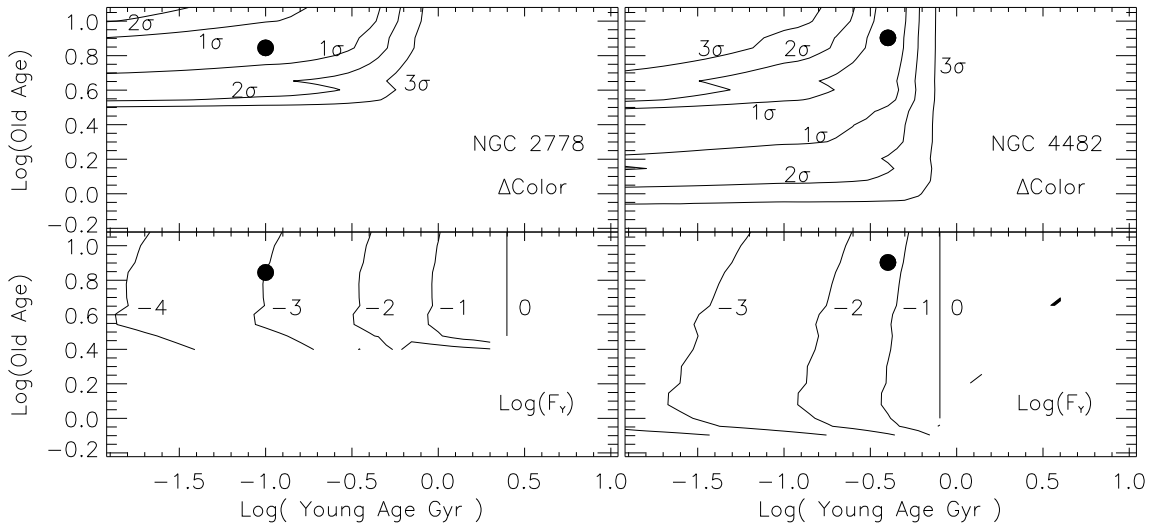


Fig. 3.6.— Results from dual-generation model fits for two galaxies. Upper panels show contour diagrams of color offsets, expressed as $\sigma = \sqrt{\chi^2}$, between models and integrated colors as a function of (τ_Y, τ_O) pairs. The models assume $2.5Z_{\odot}$. Lower panels give the fraction of mass in the younger component associated with each pair. Axes give the logarithm of ages in Gyr. The solid dots represent the location of the best fitting model among the limited set in our grid; however, the center of the “L” shaped region surrounded by the 1 σ contours contains many other models with zero residuals.

Table 3.3. Dual-Generation Fits to Integrated Colors

Galaxy NGC (1)	Z/Z_{\odot} (2)	τ_O Range Gyr (3)	τ_Y Range Gyr (4)	$-\log(F_Y)$ Range (5)
2778	2.5	5-12	0.01-0.5	4.4-1.7
3377	1.0	8-12	0.01-8	4.9-0.0
...	2.5	3-12	0.01-3	5.3-0.0
3384	1.0	11-12	0.01-10	6.3-0.3
...	2.5	3.5-12	0.01-3	5.0-0.3
3640	1.0	10-12	0.01-3	5.2-1.0
...	2.5	3.5-12	0.01-1.5	4.6-0.8
4239	0.4	12	0.01-0.04	4.3-3.6
...	1.0	4.5-12	0.01-0.7	4.1-1.3
...	2.5	2-12	0.01-0.5	4.1-1.0
4474	1.0	9-12	0.01-1.2	4.8-1.6
...	2.5	3.5-12	0.01-1	4.5-1.0
4478	1.0	11-12	0.01-0.4	4.8-2.7
...	2.5	3.5-12	0.01-0.7	4.5-1.4
4482	0.4	10-12	0.01-0.5	4.1-1.9
...	1.0	3-12	0.01-0.6	4.0-1.1
...	2.5	1.4-12	0.01-0.5	4.0-0.6
4570	2.5	4-12	0.01-0.5	4.4-1.6
4621	2.5	4-12	0.01-0.9	4.6-1.4
5576	1.0	9-12	0.01-1	4.7-1.7
...	2.5	3.5-12	0.01-0.9	4.4-1.0
7457	1.0	9-12	0.01-0.5	4.3-2.0
...	2.5	3.5-12	0.01-0.5	4.2-1.2

Note. — Parameter ranges for dual-generation models that yield 1σ fits to the $U - V$ colors of each galaxy. Ages and mass fractions are listed separately for each assumed metallicity capable of fitting the colors.

Fig. 3.7.— Isophotal aperture photometry in the two-color diagram. The large, medium, and small diamond symbols represent the color-color data in the $r \leq 0''.1$, $0''.1 < r \leq 1''$, and $1'' < r$ regions of the color profiles, respectively. Filled circles: the colors of the central components; filled squares: integrated colors. The SSP and composite model loci from Fig. 3.3 are superposed. Coding of model loci is as in Fig. 3.3. The color center in individual plots is adjusted for the values for each galaxy, but the differential color range on each axis is the same for all panels.

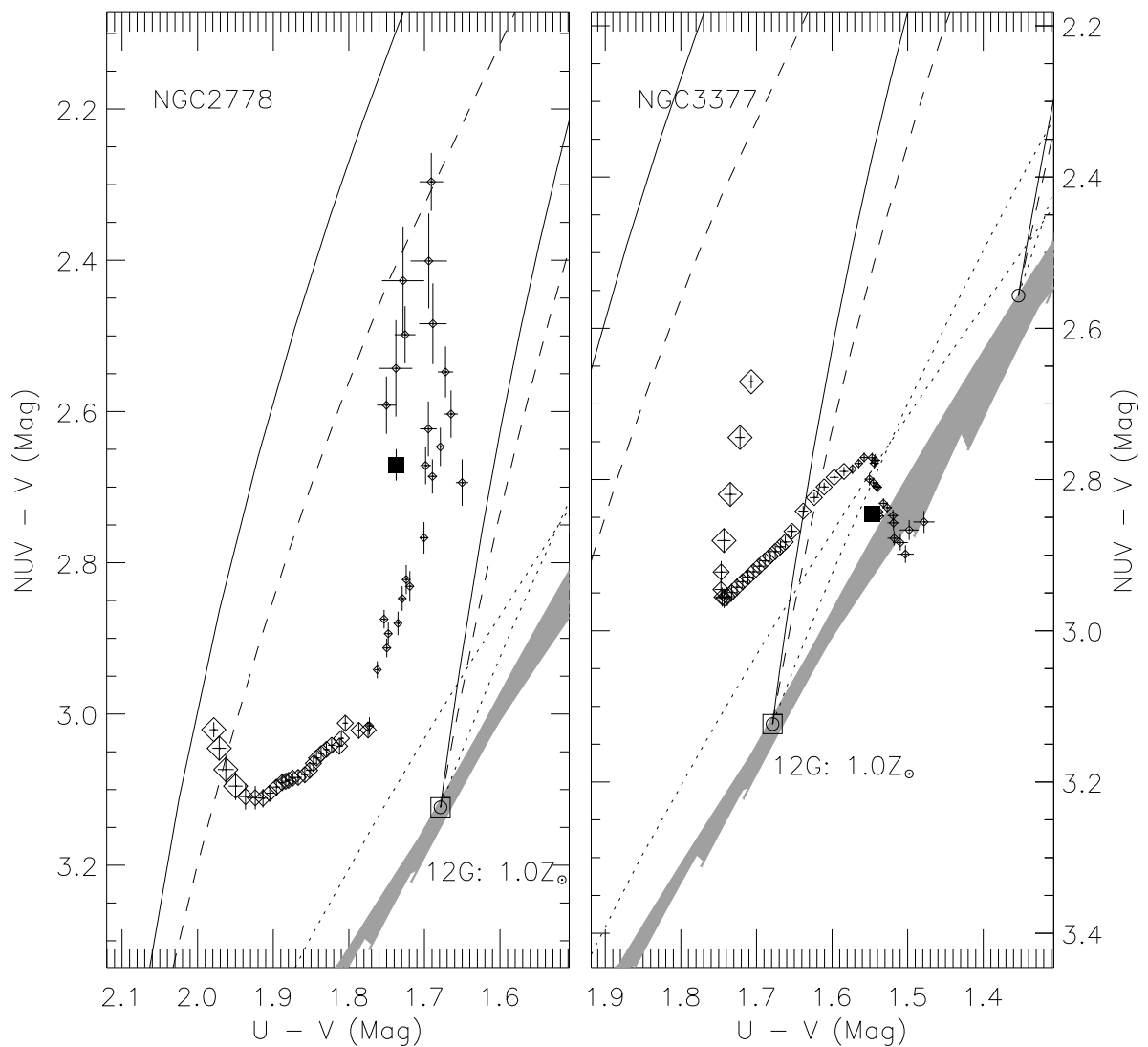


Fig. 3.7.a.— CCRDs of: **NGCs 2778 and 3377**

Fig. 3.7.b.— CCRDs of: **NGCs 3384 and 3640**

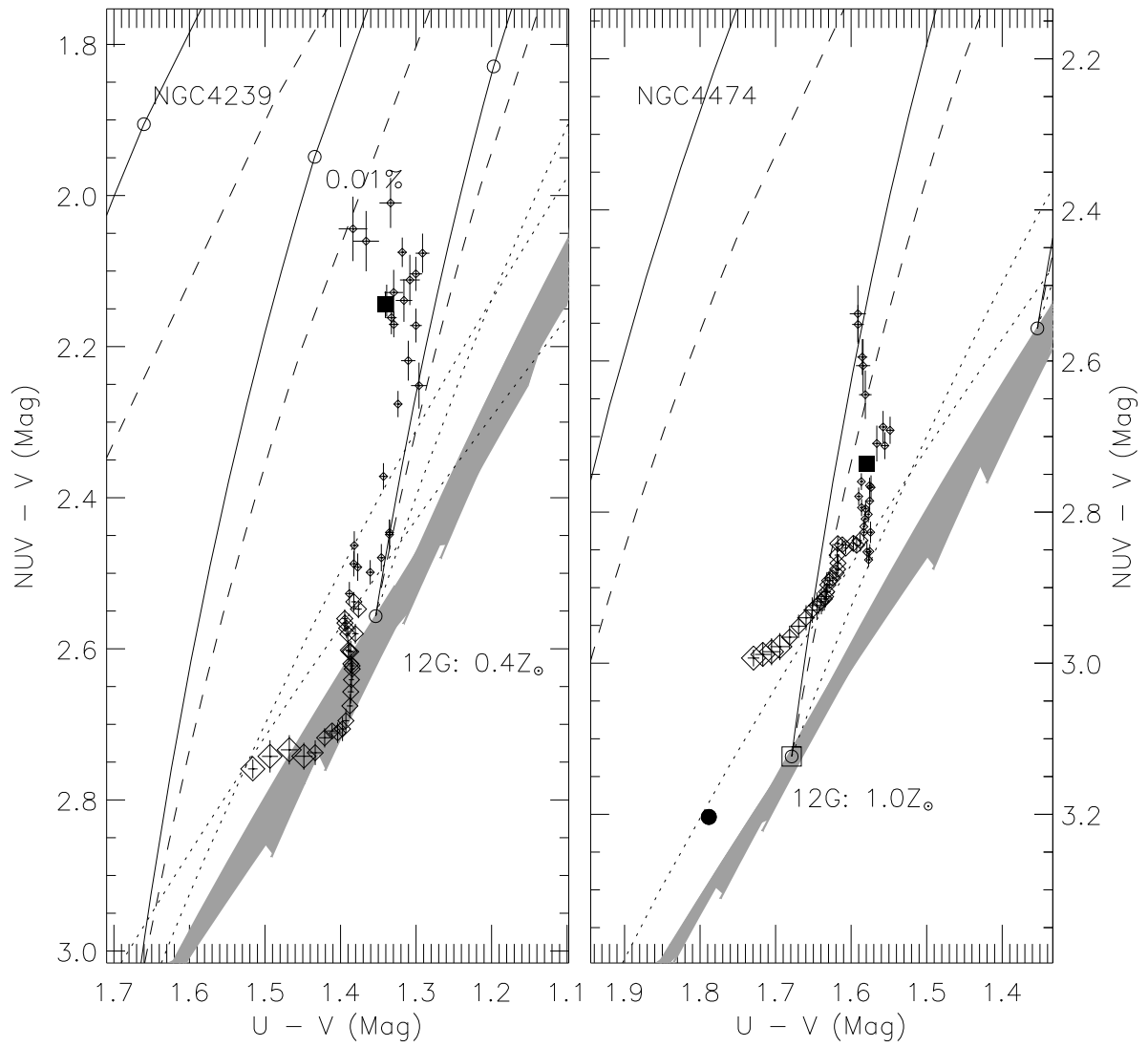


Fig. 3.7.c.— CCRDs of: **NGCs 4239 and 4474**

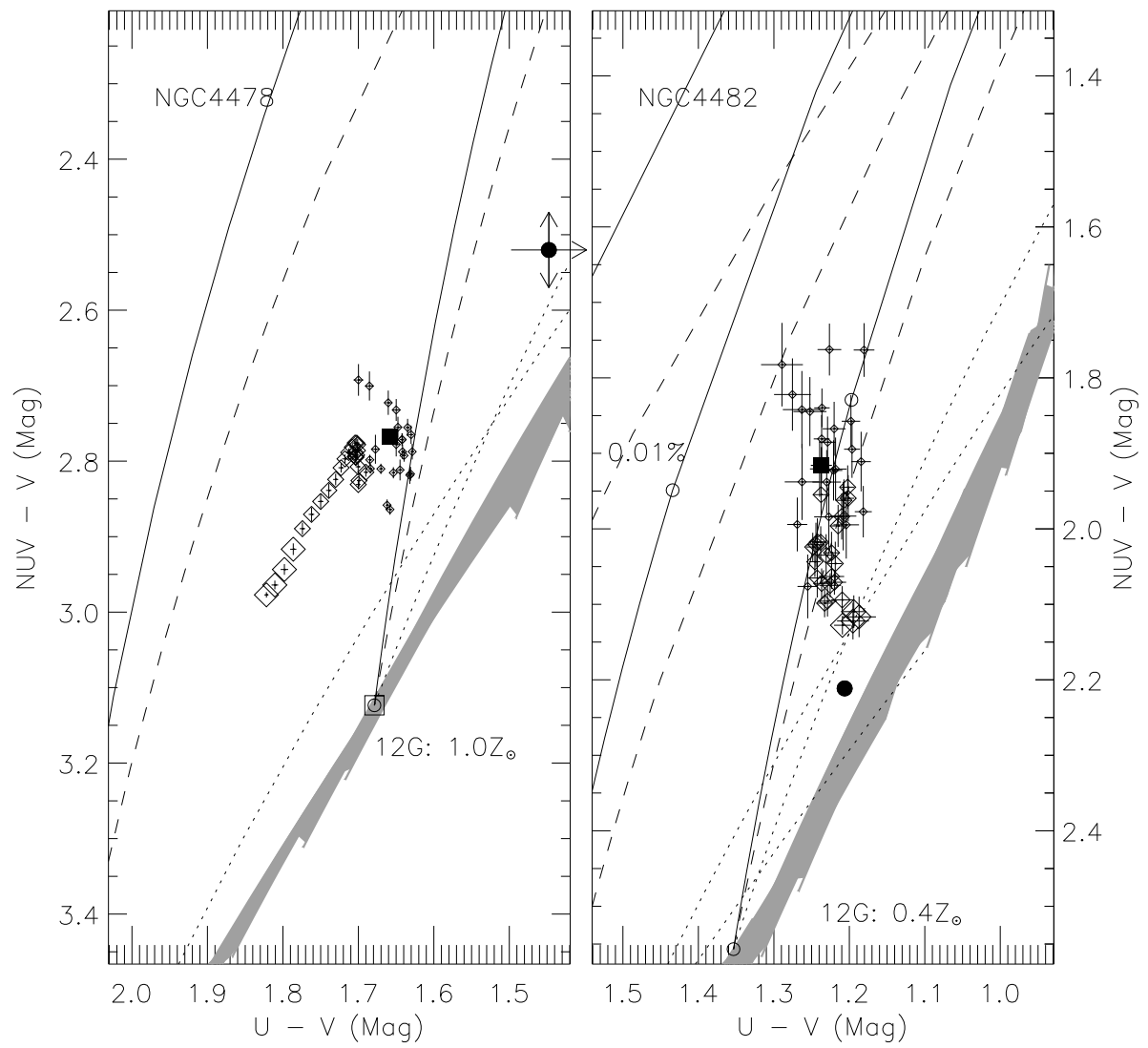


Fig. 3.7.d.— CCRDs of: **NGCs 4478 and 4482**

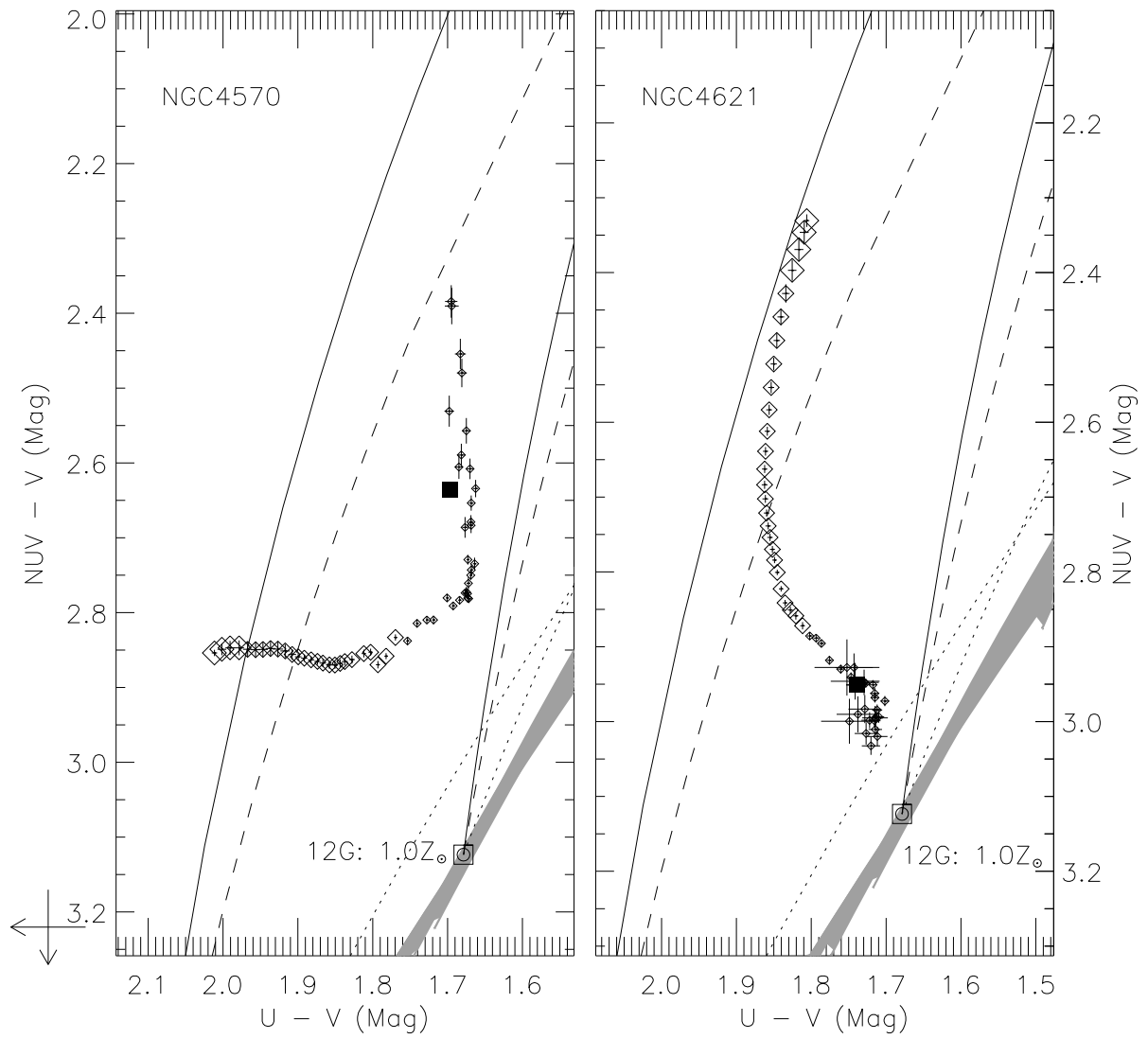


Fig. 3.7.e.— CCRDs of: **NGCs 4570 and 4621**

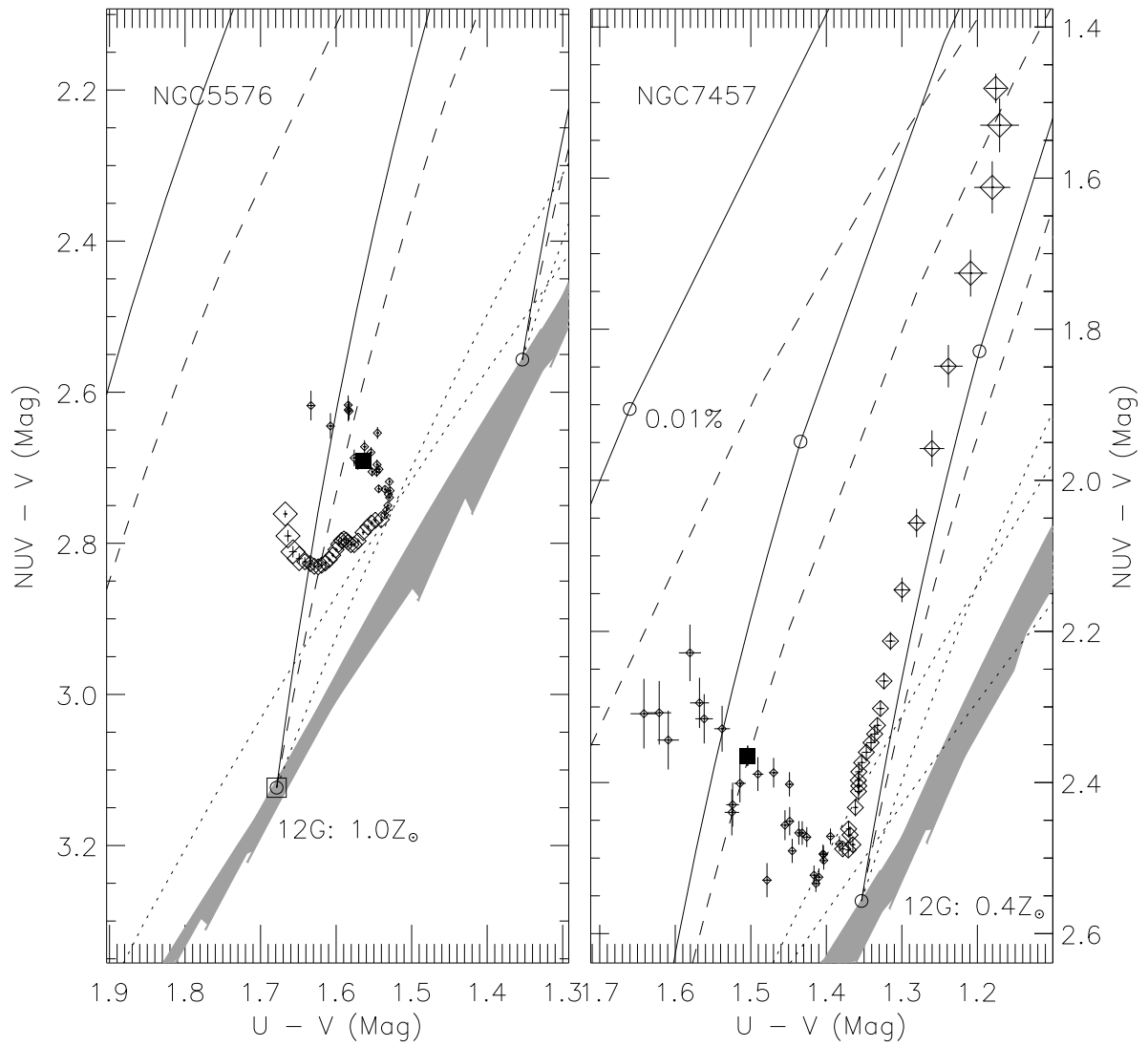


Fig. 3.7.f.— CCRDs of: **NGCs 5576 and 7457**

3.5 Multi-Aperture Color-Color Diagrams

In this section we examine the isophotal aperture photometry from our sample in the color-color diagram. The aperture photometry provides multiple, independent samples of the population structure. Changes of colors with radius can offer additional insights into the character of the populations inferred from the integrated colors and, in principle, can reduce the degeneracy between different solution sets described above.

In Figures 3.7a-f, we show each galaxy's multi-aperture color-color radial distribution (CCRD, which are colors within individual isophotes and not cumulative) with the model and SSP loci from Fig. 3.3 superposed. Three ranges of radial distance are marked by different symbol sizes (larger symbols indicate smaller radii). Given that typical photometric uncertainties in the aperture colors are ~ 0.02 mag, structures that are too subtle to be visible in the surface brightness profiles of Figs. 2 or 6 in Paper I or even the color profiles in Fig. 1 of this paper, are readily apparent here.

The first conclusion from Fig. 3.7 is that the regions observed are quite inhomogeneous in properties and that the integrated colors (plotted with the solid squares) are not, in fact, representative of the central color morphologies. Isophotal color values in a given galaxy typical range over 0.3 mags; the largest excursions are 0.6-1.0 mags. The integrated colors are heavily weighted toward the larger radii ($r \gtrsim 2''$), but the inner regions typically have rather different colors.

These diagrams exhibit much more exotic behavior than in earlier optical broadband photometry of ETGs, even that including the U band. For example, the 2-color diagrams (at ground-based resolution covering spatial ranges from $5''$ – $100''$) of Peletier et al. (1990) show relatively smooth trends without inflection points. They resemble the CCRD of NGC 3640 or perhaps NGC 4474 here. Two-color diagrams (at

Planetary Camera resolution covering spatial ranges from $0''.1$ – $10''$) of Carollo et al. (1997) also show fairly smooth trends though subtle gradients can be detected and the colors of at least one galaxy are clearly offset from her chosen tracks of constant age. Contrast these smooth color-color trends of previous observations with the behavior of NGC 3377: starting from large radii (small symbols) the CCRD moves upward from a location near the SSP locus, makes a sharp turn to redder colors, then makes another sharp reversal to bluer colors at about $0.1''$ radius. The CCRD of NGC 4570 is “J”-shaped; starting from large radii, $NUV - V$ become rapidly redder at constant $U - V$ until a sharp turn occurs at $0.5''$ and thereafter $NUV - V$ is unchanged but $U - V$ becomes rapidly redder. Some of these features are visible in the color maps of Fig. 2.2 in Paper I. Such behavior indicates the presence of distinct structural components.

The CCRD tracks are multiform but do not correlate either with morphological class or the presence of an ALP. The diverse CCRD phenomenology in this sample is probably typical of early type galaxies.

With the exception of the intermediate radii of NGC 4239, none of the CCRDs resembles the classic expectation of a coeval population with increasing metallicity at smaller radii.

As one anticipates from the integrated light photometry, most of the isophotal colors at large radius are indicative of multi-generation populations. In half the sample (e.g. NGC 4239, 4474, 4482, 4570, 7457), the trend from larger to mid-range radii is toward the SSP locus (that is, toward a more uniform age), with marked reddening in $NUV - V$ but little change in $U - V$. In the case of NGC 7457, $U - V$ colors in this region become bluer. However, there are no cases apart from NGC 3377 and 4239 where many apertures have colors lying on the SSP locus. This means

that there are few regions in any of these systems that contain homogenous stellar populations where all the stars formed within $\sim 1 - 2\text{Gyr}$ of one another.

The absence of clusters of points lying along the SSP locus in Fig. 3.7 means that the CCRDs are not consistent with the simplest kinds of discrete, multi-component configurations, where each has a homogeneous stellar population and there is a rapid transition between dominance by one to dominance by the other. (A uniformly old spheroid lying inside a uniformly young disk would be one example of such a configuration.) Instead, transitions between the subpopulations are gradual, and the mixing ratio changes slowly with location. This implies that the radial distributions of the subpopulations are similar to one another, and neither is ever viewed in isolation.

A number of the CCRDs at intermediate radii (e.g. NGC 2778, 3377, 3384, 3640, 4474, 4478, 5576) have shapes consistent with dual-generation models involving a given pair of older τ_O (e.g. the 12 Gyr entries in Table 3.3) and intermediate-age τ_Y components but an F_Y that increases slowly with increasing radius. For instance, between $0''.3$ and $2''$, NGC 3377's CCRD is fit by a 12 Gyr old component mixed with a 600 Myr component that strengthens with increasing radius. With the exception of the outer radii of NGC 4239 and the center of NGC 7457, none of the CCRDs is consistent with a simple dual-generation mixture including a 10 Myr or other hot component. This means that UVX components can play only a minor role in the color variations we see in our sample.

The CCRD structures at larger radii in objects like NGC 4570 and 7457 cut across the dual-generation loci, meaning that they cannot be interpreted as a simple change in the mixing ratio between two component populations. There must be radial changes in the properties of the components.

The dramatic hooks in the CCRDs in Fig. 3.7 at small radius in NGC 2778, 3377,

4621, 5576, and 7457 are the effects of the central sources identified in the surface brightness profile analysis of Paper I. Distortion of the CCRDs is large, however, only if these have colors significantly different than the surrounding galaxy. Therefore, there are cases with distinct central sources (e.g. NGC 3384, 4474) where effects on the CCRD are modest but other cases (e.g. NGC 2778, 5576) where evidence for a central source is marginal in the surface brightness profiles but color excursions are unambiguous. Estimated colors for the central sources are shown as solid circles in Fig. 3.7 but do not always fall within the areas of the individual panels. Central source colors are discussed further in Chapter 4.

The larger central excursions to the CCRDs all involve sources that are considerably bluer in $NUV - V$ than the surrounding population. In the cases of NGC 3377 and 5576, the sources are so blue that there is little evidence for them in the $U - V$ colors. However, there are other instances (e.g. NGC 3384, 4239, 4474, 4478, 4482) where the central objects are redder than the surrounding population. Only two of the central sources (NGC 4474 and 4482) have colors roughly consistent with SSPs.

The central sources have no effect on the behavior of the CCRDs at large radii. Based on the best fits to the central profiles from Paper I, we find that the central sources generally contribute less than 1% of the isophotal light at a radius of $1''$, though those of NGCs 4570, 4621, and 7457 produce up to a few percent. In most cases, the central sources contribute less than 10% of the isophotal light at a radius of $0''.3$. We believe, for instance, that the unusual “J” shape of the CCRD is not primarily caused by central source contamination. Given the uncertainty in the functional forms used to fit to the profiles (see Paper I), however, the estimates of contamination are only approximate.

3.5.1 Composite Synthetic Galaxies

In this section we explore how the diverse color-color morphologies discussed above might arise in the context of underlying population structures. We begin with the expected CCRD of a fiducial merger remnant (FMR-A) taken from the simulations of Hopkins et al. (2008a, see Figure 1 and associated description therein). The remnant’s progenitors contain a high gas mass fraction, $f_g \sim 0.8$, which creates in the remnant a centrally confined distribution of young stars as well as a post-starburst, large-scale, cold-rotation disk formed from tidal stream gas that rains back down after coalescence. The centrally confined young stars contribute 31% of the final total mass and the large disk contributes a nearly negligible 4%. The bulk of the galaxy, at 65% of the total mass, contains the pre-existing old stars and the stars formed after the initial capture and before coalescence, all of which undergo violent relaxation. We use the same structural parameters for each component as described in Hopkins et al. (2008a) and assign ages of 12 Gyr, 2 Gyr, and 1 Gyr to the pre-starburst, starburst, and post-starburst disk components, respectively, place the galaxy at the distance of Virgo and “observe” it with the instrumental set-up used in this work. The colors are extracted from the same set of apertures used with the observed galaxies in this work.

The surface mass distributions relative to the total central surface mass, the radial color profiles, and the CCRD for FMR-A are presented in the top panel of Figure 3.10. We immediately see that the CCRD is confined to the SSP track and does not vary significantly with radius. The large-scale disk does not affect the colors within the FOV considered here. The colors of FMR-A are dominated by the starburst component at most radii, though at large radii the colors change slightly toward the old population. The CCRD does not resemble any of the CCRDs in our sample apart

from NGC 4239 at intermediate radii.

Since the current photometry is so sensitive to multi-generational populations, we modify the fiducial remnant by decomposing the old population component into a “true” old population and a pre-coalescence population with fractional masses of 20% and 45%, respectively (FMR-B), and re-examine the colors. At large radii, both the $NUV - V$ and $U - V$ colors extend to redder values. Like FMR-A, however, FMR-B does not portray the observed color-color behaviors of the sample galaxies.

We opt to take the opposite tact of creating synthetic galaxies (SGs) with composite populations that produce $NUV - V$ and $U - V$ color trends that do resemble those of the observed galaxies to glean information about trends in population compositions and what limitations we face in determining the exact compositions. Three synthetic galaxies are presented in Figure 3.11-A-C that progress from simple to complex and the last is intended to mimic, not uniquely solve, the CCRD of NGC 3377. Like the fiducial merger remnants, the synthetic galaxies are placed at the distance of Virgo and ‘observed’ with the instrumentation setup of the current work. The stellar population and spatial distribution characteristics of the sub-components for all the FMR and SGs are summarized in Table 3.4.

SG-A is composed of two components of ages 12 Gyr and 700 Myr. To get a CCRD off the SSP track, a population must have a mixture of ages. The older population must be metal-rich in order to get the CCRD to cross out of the solar-metallicity color space into the metal-rich colors. The properties of the components in SG-A do not uniquely produce the colors presented in 3.11-A. For the same pair of population ages, components with other combinations of Sérsic indices, effective radii, and relative mass fractions can produce the same set of colors.

SG-B is created by adding a compact central object with an age of 10 Myr to SG-

A that contributes a very low fraction of the total galaxy mass. The central object causes a central blueward spike in the 2-color diagram and the CCRD of SG-B is otherwise identical to that of SG-A. The blueward spike could also be created by a slightly older population with a similarly slightly higher mass fraction.

A metal-rich 3 Gyr population is added to SG-B to create SG-C and the new CCRD has a sharp transition at large radius that depart from the 700 Myr + 12 Gyr mixture to the SSP colors dominated by the 3 Gyr population. The metal-rich 3 Gyr population has very similar colors to a solar-metallicity 8 Gyr, once again demonstrating that the stellar populations and their compositions do not map 1-1 to observable trends in radial colors. The mass contributions of the components younger than 12 Gyr in SG-A, B, and C are considerably less than those assigned to the fiducial remnant of Hopkins et al. (2008a) yet are still consistent with the mass fractions of gas in mergers which are considered “gas-rich” (down to $\sim 5\%$).

The CCRD of NGC 3377 displays more complex behavior than could have been predicted, yet, its dominant features are perhaps the most straightforward of the twelve observed CCRDs to reproduce synthetically (as in SG-C). The process of reproducing a specific set of features in any CCRD involves a delicate balance amongst the components of relative masses, concentration parameters such as the Sérsic indices, relative scale radii, and assigned population ages and metallicities. A complete, first order decomposition of the radial color profiles of any galaxy will need to be synchronized with the decomposition of the surface brightness profile to ensure that population compositions which can reproduce the correct colors can also reproduce the total distribution of mass in the galaxy. Unique solutions from a synchronized mode of decomposition are still not guaranteed.

Table 3.4. Fiducial Merger Remnant and Synthetic Galaxy Stellar Population Components

Model	Age Gyr	Z/Z_{\odot}	n	r_e kpc (")	F_P
(1)	(2)	(3)	(4)	(5)	(6)
FMR: A	12.000	1	4.0	5.0 (65")	0.65
	2.000	2.5	1.0	0.2 (2'6)	0.31
	1.500	2.5	1.0	2.6 (34")	0.04
FMR: B	12.000	1	2.5	5.0 (65")	0.20
	4.000	2.5	1.7	1.0 (13")	0.45
	2.000	2.5	1.0	0.2 (2'6)	0.31
	1.500	2.5	1.0	2.6 (34")	0.04
SG: A	12.000	2.5	1.3	0.430 (5'5)	0.975
	0.700	2.5	1.0	0.480 (6'2)	0.025
SG: B	12.000	2.5	1.3	0.430 (5'5)	0.975
	0.700	2.5	1.0	0.480 (6'2)	0.025
	0.010	2.5	1.0	0.005 (0'06)	7e-9
SG: C	12.000	2.5	1.3	0.430 (5'5)	0.775
	0.700	2.5	1.0	0.480 (6'2)	0.025
	0.010	2.5	1.0	0.005 (0'06)	7e-9
	3.000	2.5	1.0	1.2 (15'4)	0.20

Note. — The ages, metallicities, and spatial distribution characteristics of the individual components of the fiducial merger remnants (FMR) and the synthetic galaxies (SG) discussed in Section 3.4.3. (1) Model designation and the (2) Age (3) Metallicity fractions relative to solar (4) Sérsic index (5) effective radius in both kiloparsecs and arcseconds (6) and mass fraction, F_P , of each individual population.

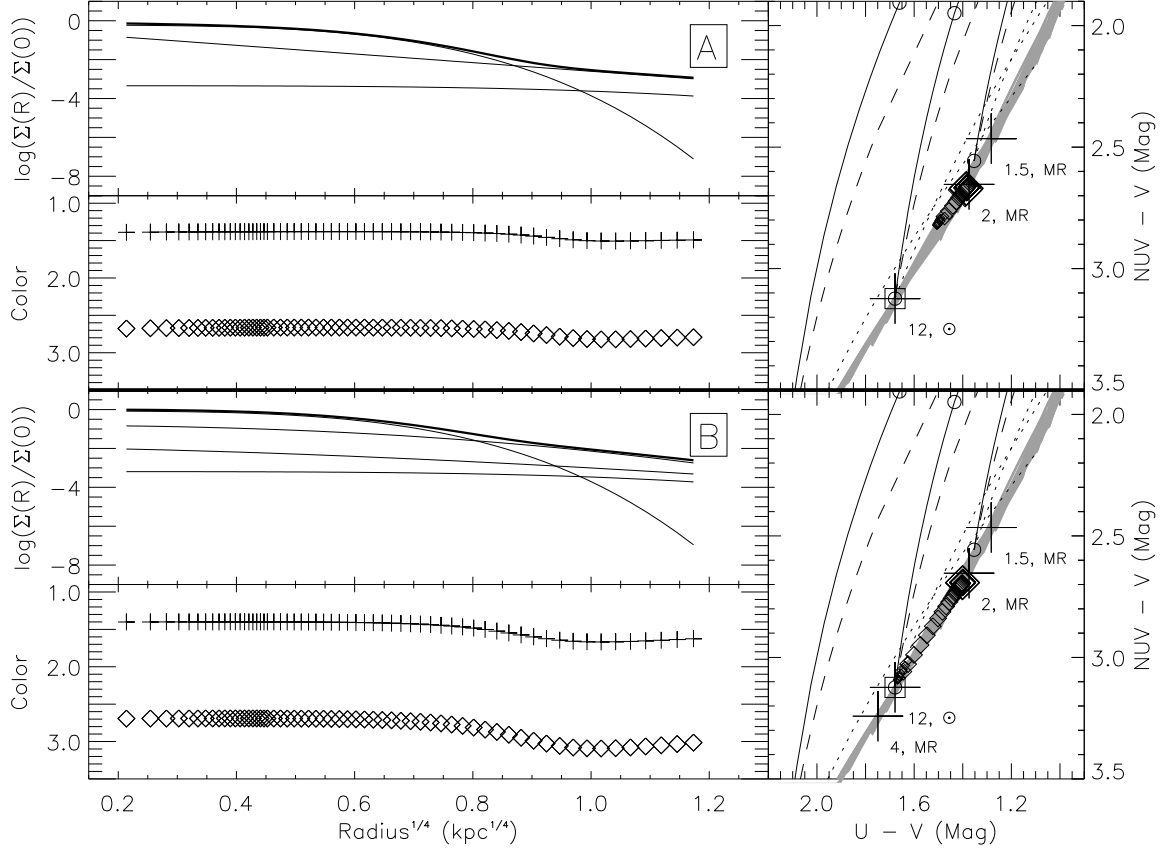


Fig. 3.10.— The properties of a fiducial merger remnant (A) and a modified fiducial merger remnant (B). For each model, the upper left plot displays the surface mass distributions relative to the mass at $R=0$ for the total galaxy in the heavy solid line and the sub-components in lighter solid lines. Often, the dominant older population and total mass distributions cannot be distinguished. The radial color profiles are presented in the bottom left plot with the $NUV - V$ colors represented by the diamonds and the $U - V$ colors by the plus signs. To the right is the CCD with the Pégase models superposed as in Figure 3.3, with several SSP model labeled. As with the observed CCDs, the colors are represented by open diamonds with the largest sizes at the smallest radii and smallest sizes at largest radii with changes at each decadal increase in arcseconds.

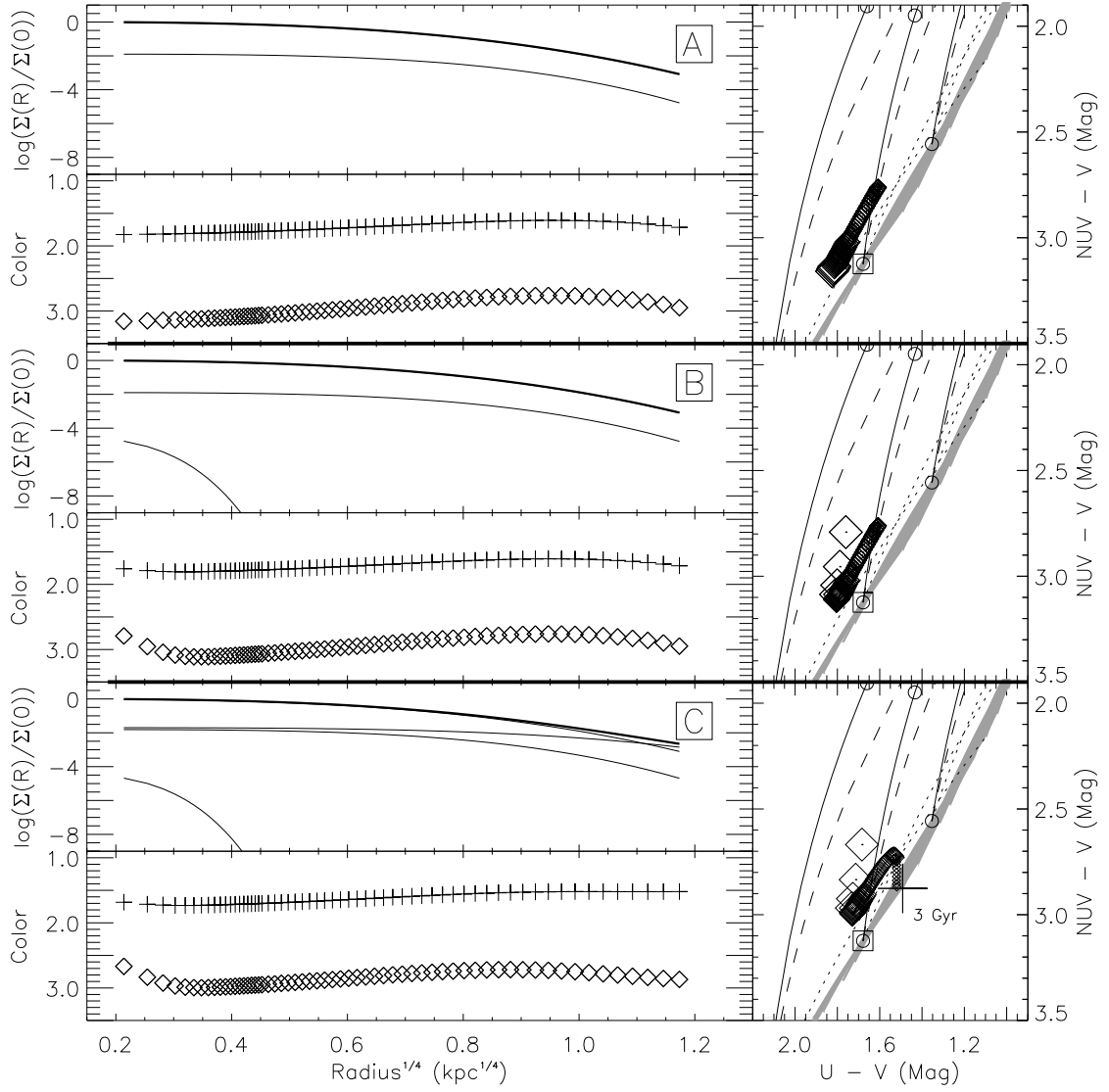


Fig. 3.11.— The radial surface mass distributions, color profiles, and 2-color diagrams of the three synthetic, composite galaxies arranged as in Figure 3.10.

3.6 Discussion

We examine the multi-band ultraviolet photometry obtained at high spatial resolution of early type galaxies for evidence of the multiple generations of star formation that are expected to occur as a result of hierarchical assembly involving gas-rich major mergers. This is the first high resolution, high signal-to-noise study of the UV/optical spatial profiles and color structure of early-type galaxies (ETGs) and their implications for stellar populations.

The total integrated colors span a magnitude range of 1.1 mag in $NUV - V$ and 0.5 mag in $U - V$. In comparison to the Pégase stellar population model colors, ten of the twelve data points lie well away from the color region of simple stellar populations and dual-metallicity models which indicates that they cannot contain homogeneous stellar populations. Ten of the twelve total galaxy colors are inconsistent with metal-poor populations, three are only consistent with metal-rich populations, and seven can be well-described by either solar- or metal-rich populations. The total galaxy colors of NGC 4239 and NGC 4482 are best-described by either solar- or super-solar metallicities, however, within the estimated uncertainties of the population models, these two colors may be described by sub-solar metallicities.

In $U - V$, the total galaxy colors are used to derive SSP ages which are expected to correspond to those derived from spectrophotometric analysis of absorption line spectra based on the Lick system (e.g. Worthey 1994). There is good agreement between the two methods and for the solar-metallicity Pégase models, the equivalent SSP ages range from 2.8 to 12 Gyr and from 1.2 to 3.9 Gyr for comparisons to the super-solar models. With dual-generation populations, for which the two ultraviolet colors are necessary, the total galaxy colors are consistent with oldest younger populations that are typically 1 Gyr and 3 Gyr for the super-solar and solar-metallicity

model comparisons, respectively, and about 20% of the population mass contributed by the younger population regardless of the metallicity.

B-V colors are often employed to trace changes in stellar populations in ETGs, however, the typical range of total galaxy colors in B-V span only 0.2 mag. By using $NUV - V$ and $U - V$, we are significantly more sensitive to detecting multi-generational populations than would be possible with optical colors.

The behaviors of the radial distribution of colors in the 2-color diagrams are multiform and the range of colors spanned by an individual galaxy can be significant with typical ranges of 0.5 mag in $NUV - V$ and 0.25 mag in $U - V$ though they reach up to 1.1 mag and 0.5 mag in $NUV - V$ and $U - V$ respectively (see for example Figure 3.7.f).

The total galaxy colors are dominated by the light from large radii which is reflected in the similarity of radial colors at large radii to the total galaxy colors. Many of the galaxies (e.g. NGC 4239, 4474, 4482, 4570, 7457) have colors at large radii which demonstrate significant population mixing as they are located in color-color space quite far from the SSP color region. The total galaxy colors of NGC 3377 and NGC 3384 are consistent with SSP colors, however, if we move inward and investigate the colors of these two galaxies at smaller radii, we see colors that indicate significant population mixtures. All told, all twelve of the sample galaxies have colors which are consistent with multi-generational populations.

Our approach of using photometry in multiple ultraviolet bands, which are the most sensitive probes for finding multi-generational stellar populations, provides us with ample evidence indicating that ETGs are composed of multiple stellar populations and that some individual stellar populations may be distributed in unique structural components as determined through abrupt radial color transitions.

Chapter 4

Near-Ultraviolet Merger

Signatures in Early-Type Galaxies

III: Central Source Identification

Abstract

The properties of the detected central objects of eight early-type galaxies in a sample of twelve galaxies are examined to identify their emission sources through multiple ultraviolet band photometry. The scale sizes and absolute magnitudes of the central objects are similar to those within other normal-sized early-type galaxies with a range of 1 to 16 pc. Five central objects have colors consistent with multi-generation stellar populations, two may contain a single generation of stars, and the colors of one central object is most consistent with a multi-generation population of metallicity greater than $2.5 Z_{\odot}$.

The colors of all the detected central objects are not consistent with non-thermal radiation or hot accretion disks. X-ray and radio emission may indicate marginal low luminosity active galactic nuclei are present in two or three galaxies but they exist in addition to the stellar central components detected and discussed here. A central point source which was detected only in the Near-UV spectral region of one galaxy may be related to non-thermal emission.

The multiple generation stellar populations indicate recent star formation (age \lesssim few Gyr) must have occurred within the central-most regions of many of these early-type galaxies.

4.1 Introduction

Nuclear stellar systems, which are discrete photometric structures with sizes of a few parsecs at the centers of galaxies and which are often referred to as stellar nuclei or nuclear star clusters, are observed across the full range of Hubble types (Böker et al. 2004; Carollo et al. 2002; Lotz et al. 2004; Côté et al. 2006; Lauer et al. 2005; Rossa

et al. 2006; van der Marel et al. 2007) yet their natures are poorly understood. They have radii comparable to globular clusters yet typically have luminosities that are a few to a hundred times brighter than luminous globulars. The commonalities among the nuclear stellar objects implies that there may be a universal formation mechanism. They may form *in situ* under the special conditions that prevail in galaxy centers, or they may form elsewhere in the galaxy and be transported to the center and retained there.

Stellar nuclei are most commonly found in intermediate-luminosity early-type galaxies (ETGs) rather than the most luminous ones (Côté et al. 2006). ETGs that form during gaseous merger events are expected to display central extra light that resulted from rapidly inflowing gas and a subsequent starburst. However, the expected size of an evolved merger starburst is larger than the few parsecs characteristic of the stellar nuclei (Mihos & Hernquist 1994a; Springel 2000; Hopkins et al. 2008a). While the central objects detected in ETGs may have formed as part of the same dissipational starburst event, the current best merger simulations cannot resolve structures with sizes below about 30 parsecs, so we lack good intuition about the effects of gas inflows on the relevant scales. An alternative formation mechanism is a merger of globular clusters (old populations) following loss of angular momentum through dynamical friction (Bekki et al. 2004; Côté et al. 2006). For the central objects of intermediate-luminosity galaxies ($-18 \lesssim M_V \lesssim -21$), step-wise assembly would be likely.

Evidence of a possible important relationship between stellar nuclei and super-massive black holes (SMBHs) has recently emerged. The masses of the stellar nuclei scale in almost the same way with their host galaxy's virial mass as do SMBHs (Rossa et al. 2006; Ferrarese et al. 2006; van der Marel et al. 2007), and this suggests that

there may be an evolutionary connection between these two types of “compact massive objects” at galaxy centers. Smaller SMBHs may exist inside the compact stellar nuclei and be growing at the expense of the stellar component, but AGN activity may be subject to a long duty cycle during much of which it is not easily detectable (Piner et al. 2001; Nagar et al. 2005).

The high spatial resolution of the High Resolution Camera of the Advanced Camera for Surveys (ACS-HRC) instrument on the Hubble Space Telescope (HST) combined with multiple ultraviolet band photometry provides a unique way to explore youthful stellar populations, mixed populations, and other hot emission sources that occur on very small spatial scales in galaxy nuclei, and we exploit that in this study.

Details of sample selection, observations, surface brightness profile analysis, and color-color analysis for this program were given in Chapters 2 and 3. Briefly, we selected a set of six dust- and active galactic nucleus (AGN)-free ETGs with central spikes in their monochromatic surface brightness profiles (SBPs, Byun et al. (1996); Ravindranath et al. (2001); Rest et al. (2001)) at long wavelengths as candidate hosts of centrally concentrated youthful stellar populations. A similar set of six ETGs without the central spikes in their SBPs were chosen as the control sample. The 12 galaxies were observed with the ACS-HRC in three filters: F250W (NUV), F330W (U), and F555W (V). The pixel scale of the HRC is $0''.027 \text{ pix}^{-1}$ with a $27'' \times 27''$ field of view. SBPs were extracted in each band using virtual elliptical apertures and were then decomposed into two components: an outer body and an inner central source as described in Chapter 2.

This chapter is organized as follows: the sizes and absolute magnitudes of the central objects are compared to those of other galactic nuclei and globular clusters in Section 2. The stellar population parameters of the central objects are determined

by comparing to single- and dual-epoch models in Section 3. In Section 4, we discuss possible non-stellar emission of the central sources by comparing to the colors of blackbodies and power-law spectra, by examining the observed X-ray emission from the central regions of the galaxies, and by comparing the estimated accretion efficiencies to the ranges of known AGN. In Section 5, we assess the likely emission sources and underlying nature of the central objects and what they imply about the formation scenarios of their host galaxies.

4.2 Central Object Sizes and Luminosities

The light profiles of the central objects are characterized by either a point source or an exponential function, as described in Chapter 2. The point source is described by scaling the semi-major axis brightness profiles of the PSF images produced by `TinyTim`. The PSF images are normalized to 1.0 so the scaling factor produced by the fitting algorithm is the total brightness of the point central source. The PSF full width half maxima are very similar across filters, with $\theta_{NUV}^F = 0''.046$, $\theta_U^F = 0''.046$, and $\theta_V^F = 0''.056$, though they differ in structure (Anderson & King 2004). The exponential function is not intended to describe a disk-like structure; instead it was adopted because it is empirically successful and convenient (see Chapter 2). The total integrated light of the exponential source, assuming circular symmetry, is

$$I_{T,exp} = I_o 2\pi r_c^2. \quad (4.1)$$

where the scale radius is r_c , and the central intensity, I_o , is the maximum brightness at $r = 0$.

Our criterion for a positive detection of a central source was that the χ_ν^2 of the fit

improved by at least a factor of two over the body-only fit in a given band. Most of our sample met that criterion in two or more bands, and all showed some marginal evidence of a nuclear source in at least one band. All ALPs met the standard in all three bands, but only two non-ALPs (NGC 3640 and 4621) did so. Robust detections of central sources, with a χ^2_ν improvement of a factor of at least 5, are limited to six cases: NGC 3384, 4239, 4474, 4482, 4621, and 7457; and only one of these (NGC 4621) is a non-ALP.

We summarize the absolute magnitudes and physical radii of the detections in Table 4.1. Radii are not listed for the point sources (NGC 3377 and 4478), and colors are not given unless two bands yielded positive detections. All magnitudes are in the STMAG system.

The errors in the integrated photometry, in the range 0.2-0.6 mags, of the central objects are larger than for the isophotal photometry discussed in Chapters 2 and 3. That is because they subtend only a small number of image pixels and because their parameters are affected by residuals in the fits to the underlying galaxy light. A secondary problem, which can add up to 0.04 mag uncertainty to the integrated magnitude measurements, stems from the unmatched PSFs across the three bands. The resulting colors are good enough, however, to draw some inferences about their nature.

The resolved central objects of the current sample are small, with only two (NGC 3640 and 4570) being significantly over 10 pc in size, and most falling in the 2-4 pc range. They have V-band absolute magnitudes ranging from -11.6 to -13.5 mags. In Figures 4.1 and 4.2, we compare the sizes and spectral energy distributions (SEDs) of our sample to those of central objects reported in earlier HST studies of late-type spirals (Böker et al. 2004), early-type spirals (Carollo 1999; Carollo et al. 2002), dwarf

Table 4.1. Central Object Properties

Galaxy NGC (1)	ALP (2)	M_V mag (3)	M_U mag (4)	M_{NUV} mag (5)	r_V pc (6)	r_U pc (7)	r_{NUV} pc (8)	$NUV - V$ mag (9)	$U - V$ mag (10)
NGC2778		> -11.7	> -10.6	> -10.1	< 1.5	< 1.5	< 1.5
NGC3377		> -6.7	> -7.4	-9.97 ± 3.31	< 0.7	< 0.7	0.4 ± 0.3	< -3.3	...
NGC3384	x	-12.61 ± 0.22	-10.47 ± 0.22	-9.37 ± 0.24	2.9 ± 0.2	2.1 ± 0.1	2.3 ± 0.2	3.25 ± 0.26	2.14 ± 0.24
NGC3640		-13.47 ± 0.23	-11.55 ± 0.28	> -10.5	15.2 ± 0.8	15.3 ± 1.1	< 1.8	> 2.9	1.92 ± 0.31
NGC4239	x	-11.58 ± 0.27	-9.82 ± 0.28	-8.80 ± 0.42	2.3 ± 0.2	2.0 ± 0.2	2.2 ± 0.3	2.78 ± 0.43	1.76 ± 0.31
NGC4474	x	-11.70 ± 0.14	-9.92 ± 0.26	-8.50 ± 0.47	3.3 ± 0.2	3.3 ± 0.3	2.5 ± 0.5	3.20 ± 0.48	1.79 ± 0.28
NGC4478	x	> -10.8	-9.32 ± 0.47	> -8.3	< 1.1	2.0 ± 0.4	< 1.1	...	< 1.4
NGC4482	x	-11.94 ± 0.13	-10.73 ± 0.14	-9.73 ± 0.31	2.7 ± 0.1	2.5 ± 0.1	2.4 ± 0.3	2.21 ± 0.33	1.21 ± 0.17
NGC4570		-14.81 ± 0.35	> -12.6	> -11.6	23.3 ± 3.2	< 1.1	< 1.1	> 3.2	> 2.2
NGC4621		-13.66 ± 0.17	-11.42 ± 0.18	-11.76 ± 0.22	11.2 ± 0.7	7.0 ± 0.3	8.0 ± 0.5	1.90 ± 0.27	2.24 ± 0.24
NGC5576		> -6.7	> -9.5	> -10.2	< 1.7	< 1.7	< 1.7
NGC7457	x	-12.74 ± 0.26	-11.66 ± 0.27	-11.52 ± 0.36	1.1 ± 0.1	1.1 ± 0.1	1.0 ± 0.1	1.21 ± 0.33	1.07 ± 0.23

Note. — ALP designation, absolute magnitudes (in the STMAG system), characteristic radii, and integrated colors of the central objects of our sample galaxies. Radii measured in the V, U, and NUV bands are given separately. Distances are provided in Chapter 2. Upper magnitude limits are provided for cases without positive detections. No size information is presented for the central point sources, whose radii are less than $\sim 0.5 \theta_{psf} = 0''.025$.

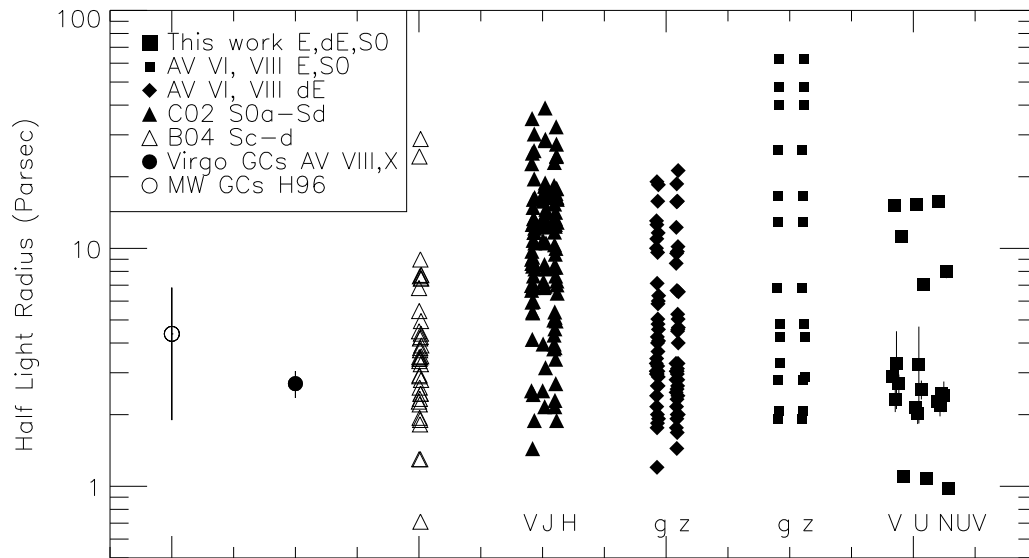


Fig. 4.1.— A comparison of the half-light radii of the central objects of galaxies in this sample, in other HST samples of various Hubble types, and of the mean values for Milky Way and Virgo Cluster globular clusters. Data are shown for different filters if more than one was used. Refs: Ferrarese et al. (2006); Côté et al. (2006) - Large Es and SOs and dwarf Es - AV VI, VIII E,SO and dE; Carollo et al. (2002) - Spirals - C02 S0a-Sd; Böker et al. (2004) - Late-type Spirals - B04 Sc-d; Côté et al. (2006); Jordán et al. (2005) - Virgo globular clusters - Virgo GCs AV VII, X; Harris (1996) - Milky Way globular clusters - MW GCs H96.

ellipticals (Lotz et al. 2004; Côté et al. 2006), and normal ETGs (Ravindranath et al. 2001; Lauer et al. 2005; Ferrarese et al. 2006). We also compare to Milky Way (MWGC; Harris 1996) and Virgo Cluster globular clusters (VCGC; Côté et al. 2006, Jordán et al. 2005). In Fig. 4.2 we include the SEDs of metal-rich ($2.5 Z_{\odot}$) populations with ages of 100 Myr, 1 Gyr, and 10 Gyr from the Pégase library (Fioc & Rocca-Volmerange 1997; see Chapter 3) as well as power-law spectra ($f_{\nu} \sim \nu^{-\alpha}$), typical of the non-thermal emission of AGN) with indices α of 2.0, 1.5, and 1.0. Photometry from all the studies presented in Figures 4.2 and 4.3 has been converted to the ST Mag system.

The radii (Figure 4.1) of the nuclear stellar systems range over a factor of 40 in size. Our sample, with typical radii of 2-4 pc, falls mainly at the small end of the range. In the 2-4 pc scale size range are the central objects of NGC 4482, a known nucleated dwarf, and NGC 4239, which has a total luminosity lower than that of NGC 4482, as well as the central objects of two S0s, NGC 3384 and 4474. The central object of NGC 7457, another S0, has the smallest size and those of NGC 3640 and 4621, two ellipticals, have the largest.

The optical magnitudes of the central objects in our sample are consistent with those of other normal E/S0 and spiral galaxies (Côté et al. 2006; Lauer et al. 2005; Carollo et al. 2002; Rossa et al. 2006). These are generally 1 to 4 mags brighter than the central objects of dwarf ellipticals. In turn, the dE stellar nuclei (Côté et al. 2006; Lotz et al. 2004) are generally 1.5 to 3.5 mags brighter than globular clusters. If the central objects form through merger of globular clusters, roughly 100 bright globulars ($M_V \sim -7.5$) would be required to achieve the typical E/S0 central object optical luminosities ($M_V \sim -12.5$). Mergers would also imply that the half-light radii scale with the luminosities of central object as $r_h \propto L^{0.23}$; however, no such trend is found

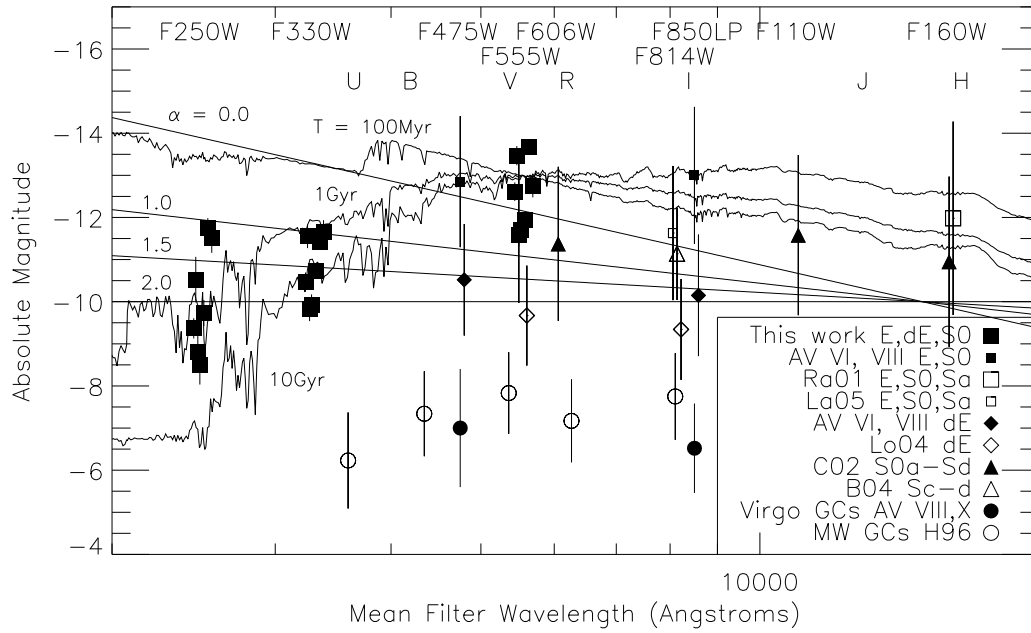


Fig. 4.2.— A comparison of the absolute magnitudes (in the STMAG system) of globular clusters and nuclear stellar systems cross the UV-optical band. Average values are given for the various subtypes in each sample from the literature. Metal rich ($2.5 Z_{\odot}$) SEDs from the Pégase library for ages of 100 Myr, 1 Gyr, and 10 Gyr and power-law spectra with indices of 1.8, 1.5, and 1.0 are overplotted. For clarity, the stellar population spectra are normalized at $\lambda = 5550\text{\AA}$ to -13 mags and the power-law spectra are normalized at $\lambda = 2500\text{\AA}$ to -10 mags. Sources: Ferrarese et al. (2006); Côté et al. (2006) - Large Es and SOs and dwarf Es - AV VI, VIII E,S0 and dE; Ravindranath et al. (2001) - Large Es and S0s and Early-type Spirals - Ra01 E,S0,Sa; Lauer et al. (2005) - Large Es and S0s and Early-type Spirals - La05 E,S0,Sa; Lotz et al. (2004) - dwarf Es - Lo04 dE; Carollo et al. (2002) - Spirals - C02 S0a-Sd; Böker et al. (2004) - Late-type Spirals - B04 Sc-d; Côté et al. (2006); Jordán et al. (2005) - Virgo globular clusters - Virgo GCs AV VII, X; Harris (1996) - Milky Way globular clusters - MW GCs H96.

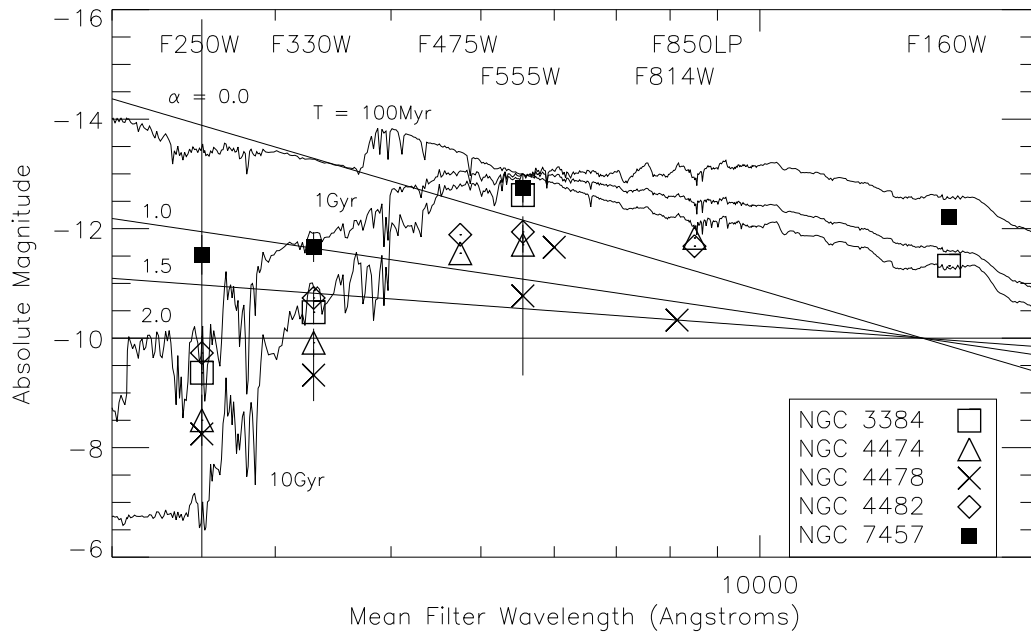


Fig. 4.3.— The SEDs of five individual central objects from our sample, incorporating data from this and earlier studies. The reference SEDs from Fig. 4.2 are overplotted. For clarity, the stellar population spectra are normalized at $\lambda = 5550\text{\AA}$ to -13 mags, the power-law spectra are normalized at $\lambda = 2500\text{\AA}$ to -11 mags, and the F555W value from Lauer et al. (2005) is offset in wavelength from the F555W measurements of the current work. Sources: Côté et al. (2006); Ravindranath et al. (2001); Lauer et al. (2005).

for the current sample.

In Fig. 4.3 we have combined our data with photometry from the literature (Côté et al. 2006; Lauer et al. 2005; Ravindranath et al. 2001) to construct crude SEDs for five of our galaxies. We omit several cases in the literature where saturation at the galaxy centers may have affected measurements. The M_{F555W} value from Lauer et al. (2005) for NGC 4478, which is offset in wavelength for clarity, is over 1 mag brighter than that measured in the current work. This is most likely due to the different methods used to obtain the central object brightnesses. Lauer et al. (2005) extrapolated a nuker fit inward and subtracted it to obtain the excess light measure. Both Côté et al. (2006) and Ravindranath et al. (2001) fit the central objects and the galaxy bodies simultaneously, as we do here. The derived SEDs are consistent with intermediate to old stellar populations, with the exception of NGC 7457, whose blue $NUV - U$ color indicates a younger population.

4.3 Nuclear Stellar Populations

It is well established that the stellar nuclei of spiral galaxies have multi-generation populations (e.g. O’Connell 1983, Stephens & Frogel 2002, Sarzi et al. 2005, Rossa et al. 2006). Less is known about the character of stellar nuclei in ETGs. The nearest example is NGC 205, which, based on one color, has a youngish (100 Myr) population (Butler & Martínez-Delgado 2005). In most other cases, single colors indicate dominant populations over 1 Gyr old, but there is not yet much information on possible star formation histories or metallicities (Côté et al. 2006).

With our two-color UV/optical photometry, we can take a step beyond earlier work and analyze the stellar populations of our stellar nuclei using the techniques we described in Chapter 3. The integrated colors from Table 4.1 are plotted in the

two-color diagram in Fig. 4.4. The grey shaded region marks the location of coeval models, either simple stellar populations (SSP) or mixed-metallicity populations, and the lines show the loci of dual-generation models; the models are all based on the Pégase library (Fioc & Rocca-Volmerange 1997). See Chapter 3 for details of these models and how to use them to interpret populations of observed systems.

Several important conclusions are evident from a simple inspection of Fig. 4.4. The integrated colors of the central objects are diverse, spread over two magnitudes in $NUV - V$ and one in $U - V$. However, all of them are reddish in color, lying in the lower (red) third of the population envelope shown in Fig. 3.3. This implies that none is dominated by a population younger than several 100 Myr. Furthermore, with perhaps only two exceptions (NGC 4474 and 4482), all of the sources have composite populations—i.e. they do not lie near the coeval locus.

The errors on the colors of the central objects are considerably larger than those for integrated light in Fig. 3.4, which introduces more ambiguity into the possible ranges of consistent stellar population models. Accordingly, we will not attempt to explore the full range of consistent models, as we did in §3.4 for integrated light, but will instead comment on the general implications of the best estimates for the colors of each object as listed in Table 4.1, with the understanding that these are subject to some uncertainty.

NGC 4474 and 4482 fall near the coeval model locus and are consistent with SSP or coeval dual-metallicity models. These have apparently not experienced more than one epoch of star formation. Inferred ages depend on the assumed metallicity. For $2.5Z_{\odot}$, NGC 4474 and 4482 are consistent with ages of 8 and 1.8 Gyr, respectively. NGC 4474 is not consistent with a lower abundance. NGC 4482’s age for Z_{\odot} and $0.4Z_{\odot}$ would be 3.5 and 11 Gyr, respectively. The color properties of NGC 4482 are consistent with

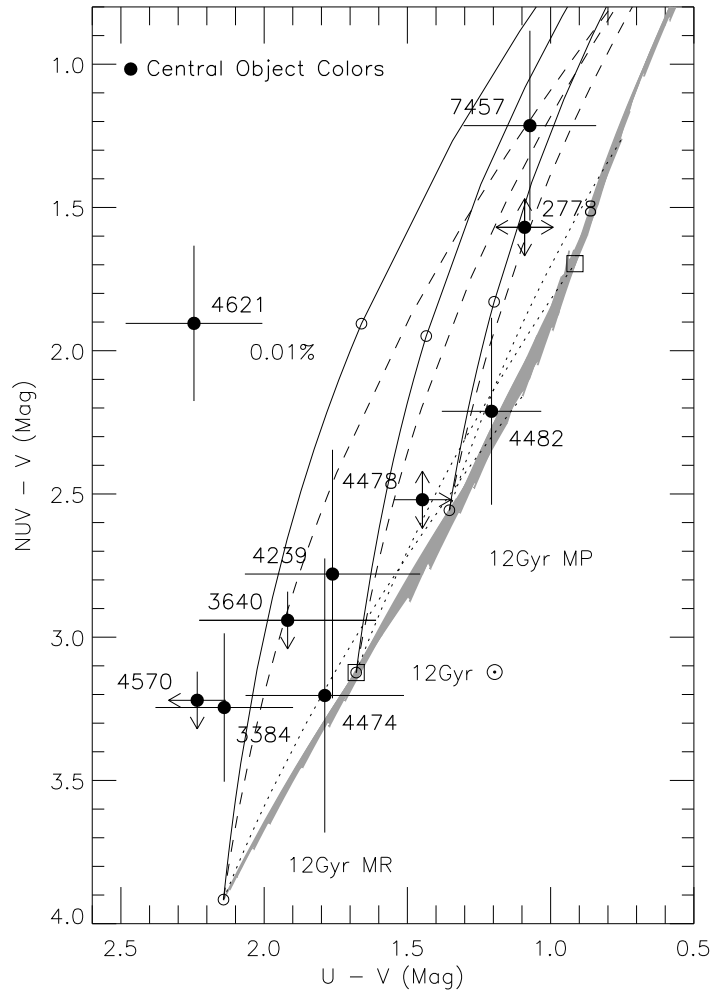


Fig. 4.4.— Integrated colors of the central sources plotted in the two color diagram. The grey region and lines mark the location of models from the Pégase library, as in Fig. 3.4. See text for more details. The locations of simple stellar populations of 12 Gyr age for three metallicities are labeled.

the merger of moderate metallicity, old globular clusters like 47 Tuc. However, the colors of NGC 4474 are not consistent with merged massive clusters unless these have a significantly higher mean metallicity than found in typical globular cluster systems.

The colors of the other central objects indicate the presence of multiple generations of stars. With the exception of NGC 7457, all also fall outside the 12 Gyr envelope for solar metallicity, implying that they must have higher average metal abundances. The colors of NGC 3640 and 4239 are comparable to those of many of the integrated galaxy colors shown in Fig. 3.4 and they therefore contain similar populations. They could be fit by an intermediate-age (2-4 Gyr), $2.5 Z_{\odot}$ base population in combination with a hot, UVX component or by an old 12 Gyr population in combination with a minority component in the 0.5-3 Gyr range constituting 3-20% of the mass.

Two other galaxies, NGC 3384 and 4478, lie at or just outside the $2.5 Z_{\odot}$, 12 Gyr boundary of models allowed by our SSP library. Literally interpreted, they would be consistent only with very old (12 Gyr) metal-rich populations containing a hot UVX-like component. It is more likely, however, that their positions have been scattered outside the envelope by measurement errors.

Yet more discrepant is NGC 4621, which is well outside the feasible range of our model set. The unusual behavior of the isophotal colors of this galaxy, with reddening in $U-V$ but blueing in $NUV-V$ at smaller radii, are shown in Fig. 3.7 and are visible in the color maps of Fig. 2.2j. The isophotal colors approach but do not cross the feasibility envelope. This could be produced by a metallicity increase at small radii (or increased extinction) coupled with a warm central source. We believe, however, that the color values extracted for the central source have been systematically shifted by residuals in the nuker fit to the background light.

The bluest central source is that in NGC 7457, which produces the largest color

excursions seen in our sample (Figs. 3.1 and 3.7f). Its location in Fig. 4.4 is only consistent with a significant contribution from a population $\lesssim 100$ Myr old.

4.4 Nuclear Activity

Although our sample was selected to lack overt evidence of SMBH-driven nuclear activity (see Chapter 2), we need to consider whether the effects of low luminosity AGNs (LLAGNs, see Ho 2008 for a thorough review), which have recently been found in many nearby intermediate-mass galaxies, could be present in our observations. The classical emission line signatures of AGN activity are absent from the optical spectra of our sample galaxies (Ho 1999). Other than emission lines, the dominant effect of an AGN in the UV/optical region is predicted to be from accretion disk thermal emission which creates the "big blue bump" (Krolik 1999). For galaxies like those of the current sample, the temperatures of the accretion disks are expected to be in the 10^4 – 10^6 K range. The SEDs of typical LLAGNs are power laws, $L_\nu \propto \nu^{-\alpha}$, with power-law indices, α , in the range of 1 to 3.5 and an average of about 1.8 (Ho 1999). We show the colors of relevant ideal blackbodies and power-law SEDs compared to those of our central sources and the Pégase stellar population models in Figure 4.5. AGN sources are expected to be spatially unresolved unless interstellar medium scattering effects or jets are present.

The colors of both blackbodies and power-law SEDs are similar to each other and lie in the same vicinity as the Pégase stellar population models with ages less than 100 Myr in the two-color diagram. Even the bluest of our central sources (NGC 7457) lies well away from this region. As explained above in section 4.3 and Chapter 3, there is no evidence for significant reddening by dust over the volumes we observe, and while a localized cloud or filament could affect the compact nuclear sources more

easily than the integrated colors, we doubt that dust is an important factor in the colors of our central sources.

Thus, none of the central sources we see is dominated by AGN-related UV/optical emission. One possible exception is that such emission could make a moderate contribution in the case of NGC 7457. This object is resolved in our light profiles (see Chapter 2), though it is quite compact. It is possible that this is a case of an AGN surrounded by a compact star cluster. The source with the second-largest color excursions in its isophotal colors is NGC 4621, but its measured radius is considerably larger than that of NGC 7457, which again indicates that a stellar system dominates.

The NUV-only central point source in NGC 3377 could also be AGN light. It is unresolved and, with a V-band brightness limit of -3.7, its $NUV - V$ colors are very blue. Lacking both V and U brightnesses, an estimate on its $U - V$ limit is not possible. The central components of NGC 4478 are also point sources yet its colors are best described by stellar emission.

One of the best signatures of AGN activity is X-ray emission. We checked the Chandra and XMM archive databases for observations of our sample. Five of the galaxies, NGC 3377, 3384, 3640, 4621, and 7457 were observed with Chandra. The software program `CIAO` was used to extract from the Chandra images sub-images in three spectral bands: 0.5-8keV, 0.5-2keV, and 2-8keV. A circular aperture of radius $5''$ was placed over the center position of each galaxy in the World Coordinate System (WCS) and the total counts in each band was measured. The total counts were divided by the respective exposure times and, with an assumed power law index of 1.8, used to get the fluxes per band from the PIMMS software. The fluxes were integrated over area to get luminosities and are otherwise unprocessed. All five galaxies have X-ray luminosities consistent with the ranges associated with known LLAGNs (Ho et al.

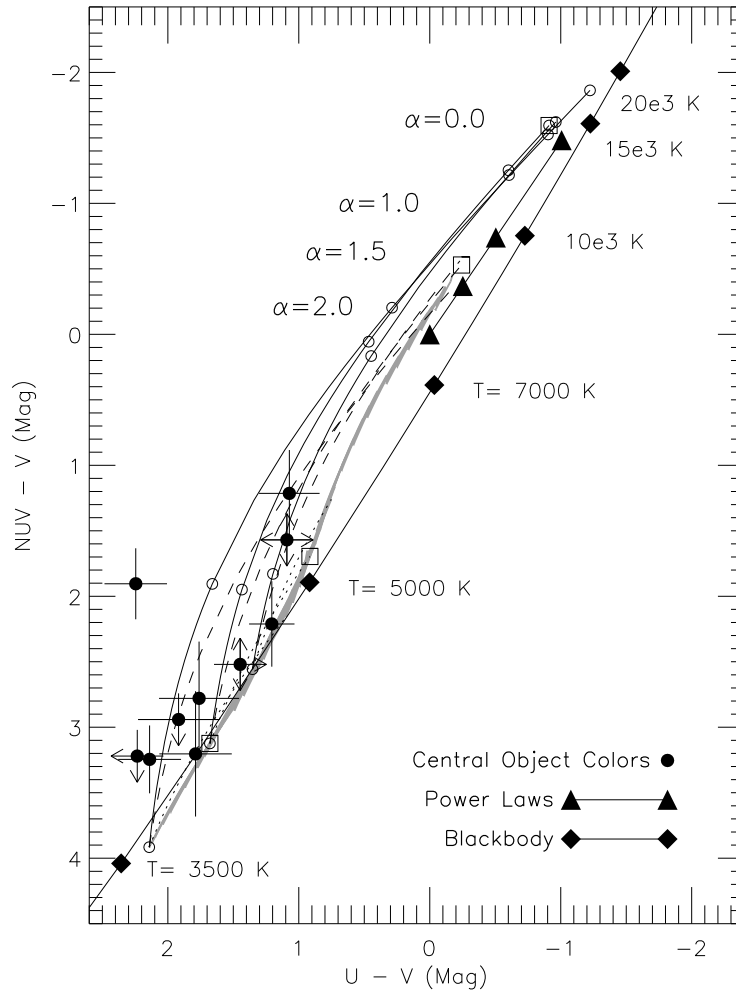


Fig. 4.5.— The color-color plot of Figure 4.4 expanded to include the colors of power-law spectral energy distributions (SEDs) and blackbodies. The locus of blackbodies is the solid line with filled black squares; the locus of power-law SEDs similar to those observed in AGNs is the solid line with filled triangles.

2001).

Table 4.2 lists the derived X-ray properties of the sources, including the UV/optical to X-ray index

$$\alpha_{OX} = 1 + 0.384 \log \left(\frac{(\nu L_\nu)_{2500 \text{ \AA}}}{(\nu L_\nu)_{2-8 \text{ keV}}} \right) \quad (4.2)$$

Eracleous et al. (2008) observe a range of α_{OX} from 0.5 to 2.77 for a sample of galaxies with low-ionization nuclear emission regions (LINERs). They believe that the highest values are characteristic of quasars and hot stars in the vicinity of the nucleus and that the true range of α_{OX} for the weak AGNs of LINERs is from 0.9 to 1.5. The corollary of this is that higher values of α_{OX} , and therefore, ultraviolet flux, indicates more star formation and less non-thermal flux. The α_{OX} of the current sample is generally smaller than that of the weak AGNs of LINERs, with a range from 0.41 to 1.07. The x-ray emission from the central 5'' of NGC 7457 totals ten counts, so all values for this galaxy are marginal.

Figure 4.5 shows X-ray contour plots for the five detected galaxies. Two of the galaxies (NGC 3384 and 3640) appear to have no nuclear emission but do show evidence of circumnuclear sources. Extra-nuclear sources in early type galaxies are primarily associated with low-mass X-ray binaries (Sivakoff et al. 2003). NGC 3377 has a distinct central X-ray component, extended emission along the major axis of the stellar body, and either a second point source or unrelated background point source nearby. Soria et al. (2006) verify that the X-ray emission of NGC 3377 has both a soft, diffuse component as well as a hard, nuclear emission source. The nuclear emission is most consistent with an actively accreting supermassive black hole rather than a central concentration of hot gas. The diffuse component has a scale radius of 4'', which corresponds with the region of isophotal colors of NGC 3377 in Chapter 3

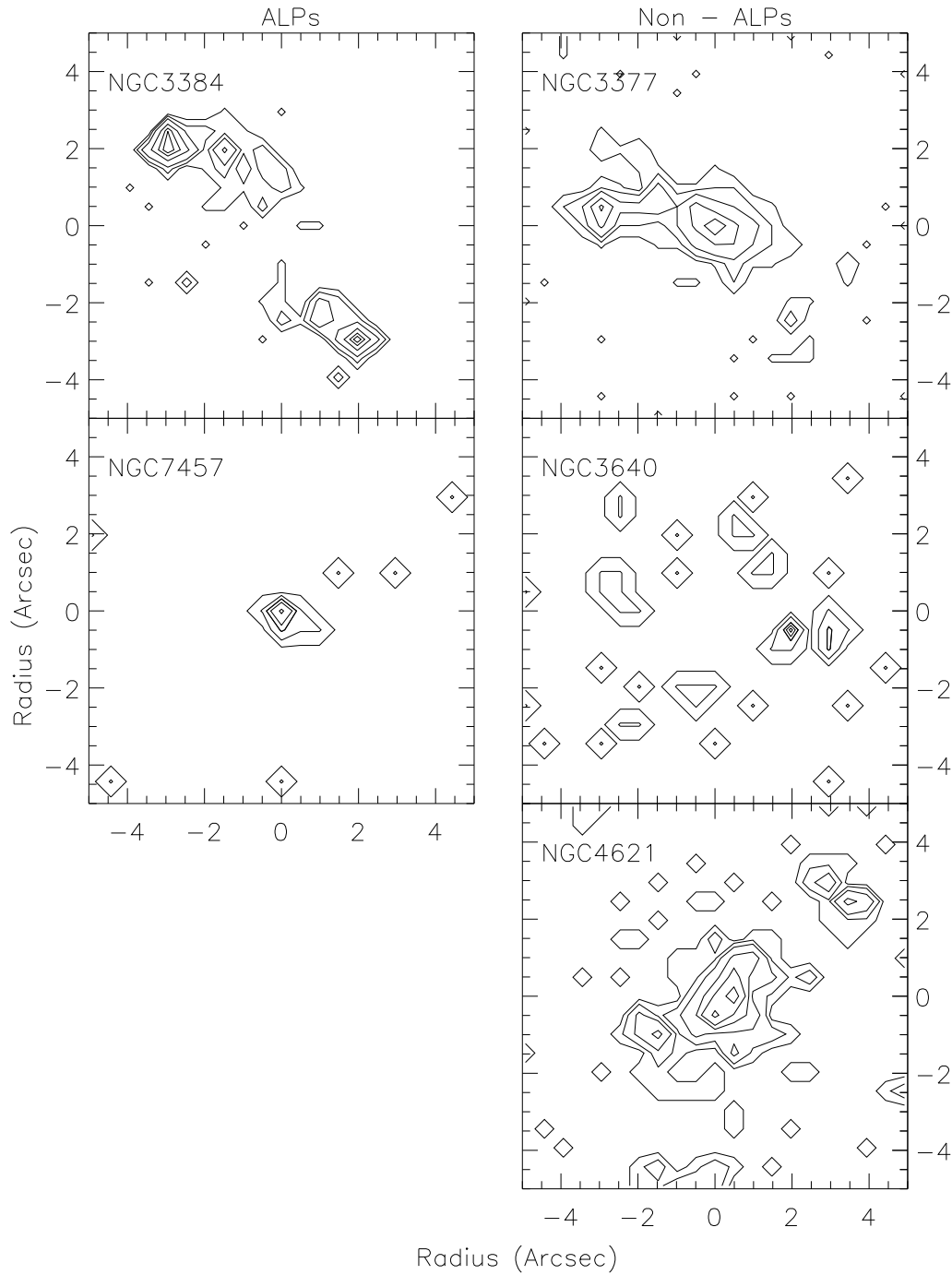


Fig. 4.5.— Contour plots of the Chandra X-ray images of 5 galaxies in the range of 0.5 to 8 keV covering the central $10'' \times 10''$ of each galaxy. The location of the galaxy nucleus is at (0,0) in all cases. All plots are aligned so that north is up and east is left. The plotted levels, in units of 10^{-4} counts/sec/pixel, are for **NGC 3377**: [0.2,0.5,1,2,3,5]; **NGC 3384**: [0.8,1.5,2.5,4.5,6,7]; **NGC 3640**: [0.2,1,2,2.01,2.5,3]; **NGC 4621**: [0.2,0.5,1,2,3,5]; **NGC 7457**: [0.2,1,2,2.01,3,5].

which are offset from the color track of simple stellar populations and may require a youthful stellar component.

NGC 4621 has a bright X-ray emission region near its center with multiple peaks extended roughly along the major axis of the galaxy. Wrobel et al. (2008) recently analyzed the X-ray and 8.5 GHz emission from NGC 4621. They find that the emission measurements are most consistent with jet-like emission driven by a low luminosity AGN but with no active accretion. Variability at 8.5 GHz may have occurred between observations taken in 1999 and 2006. There may be significant emission from low mass x-ray binaries but they argue against the presence of high mass binaries because of the lack of evidence for recent star formation.

NGC 7457 contains a compact X-ray nuclear source with a small extension to the southwest of the nucleus out to $r \sim 0''.5 - 1''$.

No radio continuum emission at 1.4 GHz was detected in the beams of any of the current sample galaxies (Chapter 5).

Hence, three of the objects in our sample that show significant central UV/optical color excursions are also likely to be active AGN. There may be a moderate contribution of direct AGN light to our observations, at least at the shorter wavelengths, in each of those cases. But in NGC 4621 and 7457 the central light appears to be dominated by a compact stellar population.

4.5 Discussion

The central objects of NGCs 3384, 3640, 4239, 4474, 4478 and 4482 have compact stellar populations as determined by their properties of scale radius, absolute V-band magnitude, NUV - V and U - V colors. The central object colors in NGCs 3384, 3640, 4239, and 4478 are most consistent with stellar populations that have a mixture of

ages. The multi-generational central objects may have formed from the coalescence of compact objects some of which could have formed during a recent star formation episode.

The central objects of NGC 4474 and NGC 4482 have colors which are most consistent with simple stellar population yet, for both galaxies, the isophotal colors at large radius indicate significantly mixed populations. Any interactions which could have formed NGC 4474 or NGC 4482 could not have recently put large quantities of gas into their central regions.

The NUV central point source and blue central upturn in isophotal colors of NGC 3377 may be related to its hard, nuclear x-ray emission suggest that it harbors an accreting super massive black hole and that we may detect associated non-thermal emission in the NUV.

Similar to the central object of NGC 7457, that of NGC 4621 is well-resolved and, while its colors are unusual, they are most likely explained by higher than considered metallicities and, possibly, mis-isolation during the surface brightness profile fitting procedure. The spectral analysis of its x-ray emission appears to have a component related to an active nucleus (Wrobel et al. 2008) but non-thermal emission is not detected in the this work for NGC 4621.

The resolved scale radius and colors of the central object we detect in NGC 7457 are consistent with a multi-generational stellar population. The X-ray point source is marginal at best and future deep x-ray observations will better characterize its x-ray emission. Low levels of HI emission associated with NGC 7457 (Sage & Welch 2006) in addition to the detected multi-generational central stellar component may demonstrate that the galaxy formed during a gas-rich merger of disk galaxies (Chapter 5).

Table 4.2. Xray Emission Properties

Galaxy NGC (1)	$L_{0.5-8}$ erg/s (2)	$L_{0.5-2}$ erg/s (3)	L_{2-8} erg/s (4)	HR (5)	α_{OX} (6)	PID (7)	Ref (8)
3377	38.739	38.362	38.533	0.19	0.54	2934	<i>a</i>
3384	38.774	38.438	38.405	-0.04	0.59	4692	<i>b</i>
3640	39.493	39.107	39.311	0.23	0.41	7142	<i>a</i>
4621	39.178	38.800	38.977	0.20	0.73	2068	<i>a</i>
7457	38.133	37.723	38.014	0.32	1.07	4697	<i>b</i>

Note. — The X-ray properties for five sample galaxies. (2-4) The Luminosities for the 0.5 - 8 keV; 0.5 - 2 keV; and the 2 - 8 keV bands within 5'' of the galaxy centers. (5) The hardness ratios. (6) The X-ray to Optical slope, α_{OX} . (7) The Chandra-ACIS proposal IDs. (8) References: *a* Values are calculated from unprocessed Chandra-ACIS archive images for NGCs 3377, 3640, and 4621. *b* Values are calculated from processed counts made available by Terashima et al. (In Prep, *Private Communication*) for NGCs 3384 and 7457.

Chapter 5

HI Emission in or near Early-Type Galaxies

Abstract

Gaseous merger events can produce elliptical and S0 galaxies with HI gas associations and central stellar overdensities according to Λ CDM cosmologies and numerical models of mergers. Here, we survey two samples of dust and AGN-free early type galaxies with the Green Bank Telescope for 21cm hydrogen emission: a test sample of those with central excesses in their stellar surface brightness profiles and a control sample of similar galaxies without the central stellar excesses. 25% of early-type galaxies with HI in interacting groups have central excesses.

5.1 Introduction

Numerical models have shown that as the gravitational potential changes during a merger event, the gaseous component is tidally stretched into streamers; half of which falls into and forms a dense gaseous knot in the center of the merger remnant (Mihos & Hernquist 1994b; Springel 2000; Bekki & Shioya 2001). Subsequent star formation leaves behind a dense stellar core whose surface density profile forms an upward break above the de Vaucouleurs $r^{1/4}$ profile of the preexisting stellar population. Hibbard & Yun (1999) observe upward breaks in the surface densities in the molecular CO (1-0) gas of three gaseous merger remnants, one of which may continue to exhibit the break in its stellar surface density when it reaches a mid-aged elliptical stage.

At the opposite end of the tidally stretched streamers, some of the rest of the gas particles can have enough energy to reach escape velocity and leave the merger remnant (Barnes 2002). These streamers and escaped gas particles can be observed as rings, filaments, and clumps of gas in the environmental regions about merger remnants. Such environmental gaseous features have been observed about ellipticals

providing additional evidence that they can form from gaseous merger events (e.g. - Schiminovich et al, 2001; Hibbard & Sansom 2003; Horellou et al 2001).

The advent of the Hubble Space Telescope (HST) has made it possible to image early type galaxies with quite high spatial resolution ($0''.0455/pixel$). Surveys of early type galaxies have shown significant structure in their central regions including central excesses above smooth profiles in a fraction of them (Lauer et al. 1995; Rest et al. 2001; Ravindranath et al. 2001). Our work is an initial test of the relationship between the high central stellar densities in early type galaxies to their possible gaseous major merger histories. Environmental neutral hydrogen (HI) is used as a coincidence tracer. Two samples of early type galaxies, one with central excesses and one without, were chosen based on preexisting published surface brightness profiles in the large surveys. The two samples were then observed with the Green Bank Telescope (GBT) in a survey to compare the frequency of neutral hydrogen detection to the presence of a central excesses.

The sample selection and observations are described in section 2. In section 3, the data analysis is discussed. The results and a discussion of the relationships of the detected HI to the observed galaxies is presented in section 4.

5.2 Sample Selection

We used the the Robert C. Byrd Green Bank Telescope (GBT) to perform observations in the 21cm line of neutral hydrogen (HI) of a sample of nearby early type galaxies (ETGs). The sample was selected from three surveys of ETGs with published surface brightness profiles (SBPs) derived from high-resolution Hubble Space Telescope (HST) observations: those of Lauer et al. (1995, observed in the F555W filter, hereafter “V”), Rest et al. (2001, F702W filter, hereafter “R”), and Ravindranath

et al. (2001, F160W filter, hereafter “H”). Our goal is to look for any correlation between the presence of irregularities observed in the published surface brightness profiles and the presence of cold HI either in or around the targeted galaxy. The specific type of SBP irregularities we focus on are signatures of excess light above a smooth function in the inner regions, which could signify the presence of a concentrated stellar population resulting from a previous (possibly ancient) dissipational merger (Mihos & Hernquist 1994b). We refer to galaxies which show such irregularities as anomalous light profile (ALP) galaxies, and those that have normal smoothly varying SBP as non-ALP galaxies.

From the above referenced HST surveys, we identified galaxies with and without ALPs. Each galaxy was inspected for the presence of active galactic nuclei (AGN), central star formation, or obvious dust features, all of which can alter stellar light profiles. Galaxies with central X-ray or radio continuum components, optical emission lines, or which were classified in the literature as AGN were eliminated from the final sample. Additionally, galaxies with obvious inner dust features apparent in the broad band images or any published color maps were also rejected. To keep our observing time request reasonable, we only considered galaxies above a declination of -25° and within a distance¹ of 36 Mpc. The remaining galaxies were divided into two groups based on the presence or lack of an ALP. Those without were further refined by requiring that the ALP and non-ALP samples span a similar range of absolute magnitude and scale radii. The final sample includes 36 galaxies: 17 with ALPs and 19 without. The sample is listed in Table 5.1 with some basic parameters.

¹Distances were taken from (Tonry et al. 2001), which uses the surface brightness fluctuation method.

5.3 Observations and Data Analysis

The galaxies were observed in L-band with the GBT over the course of two observing runs in April 2003. The total observation time was 18 hours. The Spectral Processor back-end was used with a total bandwidth of 10 MHz and 1024 channels, resulting in a channel spacing of 9.77 MHz.

Each galaxy was observed using position switching mode, with 5 minutes in the off-position forward of the target by $80'$ in right ascension, followed by 5 minutes on-target. A noise diode is used to convert the observations to temperature units. The noise diode flashed on and off in intervals of 10 seconds which gave each 10 minute scan 60 subscans.

The data were reduced and analyzed in the Interactive Data Language (IDL). Every subscan was inspected for radio frequency interference (RFI). Each affected subscan was flagged and discarded. The scan spectra were converted from voltage to temperature values through the calibration of the flashing noise diode. For these measured voltages:

$$\begin{aligned} P_{sig}(l, m, p, \nu) &= \frac{P_{sig}^{on}(l, m, p, \nu) + P_{sig}^{off}(l, m, p, \nu)}{2} \\ P_{ref}(l, m, p, \nu) &= \frac{P_{ref}^{on}(l, m, p, \nu) + P_{ref}^{off}(l, m, p, \nu)}{2} \end{aligned} \quad (5.1)$$

where P_{sig}^{on} is the power with the noise diode on when the telescope is pointed on the source,

P_{sig}^{off} is the power with the noise diode off when the telescope is pointed on the source,

P_{ref}^{on} is the power with the noise diode on when the telescope is pointed off the source,

P_{ref}^{off} is the power with the noise diode off when the telescope is pointed off the source,

and l is the subscan, m is the major scan, p is the polarization, and ν is the frequency channel.

The measured temperature spectrum of the noise diode, T_{cal} , the system temperature, T_{sys} , for each subscan is:

$$T_{sys}(l, m, p) = \langle T_{cal}(p, \nu) \rangle_{\Delta\nu} \left\langle \frac{P_{ref}(l, m, p, \nu)}{P_{ref}^{on}(l, m, p, \nu) - P_{ref}^{off}(l, m, p, \nu)} \right\rangle_{\Delta\nu} \quad (5.2)$$

the errors of which are

$$\delta T_{sys}^2 = (f \delta \langle T_{cal} \rangle_{\Delta\nu})^2 + (\langle T_{cal} \rangle_{\Delta\nu} \delta f)^2 \quad (5.3)$$

where $f = \left\langle \frac{P_{ref}}{P_{ref}^{on} - P_{ref}^{off}} \right\rangle_{\Delta\nu}$, and δf and $\delta \langle T_{cal} \rangle_{\Delta\nu}$ are the errors due to the scatter about their mean values. The observed temperature of the source and its error, T_{src}^{obs} and δT_{src}^{obs} , corrected for telescope elevation and atmospheric opacity is

$$T_{src}^{obs}(l, m, p, \nu) = T_{sys}(l, m, p) \left[\frac{P_{sig}(l, m, p, \nu) - P_{ref}(l, m, p, \nu)}{P_{ref}(l, m, p, \nu)} \right] e^{\tau(m)A(m)} \\ (\delta T_{src}^{obs})^2 = \left[\frac{P_{sig} - P_{ref}}{P_{ref}} \right]^2 (e^{\tau A} \delta T_{sys})^2 + (A T_{src}^{obs} \delta \tau^2)^2 \quad (5.4)$$

where $A = 1/\sin(elevation)$ and τ is the opacity of the atmosphere at the mean frequency (in GHz) of each major scan with error, $\delta\tau$, derived from the spread in frequency about the mean per scan. The opacity is expressed as the sum:

$$\tau(m) = \sum_{i=0}^5 a_i < \nu(m) >^i. \quad (5.5)$$

where the indices are $a_i = [0.01061, -1.1434 \times 10^{-5}, 4.39 \times 10^{-4}, -2.727 \times 10^{-5}, 7.628 \times 10^{-7}, -8.0153 \times 10^{-9}]$. An average source temperature spectrum per target, g (consists of $l \times m$ subscans), is derived via a T_{sys} -weighted mean of the individual T_{src}^{obs} spectra.

$$T_{src}^{av}(g, p, \nu) = \frac{\sum T_{src}^{obs}(l, m, p, \nu) / T_{sys}^2(l, m, p)}{\sum 1 / T_{sys}^2(l, m, p)} \quad (5.6)$$

the errors of which are

$$\delta T_{src}^{av} = \left(\frac{1}{\sum (1/T_{sys}^2)} \right)^2 \left[\sum \left(\frac{\delta T_{src}^{obs}}{T_{sys}^2} \right)^2 + \sum \left(2 \frac{\delta T_{sys}}{T_{sys}^3} \right)^2 (T_{src}^{av} - T_{src}^{obs})^2 \right] \quad (5.7)$$

A final set of T_{src} spectra are calculated by removing a baseline, T_{bl} , from the T_{src}^{av} spectra for each of the target galaxies. The best-fitting polynomial curve of order 2 is found over regions chosen to be free of spectral lines, ground-based RFI, and edge-noise. The fit is weighted by the errors, δT_{src}^{av} , which are added in quadrature to the fit scatter errors, δT_{bl} , to get the errors in the final spectra, δT_{src} .

$$T_{src}(g, p, \nu) = T_{src}^{av}(g, p, \nu) - T_{bl}(g, p, \nu) \quad (5.8)$$

$$(\delta T_{src})^2 = (\delta T_{src}^{av})^2 + \delta T_{bl}^2$$

The spectrum of the standard source, 3C295, is well fit by the following polynomial expression (Baars et al. 1977):

$$\log(S_{3c295}(\nu)) = \sum_{i=0}^3 a_i (\log(\nu))^i \quad (5.9)$$

where the indices are $a_i = [1.46744, -0.77350, -0.25912, 0.00752]$ and which is used to

convert from antenna temperatures to flux density units (Jy). The telescope gain and its error, $\Gamma(\text{K/Jy})$ and $\delta \Gamma$, is calculated via the ratio of the averaged source temperature $T_{3c295}^{av}(\text{K})$ (which has not been baselined) to the known flux $S_{3c295}(\text{Jy})$:

$$\begin{aligned}\Gamma_{3c295}(p, \nu) &= \frac{T_{3c295}^{av}(p, \nu)}{S_{3c295}(\nu)} \\ \delta \Gamma_{3c295} &= \frac{\delta T_{3c295}^{av}}{S_{3c295}}.\end{aligned}\quad (5.10)$$

Each galaxy's baselined and corrected temperature spectra is converted to flux density, $S_{Gal}(\text{Jy})$, via the gain averaged over the 10MHz bandwidth $\Delta\nu_{Gal}$ centered on the galaxy's observed frequency

$$S_{Gal}(p, \nu) = \frac{T_{Gal}(p, \nu)}{\langle \Gamma(p) \rangle |_{\Delta\nu_{Gal}}} \quad (5.11)$$

with errors

$$(\delta S_{Gal})^2 = \frac{(\delta T_{Gal})^2 + (S_{Gal} \delta \langle \Gamma \rangle |_{\Delta\nu_{Gal}})^2}{(\langle \Gamma(p) \rangle |_{\Delta\nu_{Gal}})^2}. \quad (5.12)$$

The spectra from both polarizations are averaged, their errors combined, and their frequency ranges are converted to optical velocities $v(\text{km/s}) = c(\frac{\nu_o}{\nu} - 1)$ where $\nu_o = 1.4204058\text{GHz}$ and $c=299792.458\text{km/s}$. The spectra and their errors are hanning smoothed twice

$$\begin{aligned}S'_i &= \frac{1}{4}S_{2i-1} + \frac{2}{4}S_{2i} + \frac{1}{4}S_{2i+1} \\ S''_j &= \frac{1}{4}S'_{2j-1} + \frac{2}{4}S'_{2j} + \frac{1}{4}S'_{2j+1}\end{aligned}$$

$$\begin{aligned}
(\delta S'_i)^2 &= \left(\frac{1}{4}\delta S_{2i-1}\right)^2 + \left(\frac{2}{4}\delta S_{2i}\right)^2 + \left(\frac{1}{4}\delta S_{2i+1}\right)^2 \\
(\delta S''_j)^2 &= \left(\frac{1}{4}\delta S'_{2j-1}\right)^2 + \left(\frac{2}{4}\delta S'_{2j}\right)^2 + \left(\frac{1}{4}\delta S'_{2j+1}\right)^2 .
\end{aligned} \tag{5.13}$$

An upper limit in total flux, F_{ul} (Jy km s⁻¹), is calculated for the targets with no detected emission from the scatter in the spectra, δS (Jy) for an assumed standard velocity width, $\Delta v = 300$ (km/s)

$$F_{ul} = 3 \delta S \Delta v . \tag{5.14}$$

The spectra containing emission are fitted with multiple gaussians, 2 to 4 each to reproduce each peak. Fits are not improved by using Voigt profiles. These fits are used to find the velocity channels at which the gaussian curves drop to 10% of their maximum fluxes. For each galaxy and unique emission line, the observed fluxes are numerically integrated to get total fluxes, F_{tot} (Jy km s⁻¹), and their errors:

$$\begin{aligned}
F_{tot} &= \Sigma (S_i * \Delta v_i) \\
(\delta F_{tot})^2 &= \Sigma (\delta S_i * \Delta v_i)^2
\end{aligned} \tag{5.15}$$

where $\Delta v_i = \frac{v_{i+1} - v_{i-1}}{2}$ (km/s) over the channels i .

The beam size of the GBT is large (8'8 FWHM) relative to the galaxies, which is beneficial for detecting HI outside their stellar bodies, but may also result in the detection of nearby gaseous galaxies. Published HI fluxes were collected from catalogues, databases, and the literature for the target and neighboring galaxies within 10' and with velocities within the observed passband. All data from telescopes with beams of similar size and shape were considered for comparison. Estimates of the

total detectable fluxes from the neighboring galaxies, F_{nb} were made by scaling their published fluxes and their errors by the efficiency of the GBT beam $\eta(r)$ at their relative location r within the beam:

$$\begin{aligned} F_{nb}^d &= \eta(r) F_{nb}. \\ \delta F_{nb}^d &= \eta(r) \delta F_{nb} \end{aligned} \quad (5.16)$$

The detected fluxes from neighboring galaxies are totaled and subtracted from those of the target galaxies to get a residual total flux with errors combined in quadrature from all sources.

$$\begin{aligned} F_{gal}^{res} &= F_{gal} - \Sigma \eta(r) F_{nb}. \\ (\delta F_{nb}^{res})^2 &= (\delta F_{gal})^2 + \Sigma (\eta(r) \delta F_{nb})^2 \end{aligned} \quad (5.17)$$

The integrated fluxes, residual fluxes, their respective errors, and upper limits can be converted to estimates of their respective HI masses (Roberts 1962). The distances, D (Mpc), are calculated from the surface brightness fluctuations (Tonry et al. 2001) of the galaxies. The distance errors typically contribute $\sim 99\%$ of the mass estimate errors.

$$\begin{aligned} M_{HI}(M_{\odot}) &= 2.356 \times 10^5 D^2 F_{tot} \\ (\delta M_{HI}(M_{\odot}))^2 &= (2.356 \times 10^5 D)^2 [(2 F_{tot} \delta D)^2 + (D \delta F_{tot})^2] \\ M_{HI}^{ul}(M_{\odot}) &= 2.356 \times 10^5 D^2 F_{ul}. \end{aligned} \quad (5.18)$$

5.4 Results

The sample contained 36 galaxies with a breakup of 17 with ALPs and 19 without. The spectra of 4 galaxies were dominated by intracluster continuum radiation. Seven spectra showed HI emission lines. Figures 5.1.a-g present the large-scale fields around each of the galaxies for which HI emission is detected and the corresponding spectra of the detected emission lines. Two of the HI emission galaxies have ALPs, 5 do not. Detected integrated hydrogen fluxes ranged from $0.87 \pm .02 \text{ Jy km s}^{-1}$ to $14.78 \pm .04 \text{ Jy km s}^{-1}$. All non-detections have either new or improved upper limit flux measurements which range from $0.05 \text{ Jy km s}^{-1}$ to $0.21 \text{ Jy km s}^{-1}$ where 1.4GHz continuum radiation does not compromise the HI line measurements.

The upper limits and integrated measurements of the HI fluxes and masses Table 5.2. The comparisons to expected contributions by neighboring galaxies are summarized in Table 5.3. Residual HI masses and related properties that may be attributable to the target galaxies are presented in Table 5.4.

The Virgo Cluster is known to be deficient in neutral hydrogen gas, and we verify that here. No Virgo Cluster galaxies of the current sample have detectable HI emission lines. That aside, the fraction of ellipticals (versus S0 galaxies) and the fraction of ALPs (versus non-ALPs, with the dwarf ETGs excluded) are the same within and outside of Virgo at 64% and 40%, respectively.

The HI in four of the galaxies with emission lines may actually be associated with the target galaxies, one of which, NGC 3384, is an ALP. Thus, 25% of the HI galaxies is an ALP. Of the ALP and non-ALP (non-Virgo) galaxies, 12% and 27%, respectively, have HI, with an average of 21% for the total (non-Virgo) sample. None of the galaxies have cold dust disks, per the sample definition criteria, therefore, the observed HI is most likely outside their main stellar bodies in clumps or streams of

gas. All the galaxies with observed HI are in fairly tight groups, suggesting that some kind of interactions have occurred, regardless of the presence of an ALP.

5.4.1 Individual Galaxies

NGC 2634 and 2636. All the past observations for these two galaxies and their neighbors came from the former 91m Green Bank Telescope. The detected flux in the beam centered on NGC 2634 can be attributed to its two neighbors, NGC 2634A and NGC2633, whose individual emissions cannot be separated. The large error bars on the past measurements make a relevant comparison difficult. The flux in NGC 2636's beam is dominated by IC2389. The residual emission could be due to differences in systematics or data reduction methods. All galaxies in this group have $D_{25} \ll FWHM_{G91,GBT}$.

NGC 2778 is part of a tight group (LGG 171) of galaxies with a range of heliocentric velocities from 1979km/s to 2105km/s which are all contained within the emission line region of the HI spectra. NGC 2778 and its nearest neighbor, NGC 2779 have never been observed in HI previously but the next two, NGC 2780 and UGC 4834 have been observed with Arecibo. There is significant residual flux and even though $D_{25} \ll FWHM_A$ for all 4 galaxies, quite possibly there is additional intra-group gas that wasn't previously detected with Arecibo's small beam.

NGC 3193 is in the Leo III group (LGG 194) and the heliocentric velocities and spreads of all the nearby members are contained within the emission line region of NGC 3193's HI spectrum. This group has been well mapped by Williams et al. (1991) with VLA and the target and its 3 nearby neighbors have all been observed multiply at several different single-dish telescopes. Again, significant residual HI is detected with the GBT. The HI maps by Williams et al. (1991) do show low level clumps

that may be linking tails between the galaxies but GBT's baseline has less noise than VLA's and quite likely, more intergalactic HI gas is being detected here. If it is spread out over 5 or more VLA beams, it would not have been previously detected.

NGC 3377 and NGC 3384 are part of the Leo I Group (LGG 217). The emission feature in NGC 3377's spectrum is very neatly attributable to its neighbor, NGC 3377A, which was previously observed with several different single-dish telescopes.

NGC 3384 is at the center of a ring of HI (the Leo Ring) with NGC 3379 which has been extensively mapped with both VLA and Arecibo as well as observed with single points with several other telescopes. The larger emission feature at higher velocity is attributable to the background interacting group dominated by NGC 3389. The most reliable previous measurements come from VLA mapping (Hoffman et al. 2003). Only half the gas from the bodies of the two dominant galaxies accounts for the mass currently detected, though. The GBT spectrum is clearly a blend of their HI as well as with that of the plume of gas that stretches between them, some of which can be seen in the VLA maps. The GBT observation is 10 times more sensitive than the VLA observations and is most likely detecting much more of that group's diffuse intergalactic HI gas. The lower velocity line is more likely related to NGC 3384 and the Leo Ring, although, in all the Arecibo maps (Schneider 1989) the ring stops short of NGC 3384 and the central velocity of this emission feature, 653km/s, is much less than the lower range of the ring at about 880km/s. Once again, however, the GBT observation is over 10 times more sensitive than the Arecibo observations and the total flux from this feature is below the previous lowest upper limit of NGC 3384. Possibly, the source of this HI is a decelerating continuance of the spur of HI that points to NGC 3384 and may actually connect the galaxy directly to the ring.

NGC 5576 is also in a tight group (LGG 379). The heliocentric velocities of all

members fall within the HI emission feature. One member, NGC 5577, is estimated to contribute roughly half of our detected flux. The best past detection of NGC 5576 was $0.3 \pm 0.4 \text{ Jy km s}^{-1}$ with Arecibo (Lake & Schommer 1984), which is significantly less than the $1.19 \pm 0.17 \text{ Jy km s}^{-1}$ residual flux calculated here. The most likely scenario is that a substantial fraction of the HI is in between the galaxies in this group. The only mapping of the group, which was performed with Arecibo, was 10 times less sensitive than this observation (Haynes 1981).

5.4.2 Conclusions

In the scenario where gaseous disks merge to form ETGs, the merger remnants evolve from star-forming spheroids (SF-ETGs) to ETGs with mixed young and old stellar populations (K+A ETGs) to dynamically-disturbed ETGs with mostly old-looking stellar populations (fine structure, FS-ETGs) before settling into the typical, dynamically-relaxed ETGs with mostly old stellar populations (Es and S0s). In Table 5.5, we summarize global neutral hydrogen gas and dust properties of a range of ETG samples and spirals.

The typical HI detection rate results from surveys of the general population of ETGs are lower than that which we find here at about 5% in pure ellipticals, 20% for S0s, and an average of about 15% for all ETGs (Gallagher et al. 1975; Bregman et al. 1992). Despite sensitivity improvements in the radio telescopes ($T_{sys} \sim \text{few} \times 10\text{K}$ down to $T_{sys} \sim \text{few K}$) and significant increases in sample sizes ($N_{ETG} \sim \text{few}$ to $N_{ETG} \sim \text{few} \times 100$) since the 1970s, the detection rates have mostly been re-confirmed by subsequent surveys rather than changed. One notable exception is the recent mapping survey of Morganti et al. (2006), which finds HI emission associated with 8 or 9 out of 12 ($\sim 70\%$) field ETGs. This high rate is due in part to the deep

integrations (12-48 hours per galaxy) but is also likely due to the ability to associate a low signal feature in the images to a specific target. Quantities of detected HI of all surveyed ETGs as well as spirals range from a few $\times 10^6 M_\odot$ to $\sim 10^{10} M_\odot$ and the upper limits of observations extend by about an order of magnitude on either side of the detected range. It was readily recognized, in the late 1970s to early 1980s, that the dynamically cooler ETGs (E5-7, E/S0s, S0s) are far more likely to contain HI than their larger and pressure-dominated counterparts (Gallagher et al. 1975; Biegging & Biermann 1977; Davis & Seaquist 1983; Lake & Schommer 1984). This, and the possibility that ETGs formed from the merging of gaseous disks led further researchers to survey specific subsamples of ETGs for HI. The frequency of HI detection increases with the ETG type: fine structure (FS), IRAS dust-selected, K+A and star-forming (SF) ETGs (Schiminovich et al. 1994, 1995; Huchtmeier et al. 1995; Sansom et al. 2000; Balcells et al. 2001; Hibbard & Sansom 2003; Helmboldt 2007).

The “gas richness” of an ETG is only properly understood when a galaxy’s gas content is normalized by its total mass, or as a proxy, blue luminosity ($\Gamma_{HI} = M_{HI}/L_B$). The average gas-to-light of spirals, $\log(\Gamma_{HI,Sp}) \sim -.3$ (Haynes & Giovanelli 1984), is much higher than that of most ETGs at $\log(\Gamma_{HI,ETG}) \sim -3$ (Bregman et al. 1992). Our sample’s average gas richness is in between at $\log(\Gamma_{HI,Res}) \sim -1.7$ and is most similar to that detected in Fine Structure galaxies at $\log(\Gamma_{HI,FS}) \sim -1.4$ (Sansom et al. 2000). IRAS-selected (and, therefore, dust-rich), K+A and star-forming ETGs are all very gas-rich relative to the general population and our sample at ~ -1.0 , ~ -0.2 , and ~ -0.4 , respectively (Huchtmeier et al. 1995; Helmboldt 2007).

It is expected that the current sample of non-ALP ETGs (AGN-free, dust-weak, and observed with HST) would display characteristics in the form of HI detection rate and gas-richness that would indicate they are among the most evolved of the ETGs.

However, they dominate the HI results (3 of 4) and the total current sample appears to fall between the general population of ETGs and the FS-ETGs. The dust-(IRAS-)selected ETGs (Huchtmeier et al. 1995) are less evolved as expected, falling between the FS- and the SF-ETGs.

Dust content is often correlated with neutral HI content in spirals, however, this is only true for ETGs if the dust content is inferred from the infrared fluxes, rather than from features detectable in the optical (Bregman et al. 1992). Dust has been detected in 25-45% of ellipticals and 50-80% of S0s (Bregman et al. 1992; Tran et al. 2001; Temi et al. 2004). The quantities of dust detected in ETGs ranges from $10^4 M_\odot$ to $10^8 M_\odot$. Despite selecting against strong dust features (disks and center-obscuring filaments), the IRAS fluxes available for the current sample of ETGs indicate higher than expected average dust richness, $\Gamma_D = M_D/L_B$. The detection rate of dust is similar to those of the general population of ellipticals, but the mean dust-richness of the total sample, again, indicates that these galaxies are less evolved than the general population of ETGs. The dust-to-gas mass ratio is fairly constant across all the types where the value has been measured at about $D_G = M_D/M_{HI} \sim 10^{-3}$ (Young et al. 1989; Bregman et al. 1992).

The lack of dust disks suggests that the HI accumulations detected here are not in the form of coldly rotating disks about their host galaxy cores, but are rather in the form of filaments, clumps, or other taxonomically defined accumulations. Any gas about the cores would strongly prefer a cold disk distribution, thus, the HI accumulations detected here are far more likely located outside their host galaxies' main stellar bodies and may be part of the intragroup gas. The HI Rogues' gallery displays a variety of such HI morphologies associated with ETGs. The vast majority of our targeted galaxies are in groups and several studies claim to find HI deficiencies in many clusters

and groups of galaxies (Helou et al. 1981; Verdes-Montenegro et al. 2001; Springob et al. 2005), which may explain our low detection rate. However, the HI deficiency of a single ETG is a highly dubious estimate (Haynes & Giovanelli 1984) and that of a group of galaxies with a significant fraction of ETGs is suspect as well. That said, Verdes-Montenegro et al. (2001) surveyed a sample of Hickson Compact Groups (HCGs) and find a range of gas-richness and group HI deficiency. They conclude that there may be an evolutionary sequence of HI content or richness which begins at early assembly with gas-rich galaxies where the gas is within the bodies and disks of the individual members. As interactions progress, the HI is tidally stripped away from the galaxy bodies into tidal or envelope structures before it is ionized and is no longer observable as HI. Deep HI maps centered on our target galaxies are necessary to further identify whether the HI is gravitationally bound to our targets galaxies, is in intragroup structures, or is previously undetected gas associated with neighboring galaxies. It is also noteworthy that only two of our sample galaxies are members of compact groups, NGCs 3193 and 5576 in HCG 44 and LGG 379 (Hickson et al. 1989; Garcia 1995), respectively, and that we detect residual HI in both.

Table 5.1. Basic Data of Sample

Name	RA(J2000)	Dec(J2000)	Morph	Group	ALP	B (Mag)	M_B (Mag)	D (Mpc)	v_{hel} (km/s)	σ (km/s)
(1)	(2)	(3)	(4)	(5)	(6)	(7)	(8)	(9)	(10)	(11)
N1331	03h26m28.3s	-21d21m20s	E2	097 Fornax	x	14.4	-16.6	22.9 ± 3.9	1306	...
N1426	03h42m49.1s	-22d06m30s	E4	097 Eridanus	x	12.7	-18.5	24.1 ± 2.0	1413	144
N2549	08h18m58.3s	57d48m11s	SA(r)	Field	x	12.1	-19.2	12.6 ± 1.6	1062	146
N2634	08h48m25.4s	73d58m02s	E1	160	x	13.1	-19.7	33.4 ± 10.5	2281	181
N2636	08h48m24.4s	73d40m16s	E0	160:		14.7	-17.7	33.4 ± 10.5	1896	85
N2778	09h12m24.4s	35d01m39s	E	171		13.5	-19.0	22.9 ± 3.2	2044	169
N3115	10h05m14.0s	-07d43m07s	S0-	NGC 3115 Group	x	10.1	-19.5	9.7 ± 0.40	658	266
N3193	10h18m24.9s	21d53m38s	E2	194 Leo III		12.0	-19.6	34.0 ± 2.8	1362	205
N3377	10h47m42.4s	13d59m08s	E5-6	217 Leo I		11.1	-19.0	11.2 ± 0.47	661	156
N3384	10h48m16.9s	12d37m46s	SB(s)0-	217 Leo II	x	10.8	-19.9	11.6 ± 0.75	704	148
N3599	11h15m26.9s	18d06m37s	SA0	Leo II	x	12.9	-17.6	20.3 ± 1.7	806	80
N3605	11h16m46.6s	18d01m02s	E4-5	Leo II		13.2	-16.9	20.7 ± 2.8	661	120
N3608	11h16m58.9s	18d08m55s	E2	237 Leo II		11.7	-19.5	22.9 ± 1.5	1116	204
N3613	11h18m36.1s	58d00m00s	E6	232		11.8	-20.7	29.1 ± 5.4	2005	210
N3640	11h21m06.8s	03d14m05s	E3	333 Leo II		11.3	-20.1	27.0 ± 1.6	1307	176
N4239	12h17m14.9s	16d31m53s	E	292 Virgo	x	13.7	-17.2	17.0 ± 0.23	937	92
N4291	12h20m17.7s	75d22m15s	E3	284 NGC 4386 group		12.4	-19.9	26.2 ± 3.9	1767	259

Table 5.1—Continued

Name	RA(J2000)	Dec(J2000)	Morph	Group	ALP	B (Mag)	M_B (Mag)	D (Mpc)	v_{hel} (km/s)	σ (km/s)
(1)	(2)	(3)	(4)	(5)	(6)	(7)	(8)	(9)	(10)	(11)
N4365	12h24m28.2s	07d19m03s	E3	289 Virgo		10.6	-20.7	20.4 ± 1.6	1236	248
N4387	12h25m41.7s	12d48m37s	E5	292 Virgo	x	12.9	-16.9	21.4 ± 7.2	550	117
N4417	12h26m50.6s	09d35m03s	SB0sp	292 Virgo	x	12.0	-18.6	17.0 ± 0.23	842	...
N4434	12h27m36.7s	08d09m16s	E0/S0	292 Virgo		13.0	-18.1	26.8 ± 2.1	1073	117
N4458	12h28m57.5s	13d14m31s	E0-1	292 Virgo		13.0	-17.2	17.2 ± 0.95	675	119
N4464	12h29m21.3s	08d09m24s	E3	289 Virgo		13.5	-17.9	17.0 ± 0.23	1270	141
N4467	12h29m30.2s	07d59m34s	E2	289 Virgo		14.9	-16.8	17.0 ± 0.23	1431	83
N4474	12h29m53.5s	14d04m07s	S0pec	289 Virgo	x	12.5	-19.4	17.0 ± 0.23	1581	149
N4478	12h30m17.4s	12d19m43s	E2	289 Virgo		12.2	-19.4	18.1 ± 2.3	1395	132
N4482	12h30m10.3s	10d46m46s	dE,N	296 Virgo	x	13.8	-18.4	17.0 ± 0.23	1837	...
N4551	12h35m38.0s	12d15m50s	E	289 Virgo	x	12.9	-18.3	17.3 ± 1.4	1146	100
N4564	12h36m27.0s	11d26m22s	E6	289 Virgo		11.9	-19.3	15.0 ± 1.2	1120	168
N4621	12h42m02.3s	11d38m49s	E5	Virgo		10.8	-18.5	18.3 ± 1.7	429	245
N5576	14h21m03.7s	03d16m16s	E3	379		12.0	-19.8	25.5 ± 1.6	1485	187
N5831	15h04m07.0s	01d13m12s	E3	393 NGC 5846 group		12.5	-19.5	27.2 ± 2.1	1660	175
N7457	23h00m59.9s	30d08m42s	SA(rs)0-	NGC 7331 group	x	12.1	-18.5	13.18 ± 0.85	766	75
V1199	12h29m35.0s	08d03m29s	E2	Virgo	x	16.2	-14.9	17.0 ± 0.23	1100	...

Table 5.1—Continued

Name	RA(J2000)	Dec(J2000)	Morph	Group	ALP	B (Mag)	M_B (Mag)	D (Mpc)	v_{hel} (km/s)	σ (km/s)
(1)	(2)	(3)	(4)	(5)	(6)	(7)	(8)	(9)	(10)	(11)
V1440	12h32m33.4s	15d24m55s	E0	Virgo	x	15.2	-14.0	17.0 ± 0.23	383	...
V1627	12h35m37.2s	12d22m55s	E0	Virgo	x	15.5	-13.0	17.0 ± 0.23	257	...

Note. — (1) Galaxy names (N-NGC, V-VCC). (2-3) Equinox 2000.0 coordinates. (4) RC3 morphology. (5) LGG group membership number and common group or cluster name: E=Eridanus; F=Fornax; G1=NGC 3115, G2=NGC 4386, G3=NGC 5846, G4=NGC 7331 groups; L1, 2, and 3=Leo I, II, and III; V=Virgo. (6) Indicates the presence of anomalous light profiles. (7) Apparent total B magnitude (LEDA). (8) Absolute total B magnitude. (9) SBF distances (Tonry et al. 2001). (10) Heliocentric velocities (LEDA). (11) Velocity dispersion (Whitmore et al (1985) and LEDA).

Table 5.2. HI Measurements and IRAS Dust property estimates.

Name	τ_{int} (min)	$F_{HI}(\delta)$ (Jy km s ⁻¹)	δ_S (mJy)	$M_{HI}(\delta)$ M_\odot	$\Gamma_{HI}(\delta)$ $M_\odot L_{B,\odot}^{-1}$	$F_{60}(\delta)$ (mJy)	$F_{100}(\delta)$ (mJy)	$T_D(\delta)$ (K)	$M_D(\delta)$ M_\odot	$\Gamma_D(\delta)$ $M_\odot L_{B,\odot}^{-1}$	$D_G(\delta)$
(1)	(2)	(3)	(4)	(5)	(6)	(7)	(8)	(9)	(10)	(11)	(12)
N1331 [†]	20	< 0.26	0.28	< 7.5	< -1.46
N1426	20	< 0.13	0.15	< 7.3	< -2.43	< 29	< 89	30	< 5.1	< -4.6	...
N2549	10	< 0.21	0.23	< 6.9	< -2.46	270(49)	330(116)	45.2(7.2)	3.77(0.39)	-5.60(0.41)	> -3.1
N2634	90	14.782(0.040)	0.083	9.59(0.27)	-0.22(0.27)	290(32)	870(146)	5.64(0.35)	440(360)	-4.16(0.45)	-3.95(0.45)
N2636	70	2.814(0.045)	0.066	8.87(0.27)	-0.30(0.27)	< 34	< 111	30	< 5.5	< -3.7	< -3.4
N2778	70	2.774(0.024)	0.075	8.54(0.12)	-0.78(0.12)	< 42	450(85)	30	5.79(0.15)	-3.53(0.19)	-2.75(0.19)
N3115	10	< 0.17	0.17	< 6.6	< -3.37	130(37)	< 101	30	< 4.4	< -5.5	...
N3193	20	5.137(0.078)	0.16	9.147(0.072)	-1.12(0.07)	< 28	< 320	30	< 6.0	< -4.3	< -3.2
N3377	10	0.872(0.024)	0.17	7.412(0.038)	-2.25(0.04)	140(46)	310(57)	35.7(5.4)	4.02(0.32)	-5.64(0.32)	-3.39(0.32)
N3384 [†]	10	1.238(0.026)	0.17	7.593(0.057)	-2.215(0.089)	< 39	400(75)	30	5.145(0.099)	-4.66(0.12)	-2.45(0.11)
N3384 [‡]	10	7.432(0.038)	0.17	8.371(0.056)	-1.437(0.089)	< 39	400(75)	30	5.145(0.099)	-4.66(0.12)	-3.23(0.11)
N3599	10	< 0.14	0.15	< 7.1	< -2.33
N3605	20	< 0.11	0.13	< 7.1	< -2.29
N3608	10	< 0.15	0.16	< 7.3	< -2.78
N3613	20	< 0.098	0.11	< 7.3	< -2.92	< 26	< 76	30	< 5.2	< -5.0	...
N3640	20	< 0.11	0.12	< 7.3	< -3.08	< 40	< 58	30	< 5.0	< -5.3	...
N4239	10	< 0.19	0.21	< 7.1	< -1.87	< 32	< 240	30	< 5.3	< -3.7	...

Table 5.2—Continued

Name (1)	τ_{int} (min) (2)	$F_{HI}(\delta)$ (Jy km s ⁻¹) (3)	δ_S (mJy) (4)	$M_{HI}(\delta)$ M_{\odot} (5)	$\Gamma_{HI}(\delta)$ $M_{\odot} L_{B,\odot}^{-1}$ (6)	$F_{60}(\delta)$ (mJy) (7)	$F_{100}(\delta)$ (mJy) (8)	$T_D(\delta)$ (K) (9)	$M_D(\delta)$ M_{\odot} (10)	$\Gamma_D(\delta)$ $M_{\odot} L_{B,\odot}^{-1}$ (11)	$D_G(\delta)$ (12)
N4291	50	< 0.073	0.081	< 7.1	< -2.81	< 30	580(44)	30	6.01(0.13)	-3.86(0.19)	> -1.1
N4365	20	< 0.096	0.11	< 7.0	< -3.41	< 45	< 116	30	< 5.1	< -5.3	...
N4387	10	< 0.15	0.17	< 7.2	< -2.29	< 53	< 158	30	< 5.3	< -4.2	...
N4417	10	< 0.12	0.13	< 6.9	< -2.76	< 44	< 106	30	< 4.9	< -4.8	...
N4434	10	< 0.13	0.15	< 7.4	< -2.30	< 45	< 138	30	< 5.4	< -4.2	...
N4458	10	< 0.16	0.18	< 7.0	< -2.22	< 34	< 126	30	< 5.0	< -4.3	...
N4464	20	< 0.10	0.12	< 6.8	< -2.21	< 31	310(75)	30	5.37(0.11)	-3.69(0.11)	> -1.5
N4467	20	< 0.094	0.10	< 6.8	< -1.69
N4474	30	< 0.081	0.090	< 6.7	< -2.72	< 48	< 80	30	< 4.8	< -4.7	...
N4478 [†]	20	< 3.6	4.0	< 8.4	< -1.19	< 43	< 66	30	< 4.8	< -4.9	...
N4482	60	< 0.054	0.060	< 6.6	< -2.37
N4551 [†]	10	< 0.76	0.84	< 7.7	< -1.59	< 38	< 137	30	< 5.0	< -4.3	...
N4564	10	< 0.17	0.19	< 6.9	< -2.64	< 61	< 168	30	< 5.0	< -4.6	...
N4621	10	< 0.13	0.14	< 7.0	< -3.20	< 51	< 83	30	< 4.9	< -5.3	...
N5576	30	1.970(0.025)	0.11	8.479(0.056)	-1.53(0.06)	90(27)	190(247)	36(19)	4.5(1.5)	-5.5(1.5)	-4(1.5)
N5831	40	< 0.062	0.069	< 7.0	< -2.83
N7457	10	< 0.17	0.19	< 6.8	< -2.56	110(42)	400(170)	29.2(6.7)	4.66(0.64)	-4.74(0.65)	> -2.2

Table 5.2—Continued

Name	τ_{int} (min)	$F_{HI}(\delta)$ (Jy km s ⁻¹)	δ_S (mJy)	$M_{HI}(\delta)$ M_\odot	$\Gamma_{HI}(\delta)$ $M_\odot L_{B,\odot}^{-1}$	$F_{60}(\delta)$ (mJy)	$F_{100}(\delta)$ (mJy)	$T_D(\delta)$ (K)	$M_D(\delta)$ M_\odot	$\Gamma_D(\delta)$ $M_\odot L_{B,\odot}^{-1}$	$D_G(\delta)$
(1)	(2)	(3)	(4)	(5)	(6)	(7)	(8)	(9)	(10)	(11)	(12)
V1199	10	< 0.14	0.16	< 7.0	< -1.00
V1440	10	< 0.14	0.16	< 7.0	< -1.40
V1627 [†]	10	< 1.5	1.7	< 8.0	< -0.25

Note. — (1) Galaxy name. (2) Total integration time in minutes. (3) Integrated HI flux. Upper limits defined as $3 \delta_S$ 300km/s. (4) Standard error of the baseline. (5) Logarithm of HI masses. (6) Logarithm of HI gas-to-light ratio, $\Gamma_{HI} = M_{HI}/L_B(M_\odot/L_{B,\odot})$. (7-8) IRAS 60 μ m(mJy) and 100 μ m(mJy) integrated fluxes (Knapp et al. 1989). (9) Dust temperature, T_D K; assumed $T_D \sim 30$ K when $F_{60\mu}$ unavailable. (10) Logarithm of Dust mass, $M_D(M_\odot)$. (11) Logarithm of Dust-to-light ratio, $\Gamma_D = M_D/L_B(M_\odot/L_{B,\odot})$. (12) Logarithm of Dust-to-gas ratio, $D_G = M_D/M_{HI,res}$.

[†] HI measurement affected by radio-loud regions.

¹ NGC 3384 HI properties of emission line at 650km/s.

² NGC 3384 HI properties of emission line at 1290km/s.

Table 5.3. Detected HI Emission Features, Integrated Fluxes and Residuals

Name	V_{HI} (km/s)	W_{20} (km/s)	F_{Gal} (Jy km s ⁻¹)	F_{Neigh} (Jy km s ⁻¹)	F_{Res} (Jy km s ⁻¹)	New Gas?
(1)	(2)	(3)	(4)	(5)	(6)	(7)
NGC 2634	2085	502	14.782 ± 0.040	20.2 ± 4.1	-5.4 ± 4.1	No
NGC 2636	2390	218	2.814 ± 0.045	2.27 ± 0.25	0.54 ± 0.25	No
NGC 2778	2067	585	2.774 ± 0.024	0.60 ± 0.14	2.18 ± 0.14	Likely Yes
NGC 3193	1326	742	5.137 ± 0.078	2.39 ± 0.27	2.75 ± 0.28	Likely Yes
NGC 3377	576	66	0.872 ± 0.024	1.018 ± 0.094	-0.146 ± 0.097	No
NGC 3384 ¹	652	224	1.238 ± 0.026	...	1.256 ± 0.027	Yes
NGC 3384 ²	1294	346	7.432 ± 0.038	3.73 ± 0.31	3.70 ± 0.32	Likely Yes
NGC 5576	1488	443	1.970 ± 0.025	0.78 ± 0.17	1.19 ± 0.17	Likely Yes

Note. — (1) Galaxy name. (2) HI line optical heliocentric radial velocity midpoint of 20% width. (3) HI line width at 20% of the peak flux. (4) Detected total flux from GBT (Jy km s⁻¹). (5) Estimated scaled flux contributions from neighboring galaxies from previously published values (Jy km s⁻¹). (6) Estimated residual flux detected with GBT (Jy km s⁻¹). (7) Qualitative likelihood that new HI was detected in association with the target galaxy.

Table 5.4. Residual HI Masses and other properties

Name	$M_{HI,Res}$ M_{\odot}	$\Gamma_{HI,Res}$ $M_{\odot}/L_{B,\odot}$	$D_{G,Res}$ $M_D/M_{HI,Res}$
(1)	(2)	(3)	(4)
NGC 2634
NGC 2636	8.16 ± 0.20	-1.01 ± 0.34	< -2.7
NGC 2778	8.430 ± 0.028	-0.89 ± 0.13	-2.64 ± 0.15
NGC 3193	8.875 ± 0.044	-1.389 ± 0.093	< -2.9
NGC 3377
NGC 3384 ¹	7.593 ± 0.057	-2.215 ± 0.089	-2.45 ± 0.45
NGC 3384 ²	8.069 ± 0.067	-1.739 ± 0.096	-2.92 ± 0.45
NGC 5576	8.261 ± 0.063	-1.751 ± 0.093	-3.8 ± 1.5

Note. — (1) Galaxy name. (2) Logarithm of Residual HI mass (M_{\odot}). (3) Logarithm of Residual gas-to-light ratio, $\Gamma_{HI,Res} = M_{HI,Res}/L_B(M_{\odot}/L_{B,\odot})$. (4) Logarithm of Dust-to-residual-gas ratio, $D_{G,Res} = M_D/M_{HI,Res}$.

Table 5.5. Typical Dust and gas quantities of galaxy samples.

Type	f_{HI}	M_{HI} Range	$< \Gamma_{HI} >$ $M_{\odot}/L_{B,\odot}$	f_D %	M_D Range M_{\odot}	$< \Gamma_D >$ $M_{\odot}/L_{B,\odot}$	$< D_G >$ M_D/M_{HI}	Sources
(1)	(2)	(3)	(4)	(5)	(6)	(7)	(8)	(9)
This work	21%	7.6 – 8.9	-1.69 ± 0.22	35	3.8 – 6.0	-4.60 ± 0.28	-2.94 ± 0.23	a
E	5%	6 – 10	-3.31 ± 0.07	25-45	4.0 – 7.5	-5.09 ± 0.11	...	b,c,d,e,f,g,h,i
S0	20%	6.8 – 9.0	-2.57 ± 0.11	50-80	3.8 – 7.5	-4.84 ± 0.07	...	b,c,d,e,f,g,h,i
FS ETGs	45%	7.3 – 9.7	-1.35 ± 0.20	j,k,l,m,n
IRAS ETGs	59%	8 – 10	-1.02 ± 0.13	100	4 – 9	-4.02 ± 0.11	-3.08 ± 0.12	o
K+A ETGs	56%	7.0 – 9.7	-0.22 ± 0.13	p
SF ETGs	75%	8.3 – 9.5	-0.43 ± 0.17	p
Spirals	100%	7 – 10.5	-0.30 ± 0.35	100	4 – 8	> -4.2	~ -3	q,r

Note. — (1) Galaxy Group Type: FS=Fine structure; IRAS=detected by IRAS; K+A=Young+Old stellar populations but not currently star-forming; SF=Star forming. (2) Fraction of sample with detected HI. (3) Logarithm of HI mass ranges detected. (4) Mean of Logarithm of Gas-to-Light ratios per population. (5) Fraction of sample with detected dust, either by IRAS fluxes or by visible disks, filaments. (6) Logarithm of Dust mass ranges detected. (7) Mean of Logarithm of Dust-to-Light ratios. (8) Mean of Logarithm of Dust-to-gas ratios.

(9) References: a: Knapp et al. (1989); b: Gallagher et al. (1975); c: Bieging & Biermann (1977); d: Davis & Seaquist (1983); e: Lake & Schommer (1984); f: Bregman et al. (1992); g: Tran et al. (2001); h: Temi et al. (2004); i: Morganti et al. (2006); j: Schiminovich et al. (1994); k: Schiminovich et al. (1995); l: Sansom et al. (2000); m: Balcells et al. (2001); n: Hibbard & Sansom (2003); o: Huchtmeier et al. (1995); p: Helmboldt (2007); q: Haynes & Giovanelli (1984); r: Young et al. (1989).

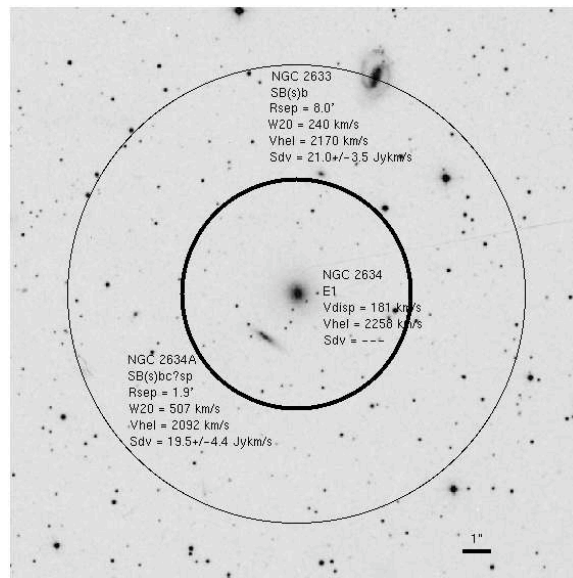


Fig. 5.1.ai.— NGC 2634 Field of View

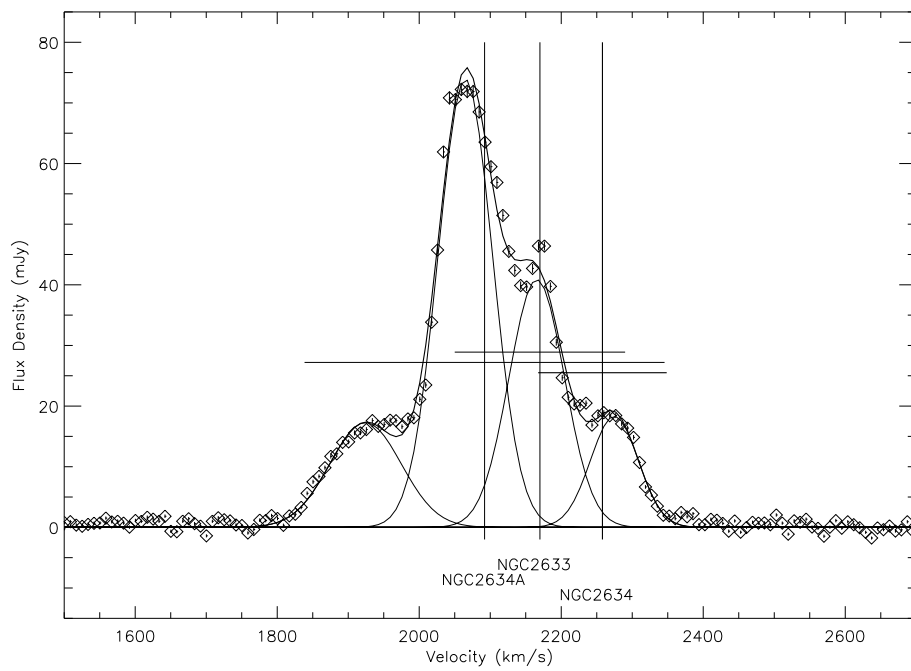


Fig. 5.1.ii.— NGC 2634 Spectrum

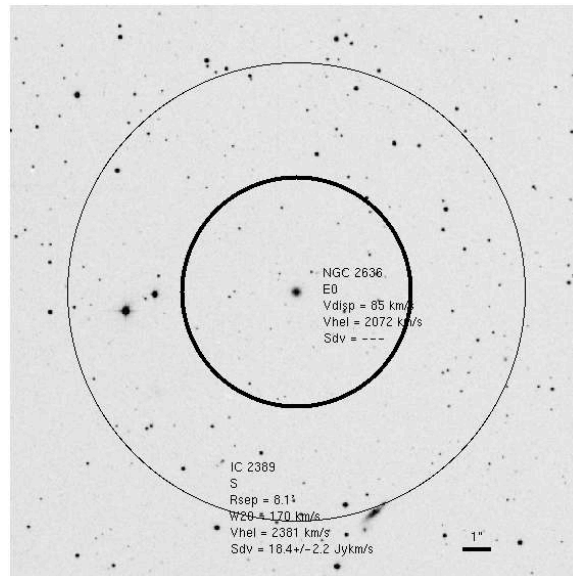


Fig. 5.1.bi.— **NGC 2636** Field of View

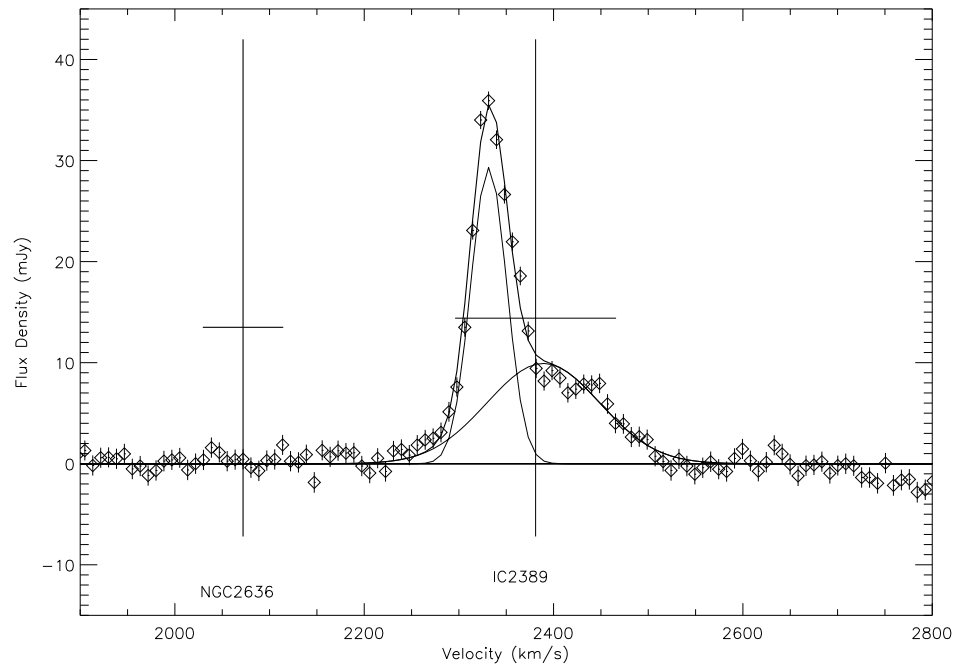


Fig. 5.1.bii.— **NGC 2636** Spectrum

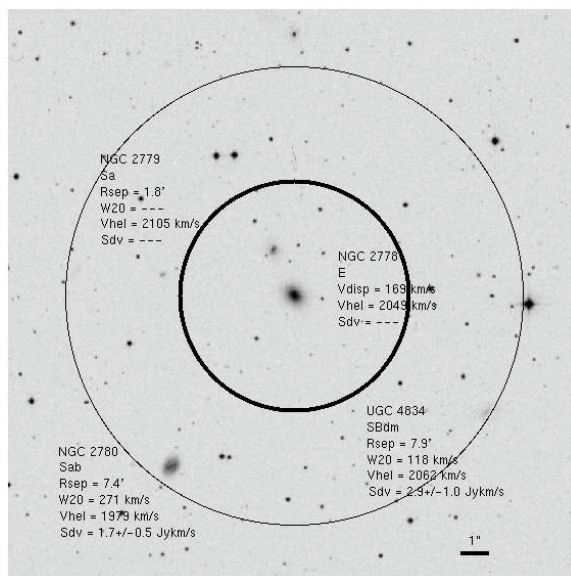


Fig. 5.1.ci.— NGC 2778 Field of View

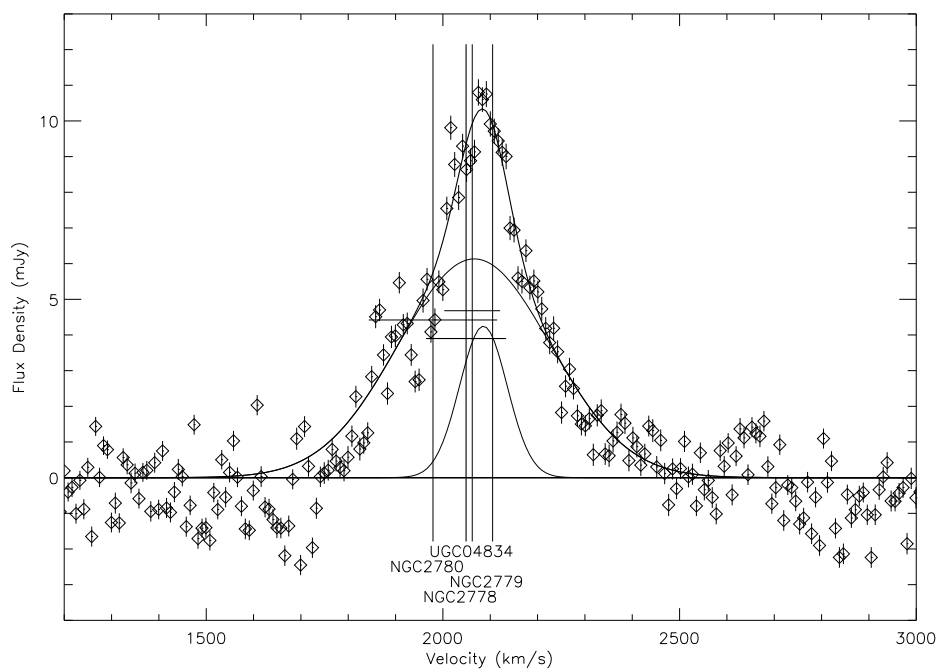


Fig. 5.1.cii.— NGC 2778 Spectrum

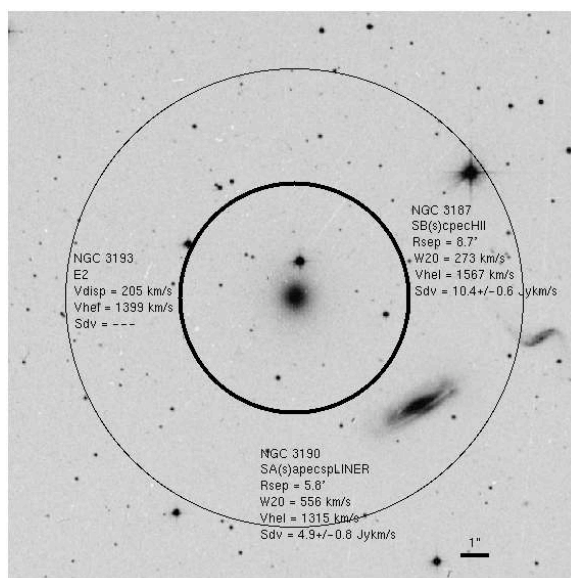


Fig. 5.1.di.— NGC 3193 Field of View

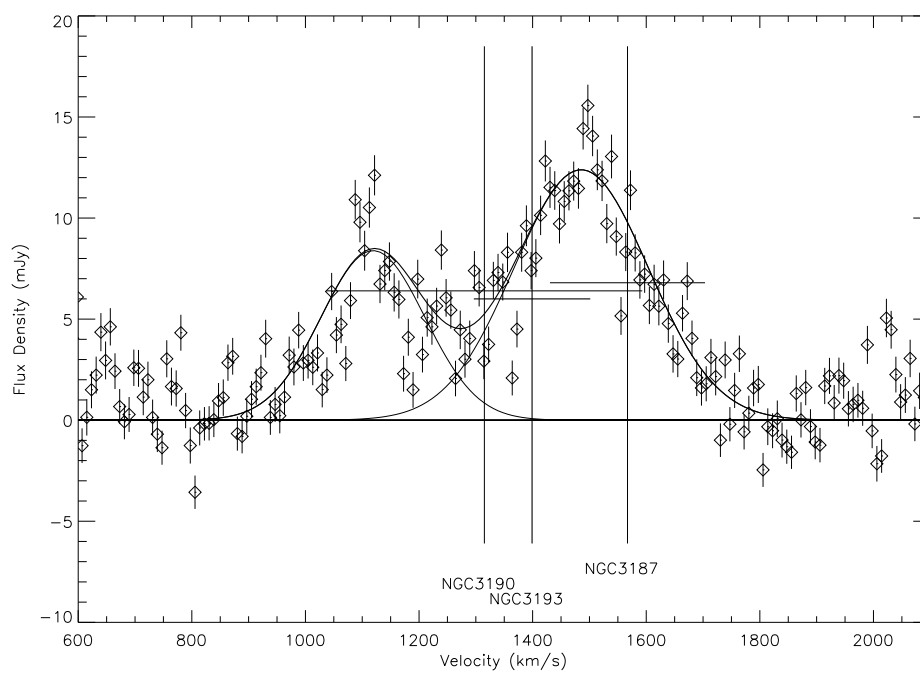


Fig. 5.1.dii.— NGC 3193 Spectrum

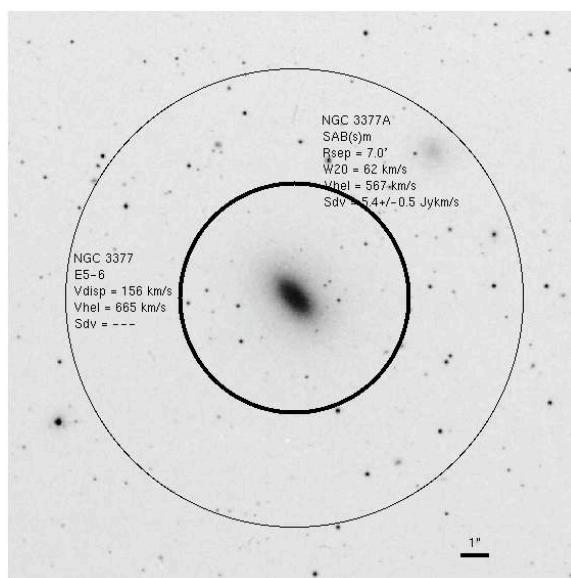


Fig. 5.1.ei.— **NGC 3377** Field of View

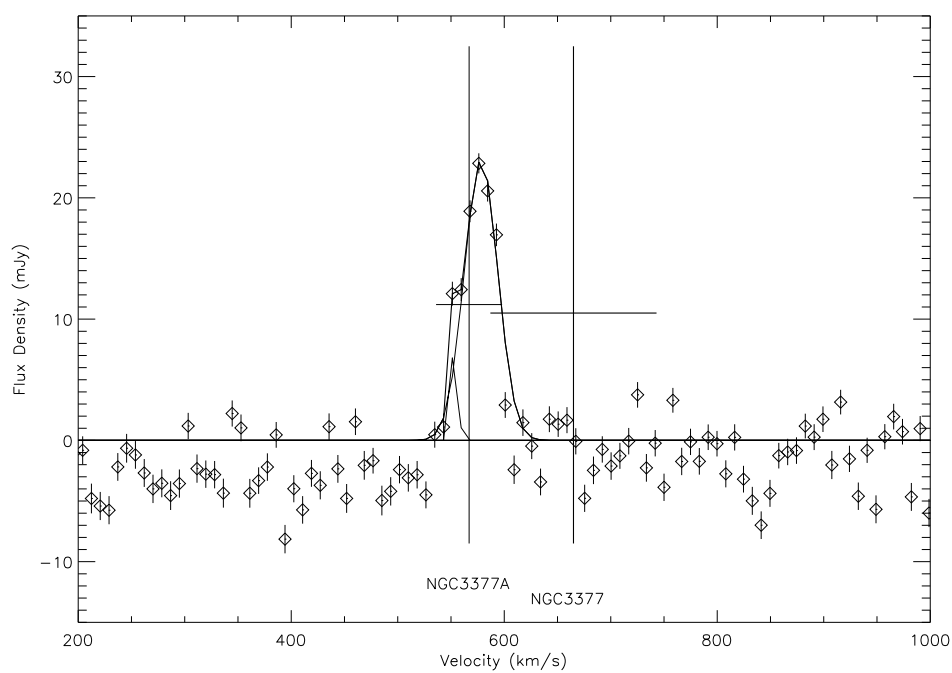


Fig. 5.1.eii.— **NGC 3377** Spectrum

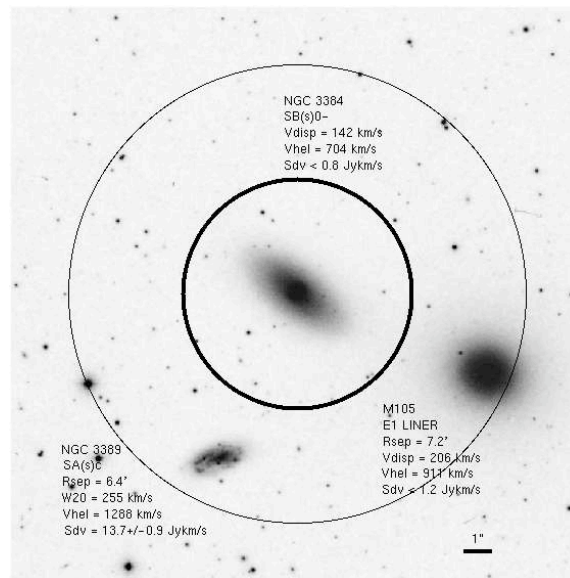


Fig. 5.1.fi.— **NGC 3384** Field of View

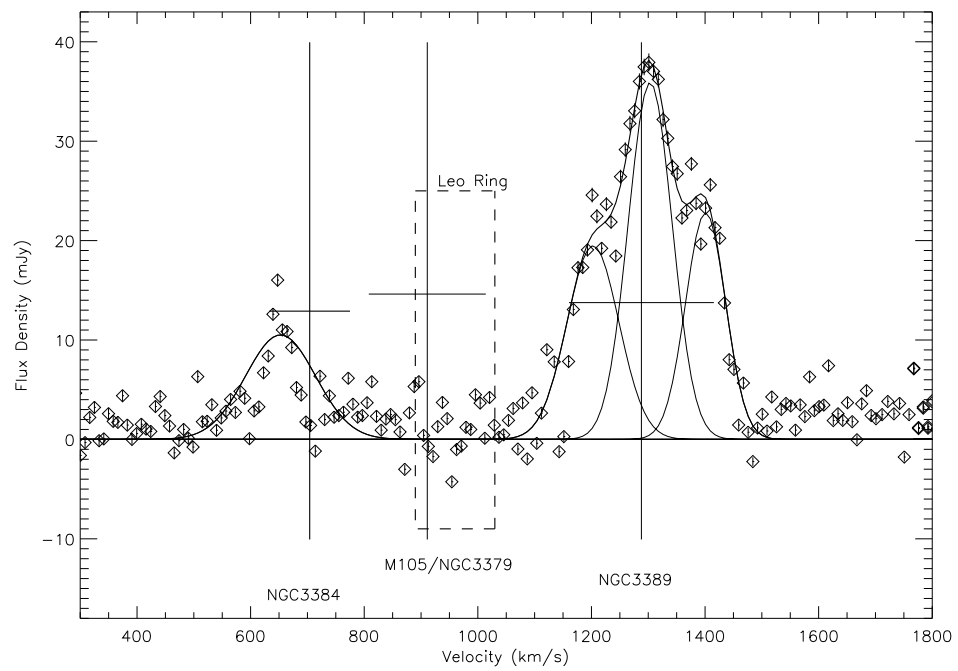


Fig. 5.1.fii.— **NGC 3384** Spectrum

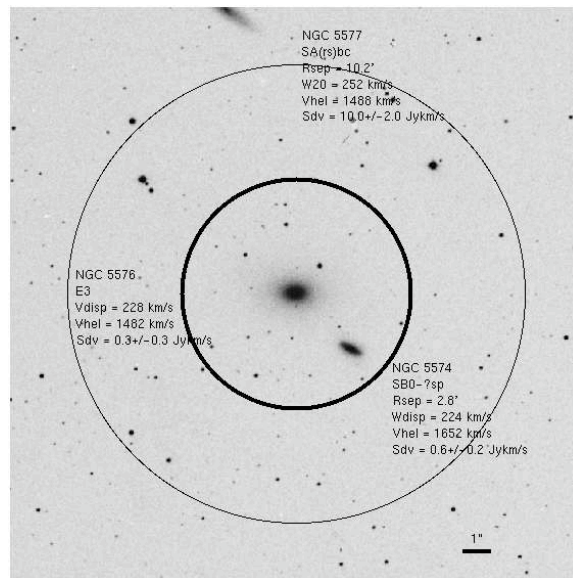


Fig. 5.1.gi.— NGC 5576 Field of View

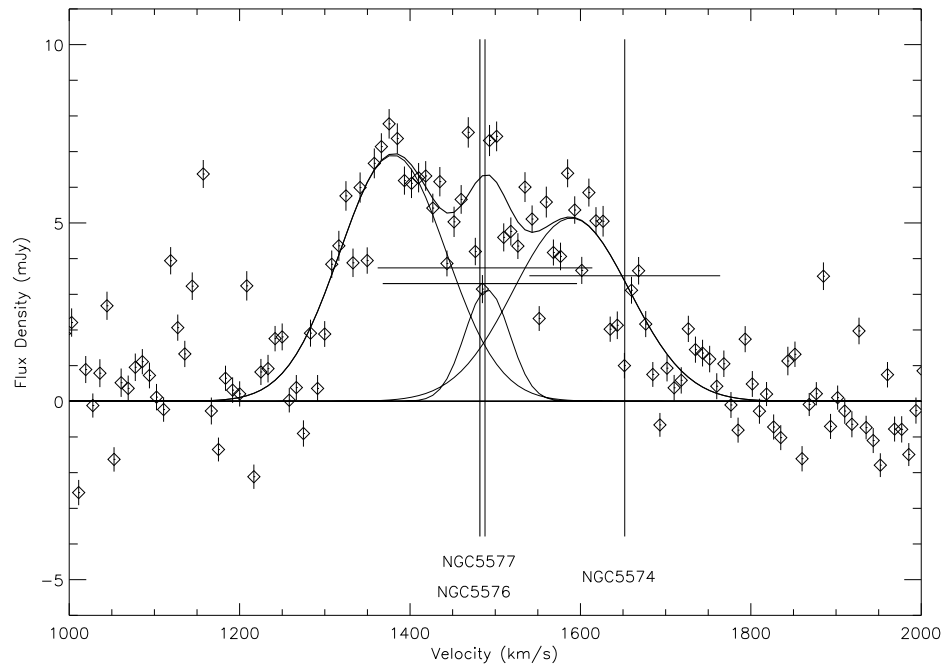


Fig. 5.1.gii.— NGC 5576 Spectrum

Chapter 6

Conclusions

The classical view of early-type galaxy (ETG) formation dictates that ellipticals and S0s formed in the early universe when the universe was very dense by the monolithic collapse of isolated protogalactic clouds (Eggen et al. 1962). A monolithic collapse causes a significant starburst event which forms all the stars in the ETG after which, the fuel is fully consumed and the stars passively evolve and fade. This view satisfied the ground-based observations which indicated that ETGs have redder colors than spiral galaxies suggesting much older average stellar populations in the ETGs. Evidence of recent as well as ongoing star formation in and additional formation methods for ETGs have been building up in recent decades and indicates that the true set of mass accumulation scenarios and star formation histories of ETGs is actually far more complex than originally thought.

High precision spectrophotometry of ETGs demonstrates that many have light-weighted mean ages above 500 Myr yet younger than 7 Gyr (e.g. Trager et al. 2000, Caldwell et al. 2003, Thomas et al. 2005, Proctor et al. 2005, Schiavon 2007, Sánchez-Blázquez et al. 2007, Trager et al. 2008, Sarzi et al. 2008). Photometric results from the near-ultraviolet spectral region (1800 - 2800 Å), which is several times more sensitive than the optical-band region to differences in population ages and abundances, also detect evidence of intermediate age populations (500 Myr to 5 Gyr) in ETGs (e.g. Ferreras & Silk 2000, Yi et al. 2005, Kaviraj et al. 2007, Schawinski et al. 2007, Kaviraj et al. 2008).

Monolithic collapse may have initiated galaxy and star formation in the universe, however, galaxies do not stay isolated from one another, original gas supplies were not necessarily depleted and gas is replenished through the returns of supernovae and stellar winds. Toomre & Toomre (1972) initiated the study of gas-rich merging galaxies as ways to form new ETGs. Modern simulations demonstrate that the

high central densities of ETGs (and not of gaseous disk galaxies) can be achieved through the dissipation of the gaseous component as it flows in toward the gravitational centers of a merging galaxy system (e.g. Mihos & Hernquist 1994b; Springel 2000; Springel & Hernquist 2005, Ferreras et al. 2002; Cox et al. 2006, Hopkins et al. 2008a). The dissipation of the gaseous component leads to star formation in centrally confined regions. Observations of coalesced merger remnants verify that they have central confined gas and ongoing star formation, that they have spatial distributions of light (and, by proxy, mass) similar to ETGs and not similar to gaseous disk galaxies (Hibbard & Yun 1999, Rothberg & Joseph 2004, Hopkins et al. 2008a). With time, these observed gaseous merger remnants should fade into morphologies which will place them into the morphological classification of ETGs.

In this thesis, we examine two samples of ETGs through very high spatial resolution studies of the surface brightnesses, colors sensitive to small admixtures of youthful stellar populations, and through a deep, neutral hydrogen gas survey to probe the recent and possible future star formation histories of these galaxies and the relative spatial distributions of older and younger populations. The two samples of ETGs are a test sample which have stellar surface brightness profiles with a central spike in light above a smoothly increasing profile and a control sample of galaxies which do not have the central light spike. The two samples were drawn from the monochrome surveys of ETGs with the Hubble Space Telescope which produced published high spatial resolution surface brightness profiles (Byun et al. 1996; Rest et al. 2001; Ravindranath et al. 2001) and from the set of ETGs with no evidence of either active galactic nuclei or dust as both features can alter the apparent distribution of stellar emission.

The first study involved photometry of twelve galaxies (six test, six control) using

the High Resolution Camera of the Advanced Camera for Surveys on the Hubble Space Telescope in the Near-Ultraviolet, the Ultraviolet, and the V bands. The high spatial resolution of $0''.027$ per pixel and the spectral sensitivity ($\langle S/N \rangle \gtrsim 10$) allow us to examine to high accuracy the spatial distribution of light in each band, the total integrated colors of the galaxies and the color changes with radius within each galaxy, and the structure and colors of the detected central components. The second study surveyed 20 test and 35 control galaxies to previously unsurpassed sensitivity ($\lim(M_{HI}) \sim 1e7 M_{\odot}$) and examined the neutral hydrogen content in the environments of ETGs.

Surface Brightness Profiles

We fit light distribution functions to the surface brightness profiles of 12 early-type galaxies which are of high spatial resolution ($\sim 0''.027$), high sensitivity ($\langle S/N \rangle_{\lambda} \sim 30, 10$, and 5 for V, U, and NUV) of the central ~ 1.5 kpc of each galaxy. The light distribution functions describe either an outer galaxy body plus a central component or just a galaxy body and the surface brightness profiles of all galaxies from all three filters are fit with both functions. We compare the fit quality results and statistically determine that a central component is not detected (relative $\chi^2_{\nu} \lesssim 2$), detected (relative $2 \lesssim \chi^2_{\nu} \lesssim 5$), or robustly detected (relative $\chi^2_{\nu} \gtrsim 5$) when results are of similar detectability or better in at least two bands.

Two central components are detected in NGC 3640 and NGC 4478 and two are robustly detected in NGC 3384, NGC 4239, NGC 4474, NGC 4482, NGC 4621, and NGC 7457. The central components are generally small with scale radii $r_c < 15$ pc and bright with absolute V-band magnitudes, M_V , ranging from -10.5 to -13.5 mag. The central components of the non-ALP galaxies, NGC 3640 and NGC 4621,

have properties which set them apart from those of the ALP galaxies. They are the two largest central components with scale radii of 15 and 8 pc, respectively. By comparison, the ALP-galaxy extended central components have scale radii which range from 1 to 3 pc. They are the two brightest central components in terms of absolute magnitudes and yet, they are fainter than those of the ALP sample galaxies compared to the surface brightness of the underlying galaxy bodies. No additional trend of central component size with brightness is observed.

All the central components detected here are much smaller than the extra light regions predicted by gaseous merger models and are possibly related to the stellar nuclei found in many galaxies across the Hubble Type spectrum. Similar central objects have been detected in normal-sized early type galaxies (Byun et al. 1996; Rest et al. 2001; Ravindranath et al. 2001; Ferrarese et al. 2006; Côté et al. 2006), however, the photometry used to detect and isolate the current set of central components has unprecedented spatial resolution and the bands were chosen for their sensitivity to the presence of multi-generational stellar populations.

Galaxy and Isophotal Colors

The $NUV - V$ and $U - V$ colors of both the total integrated light within our field of view (typically, $\lesssim 1.5$ kpc) and with each aperture of each galaxy are compared to the predicted colors of stellar populations which are of either single-generation or multiple-generation populations. The central components detected in Chapter 2 do not affect the colors of the total integrated galaxy light.

The total galaxy colors span a magnitude range of 1.1 mag in $NUV - V$ and 0.5 mag in $U - V$. Ten of the twelve data points lie well away from the color region of simple stellar populations and dual-metallicity models which indicates that they cannot

contain homogeneous stellar populations. The total galaxy colors of NGC 3377 and NGC 3384 are consistent with either single- or multi-generational stellar populations. Ten of the twelve total galaxy colors are inconsistent with metal-poor populations, three are only consistent with metal-rich populations, and seven can be well-described by either solar- or metal-rich populations. The total galaxy colors of NGC 4239 and NGC 4482 are best-described by either solar- or super-solar metallicities, however, within the estimated uncertainties of the population models, these two colors may be described by sub-solar metallicities.

The behaviors of the radial distribution of colors in the 2-color diagrams are multiform and the range of colors spanned by an individual galaxy can be significant with typical ranges of 0.5 mag in $NUV - V$ and 0.25 mag in $U - V$ though they reach up to 1.1 mag and 0.5 mag in $NUV - V$ and $U - V$ respectively. The total galaxy colors are dominated by the light from large radii which is reflected in the similarity of radial colors at large radii to the total galaxy colors. Many of the galaxies (e.g. NGC 4239, 4474, 4482, 4570, 7457) have colors at large radii which demonstrate significant population mixing as they are located in color-color space quite far from the SSP color region. The total galaxy colors of NGC 3377 and NGC 3384 are consistent with SSP colors, however, if we move inward and investigate the colors of these two galaxies at smaller radii, we see colors that indicate significant population mixtures. All told, all twelve of the sample galaxies have colors which are consistent with multi-generational populations. The behavior of the color changes with radius are diverse and do not readily fall into classes related to the presence of an ALP or to the morphological classification of the galaxies at larger scales.

B-V colors are often employed to trace changes in stellar populations in ETGs, however, the typical range of total galaxy colors in B-V span only 0.2 mag. By

using $NUV - V$ and $U - V$, we are significantly more sensitive to detecting multi-generational populations than would be possible with optical colors.

Our approach of using photometry in multiple ultraviolet bands, which are the most sensitive probes for finding multi-generational stellar populations, provides us with ample evidence indicating that ETGs are composed of multiple stellar populations and that some individual stellar populations may be distributed in unique structural components as determined through abrupt radial color transitions.

Central Component Colors

The structural and color characteristics of the eight central components detected in Chapter 2 are examined for identifying traits. The scale sizes of the central components of the current work are consistent in typical size of 2–5 pc to the central stellar components of galaxies across the Hubble Type spectrum and to the sizes of globular clusters. The range of absolute magnitudes in the V-band (-10.5 to -13.5 mag) correspond well to those of the central components in other normal-sized galaxies. The colors of two central components, in NGC 4474 and NGC 4482, are consistent with those of single-generation populations, while those of four others, NGC 3384, NGC 4239, NGC 4478, and NGC 7457, clearly require multi-generational populations to satisfy the observed colors. One central component may have either a single- or multi-generational population and one requires metallicities higher than $2.5 Z_{\odot}$. No central components have colors consistent with non-thermal emission as detected in the bands of the current work, however, analysis of x-ray emission from three galaxies, NGC 3377 (Soria et al. 2006), NGC 4621 (Wrobel et al. 2008), and NGC 7457 (Terashima et al. In Prep) may indicate low levels of activity. For two of the three, we robustly detect and resolve the stellar central components which co-exist with the

possible non-thermal source. For the third, NGC 3377, we detect a central, NUV-only point source which may be from either stars surrounding the black hole (Soria, R., *Personal Comm*) or directly related to non-thermal emission.

The photometry used in this work has exceptionally high sensitivity to changes in stellar population composition and the spatial resolution of the HRC benefits greatly the ability to robustly detect compact central components embedded in the centers of early-type galaxies which have considerably more compact mass distributions and are brighter at their centers than other Hubble Types. This work is the first to detect central components with multi-generational stellar populations. Previous studies of the nuclei of spirals need multiple generations of stellar populations to explain their observed spectral features (Rossa et al. 2006; Walcher et al. 2006).

Neutral Hydrogen Survey

Thirty-six early-type galaxies were observed in a deep HI survey with a typical mass detection limit of $10^7 M_{\odot}$ to find HI associations that could indicate recent formation via the merger of gas-rich disk galaxies. Seven spectra showed HI emission lines, four of which have significant residual HI emission after accounting for contamination by nearby gas-rich galaxies. The integrated residual hydrogen fluxes range from 1.2 to 3.7 Jy km s⁻¹. All non-detections have either new or improved upper limit flux measurements which range from 0.05 Jy km/s to 0.21 Jy km/s where 1.4 GHz continuum radiation does not compromise the HI line measurements.

None of the galaxies have cold dust disks, per the sample definition criteria, therefore, the observed HI is most likely outside their main stellar bodies in clumps or streams of gas. All the galaxies with observed HI are in fairly tight groups, suggesting that some kind of interactions have occurred.

Gaseous Merger Signatures in Early Type Galaxies

The total galaxy colors of the twelve early-type galaxies studied in the NUV photometry survey are consistent with multi-generational populations which, in a two-generation scenario have typical younger population ages of up to 3 Gyr and mass contributions of up to 20%. The specific colors detected in individual radial bins indicates that each galaxy has multiple generations of stellar populations, the significant variation of the radial colors within any one of the galaxies indicates multiple spatial structures for its stellar populations, and the significant difference in radial color distributions from one galaxy to another indicates that each galaxy has its own spatial and temporal composition of stellar populations.

The presence of multi-generational compact stellar nuclei detected in many of the ETGs suggests that either multiple groups of stellar populations or gas are able to lose enough angular momentum to fall into the gravitational centers of the galaxies. The small sizes of the detected compact stellar nuclei do not support the aggregation scenario of pre-existing stellar clusters since their infall is expected to expand the size of the congregate cluster (Bekki et al. 2004). A merger event is an opportune time for the gaseous components of a galaxy to lose angular momentum. Numerical simulations of gaseous merger events predict that the gaseous components settle into region with characteristic sizes on order of a few hundred pc in size about a remnants center, rather than only a few pc, however, additional processes may occur which the models cannot yet resolve. The colors of the compact stellar nuclei indicate that the nuclei have a disparate set of ages relative to those of their underlying galaxies. Any additional processes which can put gas into the central few parsecs of a galaxy may require a very specialized set of physical conditions and, if multiple periods of star formation occur (rather than just one or two periods), the specialized set of conditions

may be met only in a subset of the star formation periods.

The detection of HI in association with ETGs lend further support for gas-rich merger origins of some ETGs since tidal streams of HI are expected to orbit a remnant for several gigayears.

The detections in this work of multiple spatial and temporal compositions of stellar populations in early-type galaxies, multiple generation compact stellar components coincident with the centers of some early-type galaxies and the positive associations of neutral hydrogen with some early-type galaxies lends support towards the formation of some early-type galaxies through recent (0.5 to 5 Gyr ago) gas-rich processes such as the hierarchical merging of gas-rich disk galaxies.

Chapter 7

The Bibliography

References

- Anderson, J., & King, I. R. 2004, ISR ACS 2004-15
- Baars, J. W. M., Genzel, R., Pauliny-Toth, I. I. K., & Witzel, A. 1977, A&A, 61, 99
- Balcells, M., van Gorkom, J. H., Sancisi, R., & del Burgo, C. 2001, AJ, 122, 1758
- Barnes, J. E., & Hernquist, L. E. 1991, ApJ, 370, L65
- Barnes, J. E. 1992, ApJ, 393, 484
- Barnes, J. E., & Hernquist, L. 1996, ApJ, 471, 115
- Barnes, J. E. 2002, MNRAS, 333, 481
- Bekki, K., & Shioya, Y. 2001, ApJS, 134, 241
- Bekki, K., Couch, W. J., Drinkwater, M. J., & Shioya, Y. 2004, ApJ, 610, L13
- Bell, E. F., et al. 2004, ApJ, 608, 752
- Bell, E. F., et al. 2005, ApJ, 625, 23
- Bell, E. F., Zheng, X. Z., Papovich, C., Borch, A., Wolf, C., & Meisenheimer, K. 2007, ApJ, 663, 834
- Bieging, J. H., & Biermann, P. 1977, A&A, 60, 361

- Böker, T., Sarzi, M., McLaughlin, D. E., van der Marel, R. P., Rix, H.-W., Ho, L. C., & Shields, J. C. 2004, *AJ*, 127, 105
- Bournaud, F., Jog, C. J., & Combes, F. 2005, *A&A*, 437, 69
- Boylan-Kolchin, M., Ma, C.-P., & Quataert, E. 2005, *MNRAS*, 362, 184
- Bregman, J. N., Hogg, D. E., & Roberts, M. S. 1992, *ApJ*, 387, 484
- Brown, T. M., Bowers, C. W., Kimble, R. A., Sweigart, A. V., & Ferguson, H. C. 2000, *ApJ*, 532, 308
- Bruzual, G., & Charlot, S. 2003, *MNRAS*, 344, 1000
- Burkert, A., Brodie, J., & Larsen, S. 2005, *ApJ*, 628, 231
- Burstein, D., Bertola, F., Buson, L.M., Faber, S.M., & Lauer, T.R. 1988, *ApJ*, 328, 440
- Butler, D. J., & Martínez-Delgado, D. 2005, *AJ*, 129, 2217
- Byun, Y.-I., et al. 1996, *AJ*, 111, 1889
- Caon, N., Capaccioli, M., & D'Onofrio, M. 1993, *MNRAS*, 265, 1013
- Caldwell, N., Rose, J. A., & Concannon, K. D. 2003, *AJ*, 125, 2891
- Carlberg, R. G. 1984, *ApJ*, 286, 403
- Carollo, C. M., Danziger, I. J., Rich, R. M., & Chen, X. 1997, *ApJ*, 491, 545
- Carollo, C. M. 1999, *ApJ*, 523, 566
- Carollo, C. M., Stiavelli, M., Seigar, M., de Zeeuw, P. T., & Dejonghe, H. 2002, *AJ*, 123, 159

- Castellani, V., Chieffi, A., & Straniero, O. 1992, *ApJS*, 78, 517
- Chomiuk, L., Strader, J., & Brodie, J. P. 2008, *AJ*, 136, 234
- Conselice, C. J., et al. 2007, *MNRAS*, 381, 962
- Côté, P., et al. 2004, *ApJS*, 153, 223
- Côté, P., et al. 2006, *ApJS*, 165, 57
- Cox, T. J., Jonsson, Patrik, Primack, J. R., & Somerville, R. S. 2006, *MNRAS*, 373, 1013
- Davies, R. L., Sadler, E. M., & Peletier, R. F. 1993, *MNRAS*, 262, 650
- Davis, L. E., & Seaquist, E. R. 1983, *ApJS*, 53, 269
- De Lucia, G., et al. 2004, *ApJ*, 610, L77
- de Vaucouleurs, G. 1948, *Ann. d'Astrophys.*, 11, 247
- de Vaucouleurs, G. 1961, *ApJS*, 5, 233
- de Vaucouleurs, G., de Vaucouleurs, A., Corwin, H. G., Jr., Buta, R. J., Paturel, G., & Fouque, P. 1991, Volume 1-3, XII, 2069 pp. 7 figs.. Springer-Verlag Berlin Heidelberg New York
- de Vaucouleurs, G., & Pence, W. D. 1979, *ApJS*, 40, 425
- Donas, J., et al. 2007, *ApJS*, 173, 597
- Dorman, B., O'Connell, R. W., & Rood, R. T. 1995, *ApJ*, 442, 105
- Dorman, B., O'Connell, R. W., & Rood, R. T. 2003, *ApJ*, 591, 878

- Eggen, O. J., Lynden-Bell, D., & Sandage, A. R. 1962, ApJ, 136, 748
- Elson, R. A. W., Fall, S. M., & Freeman, K. C. 1989, ApJ, 336, 734
- Emsellem, E., et al. 2004, MNRAS, 352, 721
- Eracleous, M., Hwang, J., Flohic, H. 2008, In Preparation
- Faber, S. M., Wegner, G., Burstein, D., Davies, R. L., Dressler, A., Lynden-Bell, D., & Terlevich, R. J. 1989, ApJS, 69, 763
- Faber, S. M., et al. 1997, AJ, 114, 1771
- Faber, S. M., et al. 1997, AJ, 114, 1771
- Faber, S. M. et al. 2007, ApJ, 665, 265
- Fagotto, F., Bressan, A., Bertelli, G., & Chiosi, C. 1994, A&AS, 105, 29
- Ferreras, I, Scannapieco, E., & Silk, J. 2002, ApJ, 579, 247
- Ferreras, I., & Silk, J. 2000, ApJ, 541, L37
- Ferrarese, L., van den Bosch, F. C., Ford, H. C., Jaffe, W., & O'Connell, R. W. 1994, AJ, 108, 1598
- Ferrarese, L., et al. 2006, ApJS, 164, 334
- Ferrarese, L., et al. 2006, ApJ, 644, L21
- Fioc, M., & Rocca-Volmerange, B. 1997, A&A, 326, 950
- Gallagher, J. S., Faber, S. M., & Balick, B. 1975, ApJ, 202, 7
- Garcia, A. M. 1995, A&A, 297, 56

- Gebhardt, K., et al. 1996, AJ, 112, 105
- Gebhardt, K., Rich, R. M., & Ho, L. C. 2002, ApJ, 578, L41
- Gil de Paz, A., et al. 2007, ApJS, 173, 185
- Gilmore, G., Wilkinson, M. I., Wyse, R. F. G., Kleya, J. T., Koch, A., Evans, N. W.,
& Grebel, E. K. 2007, ApJ, 663, 948
- Graham, A. W., Erwin, P., Trujillo, I., & Asensio Ramos, A. 2003, AJ, 125, 2951
- Greggio, L. & Renzini, A. 1990, ApJ, 364, 35
- Gunn, J. E., 1987, in Nearly Normal Galaxies: From the Planck Time to the Present,
ed. S. M. Faber (New York: Springer), 455
- Häring, N., & Rix, H.-W. 2004, ApJ, 604, L89
- Harris, W. E. 1996, AJ, 112, 1487
- Haynes, M. P. 1981, AJ, 86, 1126
- Haynes, M. P., & Giovanelli, R. 1984, AJ, 89, 758
- Heap, S. R., et al. 1998, ApJ, 492, L131
- Helmboldt, J. F. 2007, MNRAS, 379, 1227
- Helou, G., Salpeter, E. E., Giovanardi, C., & Krumm, N. 1981, ApJS, 46, 267
- Hernandez, X., & Gilmore, G. 1998, MNRAS, 297, 517
- Hibbard, J. E., Guhathakurta, P., van Gorkom, J. H., & Schweizer, F. 1994, AJ, 107,

- Hibbard, J. E., & Yun, M. S. 1999, ApJ, 522, L93
- Hibbard, J. E., & Mihos, J. C. 1995, AJ, 110, 140
- Hibbard, J. E., & Sansom, A. E. 2003, AJ, 125, 667
- Hibbard, J. E., & Yun, M. S. 1999, ApJ, 522, L93
- Hickson, P., Kindl, E., & Auman, J. R. 1989, ApJS, 70, 687
- Ho, L. C., Filippenko, A. V., & Sargent, W. L. 1995, ApJS, 98, 477
- Ho, L. C. 1999, ApJ, 516, 672
- Ho, L. C., et al. 2001, ApJ, 549, L51
- Ho, L. C., Filippenko, A. V., & Sargent, W. L. W. 2003, ApJ, 583, 159
- Ho, L. C. 2008, ARA&A, 46, 475
- Hoffman, G. L., Brosch, N., Salpeter, E. E., & Carle, N. J. 2003, AJ, 126, 2774
- Hopkins, P. F., Hernquist, L., Cox, T. J., Dutta, S. N., & Rothberg, B. 2008, ApJ, 679, 156
- Hopkins, P. F., Cox, T. J., Dutta, S. N., Hernquist, L., Kormendy, J., & Lauer, T. R. 2008, *In Preparation*
- Hopkins, P. F., Lauer, T. R., Cox, T. J., Hernquist, L., & Kormendy, J. 2008, *In Preparation*
- Horellou, C., Black, J. H., van Gorkom, J. H., Combes, F., van der Hulst, J. M., & Charmandaris, V. 2001, A&A, 376, 837
- Huchtmeier, W. K., Tammann, G. A., & Wendker, H. J. 1975, A&A, 42, 205

- Huchtmeier, W. K., Tammann, G. A., & Wendker, H. J. 1977, *A&A*, 57, 313
- Huchtmeier, W. K., Sage, L. J., & Henkel, C. 1995, *A&A*, 300, 675
- Jedrzejewski, R. I. 1987, *MNRAS*, 226, 747
- Jensen, J. B., Tonry, J. L., Barris, B. J., Thompson, R. I., Liu, M. C., Rieke, M. J., Ajhar, E. A., & Blakeslee, J. P. 2003, *ApJ*, 583, 712
- Jesseit, R., Naab, T., & Burkert, A. 2005, *MNRAS*, 360, 1185
- Jordán, A., et al. 2005, *ApJ*, 634, 1002
- Kaviraj, S., et al. 2007, *ApJS*, 173, 619
- Kaviraj, S., et al. 2008, *MNRAS*, 388, 67
- Kennicutt, R. C., Jr. 1998, *ARA&A*, 36, 189
- Khochfar, S., & Burkert, A. 2005, *MNRAS*, 359, 1379
- King, I. R. 1966, *AJ*, 71, 64
- Knapp, G. R., Guhathakurta, P., Kim, D.-W., & Jura, M. A. 1989, *ApJS*, 70, 329
- Koekemoer, A. M., et al. 2002, *ApJ*, 567, 657
- Kollmeier, J. A., et al. 2006, *ApJ*, 648, 128
- Kormendy, J., et al. 1997, *ApJ*, 482, L139
- Kormendy, J., Bender, R., Evans, A. S., & Richstone, D. 1998, *AJ*, 115, 1823
- Kormendy, J. 1999, *Galaxy Dynamics - A Rutgers Symposium*, 182, 124
- Kormendy, J., & Bender, R. 1996, *ApJ*, 464, L119

- Kormendy, J., Fisher, D. B., Cornell, M. E., & Bender, R. 2008, ApJS, in press
- Kormendy, J., & Sanders, D. B. 1992, ApJ, 390, L53
- Krolik, J. H. 1999, Active galactic nuclei : from the central black hole to the galactic environment /Julian H. Krolik. Princeton, N. J. : Princeton University Press, c1999.,
- Krist, J. E., & Hook, R. N. 1997, The 1997 HST Calibration Workshop with a New Generation of Instruments, p. 192, 192
- Kuntschner, H., et al. 2006, MNRAS, 369, 497
- Lacey, C., & Cole, S. 1993, MNRAS, 262, 627
- Laine, S., van der Marel, R. P., Rossa, J., Hibbard, J. E., Mihos, J. C., Böker, T., & Zabludoff, A. I. 2003, AJ, 126, 2717
- Lake, G., & Dressler, A. 1986, ApJ, 310, 605
- Lake, G., & Schommer, R. A. 1984, ApJ, 280, 107
- Larson, R. B. 1976, MNRAS, 176, 31
- Lauer, T. R. 1985, ApJ, 292, 104
- Lauer, T. R., et al. 1991, ApJ, 369, L41
- Lauer, T. R., et al. 1995, AJ, 110, 2622
- Lauer, T. R., Faber, S. M., Ajhar, E. A., Grillmair, C. J., & Scowen, P. A. 1998, AJ, 116, 2263
- Lauer, T. R., et al. 2005, AJ, 129, 2138

- Lauer, T. R., et al. 2007, *ApJ*, 662, 808
- Leitherer, C., et al. 1999, *ApJS*, 123, 3
- Lotz, J. M., Ferguson, H. C., & Bohlin, R. C. 2000, *ApJ*, 532, 830
- Lotz, J. M., Telford, R., Ferguson, H. C., Miller, B. W., Stiavelli, M., & Mack, J. 2001, *ApJ*, 552, 572
- Lotz, J. M., Miller, B. W., & Ferguson, H. C. 2004, *ApJ*, 613, 262
- Maraston, C. 1998, *MNRAS*, 300, 872
- Maraston, C. 2005, *MNRAS*, 362, 799
- Maraston, C., Nieves, L. A., Bender, R., & Thomas, D. 2008, *arXiv:0811.0619*
- Martin, D. C. et al. 2005, *ApJ*, 619, L1
- Mathews, W. G., & Brighenti, F. 2003, *ApJ*, 590, L5
- Mei, S., et al. 2007, *ApJ*, 655, 144
- Meusinger, H., Ismail, H. A., & Notni, P. 2007, *Astr.Nachr.*, 328, 562
- Michard, R., & Marchal, J. 1994, *A&AS*, 105, 481
- Mihos, J. C., & Hernquist, L. 1994, *ApJ*, 427, 112
- Mihos, J. C., & Hernquist, L. 1994, *ApJ*, 437, L47
- Morelli, L., et al. 2004, *MNRAS*, 354, 753
- Morganti, R., et al. 2006, *MNRAS*, 371, 157
- Mould, J. R., et al. 2000, *ApJ*, 529, 786

- Naab, T., & Burkert, A. 2003, *ApJ*, 597, 893
- Naab, T., Jesseit, R., & Burkert, A. 2006, *MNRAS*, 372, 839
- Negroponte, J., & White, S. D. M. 1983, *MNRAS*, 205, 1009
- Nagar, N. M., Falcke, H., & Wilson, A. S. 2005, *A&A*, 435, 521
- O’Connell, R. W. 1983, *ApJ*, 267, 80
- O’Connell, R. W. 1986, *Stellar Populations*, 167
- O’Connell, R. W. 1999, *ARA&A*, 37, 603
- O’Connell, R. W. 1999, *ARA&A*, 37, 603
- Ohl, R. G., et al. 1998, *ApJ*, 505, L11
- Ostriker, J. P. 1980, *Comments on Astrophysics*, 8, 177
- Pavlovsky, C., et al. 2006, "Advanced Camera for Surveys Instrument Handbook for Cycle 16", Version 7.1, (Baltimore: STScI)
- Peletier, R. F., Davies, R. L., Illingworth, G. D., Davis, L. E., & Cawson, M. 1990, *AJ*, 100, 1091
- Peletier, R. F., Davies, R. L., Illingworth, G. D., Davis, L. E., & Cawson, M. 1990, *AJ*, 100, 1091
- Peng, C. Y., Ho, L. C., Impey, C. D., & Rix, H.-W. 2002, *AJ*, 124, 266
- Peterson, R. C., Dorman, B., & Rood, R. T. 2001, *ApJ*, 559, 372
- Piner, B. G., Jones, D. L., & Wehrle, A. E. 2001, *AJ*, 122, 2954

- Pinkney, J., et al. 2003, ApJ, 596, 903
- Pogge, R. W., & Martini, P. 2002, ApJ, 569, 624
- Ponder, J. M., et al. 1998, AJ, 116, 2297
- Proctor, R. N., Forbes, D. A., Forestell, A., & Gebhardt, K. 2005, MNRAS, 362, 857
- Proctor, R. N., & Sansom, A. E. 2002, MNRAS, 333, 517
- Ravindranath, S., Ho, L. C., Peng, C. Y., Filippenko, A. V., & Sargent, W. L. W. 2001, AJ, 122, 653
- Rest, A., van den Bosch, F. C., Jaffe, W., Tran, H., Tsvetanov, Z., Ford, H. C., Davies, J., & Schafer, J. 2001, AJ, 121, 2431
- Rich, R. M., et al. 2005, ApJ, 619, L107
- Rix, H.-W., & White, S. D. M. 1990, ApJ, 362, 52
- Roberts, M. S. 1962, AJ, 67, 437
- Rossa, J., van der Marel, R. P., Böker, T., Gerssen, J., Ho, L. C., Rix, H.-W., Shields, J. C., & Walcher, C.-J. 2006, AJ, 132, 1074
- Rothberg, B., & Joseph, R. D. 2004, AJ, 128, 2098
- Sage, L. J., & Welch, G. A. 2006, ApJ, 644, 850
- Salpeter, E. E. 1955, ApJ, 121, 161
- Sánchez-Blázquez, P., Forbes, D. A., Strader, J., Brodie, J., & Proctor, R. 2007, MNRAS, 377, 759
- Sansom, A. E., Hibbard, J. E., & Schweizer, F. 2000, AJ, 120, 1946

- Sarzi, M., Rix, H.-W., Shields, J. C., Ho, L. C., Barth, A. J., Rudnick, G., Filippenko, A. V., & Sargent, W. L. W. 2005, *ApJ*, 628, 169
- Sarzi, M., et al. 2008, *Pathways Through an Eclectic Universe*, 390, 218
- Satyapal, S., Vega, D., Heckman, T., O'Halloran, B., & Dudik, R. 2007, *ApJ*, 663, L9
- Schawinski, K., et al. 2007, *ApJS*, 173, 512
- Schiavon, R. P., et al. 2006, *ApJ*, 651, L93
- Schiavon, R. P. 2007, *ApJS*, 171, 146
- Schiminovich, D., van Gorkom, J. H., van der Hulst, J. M., & Kasow, S. 1994, *ApJ*, 423, L101
- Schiminovich, D., van Gorkom, J. H., van der Hulst, J. M., & Malin, D. F. 1995, *ApJ*, 444, L77
- Schiminovich, D., Friedman, P. G., Martin, C., & Morrissey, P. F. 2001, *ApJ*, 563, L161
- Schinnerer, E., Böker, T., Emsellem, E., & Lisenfeld, U. 2006, *ApJ*, 649, 181
- Schlegel, D. J., Finkbeiner, D. P., & Davis, M. 1998, *ApJ*, 500, 525
- Schneider, S. E. 1989, *ApJ*, 343, 94
- Schweizer, F. 1982, *ApJ*, 252, 455
- Schweizer, F. 1978, in *IAU Symp. No. 77, The Structure and Properties of Nearby Galaxies*, ed. E. M. Berkhuijsen and R. Wielebinski (Reidel, Dordrecht), 279

- Sérsic, J. L. 1968, Cordoba, Argentina: Observatorio Astronomico, 1968
- Shields, J. C., Walcher, C. J., Böker, T., Ho, L. C., Rix, H.-W., & van der Marel, R. P. 2008, *ApJ*, 682, 104
- Simões, F., et al. 2007, *Planet. Space Sci.*, 55, 1978
- Sivakoff, G. R., Sarazin, C. L., & Irwin, J. A. 2003, *ApJ*, 599, 218
- Sivakoff, G. R., Martini, P., Zabludoff, A. I., Kelson, D. D., & Mulchaey, J. S. 2008, *ApJ*, 682, 803
- Soria, R., Fabbiano, G., Graham, A. W., Baldi, A., Elvis, M., Jerjen, H., Pellegrini, S., & Siemiginowska, A. 2006, *ApJ*, 640, 126
- Springel, V. 2000, *MNRAS*, 312, 859
- Springel, V., Di Matteo, T., & Hernquist, L. 2005, *MNRAS*, 361, 776
- Springel, V., & Hernquist, L. 2005, *ApJ*, 622, L9
- Springob, C. M., Haynes, M. P., & Giovanelli, R. 2005, *ApJ*, 621, 215
- Stephens, A. W., & Frogel, J. A. 2002, *AJ*, 124, 2023
- Temi, P., Brighenti, F., Mathews, W. G., & Bregman, J. D. 2004, *ApJS*, 151, 237
- Terashima et al., in prep.
- Thomas, D., Maraston, C., Bender, R., & Mendes de Oliveira, C. 2005, *ApJ*, 621, 673
- Tonry, J. L., Dressler, A., Blakeslee, J. P., Ajhar, E. A., Fletcher, A. B., Luppino, G. A., Metzger, M. R., & Moore, C. B. 2001, *ApJ*, 546, 681

- Toomre, A., & Toomre, J. 1972, *ApJ*, 178, 623
- Trager, S. C., Faber, S. M., Worthey, G., & González, J. J. 2000, *AJ*, 120, 165
- Trager, S. C., Faber, S. M., & Dressler, A. 2008, *MNRAS*, 386, 715
- Tran, H. D., Tsvetanov, Z., Ford, H. C., Davies, J., Jaffe, W., van den Bosch, F. C., & Rest, A. 2001, *AJ*, 121, 2928
- Tremaine, S. D. 1976, *ApJ*, 203, 72
- Tremaine, S., et al. 2002, *ApJ*, 574, 740
- Trujillo, I., Erwin, P., Asensio Ramos, A., & Graham, A. W. 2004, *AJ*, 127, 1917
- van der Marel, R. P., Rossa, J., Walcher, C. J., Boeker, T., Ho, L. C., Rix, H.-W., & Shields, J. C. 2007, *IAU Symposium*, 241, 475
- Vázquez, G. A., & Leitherer, C. 2005, *ApJ*, 621, 695
- Verdoes Kleijn, G. A., Baum, S. A., de Zeeuw, P. T., & O'Dea, C. P. 1999, *AJ*, 118, 2592
- Verdes-Montenegro, L., Yun, M. S., Williams, B. A., Huchtmeier, W. K., Del Olmo, A., & Perea, J. 2001, *A&A*, 377, 812
- Walcher, C. J., Böker, T., Charlot, S., Ho, L. C., Rix, H.-W., Rossa, J., Shields, J. C., & van der Marel, R. P. 2006, *ApJ*, 649, 692
- Wehner, E. H., & Harris, W. E. 2006, *ApJ*, 644, L17
- Welch, G. A., & Sage, L. J. 2003, *ApJ*, 584, 260
- Whitmore, B. C., McElroy, D. B., & Tonry, J. L. 1985, *ApJS*, 59, 1

- Williams, B. A., McMahon, P. M., & van Gorkom, J. H. 1991, *AJ*, 101, 1957
- Worthey, G. 1994, *ApJS*, 95, 107
- Wrobel, J. M., Terashima, Y., & Ho, L. C. 2008, *ApJ*, 675, 1041
- Yamada, Y., Arimoto, N., Vazdekis, A., & Peletier, R. F. 2006, *ApJ*, 637, 200
- Yang, Y., Zabludoff, A. I., Zaritsky, D., Lauer, T. R., & Mihos, J. C. 2004, *ApJ*, 607, 258
- Yi, S., Lee, Y.-W., Woo, J.-H., Park, J.-H., Demarque, P., & Oemler, A. J. 1999, *ApJ*, 513, 128
- Yi, S., Demarque, P., Kim, Y.-C., Lee, Y.-W., Ree, C. H., Lejeune, T., & Barnes, S. 2001, *ApJS*, 136, 417
- Yi, S. K., et al. 2005, *ApJ*, 619, L111
- Young, J. S., Xie, S., Kenney, J. D. P., & Rice, W. L. 1989, *ApJS*, 70, 699